

RIVER CHANNEL RESPONSE TO CHANGING GOVERNING  
CONDITIONS: RATIONAL REGIME MODELS AND  
EXPERIMENTAL OBSERVATIONS

by

BRETT CURTIS EATON

B.Sc. (Hons.), The University of British Columbia, 1995  
M.Sc., McGill University, 1999

A THESIS SUBMITTED IN PARTIAL FULFILMENT OF THE REQUIREMENTS FOR THE  
DEGREE OF

DOCTOR OF PHILOSOPHY

in

THE FACULTY OF GRADUATE STUDIES

(Department of Geography)

We accept this thesis as conforming  
to the required standard

THE UNIVERSITY OF BRITISH COLUMBIA

July 2004

© Brett Eaton, 2004

## ABSTRACT

Rational regime models can be used to develop meaningful frameworks for understanding reach scale alluvial channel response to environmental changes. The key obstacle to their general acceptance is that they cannot be analytically closed, and they predict a range of solutions that are theoretically viable. As a result, modellers have had to invent some sort of optimality criterion, many of which are conceptually unsatisfactory, in order to isolate unique solutions. The optimality criterion described here is understood physically in terms of flow resistance maximization for the *fluvial system*, which produces the most nearly stable, hence most likely configuration. The flow resistance for the system comprises three components: grain-scale flow resistance, bedform-scale form resistance, and reach-scale form resistance. Analyses using various other proposed optimality criteria demonstrate that, for bedload dominated streams, the choice of optimization is not critical, since, for unique values of slope, discharge and characteristic grain size, they predict nearly identical channel configurations. In particular, when the reach-scale form resistance dominates the system adjustment, the maximum flow resistance criterion becomes theoretically equivalent to the previously proposed minimum slope hypothesis.

The framework for evaluating channel response can be most generally represented as a series of three-dimensional surfaces in an alluvial state space defined by width/depth ratio, relative roughness and channel slope or – equivalently – dimensionless shear stress. Each surface represents the set of solutions for a unique value of bank strength. Experiments designed to test the theoretical implications associated with the maximum flow resistance criterion demonstrate that the system scale flow resistance responds as predicted. When the channel banks are as erodible as the bed, the reach-scale flow resistance is the dominant component of the system adjustment, resulting in a functional relation between the average water surface slope along the channel thalweg and the ratio of the sediment supply and the imposed discharge. This is equivalent to the well known and generally accepted graded relation between channel slope and sediment supply. When the banks are fixed, the channel slope remains nearly constant – as does the cross section shape – for a range of sediment supply rates. In this case, equilibrium seems to result from a textural modification of the bed surface and thus the grain scale or bedform flow resistance. These results are consistent with the concept of system-scale flow resistance being the key to understanding channel stability, and they indicate that the previous hypotheses, such as slope minimization, are too limited in the range of adjustments that they embrace.

The maximum flow resistance criterion says nothing about the process-form interactions that produce the characteristic adjustment for the experimental channels, which comprises the

development of a series of regular, alternating pools and riffles established within meander bends with constant meander amplitude. By reducing the scale of inquiry to that of individual morphologic units, such as riffles and pools, one arrives at a physically based understanding of the optimality criterion. A feedback mechanism between the local, cross sectional shear stress distribution, the local transport capacity, and the channel planform is presented. It predicts evolution of an initially straight channel toward a more sinuous path that stabilizes once the local transport capacity becomes equalized throughout the system (i.e. steady state fluid and sediment flux conditions are reached), and the cut banks at the meander apices reach a critically stable state. The longitudinal scale for this feedback process is related to the diffusion of a sediment wave across the channel, which sets a minimum wavelength for the resultant alternate bars. The regime model is re-formulated to characterize the individual morphologic units produced by the feedback process using two bounding geometries; a trapezoid, representing the typical riffle section, and an asymmetric triangle, representing the bar-pool sections at the meander apices. These two geometries correspond to the maximum and the minimum local shear stress variance, respectively. These solutions predict the theoretical limits for the slope and cross sectional shape for a given sediment supply and discharge. Comparisons between these predicted limits and the experimental data confirm the general applicability of this approach, despite the simplified model specification.

Ultimately, then, the form of the lateral adjustment can be understood as the product of a metastable dynamic, wherein individual cross sections are only conditionally stable. Trapezoidal solutions are susceptible to perturbations in their nearly uniform cross sectional shear stress distributions, which causes an evolution toward an asymmetric, triangular section that can transport the same sediment supply at a lower channel slope. The triangular sections are stable, only so long as sufficient centripetal acceleration occurs, generating a secondary circulation that permits an asymmetric cross section to persist. More generally, the cause of meandering in bedload streams is the result of the oscillation between two conditionally stable states, and thus reach-scale stability is produced by the continual transition from one conditionally stable state to the next. The fundamental instability of straight channels with uniform cross sectional distributions results in a trajectory toward increased channel sinuosity and decreased channel slope, which produces an increase in the system scale flow resistance via the reach-scale flow resistance component. The maximum flow resistance criterion (and, by extension, all equivalent optimality criteria) represents a formalism that permits a 1D model to describe a 3D reality, by encapsulating this dynamic.

## TABLE OF CONTENTS

ABSTRACT .....	ii
TABLE OF CONTENTS.....	iv
LIST OF TABLES .....	vi
LIST OF FIGURES .....	vi
ACKNOWLEDGEMENTS.....	xv
LIST OF INCORPORATED WORK.....	xvi
1.0 INTRODUCTION .....	1
1.1 Processes in Alluvial Stream Channels .....	3
1.2 Thesis Objectives.....	7
1.3 Thesis Structure Overview.....	8
2.0 RATIONAL REGIME MODEL.....	9
2.1 Background.....	9
2.2 Model Formulation .....	10
2.2.1 Conceptual Structure .....	10
2.2.2 Basic Equations .....	11
2.3 Rationale for Application to Alluvial Systems.....	18
2.3.1 Formative Discharge.....	18
2.3.2 Timescale.....	19
2.3.3 Bank Stability .....	20
2.3.4 Channel Shape .....	20
2.3.5 Formulation of Bed Material Transport.....	21
2.3.6 Formulation of Flow Resistance.....	22
2.4 Optimization .....	23
2.5 Defining a Dimensionless Alluvial State Space .....	27
2.5.1 Dimensionless Scaling Relations.....	29
2.5.2 Model Sensitivity to Choice of Optimization.....	32
2.5.3 Effect of Form Roughness .....	34
2.5.4 Limits of Applicability.....	37
2.5.5 Comparison with Existing Data.....	39
2.5.6 Construction of a Response Framework.....	45

3.0	EXPERIMENTAL DESIGN .....	48
3.1	Hypotheses for Experimental Tests .....	48
3.2	Scale Considerations and Model Limitations .....	49
3.3	Defining Geomorphic Equilibrium.....	51
3.4	Experimental Arrangements .....	52
3.4.1	Rationale for Experimental Arrangement.....	52
3.4.2	Objectives for the Various Experimental Phases.....	55
3.4.3	Experimental Apparatus .....	56
3.5	Measurement Techniques .....	58
3.5.1	Water Surface Elevations and Bed Topography.....	58
3.5.2	Sediment Transport and Bed Surface Texture.....	59
3.6	Limitations.....	59
4.0	EXPERIMENTAL RESULTS.....	61
4.1	Phases 1 and 2: Pilot Studies .....	61
4.2	Phase 3: Mobile Bank Experiments.....	65
4.2.1	Trajectories Toward Equilibrium.....	66
4.2.2	Constant Valley Slope Experiments .....	71
4.2.3	Constant Sinuosity Experiments.....	80
4.2.4	Non-graded Responses .....	86
4.2.5	Discussion of Phase 3 Experimental Results.....	88
4.3	Phase 4: Fixed Bank Experiments .....	93
4.3.1	Trajectories Toward Equilibrium.....	94
4.3.2	Equilibrium Results .....	102
4.3.3	Discussion of Phase 4 Experimental Results.....	108
5.0	PHYSICAL MODEL FOR SLOPE MINIMIZATION .....	111
5.1	Transport Capacity for Asymmetric Shear Stress Distributions.....	113
5.2	Slope Minimizing Feedback Mechanism .....	115
5.2.1	Characteristics of Positive Feedback Mechanism .....	116
5.2.2	Linking the Positive Feedback to Planform Adjustment and Stability.....	117
5.2.3	On the Persistence of the Instability .....	127
5.3	Comparisons with Experimental Data .....	129
6.0	IMPLICATIONS FOR REGIME THEORY .....	133
6.1	Experimental Evidence.....	133

6.2	A Revised Formulation of the Regime Model.....	134
6.2.1	The Maximum Variance Solution .....	135
6.2.2	Comparison of Minimum and Maximum Variance Solutions .....	141
6.2.3	Comparison with Experimental Results .....	146
7.0	CONCLUSIONS .....	149
8.0	REFERENCES .....	160

### LIST OF TABLES

Table 1:	Simulated dataset based on random pairs of $Q$ and $D_{50}$ .....	28
Table 2:	Power relations fit to dimensionless scale collapse.....	30
Table 3:	Power relations fit to braiding-meandering threshold .....	39
Table 4:	Slope coefficients for regression of bias against channel scale.....	44
Table 5:	Reference grain sizes for all experimental grain size distributions .....	56
Table 6:	Governing conditions and equilibrium response for Phase 3 experiments.....	66
Table 7:	Regressions of $S$ against $Q_b/Q$ .....	76
Table 8:	Armour ratios for Phase 3 experiments .....	77
Table 9:	Governing conditions and equilibrium response for Phase 4 experiments .....	94
Table 10:	Linear regression statistics for relation between armour ratios and sediment concentration.....	108
Table 11:	Coefficient for polynomial fits, per Equation 37.....	115
Table 12:	Regime solution comparison .....	142

### LIST OF FIGURES

Figure 1:	Definition diagram for trapezoidal geometry considered in this chapter, having an aspect ratio of approximately 25 for bank strength $\phi' = 50^\circ$ : (a) four-times vertical exaggeration; (b) true scale.....	11
-----------	---	----

Figure 2: Solution curves for the regime model subject to the constraints  $Q = 100 \text{ m}^3/\text{s}$ ,  $S = 0.003$ . Bedload concentration predicted using the Meyer-Peter and Muller (1948) equation for constant  $D_{50}$  (32 mm) and variable  $\phi'$  ( $40^\circ$ ,  $50^\circ$ ,  $60^\circ$  and  $70^\circ$ ) is plotted against (a) bed width of the solution cross section, and (b) aspect ratio (width/average depth). Bedload concentration for constant  $\phi'$  ( $= 50^\circ$ ) and variable  $D_{50}$  (22 mm, 32 mm, 45 mm) is plotted against (c) bed width, and (d) aspect ratio. ....17

Figure 3: Solution curve for regime model subject to the constraints  $Q = 100 \text{ m}^3/\text{s}$ ,  $Q_b = 50 \text{ kg/s}$ , and  $D_{50} = 32 \text{ mm}$ . The slope necessary to produce an equilibrium channel with the specified  $Q$  and  $Q_b$  for the given  $D_{50}$  is plotted against aspect ratio ( $W/d$ ).....18

Figure 4: Definition of the fluvial system. (a) defines the properties of the fluvial system that are constant at regime time scales: valley gradient ( $S_v$ ), valley length ( $L_v$ ), and total head drop ( $z_1-z_2$ ); as well as those that are variable: channel slope ( $S$ ) and channel length ( $L_c$ ).(b) illustrates, following Figure 2, that for a constant  $Q$ ,  $Q_b$ ,  $D_{50}$  and  $\phi'$ , a solution curve exists, for which a continuum of theoretically viable channels exist for slopes less than the valley slope ( $S_v$ ) and greater than the minimum slope ( $S_{min}$ ) capable of transporting the imposed sediment load. ....25

Figure 5: Friction factors for the channel ( $f$ ) and for the alluvial system ( $f_{sys}$ , arbitrarily assuming  $S_v = 0.0035$ ) are plotted against slope, assuming the same values of  $Q$ ,  $Q_b$  and  $D$  as in Figure 2, and setting  $\phi' = 50^\circ$ .....26

Figure 6: (a) Dimensionless scale relations between  $\tau^*$  and  $W/d$  for various bank strength values (represented by different  $\phi'$  values, in degrees). (b) Dimensionless scale relations between transport rate  $G$  (Parker, 1990) and channel shape  $W/d$ .....31

Figure 7: Relations of  $Q_b/Q$ , Froude number, and  $S$  with  $D/d$  for constant value of  $W/d$  (32) and  $\tau^*$  (0.067), for the paired values of  $Q$  and  $D$  in Table 1. ....32

Figure 8: Sensitivity of scaling relations to choice of optimizations (MTC, MSS and MUSP) for  $\phi' = 60^\circ$  and  $\phi' = 80^\circ$ .....33

Figure 9: Sensitivity of scaling relations to assumed form roughness. The form roughness, represented by the parameter  $C_{50}$ , is varied from 2 (open symbols) to 40 (closed symbols) for two different bank strength values. ....34

Figure 10: Effect of varying $C_{50}$ on (a) dimensionless scaling parameters, $W/d$ and $\tau^*$ ; and (b) scale measures, $W$ and $Q_b$ .....	35
Figure 11: Effect of varying $C_{50}$ on $\tau^*$ , $S$ , and $W$ . $Q$ , $D$ , $\phi'$ and $Q_b$ are held constant at arbitrary values of 383 m <sup>3</sup> /s, 44 mm, 40°, and 0.03 kg/s, respectively.....	36
Figure 12: Alluvial state diagram for $\phi' = 40^\circ$ , $50^\circ$ and $60^\circ$ , using the $W/d$ , $D/d$ , $\tau^*$ coordinate system. Parker's (1976) threshold for the inception of braiding is shown on the $\phi' = 60^\circ$ plane (solid line) .....	37
Figure 13: Braiding threshold for various values of $\phi'$ projected onto the $(D/d, W/d)$ plane .....	38
Figure 14: Comparison of channels developed in the laboratory and in the field with predicted scaling relations. (a) The data from laboratory experiments of Schumm and Khan (1972) are plotted on an alluvial scaling diagram based on the model assuming $\phi = 30^\circ$ , $\tau^*_c = 0.035$ (after Yalin, 1971b). "M" refers to channels exhibiting a meandering thalweg and/or planform, and "S" refers to straight channels. The lines represent scaling functions assuming various bank friction angles. (b) The average behaviour of natural gravel channels classified by bank vegetation class is plotted over the gravel bed scaling diagram (Figure 6) .....	40
Figure 15: Degree of under-prediction for unconstrained MTC models (given by the ratio $W_{predicted}/W_{observed}$ ) plotted against $Q_{bf}^{1/2}$ for gravel bed channels, classified according to bank vegetation density (Hey and Thorne, 1986). Linear regressions of $W_{predicted}/W_{observed}$ on $Q_{bf}^{1/2}$ for each vegetation type are shown (solid line), as is the mean degree of under-prediction in the absence of a vegetation effect i.e. class 1 (horizontal dashed line) .....	43
Figure 16: Data from meandering and braiding streams (Van den Berg, 1995) are plotted on the $W/d$ , $D/d$ plane. Threshold curves based on Parker's (1976) meandering-braiding equation are presented for a range of bank friction angles. ....	45
Figure 17: Optimum channel slope and scale ( $W/d$ ) as a function of $Q$ and $Q_b$ . For this case, $\phi' = 40^\circ$ , and $D_{50} = 32$ mm .....	46
Figure 18: Optimal channel slope and scale ( $W/d$ ) as a function of $\phi'$ and $Q_b$ . $Q$ is held constant at 100 m <sup>3</sup> /s, and $D_{50} = 32$ mm .....	47

Figure 19: Predicted relation between channel slope and sediment concentration (g/L) for an appropriately configured regime model, using a range of bank strengths. The circles represent the relation assuming $\phi' = 30^\circ$ , the upward pointing triangles $\phi' = 35^\circ$ and the downward pointing triangles $\phi' = 40^\circ$ .....	53
Figure 20: (a) bed material grain size distributions for Phase 1 to Phase 4 experiments. The range of grain sizes less than 354 $\mu\text{m}$ is shaded in grey. (b) design and experimental grain size distributions for Phase 3 experiments.....	57
Figure 21: Scour holes and sheets of sand deposited downstream (typical of Phase 1 experiments). Flow is from left to right.....	62
Figure 22: Initial stages of channel development during Phase 1 experiments, involving evenly spaced, paired scour holes. Flow is from left to right.....	62
Figure 23: Typical morphology for Phase 1 experiments, with overlapping unit bars and scour holes. Flow is from left to right. ....	62
Figure 24: Adjustment of system-scale friction factor during a Phase 1 experiment.....	63
Figure 25: Meandering pattern with alternate bars typical of Phase 2 experiments .....	64
Figure 26: Fractional transport analysis for Phase 2 experiments. $L_i$ is the proportion of the transported material for the $i^{\text{th}}$ size fraction, and $P_i$ is the corresponding proportion for the bed material .....	64
Figure 27: Typical bar texture for Phase 2 experiments, where the finer (white) sediment is found along the thalweg and the coarser material is found on the bar top.....	65
Figure 28: Thalweg locations during experiment 1-1. Flow is from right to left .....	67
Figure 29: Photograph of channel planform after 4 hours during experiment 1-1. The approximate thalweg location and flow direction are shown. ....	68
Figure 30: (a) Sediment transport (30 minute averages) recorded at the stream table outlet for experiments 1-1 and 1-3. For both experiments the sediment feed rate is 128 g/min, shown with a horizontal dashed line. (b) Comparison of the bed material and the transported material for experiment 1-1 .....	69
Figure 31: Thalweg locations and elevations during experiment 1-3.....	70

Figure 32: Water surface slope along the thalweg during experiments 1-5a and 1-5b.....71

Figure 33: System-scale flow resistance, indexed by  $f_{sys}$ , is plotted against time. The values of  $f_{sys}$  closest to the y axis represent the flow resistance in the initial rectangular channel cut straight down the stream table. ....73

Figure 34: Constant valley slope equilibrium channel configuration: (a) thalweg water surface slope (%) and (b) sinuosity (m/m) vs. sediment concentration in the typical units (g/L): the line in panel b has been fit by eye to the data having nearly the same  $S_{sys}$ . ....76

Figure 35: (a) Armour ratios for the constant  $S_v$  experiments, based on two separate definitions are plotted against sediment concentration. (b) Armour ratios plotted against the time available for armour development. Regression lines relating the armour ratios and the independent variable are shown. None is significant at  $\alpha = 0.05$ . (c) Grain size distributions for experiment 1-3 prior to the development of alternate bar morphology (lower part of the stream table at 11 hrs) and during the development of appreciable sinuosity (surface at 16 and 24 hrs). The average surface grain size distribution for the graded channel experiments with a duration of 1 hr are shown for comparison. ....78

Figure 36: Average  $W/d$  ratio is plotted against channel slope (a) and then against sinuosity (b) for the constant  $S_v$  experiments. Data calculated from all cross sections and from only the apex cross sections are plotted separately, and linear trends are fit to each data series.....79

Figure 37:  $S$  is plotted against sediment concentration for both sets of Phase 3 experiments. Symbols for equilibrium experiments (solid circles) are scaled to represent a measurement uncertainty of  $\pm 1$  standard error for estimates of  $S$ . The solid triangles represent  $Q_b/Q$  for non-equilibrium experiments based on the imposed governing conditions while the open ones represent  $Q_b/Q$  based on the measured sediment output in the same experiments. The anomalous experiment 1-7 is indicated by an open circle. ....81

Figure 38: (a) armour ratios for the experiments above the maximum sediment influx threshold (open triangles) are plotted against sediment concentration using the measured transport at the outlet. The same data for the graded channels that reached equilibrium after 1 hr are shown for comparison (circles). (b) the average  $W/d$  ratios for the above-threshold experiments are plotted against the same independent variable, while the data from the

graded constant  $L^*$  experiments are shown for comparison. Sinuosity for the above-threshold channels is presented in brackets .....82

Figure 39: (a) equilibrium  $f_{sys}^*$ , based on the effective width and depth scaling implicit in the constant sinuosity experiments, is plotted against  $Q_b/Q$  for the constant  $S_v$  experiments (grey circles), the graded constant  $L^*$  experiments (black circles), and the non-equilibrium constant  $L^*$  experiments (triangles). (b)  $f_{sys}^*$  is plotted against total stream power ( $\gamma QS$ ). In (a) the data are stratified (horizontal dashed line) by the degree to which the experimental channels produced the expected alluvial behaviour. In (b) the inferred maximum possible flow resistance is indicated by an envelop curve, drawn by eye (dashed line). .....83

Figure 40: Comparison of  $W_{eff}$  and  $d_{eff}$  for channels with similar sinuosity (and with  $Q = 3.4$  L/s), plotted against channel slope, with  $W$  and  $d$  predicted by a regime model assuming,  $\phi' = 30^\circ$ ,  $D = 2.0$  mm and specifying a range of entrainment thresholds for the bank material ( $\tau_c^*$  for the bank ranges from 0.04 to 0.05). .....85

Figure 41: Bed mobility for at-grade channels, for channels below the lower threshold ( $Q < 3.0$  L/s) and for channels above the upper threshold ( $Q_b > 450$  g/L). The proportion of the transported grain size in each size fraction ( $Li$ ) is normalized by the proportion of the bed material grain size in the same size fraction ( $Pi$ ), after Wilcock and Southard (1989). Material  $> D_{50}$  shown. ....88

Figure 42: Experimental apparatus for the fixed bank experiments. Flow is from left to right. The average thalweg alignment is indicated with a dashed line, as are the typical pool and riffle configurations. The bars are shown (schematically) in grey, as is the sediment feeder at the upstream end of the channel. The channel bank crests and the thalweg location are drawn to scale; the dimensions are in cm. ....95

Figure 43: Photograph after 4 hours (experiment 4-4), looking downstream from cross section 7, near the middle of the study reach .....95

Figure 44: The surveyed thalweg locations for all Phase 4 experiments are shown. The fixed bank alignments are shown for reference. The scale is in cm. ....96

Figure 45: Recorded sediment output for all Phase 4 experiments is plotted against time. The data represent 15 minute average transport rates, and are reported as a sediment concentration (g/L) to permit direct comparison. The experiment number is shown in the

upper right hand corner of the relevant panel. The sediment feed rate is shown for comparison (horizontal dashed line), as is the quasi-equilibrium sediment output during the last two hours of experiment 4-5 (dotted horizontal line). .....	97
Figure 46: Photograph of the channel near the outlet (below the study reach) after 4 hours (experiment 4-4) .....	98
Figure 47: Cross sections for experiment 4-2 at 1 hour and at 4 hours .....	99
Figure 48: Cross sections for experiment 4-3 at 1 hour and at 4 hours .....	100
Figure 49: Cross sections for experiment 4-4 at 2 hours and at 4 hours.....	101
Figure 50: Equilibrium thalweg slope plotted against sediment concentration. The data for the Phase 4 experiments that reached equilibrium are represented by black circles: a linear trend was fit to these data. The trend for the Phase 3 experiments with mobile banks is shown in grey, for comparison. Experiment 4-5 is indicated with a black triangle: the plotting position is based on the quasi equilibrium conditions during last two hours. Experiment 4-3 is indicated by the grey triangle, and the slope recorded at 4 hours is plotted based on the imposed sediment supply.....	103
Figure 51: Cross sections through the meander apices at 4 hours for various experiments. The sections for experiments that did not reach equilibrium (4-3 and 4-5) are shown in grey ..	105
Figure 52: Surface grain size distribution for fixed bank experiments. The proportion of the surface in each size class is shown for all Phase 4 experiments, except 4-2 (data missing). The experiments that reached equilibrium have grey-shaded bars. For reference, the distribution for the bed subsurface is shown with dashed lines.....	106
Figure 53: Analysis of surface grain size distributions for Phase 4 experiment. (a) relation between three indices of the cumulative grain size distribution and the governing condition, $Q_b/Q$ for the Phase 4 experiments. (b) fractional representation of the surface distribution, relative to the subsurface distribution. (c) logarithmic fits to relation between armour ratios and distance from threshold.....	107
Figure 54: Assumed shear stress distributions employed by the theoretical model to evaluate the transport capacity .....	113

Figure 55: (a) proportional increase in $TC$ relative to $\overline{TC}$ is plotted against excess shear stress for a range of relative variances ( $\beta/\beta_{max}$ ). (b) polynomial curves fit to the data from (a) are shown.....	116
Figure 56: A surface of excess $TC$ is generated from the curves shown in Figure 55a.....	117
Figure 57: Schematic diagram of cross sectional and planimetric adjustments resulting from the action of the positive and negative feedback described in Figure 55. ....	119
Figure 58: Flow chart representing the feedback responsible for the initiation of meander development and the feedback halting meander development at the equilibrium slope and sinuosity.....	120
Figure 59: (a) diffusion of a sediment wave originating at an initial perturbation. (b) the resultant morphology associated with a number of such equilibrium, morphologically expressed wave fronts.....	123
Figure 60: Relation between $\alpha$ from Equation 40 and Froude number for the constant sinuosity experiments reported in Chapter 4 (black circles) and the development of alternate bars in a straight channel (grey circles) reported by Garcia and Nino (1993). An approximate curve describing the general trend of the data was fit by eye. ....	126
Figure 61: Time to equilibrium versus initial specific discharge for stream table experiments..	129
Figure 62: Water surface slopes along the thalweg for three equilibrium channel configurations. The minimum slope in each bend is shown in bold italics, and the maximum is shown in bold. $S_c$ is 1.09 for these experiments. The direction of flow is from right to left. ....	131
Figure 63: Geometry of the maximum variance regime solution. (a) shows the two channel shapes with 4 times vertical exaggeration, and (b) at true scale.....	135
Figure 64: Sediment transport rate as a function of the thalweg depth ( $Y_o$ ) and the energy slope ( $S$ ), assuming an active width of 0.77 m. On the contour map in the lower panel, the threshold for zero transport is shown. The maximum variance solution for a sediment concentration of 0.63 g/L (see Table 12) is indicated on both panels with a grey circle.....	138
Figure 65: Calculated transport and the quadratic function fit to the data. $W_a = 0.77$ m, $S = 0.0065$ m/m, $D = 2$ mm.....	139
Figure 66: Coefficients for quadratic fits, assuming $W_a = 0.77$ m and $D = 2$ mm.....	140

Figure 67: Slopes for the minimum variance and maximum variance solutions given in Table 12 are plotted against sediment concentration.....143

Figure 68: The sediment concentration based on the polynomial fits that describe  $Q_b$  as a function of  $S$  and  $Y_o$ , is plotted against the sediment concentration based on evaluation of Equation 42 using the values of  $Y_o$  and  $S$  in Table 12. A one-to-one line is also shown.....144

Figure 69: A sensitivity analysis of the maximum variance solution to the imposed value of  $W_a$ . The proportional change in slope and  $Y_o$  is plotted against the normalized  $W_a$ .....144

Figure 70: a) the ratio of thalweg depth ( $Y_o$ ) to trapezoid depth ( $\bar{Y}$ ) is plotted against sediment concentration. b) the ratio of the maximum variance slope to the minimum variance slope is plotted against sediment concentration.....145

Figure 71: Ratio of predicted shear stress acting on the channel bank(s) to the average cross sectional shear stress. The maximum variance solutions are shown with the upward pointing triangles, the minimum variance solutions with the downward triangles. ....146

Figure 72: Measured average maximum and minimum slopes per half wavelength for the phase 3 experiments. The average slopes are shown for reference. The dashed lines represent linear fits to the data.....147

Figure 73: Ratios of the local slopes and depths from the Phase 3 experiments. The ratio of the local minimum slope to the local maximum slope and the ratio of the thalweg depth to the average depth are plotted against sediment concentration (a), and mean channel slope (b). The analogous ratios predicted by the regime model (shown in Figure 70) are reproduced as dashed lines.....148

Figure 74: Meandering as a product of oscillation between maximum variance attractor states with opposite polarity. The associated patterns of change for the local slope and cross sectional shear stress variance are shown on the right (variance = 0 implies a uniform shear stress distribution, while variance =1 implies the maximum variance of the shear stress distribution).....159

## ACKNOWLEDGEMENTS

Much of this thesis is derived from papers that I drafted in conjunction with Professors M. Church, R.G. Millar and T.R.H. Davies (see following page for details). I would like to especially acknowledge Professor Millar for his early and influential input, without which I would never have become a true believer. Additionally, Professor Church's guidance was critical: he realized before I did the potential for the ideas I was developing, and many of the original ideas in this work I can trace back to questions that he asked me. Many of the remaining original ideas I think originated from discussions with Professor Davies. Since in science, finding answers is trivial, provided one asks the right questions, these contributions are especially important, I think. I would also like to acknowledge Professor Davies's material support of the research: without access to his lab, and to the services of Warwick Hill (Chief Technician), the experimental results would not be nearly as convincing as they are. At a more basic level, I would like to thank my friend Marwan, whose encouraging words from as far back as 1992 have kept me on the road of geomorphic inquiry. His advice (for which he keeps threatening to send me a bill) on various matters both scientific and general is also greatly appreciated. I also must thank my wife, Isabelle, who, in the face of what could have been an outrageous and fatal imposition on our personal relationship – a year spent on the other side of the world – helped me to turn it into a positive experience from which I think that our friendship has benefited, and from which my professional career has certainly benefited. As a result of her continued support since my return, I have nearly regained whatever degree of sanity I once had. I only hope that someday I can do enough to repay her. There are also those graduate students and technical assistants upon whom I have imposed to discuss my ideas (J. Tunnicliffe, especially) and for help in the lab (J. Rempel in particular) – thank you to all of you. This research was supported by the Natural Sciences and Engineering Research Council of Canada through a fellowship to B.E. and research grants to M.C. and R.M.

## LIST OF INCORPORATED WORK

Eaton BC, Church M, Millar RG. 2004. Rational regime model of alluvial channel morphology and response. *Earth Surface Processes and Landforms*, 29: 511-529. *This paper is incorporated in Chapter 2 nearly in its entirety. B. Eaton conducted the analysis, wrote the manuscript, and produced the figures. The work originated as the proposal for the current Ph.D. thesis. M. Church helped to guide the process at each step, and R. Millar suggested the regime model approach: he is also largely responsible for the regime model formulation used.*

Eaton BC, Millar RG. 2004. Optimal alluvial channel width under a bank stability constraint. *Geomorphology*: DOI 10.1016/j.geomorph.2004.02.003. *The original idea for this work came from R. Millar, although B. Eaton conducted the analysis, prepared the figures and wrote the manuscript. The investigation of scaling issues associated with bank vegetation – which has been incorporated in Chapter 2 – was original work by B. Eaton. The remainder of the paper has not been directly incorporated in this thesis, but represents the ideological footing upon which it is firmly planted.*

Eaton BC, Church M. *In Press*. A graded stream response relation for bedload dominated streams. *Journal of Geophysical Research – Earth Surface*. *This paper presents the primary results and interpretation of experiments conducted by B. Eaton in support of this thesis, and forms the basis for most of Chapter 4 and parts of Chapters 3 and 7. The analysis, figure preparation and writing were conducted by B. Eaton, with input from M. Church at several stages.*

Eaton, B.C. and Davies, T.R.H. *In Preparation*. A physical basis for slope minimizing behavior in bedload dominated streams. *This theoretical contribution is presented as Chapter 5 of this thesis. The ideas behind the work came from discussions between B. Eaton and T. Davies. B. Eaton developed the ideas, conducted the modeling, and prepared the manuscript and figures. The paper is currently being revised based on further developments presented in this thesis, and will be submitted to a peer-reviewed journal.*

## 1.0 INTRODUCTION

Rivers have been and continue to be substantially impacted by human civilization. It is increasingly obvious that humans are, in general, altering the physical environment in important and irreversible ways. It is accepted by the scientific community that the Earth's climate has changed as a result of atmospheric pollutants generated by our increasingly industrialized and motorized populations. As a result, global hydrology seems to be changing, and is likely to continue changing, with unknown impacts on alluvial systems. In addition to changes associated with climate and hydrology, rivers are being affected by deforestation of their floodplains, direct alteration of channel processes by so-called "hard" engineering projects, alteration of their sediment supply and hydrologic regime by hydro-electric projects, re-alignment of their stream courses to accommodate development and reduce flood risks, and by progressive changes of land use throughout their basins, which combine elements of all of the above. In the foreseeable future, these impacts are likely to intensify and, once significant numbers of high-head dams exceed their design life and must be removed, a new suite of impacts is likely to emerge wherein sediment supply will increase dramatically unless mitigated by other hard engineering solutions.

Environmental managers are being asked to take measures to mitigate the potential effects on stream channel environments. They are being asked to protect aquatic ecosystems, ensure that water quality is maintained and to manage flood and erosion risks to human development adjacent to stream channels. There appears to be the political will to "do the right thing" in much of North America and, in the current social climate, where environmental advocates wield substantial economic power, there is no economic benefit to exploiting our natural resources in an environmentally unsound (that is, socially unacceptable) way. But what are the anticipated and extant impacts on stream channel environments? The scientific basis available to environmental managers upon which to judge these matters is incomplete. In particular, there is no generally accepted, unambiguous model of stream channel response to changes of the type described above. The knowledge that does exist tends to be site specific and the explanations of channel response tend to be quite complicated. As a result, judging actual or potential channel impacts and devising appropriate risk-avoidance or mitigative measures is very difficult. Even experts in the field are often left guessing.

This work is an attempt to develop a conceptually transparent framework for evaluating the potential response of stream channels to changes in the forcing factors, such as climate and

sediment supply, and to changes affecting the channel boundary. The theoretical framework is based on a one dimensional rational regime approach, which represents most of the processes that are known to affect channel dynamics, but in a very simplified form. Rather than a weakness, the simplicity of this 1D approach is a strength, since it ensures that the disturbance-response relations remain transparent. This point becomes clear in the following example. Researchers are developing increasingly complex 2D and 3D spatially distributed models of channel hydraulics and coupling them with sediment transport formulae. When enough of the physical processes are replicated in a model that one can accurately predict channel shape and channel change, one may remain ignorant of the process interactions producing that shape, since the spatial interactions within the model (i.e. at scales larger than the individual cells) are not explicitly identifiable, and thus they remain hidden, just as they are hidden in reality. Such models are not conceptually transparent, since it is not clear *how* or *why* they produce the observed behaviour, only that they *do* reproduce it, and are really best interpreted as virtual reality experiments, instead of pedagogic models: in this respect, they are superior to black box, statistical or empirical models (such as hydraulic geometry relations), since the process interactions are there to be seen, if one knows what to look for. It is just that the process interactions need not specified explicitly in the model, they are implicit in the interactions between cells in a physically distributed model. To understand geomorphic processes, it is necessary to make some degree of abstraction, to reduce the problem to the level where the process can be represented explicitly (i.e. analytically).

On the other hand, if one uses a model that over-simplifies the processes, one may lose the essence of the system dynamics. This requires some form of comparison with reality. Data of the sort that one would need to make a meaningful comparison of regime model predictions against channels in the field are not easily collected, and such comparisons are usually indeterminate. There is an alternative: physical models, or laboratory experiments, reproduce the full range of complexity, since they involve neither approximations nor simplifications. In such models the forcing factors can be known to a much greater degree of certainty than in the field, and the system dynamics are assured to be similar to those operating in the field. There are scaling issues involving the magnitude of the forces modeled and the timescale over which they act (and vary). There is also the issue of system history: the alluvial system in the field has a history that produces non-uniformities in the distribution and character of the sediment and of the channel morphology, whereas the laboratory experiment has no such history. There are also

processes acting in the field that cannot easily be replicated in the laboratory, perhaps the most important of which are the role of suspended sediment transport and of surface colonization by vegetation.

Despite these limitations, comparisons of a simple model (rational regime theory) and a more complete – if admittedly not perfect – model (laboratory experiment) seem to be the best hope for developing and validating a conceptually transparent framework for understanding channel response. The remainder of this chapter presents the background material necessary to understand the relevant issues, the rational regime theory, the experimental tests and a combined understanding of channel response. It concludes with a formal statement of the thesis objectives and a summary of the thesis structure.

## 1.1 PROCESSES IN ALLUVIAL STREAM CHANNELS

Alluvial channel morphology has long been *qualitatively* understood to reflect the action of several key factors, or governing conditions (Mackin, 1948; Lane, 1957), the most important of which comprise: (i) the time distribution of fluid flow,  $Q(t)$ ; (ii) the time and size distribution of sediment flux,  $Q_b(t,D)$ ; (iii) the longitudinal valley slope,  $S_v$ ; (iv) the boundary materials and strength, including vegetation; and (v) the geological history. While it is possible to distinguish single thread from multiple thread channels in a general way, based on characteristics of the stream channel (Lane, 1957; Leopold and Wolman, 1957; Henderson, 1966; Parker, 1976; Begin, 1981), it is much more difficult to predict the sinuosity of single thread channels, (e.g. Van den Berg, 1995; Dade, 2000). Similarly, our understanding of channel response to changes in the governing conditions is incomplete. The current understanding of channel response has generally been summarized in tables showing the possible direction and/or likelihood of an adjustment in some aspect of the channel geometry (e.g. width, depth, slope) to changes in, primarily, discharge and sediment supply. These summaries are indeterminate, since one or more channel response remains undefined. For example, Schumm's (1969) analysis suggests that, in response to a simultaneous increase or decrease in both  $Q$  and  $Q_b$ , mean depth and sinuosity may either increase or decrease. These summaries are based on empirical hydraulic geometry relations (discussed below), field evidence and the typical form of relations predicting sediment transport and flow resistance (Schumm, 1971; Kellerhals and Church, 1989; Montgomery and Buffington, 1998).

The first attempts at discerning *quantitative* process-form relations between these governing conditions and channel morphology resulted from studies of stable canals in India. Kennedy (1895) observed that stable canals – those that were able to transport the imposed sediment loads while neither aggrading nor degrading – exhibited a relation between velocity and depth of the form:

Equation 1 .....  $v = \alpha(d)^\eta$

Where  $v$  is the mean velocity and  $d$  is the water depth: the coefficient  $\alpha$  and exponent  $\eta$  were found to be site-specific parameters. However, this relation ignores the more general canal geometry, which includes the additional parameters of channel width ( $W$ ) and slope ( $S$ ). Lindley (1919) identified this issue, and proposed the concept of “regime”, wherein the canal geometry is adjusted to some stable configuration that, while modified locally, does not change detectably over time.

The work on Indian canals was consolidated by Lacey (1930) who attempted to generalize the site-specific, empirical equations, by introducing the silt factor ( $F = 8\sqrt{D}$ , where  $D$  is the bed material particle diameter in inches) to account for the composition of the boundary materials. He attempted to define generally applicable relations between the adjustable quantities for canal geometry,  $P$ ,  $R$  and  $S$  (where  $R$  is the hydraulic radius and  $P$  is the wetted perimeter), and the governing conditions,  $Q$  and  $F$ . His results are summarized in three equations:

Equation 2 .....  $v = 1.17\sqrt{FR}$

Equation 3 .....  $P = 2.67\sqrt{Q}$

Equation 4 .....  $v = 16R^{2/3}S^{1/3}$

All equations assume values in foot-second units. Equation 4 comes from combining a sediment transport law and a resistance law to eliminate bed material calibre (Henderson, 1966 p. 457). Blench (1969) further developed this method by defining separate silt factors describing the bed

state  $\left(F_b = \frac{v^2}{d}\right)$  and the bank state  $\left(F_s = \frac{v^3}{W}\right)$ , which are incorporated in a similar set of three equations, so as to accommodate a wider range of canal configurations. He also included the effect of sediment concentration in his regime formulation, after Inglis (1949).  $F_b$  is clearly related to the Froude number, and  $F_s$  is a measure of the shear stress on banks under hydraulically smooth conditions (Richards, 1982 p. 292). Blench also presents an interpretation of the three equations as dynamical statements<sup>a</sup> about canal behaviour, but they are not convincing, especially since his equations do not seem to be generally applicable (c.f. Simons and Albertson, 1963). The sets of equations presented by Lacey and Blench both predict general channel scaling relations of the form:

Equation 5 .....  $W \propto Q^{1/2}$

Equation 6 .....  $d \propto Q^{1/3}$

Equation 7 .....  $S \propto Q^{1/6}$

Lacey (1930) originally selected simple exponents that were consistent with the data for his analysis, since he thought that these were most likely to represent physically based, general relations.

Simons and Albertson (1963) further generalized this approach by identifying additional sedimentologic classes of canals and then empirically determining the coefficients for equations similar to Equation 5, Equation 6, and Equation 7. In effect, they abandoned any attempt to procure a physically based theoretical framework, and focused on calibrating a useful, empirical design tool. In a sense, the necessity for class-specific calibration of the sort that Simons and Albertson (1963) present demonstrates that the “theory” of canal regime, as summarized above, is not fundamental, but instead is fundamentally empirical.

---

<sup>a</sup> They are: (i) channels with the same water and sediment mixture attain similar Froude numbers by adjusting their depth; (ii) erosion of the sidewalls is proportional to the side wall factor,  $F_s$ ; and (iii) channels with the same  $F_b$  and  $F_s$  adjust to the same rate of energy dissipation

By direct inference any attempts to fit analogous empirical functions to alluvial river channels will, while informative, be similarly theoretically impoverished. This sort of work was first pioneered by Leopold and Maddock (1953), who identified general hydraulic geometry relations between channel geometry ( $W$ ,  $d$  and  $S$ ) and discharge that had similar exponents to those characteristically adopted for regime canal equations:

Equation 8.....  $W \propto Q^{0.5}$

Equation 9.....  $d \propto Q^{0.4}$

Equation 10.....  $S \propto Q^{-0.49}$

Others have persisted in using the hydraulic geometry approach to study process-form relations (e.g. Bray, 1975; Hey and Thorne, 1986; Van den Berg, 1995; Huang and Nanson, 1998), with some success. Notably, Hey and Thorne (1986) and Andrews (1984) have been able to demonstrate the effect of vegetation on channel form using hydraulic geometry relations. They have also been able to demonstrate the effect of bed material texture and estimated sediment load on the equilibrium slope, although they cannot provide a theoretical explanation for it (nor do they attempt to do so). Hey and Thorne also propose that channel sinuosity – an element of geometry not present in stable canals – can be related to their hydraulic geometry equation once the valley slope is known, thereby making an explicit link between cross sectional characteristics and planimetric ones.

Various *rational regime* approaches have been developed in an attempt to construct a physically based theory for the hydraulic geometry of self-formed stream channels. These theories have been based on one of two ideas: the threshold approach and the maximum efficiency approach (Ferguson, 1986). In the threshold approach (Lane, 1955; Henderson, 1966; Stevens, 1989), the channel at bank full is assumed to be everywhere at the threshold of motion (c.f. Dade and Friend, 1998, bedload channels). By applying continuity, a flow resistance law, and assuming a uniform flow approximation for estimating local shear stress, stable cross sectional geometries are solved. For a given discharge and sediment size, a range of stable channel widths and slopes can be found, ranging from narrow, deep sections with an approximately parabolic shape at low slopes to wider, shallower shapes with a horizontal bed and parabolic banks at higher slopes.

These analyses are thus indeterminate, since they predict no unique solution. However, by using the narrowest stable section, a theoretical set of hydraulic geometry equations can be generated, similar to the characteristic hydraulic geometry of natural channels (Henderson, 1966 p. 454; Li et al., 1976). This approach is adequate for describing stable canals that do not mobilise their beds, but it is not sufficient for channels that can deform their bed and banks, even when the shear stress at bank full is near the critical value for entrainment.

For channels that are assumed to transport their bed material, another approach is necessary, based on some representation of Gilbert's (1914) principle of maximum efficiency, wherein a channel is assumed to adjust so that its bedload is transported most efficiently (Ferguson, 1986). In place of the threshold shear stress condition, a sediment transport law is added. In the same way as a threshold channel geometry can be identified for a range of slopes, a given transport rate can be produced by channel shapes ranging from narrow and deep (at low slopes) to wide and shallow (high slopes), hence the necessity of some additional principle like that proposed by Gilbert (1914). Various principles of stream channel behaviour have been advanced (Langbein and Leopold, 1966; Yang, 1976; Kirkby, 1977; Chang, 1979; White et al., 1982; Davies and Sutherland, 1983; Cao, 1996; Huang and Nanson, 2000) in order to select a unique solution from within this range and, more importantly, to elucidate the basis for the process-form interactions giving rise to the observed hydraulic geometry for streams in the field.

Many of these principles turn out to be equivalent (White et al., 1982; Davies and Sutherland, 1983), but none is based on a satisfactory physical explanation, nor have their proponents been able to identify the process-form interaction by which the proposed action is achieved. Nevertheless, this avenue of inquiry still appears to represent the best hope for gaining a physically based understanding of reach-scale channel dynamics.

## 1.2            **THESIS OBJECTIVES**

The **general objective** of this thesis is the development and validation of a theoretical framework for understanding the equilibrium channel response to changes in the governing conditions. The **specific objectives** are: (i) to critically assess the potential for using a regime model as a channel response framework; (ii) to experimentally test *the hypotheses that establish the validity of such a model*; and (iii) to relate the reach-scale dynamics described in a regime model to the process-form interactions that occur at the scale of individual morphologic units.

**Chapter 2** presents a critical review of the applicability of the rational regime approach, and presents a dimensionless framework for evaluating potential channel response for single thread channels (regime models are not well suited to modelling multiple thread configurations because of the simple geometry assumed in such models). Comparisons of the theory with published data from natural and laboratory channels are also presented. The experimental apparatus used to investigate the identified hypotheses is described in **Chapter 3**, as are the critical hypotheses that test the key assumptions made in the model formulation. Two different sets of equipment and, to a lesser extent, sets of techniques, are described. One of the stream tables described is located at the Soil and Water Laboratory at Lincoln University, Canterbury, New Zealand, where the mobile bank experiments were performed. The other stream table is at the University of British Columbia, Canada, where various pilot studies were initially run, and where the fixed bank experiments were conducted. **Chapter 4** presents the results of the experiments. The primary modes of channel response to changes in the governing conditions are identified and described in this chapter. The objective of the experiments described in Chapters 3 and 4 is to verify whether or not the regime approach is an appropriate candidate for a model of channel response to changes in the governing conditions. An additional theoretical model that refines the original understanding of the optimality criterion used in the regime model, based on observations of the process-form interactions occurring during the experiments, is presented in **Chapter 5**. In **Chapter 6**, the rational regime model is reformulated based on the implications of the theory in Chapter 5. The traditional reach-scale 1D description of an alluvial system is abandoned for a pseudo-2D description based on two possible regime solutions. This revised formulation describes the longitudinal variation of local slope and bed geometry within a single meander. The individual rational regime solutions in this formulation are interpreted as individual riffle or bar-pool units, rather than representations of alluvial stream reaches. A summary of the findings and the conclusions is presented in **Chapter 7**.

## 2.0 RATIONAL REGIME MODEL

In this chapter, a rational regime model invoking a bank stability constraint is presented and critically examined. Throughout this chapter, the regime model solutions are viewed as 1D descriptions of an alluvial stream reach. Thus, the solution width, depth and slope correspond to the channel width, depth and slope averaged over (at least) one meander wavelength. Even with the introduction of a bank stability constraint, the available set of equations remains incomplete. To obtain explicit solutions, some optimality criterion must be adopted. A physical explanation for the necessary optimality criterion is presented, based on the maximization of the system scale flow resistance. A dimensionless framework describing the alluvial state is derived, which can be used as a model of channel response to changes in the governing conditions, and is compared with existing data from alluvial channels in the field and in the laboratory.

## 2.1 BACKGROUND

A quantitative understanding of alluvial channel form and response to changes in governing conditions remains an important yet elusive goal in fluvial geomorphology. Arguably the nearest approach so far is embodied in the various regime equations constructed to predict the geometry of unlined irrigation canals (Lacey, 1930; Simons and Albertson, 1963; Blench, 1969, amongst others). These developments were essentially empirical, as were their adaptation to describe river channels in the form of hydraulic geometry (Leopold and Maddock, 1953).

Rational regime theory formalizes the relations amongst governing equations traditionally applied to predict the geometry of mobile-bed canals. The geometry of a canal is governed by three relations: (i) a bed material transport equation; (ii) a flow resistance equation; and (iii) a bank stability criterion (Henderson, 1966 p. 451). Since the geometry of an alluvial channel is related primarily to the transport and deposition of the sediment found in it, the sediment transport equation must reflect bed material load, rather than the total load. If the discharge ( $Q$ ), sediment transport rate ( $Q_b$ ), and sediment calibre ( $D$ ) are specified, a canal geometry comprising gradient ( $S$ ), hydraulic radius ( $R$ ) and wetted perimeter ( $P$ ) can be calculated. However, the bank stability criterion does not impose a unique value since there is a range of canal geometries that satisfy the bank stability constraint (Henderson, 1966).

Rivers are not subject to the same controlling conditions as canals. An important difference is the larger temporal variation in both water and sediment supplies that most rivers experience. In

alluvial rivers, moreover, channels are self-formed and may migrate. The sediment and water supplied to the channel are assumed to be transported with no net change in channel form despite sediment exchange and active lateral migration, provided that the stream is, in some sense, at equilibrium. Valley gradient ( $S_v$ ) remains constant at the timescale upon which channel geometry and alignment adjust and therefore represents an important constraint on the system – the steepest gradient that the channel may adopt over any significant distance. However, as in the case of bank stability,  $S_v$  merely establishes a limit to the range of possible solutions.

To close the regime description of alluvial streams, researchers have resorted to applying some sort of optimality criterion to the solution curves generated by the three governing relations. Accordingly, various hypotheses have been invoked, including minimum unit stream power (Yang, 1976), maximum sediment transport efficiency (Kirkby, 1977), minimum stream power (Chang, 1979), maximum sediment transport capacity (White et al., 1982), and maximum friction factor (Davies and Sutherland, 1983). Under appropriately defined circumstances, many of these conditions turn out to be equivalent (White et al., 1982; Davies and Sutherland, 1983). In a variation on this theme, Huang and Nanson (2000) employed the principle of least action to demonstrate the equivalence of minimum stream power and maximum sediment transport capacity. A slightly different approach was presented by Cao (1996), wherein a regime theory is based on the assumption that – for a system at equilibrium – the probability of width adjustment is the same as that for depth adjustment.

## **2.2 MODEL FORMULATION**

### **2.2.1 Conceptual Structure**

The present model is based on that presented by Millar and Quick (1993), which explicitly considers the role of bank strength. The system of equations that forms the model framework includes equations for evaluating flow resistance, sediment transport and bank stability. The model assumes a trapezoidal cross section with banks at an angle  $\theta$  from the horizontal (Figure 1), the dimensions of which are iteratively varied to solve the relevant system of equations subject to the appropriate constraints (see Millar and Quick, 1993). It is designed to describe single thread channels only, and is less apt to adequately describe wandering or braided channels, due to the geometry upon which the model is based.

In practice, the model works by specifying the formative discharge ( $Q$ ), gradient ( $S$ ), and characteristic grain size ( $D$ ). The bottom width ( $P_{bed}$ ), water depth ( $Y_o$ ) and side slope ( $\theta$ ) are

then iteratively varied to produce channels wherein continuity is maintained ( $Q = vA$ , where  $v$  is the mean velocity and  $A$  is the area of the trapezoidal cross section) and the banks are critically stable. The stability of the banks is assessed by determining the mean shear stress exerted on them, and comparing that to the threshold for bank entrainment. Solutions can be generated for a range of bottom widths, but – for a given value of  $P_{bed}$  – the solution is associated with unique values of  $Y_o$  and  $\theta$ . This yields a solution curve defining channels over a range of bottom widths and with a range of sediment transport capacities.

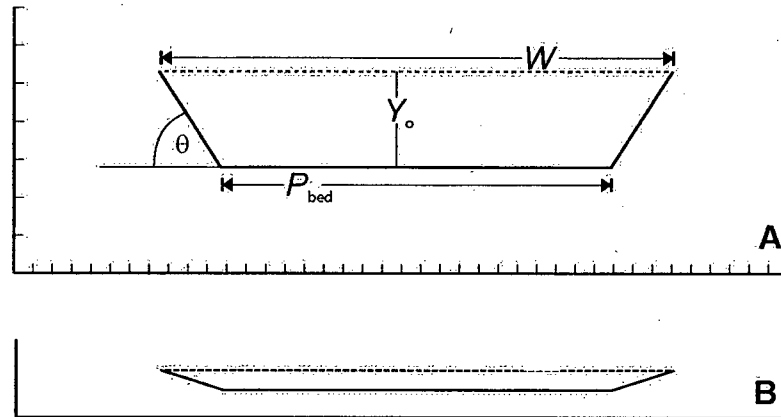


Figure 1: Definition diagram for trapezoidal geometry considered in this chapter, having an aspect ratio of approximately 25 for moderately strong banks ( $\phi' = 50^\circ$ , in Equation 16): (a) four-times vertical exaggeration; (b) true scale.

### 2.2.2 Basic Equations

The system of equations that forms the model framework includes equations for evaluating flow resistance, sediment transport and bank stability. Of course, continuity of flow is also used to constrain the model. The mean flow velocity is calculated using the Darcy-Weisbach equation:

Equation 11 ..... 
$$v = \sqrt{\frac{8gRS}{f}}$$

where  $g$  is the acceleration of gravity,  $S$  is the energy gradient, and  $f$  is the friction factor, calculated using the Keulegan equation:

Equation 12.....  $\frac{1}{\sqrt{f}} = 2.03 \log \left( \frac{12.2R}{k_s} \right)$

where  $k_s$  is the equivalent roughness, given by  $k_s = C_{50}D_{50}$ .  $C_{50}$  is a multiplier to account for form roughness. For most trials,  $C_{50}$  is given a value of about 6.8 (after Millar, 2000), although  $C_{50}$  is observed to vary in natural streams from about 1 to 40, representing varying degrees of form-related roughness (Millar, 1999). Since there is currently no predictive relation for form roughness in alluvial channels, the effect of increasing form roughness is examined in the subsequent analyses by varying the value of  $C_{50}$ .

Bank stability is evaluated after distributing the shear stress between the bed and the banks. The percent of the total shear force exerted on the channel banks ( $SF_{bank}$ ) is estimated, then used to calculate the mean shear stress exerted on both the bed and banks (Knight, 1981; Knight et al., 1984; Flinham and Carling, 1988). The equations presented below are empirical, and were derived from measured velocity distributions in rectangular and trapezoidal channels, from which the mean shear force on the bed and banks were estimated. The basic equation is:

Equation 13.....  $\log SF_{bank} = -1.4 \log \left( \frac{P_{bed}}{P_{bank}} + 1.5 \right) + 0.25$

wherein the proportion of the shear force acting on the bank is related to the shape of the channel, indexed by the ratio of the wetted perimeter of the bed to that of the bank ( $P_{bed}/P_{bank}$ ). Since the

average shear stress acting on the bank is given by  $\tau_{bank} = \tau_{total} P_{total} \left( \frac{SF_{bank}}{P_{bank}} \right)$ , and knowing that

$\tau_{total} P_{total} = \tau_{bank} P_{bank} + \tau_{bed} P_{bed}$ , equations for predicting  $\tau_{bank}$  and  $\tau_{bed}$  based on a trapezoidal channel geometry can be worked out. The relevant equations are:

Equation 14.....  $\frac{\tau_{bank}}{\gamma Y_o S} = SF_{bank} \left( \frac{(W + P_{bed}) \sin \theta}{4 Y_o} \right)$

Equation 15.....  $\frac{\tau_{bed}}{\gamma Y_o S} = (1 - SF_{bank}) \left( \frac{W}{2 P_{bed}} + 0.5 \right)$

where  $\tau$  is the shear stress,  $Y_o$  is the maximum water depth,  $W$  is the width of the channel and  $\gamma$  is the unit weight of water. The subscripts are self-evident. The stability of the bank is assessed by comparing the value  $\tau_{bank}$  calculated from Equation 14 with a bank stability criterion (after Millar and Quick, 1993).

The entrainment threshold for the bank is based on the particle size of the bank material ( $D_{50bank}$ ), the angle of the bank ( $\theta$ ) and an apparent friction angle ( $\phi'$ ) that incorporates the effects of vegetation and bulk sediment properties. It can be expressed as a modified Shields-type relation:

$$\text{Equation 16} \dots\dots\dots \tau^*_{cb} = \frac{\tau_{bank}}{(\gamma_s - \gamma)D_{50bank}} = \tau^*_c \frac{\tan \phi'}{\tan \phi} \sqrt{1 - \frac{\sin^2 \theta}{\sin^2 \phi'}}$$

where  $\tau^*_{cb}$  is the critical value of the Shield's parameter for the bank,  $(\gamma_s - \gamma)$  is the submerged weight of the sediment grains,  $\tau^*_c$  is the critical dimensionless shear stress for bed material of the same calibre as the bank, and  $\phi$  is the angle of repose. The behaviour of Equation 16 is such that, in the limit as the bank slope approaches its maximum value ( $\theta \rightarrow \phi$ ), the threshold for entrainment approaches zero ( $\tau^*_{cb} \rightarrow 0$ ), whereas in the limit as the bank slope approaches its minimum value ( $\theta \rightarrow 0$ ), the threshold for entrainment is maximized ( $\tau^*_{cb} \rightarrow \tau^*_c \frac{\tan \phi'}{\tan \phi}$ ),

which reflects the action of vegetation and/or the bulk properties of the bank sediment in delaying grain entrainment. The algebraic form of Equation 16 is based on an elementary consideration of the forces acting on a particle on a slope ( $\theta$ ) with a known angle of repose ( $\phi$ ) (see Henderson, 1966 p. 419 for a derivation from first principles). The modifications presented by Millar and Quick (1993) account for the apparent increase in bank strength by invoking an apparent friction angle ( $\phi'$ ) for which – in contrast to angle of repose ( $\phi$ ) – there may be no corresponding physical manifestation observable in the field, particularly since the physical mechanisms contributing to bank strength can be diverse and complex. The term  $\tau^*_c \frac{\tan \phi'}{\tan \phi}$  in

Equation 16 represents the threshold for entrainment for  $\theta$  equal to zero, while the term  $\sqrt{1 - \frac{\sin^2 \theta}{\sin^2 \phi'}}$  represents the increasing contribution of gravity to grain entrainment as  $\theta$  approaches  $\phi'$ .

The apparent friction angle ( $\phi'$ ) ranges from a lower bound where neither bank vegetation nor interstitial cohesive sediment moderate the entrainment of the bank particles ( $\phi = \phi'$ ), up to an upper limit where the banks are essentially non-erodible ( $\phi' \rightarrow 90^\circ$ ) (Millar and Quick, 1993). The value of  $\tau_c$  clearly depends on the surface grain size distribution (Komar, 1987; Wilcock, 1993), surface structure (Church et al., 1998) and sediment supply (Dietrich et al., 1989) – which all influence the value of  $\tau_c^*$  – as well as on bank sediment texture, since  $\phi$  varies with grain size and shape (Henderson, 1966 p. 420).

An important distinction between sand-bed and gravel-bed alluvial channels is the readiness with which the bed material may be entrained. This leads to different representations of the sediment transport relation. In this analysis, the focus is on gravel-bed rivers and their laboratory analogues (Dade and Friend, 1998), so the Parker (1990) and Meyer-Peter and Muller (1948) equations are used to predict sediment transport. The equations of Parker (1990) that are based on a single characteristic grain diameter are used. The advantage of Parker's equation is that there is no threshold for sediment transport, which simplifies the optimization procedure. Parker's model specifies three different equations for the dimensionless sediment transport rate,  $G$ , as a function of the ratio of the dimensionless shear stress to a reference dimensionless shear stress ( $\tau^*/\tau_r^*$ ), evaluated for the median bed particle diameter ( $D_{50}$ ). The reference shear stress is analogous to the critical shear stress, but is associated with a small, measurable transport rate which is arguably easier to identify than the threshold of entrainment.

$$\text{Equation 17 } G(\tau_{bed}^*/\tau_r^*) = \begin{cases} 5474 \left(1 - \frac{0.853}{\tau_{bed}^*/\tau_r^*}\right)^{4.5} & \tau_{bed}^*/\tau_r^* > 1.59 \\ \exp\left(14.2(\tau_{bed}^*/\tau_r^* - 1) - 9.28(\tau_{bed}^*/\tau_r^* - 1)^2\right) & 1 \leq \tau_{bed}^*/\tau_r^* \leq 1.59 \\ (\tau_{bed}^*/\tau_r^*)^{4.2} & \tau_{bed}^*/\tau_r^* < 1 \end{cases}$$

where  $\tau_{bed}^* = \frac{\tau_{bed}}{(\gamma_s - \gamma)D_{50}}$  is the Shields number. According to Parker (1990) Equation 17 can be rendered in dimensional form:

$$\text{Equation 18} \dots\dots\dots q_b = G \left( \frac{0.0025(\tau_{bed} / \rho)^{3/2}}{g(s-1)} \right)$$

where  $s$  is the specific sediment weight,  $q_b$  is the volumetric transport rate per unit width ( $m^3/s/m$ ), and  $\rho$  is the density of water. The total sediment transport rate for the entire channel,  $Q_b$ , is then the product of the active width ( $P_{bed}$  in Equation 13, Equation 14 and Equation 15) and  $q_b$ . It is assumed that the entire bed of the channel is equally subject to the transport process.

The Meyer-Peter and Muller (1948) equation is also used to estimate sediment transport. However, to integrate this equation with the regime model, the effective shear stress calculated in the original formulation by applying correction factors for form roughness and grain roughness is replaced with the shear stress acting on the bed ( $\tau_{bed}$ ), since this is a conceptually similar quantity. Hence, the total sediment transport rate,  $I_b$  (in kg/s), is given by:

Equation 19..... 
$$I_b = P_{bed} \left( \frac{\rho_s}{\rho_s - \rho} \right) \left( \frac{\tau_{bed}/\gamma - 0.047 D_{50} \left( \frac{\gamma_s - \gamma}{\gamma} \right)}{\left( 0.25/\rho \right) \left( \rho/g \right)^{1/3}} \right)^{3/2}$$

The volumetric transport rate,  $Q_b$ , is given by dividing  $I_b$  by  $\rho_s(1-n)$ , the mineral density of the sediment grains adjusted by the porosity of the bulk sediment deposit. Investigations using other bedload transport formulae yield nearly identical predictions of channel geometry for fixed values of  $Q$  and  $S$ , implying that the choice of transport formula is not critical. It is the bank strength criterion that exerts the strongest control on the predicted dimensions. Various combinations of different sediment transport and flow resistance equations produce nearly identical channel dimensions and therefore can be treated as scaling functions of  $Q_b$  (Church, 1985; Millar and Quick, 1993). As a result, one cannot expect the actual sediment transport rate exhibited in nature to resemble the transport rate predicted by the regime model<sup>b</sup>.

Examples of typical solution curves are presented in Figure 2. The curves in Figure 2a and Figure 2b were generated by holding  $Q$ ,  $S$  and  $D$  constant and systematically varying  $P_{bed}$  for four

---

<sup>b</sup> This constraint limits the comparisons that can be made between all of the theoretical, regime model-based solutions and the experimental results, as will be seen in Chapter 4 and Chapter 6, especially.

different values of bank strength ( $\phi$ ). Prior investigators have made similar calculations outside the context of a supporting theory (e.g. Pickup and Warner, 1984). When bed material sediment concentration is plotted against  $W/d$  ratio (Figure 2b) all four curves coincide for wide, shallow channels, since the relative importance of the banks becomes small, but the maximum of the function shifts toward a smaller aspect ratio with higher bed load concentration as the bank strength increases. For  $\phi' = 40^\circ$ , the curve changes direction abruptly at the peak sediment concentration and never reaches the lower range of  $W/d$ . This occurs because the bank angle ( $\theta$ ) necessary for maintaining bank stability (for a given value of  $P_{bed}$ ) decreases rapidly as the bottom width of the trapezoid becomes small. As a result, the total channel width ( $P_{bed} + 2(Y_o/\tan\theta)$ ) actually increases as  $P_{bed}$  is reduced. The assumption that the bed is mobile but the banks are stable breaks down as  $\theta$  becomes small and the distinction between bed and bank becomes blurred.

Sediment concentration is plotted against bed width (Figure 2c) and aspect ratio (Figure 2d) for a solution set assuming three different characteristic grain sizes, bank strength,  $Q$  and  $S$  being held constant. The general form of the curves is the same as for the previous solution set, but peak sediment concentration increases and shifts toward larger aspect ratios as grain size is reduced. For a reduction in grain size from 45 mm to 22 mm, the aspect ratio associated with the peak sediment concentration approximately doubles, while the peak sediment concentration nearly triples. As grain size decreases, the lower limb of the solution curve “flips”, and  $W/d$  increases as  $P_{bed}$  decreases, just as it does for the weakest bank strength ( $40^\circ$ ) in Figure 2b.

An alternative way to explore solutions is to vary the channel gradient, holding the sediment transport rate,  $Q_b$ , constant. This situation ( $Q$ ,  $Q_b$  and  $D$  imposed) approximates the circumstances one expects in nature. Figure 3 presents examples of this type of solution curve for  $\phi'$  varying between  $40^\circ$  and  $70^\circ$ . No stable solutions were found for aspect ratios much smaller than that associated with the minimum gradient, and hence the different solution curves do not extend over the same range of  $W/d$  ratios. Stability, in this case, is defined by bank angles greater than  $10^\circ$ , following the discussion of Figure 2. As for the solution curves in Figure 2b, these curves converge with increasing aspect ratio and bank strength limits the minimum  $W/d$  that can be attained.

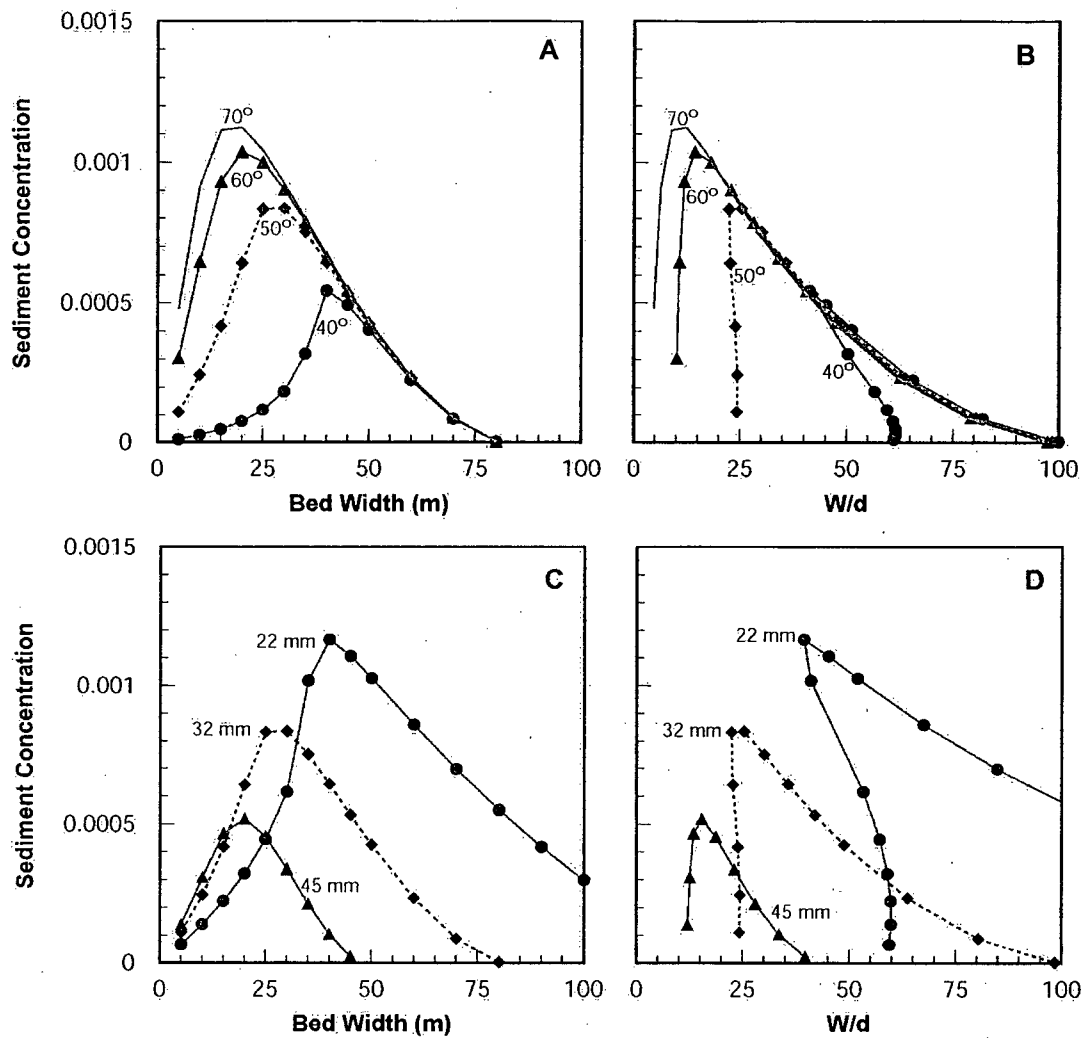


Figure 2: Solution curves for the regime model subject to the constraints  $Q = 100 \text{ m}^3/\text{s}$ ,  $S = 0.003$ . Bedload concentration predicted using the Meyer-Peter and Muller (1948) equation for constant  $D_{50}$  (32 mm) and variable  $\phi'$  (40°, 50° 60° and 70°) is plotted against (a) bed width of the solution cross section, and (b) aspect ratio (width/average depth). Bedload concentration for constant  $\phi'$  (= 50°) and variable  $D_{50}$  (22 mm, 32 mm, 45 mm) is plotted against (c) bed width, and (d) aspect ratio.

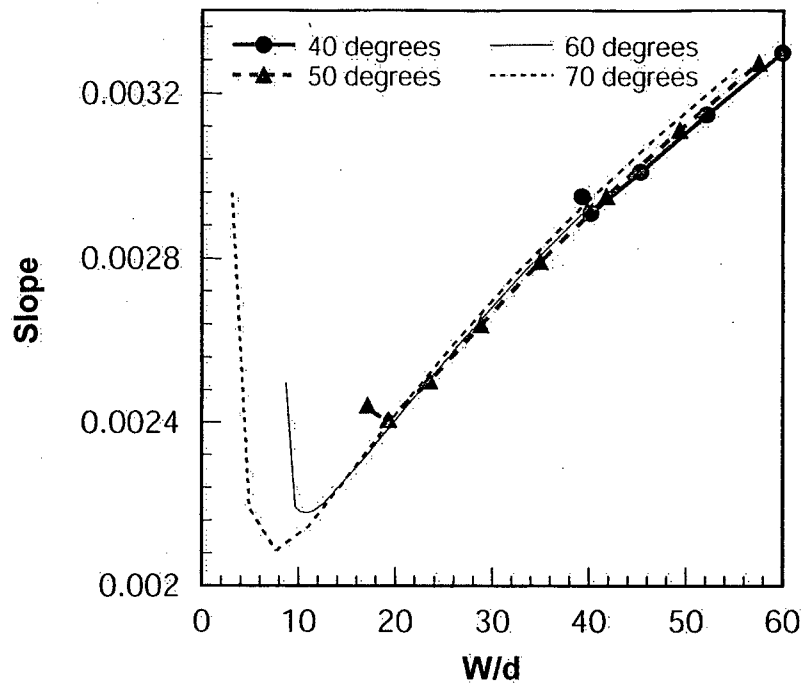


Figure 3: Solution curve for regime model subject to the constraints  $Q = 100 \text{ m}^3/\text{s}$ ,  $Q_b = 50 \text{ kg/s}$ , and  $D_{50} = 32 \text{ mm}$ . The slope necessary to produce an equilibrium channel with the specified  $Q$  and  $Q_b$  for the given  $D_{50}$  is plotted against aspect ratio ( $W/d$ ).

The range of  $W/d$  ratios over which regime solutions can be found is larger than that usually exhibited in nature (Schumm, 1963; Pickup and Warner, 1984). Channels in nature seem preferentially to occupy restricted portions of their respective stability curves. This aspect of fluvial systems remains poorly understood and finding a physical explanation for this perceived behaviour of alluvial systems remains an important problem in fluvial geomorphology (Davies, 1987).

### 2.3 RATIONALE FOR APPLICATION TO ALLUVIAL SYSTEMS

The following sections present an attempt to identify a physical basis for applying regime models to characterise alluvial streams. The underlying issue that pervades this discussion is whether or not an equilibrium-based model that invokes single, characteristic parameters describing the generalized grain size distribution, hydrologic regime and sediment supply regime can in fact say anything useful about alluvial channel behaviour.

#### 2.3.1 Formative Discharge

The first issue that requires attention is the assumption that a single discharge and associated equilibrium sediment transport rate are sufficient to predict the channel form for laterally active

stream channels. Adaptations of regime theory to the study of alluvial streams are customarily predicated on the following assumptions: (i) that bankfull discharge represents the formative discharge (i.e. the discharge responsible for the observed channel form); and (ii) that the predicted sediment transport rate associated with the bankfull discharge is equivalent to the long-term sediment supply. This approach is limited to situations where discharge fluctuations are small, and may not be generally applicable to alluvial streams (Pickup and Rieger, 1979). However, what may be reasonably recognized as the equivalent effective discharge is tied up with the question of time scale for analysis.

### 2.3.2 Timescale

The timescale at which the observed channel form is realised must be substantially shorter than the timescale at which average rates of landscape denudation vary substantially (i.e. the scale of significant climate shifts and topographic changes, perhaps  $10^3$  to  $10^5$  yrs). On the other hand, channel form timescale is likely longer than that for individual events, since both discharge and sediment supply are highly variable and are generally not thought to be in equilibrium at the event scale. The assumption of equilibrium, then, must apply to some intermediate timescale ( $10^1$  to  $10^3$  yrs), over which both discharge and sediment supply can be considered to be constants or are at least fairly represented by some single "effective" value. Unfortunately, this is likely to be the timescale at which the geomorphic history and land use changes become evident, which will also produce variations in  $Q$  and  $Q_b$ , even if climate can be viewed as more or less constant. The changes in channel form due to changes in  $Q$  are likely to be relatively conservative, since  $W$  and  $d$  vary as fractional powers of  $Q$ . This is implied by the condition for steady-state continuity,  $Q = Wdv$ , and supported by the observed downstream hydraulic geometry for alluvial streams, wherein  $W \propto Q^{0.50}$  and  $d \propto Q^{0.37}$ , on average (Knighton, 1998 p. 173). However, changes in channel geometry in response to changes in  $Q_b$  are not likely to be so conservative, since these are apt to provoke changes in the regime of the channel as the result of changes in bed material calibre (see Figure 2).

It is not clear, then, what the appropriate timescale is – or even if it exists at all, in nature. If regime models can be shown to work under conditions that are known to be at equilibrium (e.g. in experimental studies), then deviations from the predictions might be attributed to variations in  $Q$  and  $Q_b$ , provided the model is properly parameterised for alluvial streams. Furthermore, the magnitude of such effects and the degree to which the equilibrium assumption is violated can be

assessed. It may turn out that – despite the natural variability in the governing conditions – equilibrium-based models produce relatively accurate descriptions of non-equilibrium phenomena.

### **2.3.3 Bank Stability**

Another difficult issue is the bank stability criterion. Self-formed canals are thought to assume a form for which the average shear stress exerted on the bank is equal to the critical shear stress for bank erosion (Lane, 1957). For a self-formed canal at equilibrium whose banks are stable, this is a valid assumption. For laterally active streams, the matter is less clear. Obviously at the reach scale considered in this chapter, there are sections of the bank where erosion occurs and sections where deposition occurs. It can be argued that if the average channel width does not change over time, then the banks are *statistically* stable, insofar as the mean shear stress (averaged over a suitable length of channel bank) is equal to the critical value for entrainment. This proposal requires that the rate of bank retreat be linearly related to excess shear stress, and also that bank advance follow the same linear relation for shear stress less than the critical value, which may be an adequate description of meandering streams (Odgaard, 1989a, 1989b).

### **2.3.4 Channel Shape**

Regime model predictions can be expected to most closely resemble an alluvial channel at or near the inflection point between successive point bars. There, the cross section is relatively symmetrical, and most closely represents the trapezoidal shape employed by the model, thus permitting the most direct comparison. The question of how the mean hydraulic variables for such trapezoidal sections relate to other, asymmetrical cross sections is dealt with in Chapter 6, where the standard regime approach described in this chapter is combined with experimental results and additional theoretical developments to produce a revised formulation of regime theory. In that chapter, the individual regime solutions are interpreted as individual morphologic units, such as riffles and pools, and two threshold solutions are identified that bound the within-reach scale variation in local slope, width and depth.

In the context of a 1D description of an alluvial reach, however, it is sufficient to acknowledge that the trapezoidal geometry may introduce systematic bias in the regime solutions. In any case, since one is interested in regime models as a framework describing channel response to changes

in the governing conditions, it is the rates of change and direction of change that are of interest, not the precise prediction of individual alluvial state properties.

### 2.3.5 Formulation of Bed Material Transport

The sediment transport formula used in the model is also problematic. Careful examination of sediment transport formulae performance when tested against some of the best bedload transport data available revealed that such equations are unreliable (Gomez and Church, 1989). While the test was to a degree unfair in that the formulae were applied to cross-sectional averages rather than local flow conditions, it did reflect the way in which such formulae are used in regime models.

Bedload transport exhibits both spatial and temporal non-equilibrium behaviour. Transport is seldom uniformly distributed across the channel (Carson and Griffiths, 1987), is often locally concentrated in discrete threads that may migrate back and forth across the channel during a given flood, and does not necessarily reflect the fluid force distribution (Muhlhofer, 1933). Even with constant  $Q$  in a recirculating flume, channel morphology can interact with the sediment transport field to produce lateral and longitudinal variations in sediment transport (Ashmore, 1991). These variations are in fact responsible for the characteristically non-regular morphology of alluvial stream channels, and the progressive changes in stream position. The development of spatial disequilibrium in sediment transport results in temporal variation at a single point, so the distinction between spatial and temporal disequilibrium is not always clear. Formulae may provide reasonable sediment transport estimates at the event scale (Eaton and Lapointe, 2001), but only when the change in the entrainment threshold ( $\tau^*_c$ ) is considered (see Dietrich et al., 1989; Buffington and Montgomery, 1997). Nowhere in a regime model framework is the variation of  $\tau^*_c$  over time incorporated. It is therefore not clear how useful equilibrium-based sediment transport formulae are in describing alluvial systems.

Some of the departures from equilibrium discussed above may be driven by variations in local sediment supply, and are eliminated if sediment supply is held constant in an experimental setting. A further distinction can be made between disequilibrium and unsteady sediment transport. By definition, disequilibrium sediment transport involves time-varying (i.e. unsteady) sediment transport. But, one can also expect unsteady sediment transport under equilibrium conditions. Unsteady sediment transport that fluctuates about some average equilibrium value may be characteristic of laterally active alluvial systems: Ashmore (1991) reports exactly this sort

of behaviour for a laboratory experiment in which discharge and sediment supply were held constant. In short, disequilibrium sediment transport refers to temporal changes in the average sediment transport rate, which calls into question the applicability of regime models. On the other hand, unsteady sediment transport may be characteristic of equilibrium conditions, where the sediment transport rate varies about some equilibrium value. Since the choice of sediment transport equation in a regime model does not strongly influence the predicted channel dimensions (Millar and Quick, 1993), perhaps these issues are not critical. In any case, one recognizes that the sediment transport rates predicted by the existing formulae may differ substantially from the actual rates in alluvial streams, and treat the predicted transport rate as a scale representation of the actual transport rate (Church, 1985). Regime models may well be able to describe the average channel form using a sediment transport formula as a scale relation of the equilibrium transport conditions, even if the system exhibits unsteady (but not disequilibrium) sediment transport. But, one should expect some sort of bias between the predicted and the actual transport rates, which limits one's ability to compare model predictions with stream channels developed in the field and in the laboratory.

### **2.3.6 Formulation of Flow Resistance**

The resistance equations typically used in regime models rely on some measure of the roughness length associated with grain diameter, rather than channel morphology and pattern. They are not generally capable of predicting the flow resistance associated with channel sinuosity, bars and other bedforms present in alluvial channels, which may account for between 0 and 90% of the total flow resistance at bankfull conditions (Millar, 1999), and may play an important role in pattern development (Lewin and Brewer, 2001). When comparing regime model predictions against real channels, the obvious solution to this problem is to apply the same roughness in the model as is observed in the comparison stream. Generally, it is better to use a measured parameter than to use an estimated one, and this principle certainly applies when using regime models. While one can conceptually understand the various components of flow resistance within an alluvial system (see Section 2.4), it is not yet possible to predict the magnitude of each component, nor the total flow resistance for a given river system. Thus, regime models may be able to describe channels that exist and for which the resistance is known, but may not be able to predict the channel form accurately under different conditions.

## 2.4 OPTIMIZATION

As things stand, then, the regime approach presented in this chapter may describe reach-averaged dimensions of laterally active streams for which discharge and sediment supply are relatively constant, provided that some sort of expected condition can be specified for sediment transport capacity and/or flow resistance. Typically, this requirement has taken the form of some sort of optimization, such as minimum gradient, maximum transport capacity or maximum flow resistance. The optimization is needed to choose a unique solution from the range of possible solutions for specified  $Q$ ,  $S$  and  $D$  (Figure 2) or for specified values of  $Q$ ,  $Q_b$  and  $D$  (Figure 3).

Essentially, then, one needs to be able to identify the most probable channel configuration from among the range of theoretically viable configurations. It is remarkable that the overall morphology of many active alluvial channels remains relatively constant, that is they remain relatively stable over time. The most probable channel configuration, then, corresponds to the most stable configuration, the configuration for which subsequent channel adjustment is minimized. The progressive development of channel stability (for a single-thread alluvial channel) can be understood in terms of a tendency to maximize flow resistance. By maximizing the flow resistance, the energy available to change the channel configuration (which is analogous to the concept “free energy” in a chemical reaction) is minimized, hence the channel stability is maximized, as is the probability of finding that channel configuration in nature.

The alluvial system must be considered as a whole, wherein the independent variables are  $Q$ ,  $D$ ,  $Q_b$  and  $S_v$  (Figure 4);  $W$ ,  $d$  and  $S$  (hence channel length,  $L_c$ ) are free to vary. The key consideration is how to quantify the flow resistance *of the system*. Equations that index flow resistance per unit length of channel (e.g.  $f = \frac{8gRS}{v^2}$ ) do not describe the flow resistance per unit length of the system. Once channel length is allowed to vary, the two are not equivalent. The total resistance to flow in the system can be indexed by substituting  $S_v$  for  $S$  in a flow resistance equation. Thus:

Equation 20.....  $f_{sys} = \frac{8gRS_v}{v^2}$

This transforms the friction parameter from a property of the stream channel ( $f$ ) to a property of the alluvial system ( $f_{sys}$ ) that incorporates the effects of channel planform as well as grain size

and bedforms of intermediate size (such as dunes and bars). These features point to three components of flow resistance for the system:

Equation 21 .....  $f_{sys} = f' + f'' + f'''$

where  $f'$  is the grain resistance equivalent to setting  $k_s = D$  in Equation 12 (after Millar, 1999);  $f''$  is the within-channel form resistance due to bars, dunes and other in-channel features ( $f'' \equiv f - f'$ , according to Parker and Peterson (1980)); and  $f'''$  is the reach-scale form resistance due to channel sinuosity ( $f''' \equiv f_{sys} - f$ ). Ackers and Charlton (1970) applied a similar division of roughness to meandering laboratory channels with thalweg sinuosities of up to 1.76, concluding that “some 60% of the head loss in meandering channels [is attributable to] bends and major variations in cross sections” (p. 369).

According to regime theory, viable solutions exist for all gradients  $S_{min} \leq S \leq S_v$  (provided  $S_v > S_{min}$ , and that  $S_v$  is not too large to prevent alluvial material from accumulating at all), where  $S_{min}$  is the minimum gradient at which the imposed fluxes  $Q$  and  $Q_b$  can be transported (Figure 4). For less sinuous channels (see (1) in Figure 4a), most of the flow resistance for the system derives from grain roughness and from within-channel bedform roughness such as bars, dunes and clast structures. As sinuosity increases, so does the relative importance of reach-scale form resistance (see (2) and (3) in Figure 4a).

The friction factor,  $f$ , calculated for the channel (Equation 11) and for the system (Equation 20) is presented in Figure 5. While  $f$  based on the channel gradient increases monotonically,  $f_{sys}$  reaches a maximum value at the minimum gradient. It appears that the flow resistance per unit length of channel is greatest for the channels with the least sinuosity (i.e. the highest gradient), assuming that  $C_{50}$  (which represents both  $f'$  and  $f''$ ) does not vary significantly as sinuosity increases. On the other hand, the friction factor for the system reaches a maximum for the lowest stream gradient, which corresponds to the maximum degree of sinuosity, and dominates the total resistance for the system, indexed by  $f_{sys}$ .

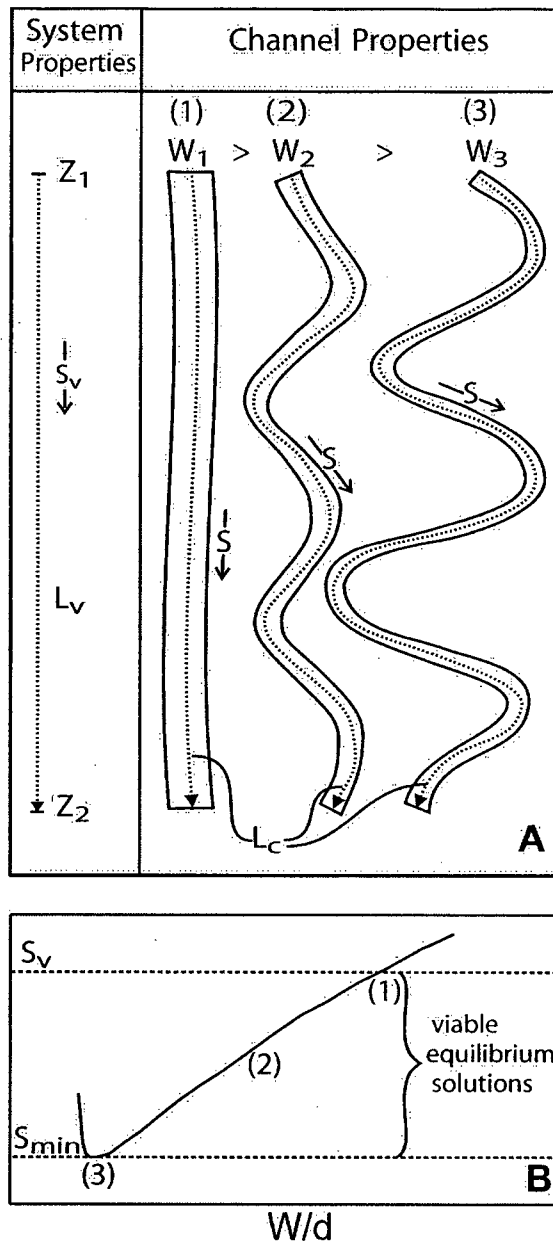


Figure 4: Definition of the fluvial system. (a) defines the properties of the fluvial system that are constant at regime time scales: valley gradient ( $S_v$ ), valley length ( $L_v$ ), and total head drop ( $Z_1 - Z_2$ ); as well as those that are variable: channel slope ( $S$ ) and channel length ( $L_c$ ). (b) illustrates, following Figure 2, that for a constant  $Q$ ,  $Q_b$ ,  $D_{50}$  and  $\phi'$ , a solution curve exists, for which a continuum of theoretically viable channels exist for slopes less than the valley slope ( $S_v$ ) and greater than the minimum slope ( $S_{min}$ ) capable of transporting the imposed sediment load.

One now has a framework within which to describe adjustments of alluvial systems toward a condition of maximum flow resistance. If an alluvial channel is located somewhere on the relevant stability curve but the flow resistance for the system is not at a maximum (e.g. channels (1) and (2) in Figure 4), then the flow possesses kinetic energy that can act to further deform the

system until it happens by chance to achieve a form that has a higher resistance to flow and is therefore more stable. Since the potential to deform the system (and hence reach another configuration) is least when this “excess” kinetic energy for the system is least (subject to the constraint that both the imposed fluid and sediment supply be transported), a state of maximum flow resistance is the most statistically probable. This aspect of system behaviour has been ascribed by Huang and Nanson (2000) to the “principle of least action”, whereby equilibrium is achieved by minimizing the potential for further deformation of the system.

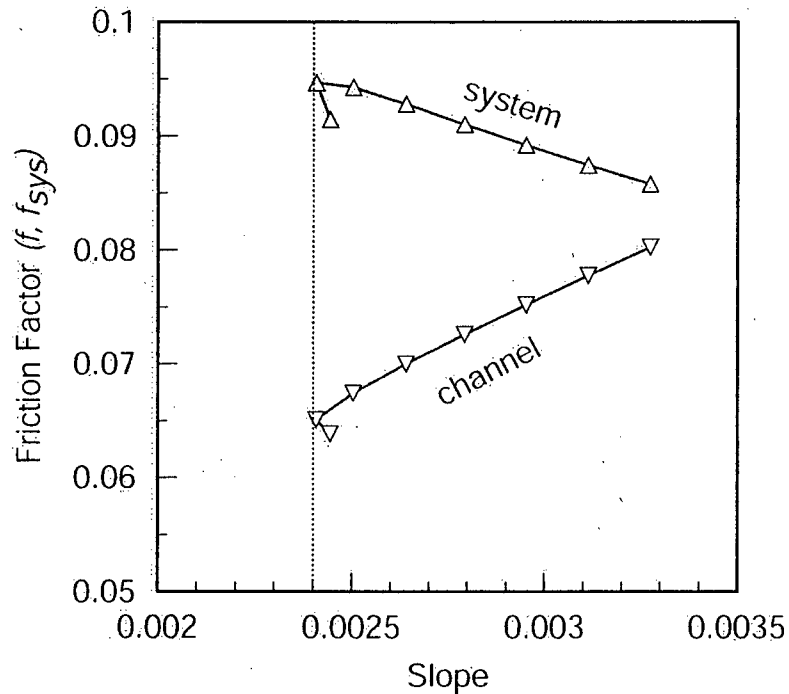


Figure 5: Friction factors for the channel ( $f$ ) and for the alluvial system ( $f_{sys}$ , arbitrarily assuming  $S_v = 0.0035$ ) are plotted against slope, assuming the same values of  $Q$ ,  $Q_b$  and  $D$  as in Figure 2, and setting  $\phi' = 50^\circ$ . The minimum slope is indicated by a vertical dashed line.

A mechanism by which this state might be achieved is presented in Chapter 5. It involves a feedback between channel shape and transport capacity acting in the cross sectional plane that tends to reduce channel slope. Regime solutions where  $f_{sys}$  is not maximized represent unstable equilibria, since small perturbations to these systems create a feedback that causes a decrease in slope and an increase in  $f_{sys}$ . Optimality criteria – insofar as they approximate the behaviour of this feedback – are simply formalisms permitting 1D regime models to describe the product of 3D geomorphic processes.

By applying some form of optimization, the model yields predictions of alluvial channel dimensions for different imposed flows and grain sizes. These predictions can be collapsed onto dimensionless relations among the key variables describing the state of the alluvial system for specified bank strengths ( $\phi'$ ).  $\phi'$  represents a fundamental boundary condition that controls the development of the system. All channels with the same  $\phi'$  are described by a single function relating  $\tau^*$  and  $W/d$ . Scaling based on these two dimensionless parameters is consistent with previous arguments about the controls of sediment transport, channel deformation and channel pattern (Ferguson, 1987; Todd, 1996; Dade and Friend, 1998; Dade, 2000). Once  $D/d$  is known (in addition to  $\tau^*$  and  $W/d$ ), the alluvial state is fully specified, exhibiting unique values of Froude number ( $Fr$ ), gradient ( $S$ ) and sediment concentration ( $Q_b/Q$ ). Put another way, channels that exhibit Froude similarity occupy the same alluvial state predicted by the model, and exhibit approximate dynamic similarity.

A complete description of an alluvial state by the regime model is thus summarized by three dimensionless quantities: (i) average dimensionless shear stress ( $\tau^*$ ) or, equivalently, channel gradient ( $S$ ); (ii) channel shape ( $W/d$ ); and (iii) relative roughness ( $D/d$ ). The alluvial state is defined by the location in a three-dimensional space ( $W/d$ ,  $D/d$ ,  $\tau^*$  or  $S$ ). Implicit in this description of the alluvial state are constant values for  $C_{50}$  and  $\tau^*_c$ . Since these parameters may be variable, they can be considered to be additional secondary descriptors of the alluvial state, or alternatively, representations of the boundary conditions associated with the development of surface armour and stabilizing structures ( $\tau^*_c$ ) or the more general role of geomorphic history in determining the dominant suite of bedforms that form in a channel ( $C_{50}$ ).

These parameters are related to the grain-scale flow resistance and the within-channel flow resistance in Equation 21, and thus represent quantities that can be adjusted in the approach toward flow resistance maximization. When these two quantities are held constant, then the adjustment of the system in response to changes in the governing conditions is limited to changes in channel slope, which is essentially a graded relation (Mackin, 1948). Graded channel response, then, is a special case of flow resistance maximization wherein the adjustment is limited to changes in the reach-scale flow resistance. A more complete description of channel change through time can likely be included in the regime framework by developing relations predicting the changes in  $\tau^*_c$  and  $C_{50}$  in response to changes in the governing conditions.

Table 1: Simulated dataset based on random pairs of  $Q$  and  $D_{50}$

$Q$ (m <sup>3</sup> /s)	$D_{50}$ (mm)	Slope	$Q$ (m <sup>3</sup> /s)	$D_{50}$ (mm)	Slope
15.5	<b>11.3</b>	$7.53 \times 10^{-3}$	374	56.0	$8.41 \times 10^{-3}$
18.1	29.8	$2.25 \times 10^{-3}$	383	44.4	$2.33 \times 10^{-3}$
33.3	14.1	$4.98 \times 10^{-3}$	408	30.8	$9.84 \times 10^{-3}$
41.7	98.7	$6.19 \times 10^{-3}$	427	51.9	$6.19 \times 10^{-3}$
46.4	32.1	$1.43 \times 10^{-2}$	467	91.9	$2.95 \times 10^{-3}$
54.4	95.7	$1.16 \times 10^{-2}$	467	97.5	$6.54 \times 10^{-3}$
65.0	27.9	$4.99 \times 10^{-3}$	488	42.3	$3.81 \times 10^{-3}$
75.3	79.8	<b><math>2.18 \times 10^{-2}</math></b>	512	53.8	$2.46 \times 10^{-3}$
102	19.1	$4.02 \times 10^{-3}$	554	40.9	$9.10 \times 10^{-4}$
139	87.7	$1.45 \times 10^{-2}$	597	63.7	$4.15 \times 10^{-3}$
165	12.9	$1.57 \times 10^{-3}$	705	14.8	$2.39 \times 10^{-3}$
199	16.7	$7.33 \times 10^{-4}$	750	37.0	$2.25 \times 10^{-3}$
220	24.8	$2.98 \times 10^{-3}$	776	41.6	<b><math>5.51 \times 10^{-4}</math></b>
231	13.7	$2.57 \times 10^{-3}$	807	97.8	$3.36 \times 10^{-3}$
246	22.5	$3.10 \times 10^{-3}$	817	73.5	$6.60 \times 10^{-3}$
257	<b>99.2</b>	$2.69 \times 10^{-3}$	863	46.7	$6.87 \times 10^{-4}$
286	11.5	$2.08 \times 10^{-3}$	885	89.6	$5.88 \times 10^{-3}$
301	52.0	$7.35 \times 10^{-3}$	899	90.9	$7.52 \times 10^{-3}$
305	48.4	$3.49 \times 10^{-3}$	910	42.0	$6.42 \times 10^{-4}$
344	35.7	$2.98 \times 10^{-3}$	952	33.1	$1.17 \times 10^{-3}$
352	77.5	$4.78 \times 10^{-3}$	959	96.3	$8.68 \times 10^{-3}$
356	43.5	$3.20 \times 10^{-3}$	973	83.5	$6.18 \times 10^{-3}$
358	59.8	$8.20 \times 10^{-3}$	976	37.4	$7.22 \times 10^{-4}$
359	15.8	$2.27 \times 10^{-3}$	986	43.6	$2.44 \times 10^{-3}$
372	42.2	$3.69 \times 10^{-3}$	991	82.6	$2.93 \times 10^{-3}$

Note: A random number generator with a uniform distribution was used to select  $Q$  (10 - 1000 m<sup>3</sup>/s),  $D$  (10 - 100 mm) and  $\tau^*$  (0.04 to 0.1).  $\tau^*$  was used to avoid generating channels in which the bed material could not be transported. Values of  $S$  were generated for the lowest bank strength ( $\phi' = 40^\circ$ ) that produced the specified  $\tau^*$  values. The random pairs are presented in order of increasing  $Q$ , and the minimum and maximum values of  $D_{50}$  and  $S$  for the dataset are highlighted in bold. The minimum values of  $Q$  and  $D_{50}$  correspond entirely by chance, since all values were produced by a random number generator.

Altogether, the state-space ( $W/d$ ,  $D/d$ ,  $\tau^*$  or  $S$ ) defines the scaling behaviour of alluvial channels. This scaling behaviour is investigated using random combinations of  $Q$ ,  $D$  (which together specify the relative roughness), and  $S$ . A dataset of 50 such randomly generated alluvial channels (Table 1) is used: (i) to illustrate the characteristics of the alluvial scaling implied by the regime model; (ii) to examine the sensitivity of the model to the particular optimizations used; (iii) to determine the effect of varying the channel-scale form roughness,  $C_{50}$ ; and (iv) to establish the limits of applicability of the model.

The dataset was generated by first selecting 50 random sets of  $Q$ ,  $D$  and  $\tau^*$ . A random number generator with a uniform distribution was used: the range for the uniform distribution for  $Q$  was

10 to 1000 m<sup>3</sup>/s, for  $D$  was 10 to 100 mm, and for  $\tau^*$  was 0.04 to 0.1. The variable  $\tau^*$  was used in preference to  $S$  to avoid generating channels where the bed material could not be transported. Subsequently, values of  $S$  were generated for the lowest bank strength ( $\phi' = 40^\circ$ ) that produced the specified  $\tau^*$  values, thereby ensuring that the bed material will be theoretically transportable under all conditions. These values of  $S$  were used in all subsequent analyses with the dataset, regardless of bank strength.

### 2.5.1 Dimensionless Scaling Relations

It has been shown that many of the existing extremal hypotheses are equivalent (White et al., 1982; Davies and Sutherland, 1983). In accordance with the approach taken by Davies (1987), most of the predictions presented here are the result of maximizing the shear stress,  $\tau$ . The sensitivity of the model predictions to the choice of optimization is investigated in Section 2.5.2. By setting  $\phi'$  equal to  $40^\circ$ ,  $50^\circ$ ,  $60^\circ$ ,  $70^\circ$  and  $80^\circ$ , five curves relating  $\tau^*$  and  $W/d$  were generated using the simulated dataset (Table 1). These curves are presented in Figure 6a. For  $W/d$  greater than about 7 (i.e. for nearly all  $W/d$  exhibited by natural channels), all the relations are nearly log-log linear and almost parallel; they are well described by power functions where the exponent generally increases from 2.98 to 3.19 with increasing bank strength (Table 2). However, the main effect of bank strength is to change the coefficient in the power relation, whereby stronger banks result in smaller  $W/d$  ratios for the same dimensionless shear stress. For  $W/d$  less than 7, there is a pronounced curvature to the functions, which arises from the rapidly changing relative importance of the bank height in the definition of the hydraulic radius, and thus in the shear stress,  $\tau$ .

These functions capture much of the system behaviour, in dimensionless form. This is particularly evident when  $\tau^*$  is replaced by Parker's (1990) dimensionless sediment transport rate,  $G_b$  (Figure 6b). The same general structure persists. The only effect is that there has been a distortion of the  $x$  axis. The relations on Figure 6a and Figure 6b may thus be interpreted as a dimensionless relation between the sediment transport intensity, represented by either  $\tau^*$  or  $G_b$ , and the channel shape ( $W/d$ ). The nature of the relation between transport intensity and channel shape is dictated by the strength of the channel banks relative to the channel bed.

As mentioned above, there is another dimension to be considered, since each point ( $\tau^*$ ,  $W/d$ ) subsumes a wide range of possible relative roughness values, gradients, Froude numbers, and sediment concentrations. Behaviour in this dimension is investigated using the same  $Q$  and  $D$

values in Table 1, but varying  $S$  so as to produce a constant value of  $\tau^*$  for a given value of  $\phi'$ . Since one is thus specifying  $\tau^*$  and  $\phi'$ , it follows that  $W/d$  will be constant, but that the relative roughness will vary in accordance with the relative magnitude of  $Q$  and  $D$ . By setting  $\phi' = 50^\circ$ , and  $\tau^* = 0.067$ , channels are generated that have a constant  $W/d$  ratio of 32. Relative roughness varies from 0.0047 to 0.15,  $S$  varies from 0.005 to 0.016,  $Fr$  number varies from 0.39 to 1.23, and sediment concentration varies from 0.017 to 1.0 g/L. Clearly, there can be substantial variations in the character of alluvial systems with identical values of  $\tau^*$  and  $W/d$ . However, all of the variation in  $S$ ,  $Fr$  and  $Q_b/Q$  is functionally related to relative roughness,  $D/d$ , which completes the definition of the alluvial state (Figure 7). Once  $D/d$  is known, the parameters  $S$ ,  $Fr$ , and  $Q_b/Q$  are uniquely specified, regardless of the absolute size of the system under consideration. Thus, the dimensionless scaling implied by the model obeys the concept of Froude similarity as applied in classical fluid mechanics (Yalin, 1971b), while also providing a quantitative framework that explicitly considers the role of relative bank strength in constraining the system development.

Table 2: Power relations fit to dimensionless scale collapse

$\phi'$	$a$	$b$	$n$	$R^2$
40°	$3.58 \times 10^5$	2.98	50	0.998
50°	$1.46 \times 10^5$	3.12	50	0.998
60°	$4.03 \times 10^4$	3.11	49 <sup>+</sup>	0.997
70°	$9.48 \times 10^3$	3.16	43 <sup>+</sup>	0.996
80°	$8.99 \times 10^2$	3.19	24 <sup>+</sup>	0.998

Note: the relations were fitted to data in which  $W/d > 7$  only.

\*The fitted model is  $W/d = a(\tau^*)^b$

<sup>+</sup>Supplemental data were added for the relations for 60°, 70° and 80° to extend the range of  $W/d$  up to 150 (see Figure 6a).

Each  $(\tau^*, W/d)$  pair, then, represents a suite of hydraulic geometry equations describing alluvial channels across a wide range of scales for which  $\phi'$  and  $\tau^*$  are constant. In this case, the variation in  $S$ ,  $Fr$ , and  $Q_b/Q$  with basin scale is related to the relative magnitude of  $Q$  and  $D$  – hence  $D/d$ . The characteristic exponent is 0.46, giving  $W, d \propto Q^{0.46}$  – width and depth vary in simple proportion with each other. This is precisely the same as the results reported by Henderson (1966) and Li et al. (1976) for their analyses of threshold channels. The widely reported proportionality  $W \propto Q^{0.5}$  for natural streams (see Leopold et al., 1964 p. 271; Knighton, 1998 p. 173) is quite similar to the theoretically based exponent (0.46), and may reflect the

aesthetic attraction of the simple solution  $W \propto Q^{1/2}$ . The behaviour of  $d$  for natural channels is less similar to our theoretical result (and that predicted by threshold theory), since it is commonly reported that  $d \propto Q^{0.30}$  to  $Q^{0.40}$  (Leopold et al., 1964 p. 271; Knighton, 1998 p. 173). Insofar as this discrepancy represents a real difference between theory and empirical evidence, it may be interpreted as the result of systematic variation of  $\phi'$ ,  $\tau^*$ , and/or  $D/d$  with basin scale. Certainly, one observes the latter in nature.

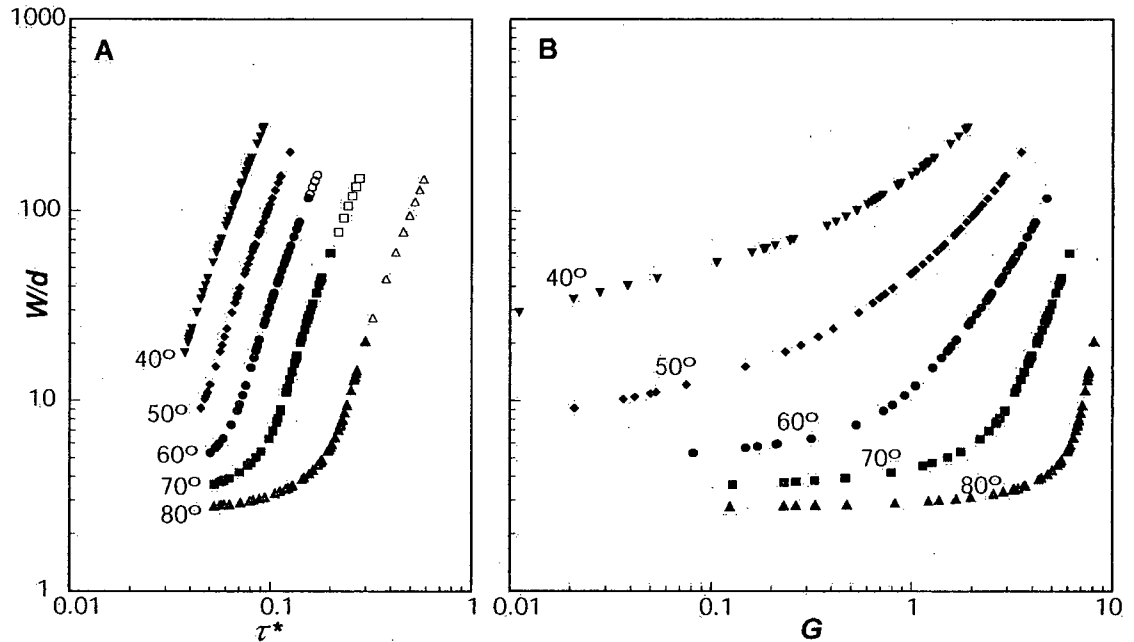


Figure 6: (a) Dimensionless scale relations between  $\tau^*$  and  $W/d$  for various bank strength values (represented by different  $\phi'$  values, in degrees). (b) Dimensionless scale relations between transport rate  $G$  (Parker, 1990) and channel shape  $W/d$ . The curves were generated using a regime model (that maximizes shear stress) with the dataset in Table 1. Supplemental data (open symbols) were generated for  $\phi' = 60^\circ, 70^\circ$ , and  $80^\circ$  so as to extend the range of  $W/d$  up to 150 to confirm the general structure of the scaling relations.

We can construct an artificial hydraulic geometry based on a somewhat rational basis to test this argument. First, it is assumed that slope varies as  $S \propto Q^{-0.3}$ , which seems to be a reasonable proportionality, based on the summary presented by Knighton (1998). One can then fit power functions of the form  $Q_b/Q = a(D/d)^b$  to the data for various points in the alluvial state space ( $\tau^*$ ,  $W/d$ ). Assuming  $\phi' = 45^\circ$  and considering a range of  $\tau^*$  from 0.045 to 0.08, we find that the exponent in the power relation is constant ( $b = 1.167$ ), and that  $a = 6.46 \times 10^3(\tau^*) - 221$ . By specifying a range of  $Q$  values and then solving for  $D/d$ , such that  $Q_b/Q$  is constant, one can

produce a scaling of the form  $W/d \propto Q^j$ , where  $j$  is 1.30, since  $D/d$  and  $S$  together imply a unique value of  $\tau^*$ , which in turn specifies a unique value of  $W/d$ . Based on the reported hydraulic geometry exponents, we empirically observe that  $j$  falls in the range 1.25 to 1.5. Thus, the observed downstream changes in hydraulic geometry are at least consistent with the above analysis, wherein downstream fining is driven by an imposed change in slope, subject to  $Q_b/Q$  being held constant.

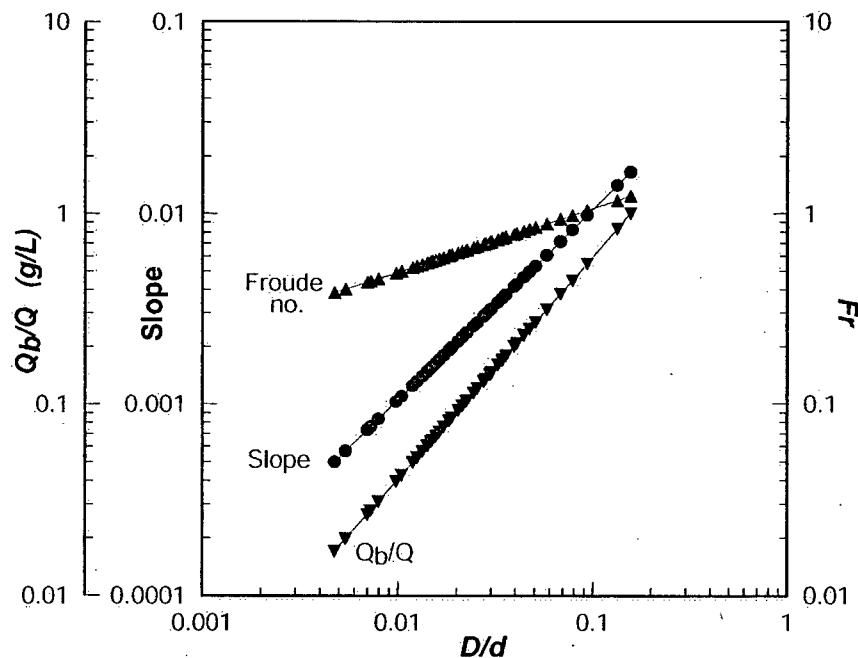


Figure 7: Relations of  $Q_b/Q$ , Froude number, and  $S$  with  $D/d$  for constant value of  $W/d$  (32) and  $\tau^*$  (0.067), for the paired values of  $Q$  and  $D$  in Table 1.

### 2.5.2 Model Sensitivity to Choice of Optimization

The foregoing analysis was based on maximizing shear stress (MSS), but could just as easily be based on maximizing unit stream power (MUSP), or sediment transport capacity (MTC) predicted by a number of different transport formulae. For relatively weak stream banks (i.e.  $\phi' = 40^\circ$ ), the various possible optimizations produce virtually identical scaling relations, since the peak in transport capacity corresponds to the peak in transport intensity, which is directly related to fluid force in all transport formulae. However, as bank strength increases, a disparity between the MTC optimizations and the fluid force optimizations (MSS and MUSP) becomes evident.

Figure 8 presents the scaling curves for MSS, MUSP and MTC (based on both Meyer-Peter and Muller (1948) and Parker (1990) equations) over the range of bank strengths where disparities become apparent ( $\phi' > 60^\circ$ ). All of the optimizations coincide for  $\phi' = 60^\circ$  and  $W/d > 20$ : for  $W/d < 20$ , the MTC optimizations are nearly identical, as are fluid force optimizations; both types of MTC predict channel dimensions that, for a given  $\tau^*$ , are wider than the MSS and MUSP predictions. Since the fluid force optimizations represent maximization of sediment transport intensity (i.e. transport per unit width), it is obvious that the differences between these optimizations and the MTC optimizations arise from a trade-off between transport intensity and the active width of the channel. For relatively wide channels ( $W/d > 20$ ), the peak in total sediment transport corresponds with the peak in the transport intensity, or transport-per-unit width, just as it does for the entire range of solutions for weaker banks. However, for narrower channels, the total transport capacity is reached when the channel has a transport-per-unit width slightly less than the maximum, but has a larger channel width.

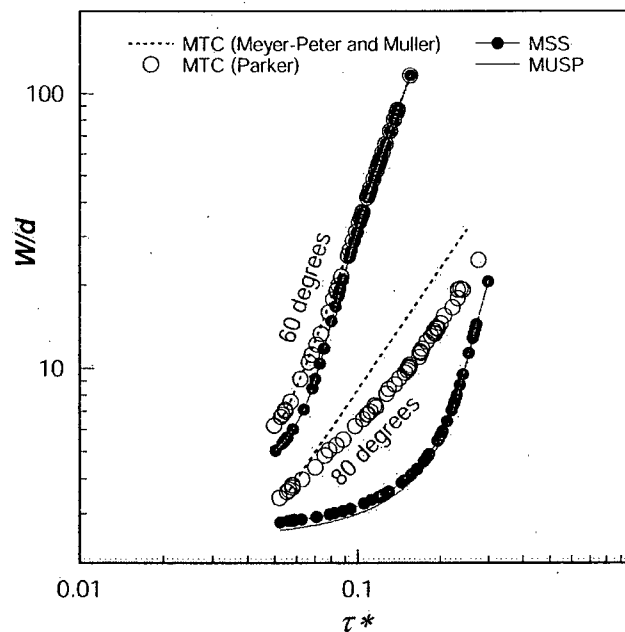


Figure 8: Sensitivity of scaling relations to choice of optimizations (MTC, MSS and MUSP) for  $\phi' = 60^\circ$  and  $\phi' = 80^\circ$ . The Meyer-Peter and Muller (1948) equation and the Parker (1990) equation are both used to generate MTC optimizations. See text for definition of acronyms.

For even stronger banks ( $\phi' = 80^\circ$ ) there is greater disparity between the MTC optimizations and the fluid force optimizations, which do not correspond anywhere (Figure 8), although this is

clearly a function of the limited range of  $W/d$  ratios produced by the simulated dataset. Furthermore, a discrepancy between the Meyer-Peter and Muller equation and the Parker equation arises, especially at higher shear stresses. In contrast, the MSS and MUSP optimizations still agree fairly well with each other. Clearly, as the bank strength increases, the choice of optimization becomes critical (as does the choice of transport relation), and it is no longer satisfactory to assume that they are equivalent. Happily, gravel-bed rivers seem to be characterized by values of  $\phi' < 65^\circ$  (Millar and Quick, 1993), which permits us to assume the general equivalency of the various optimizations in such channels.

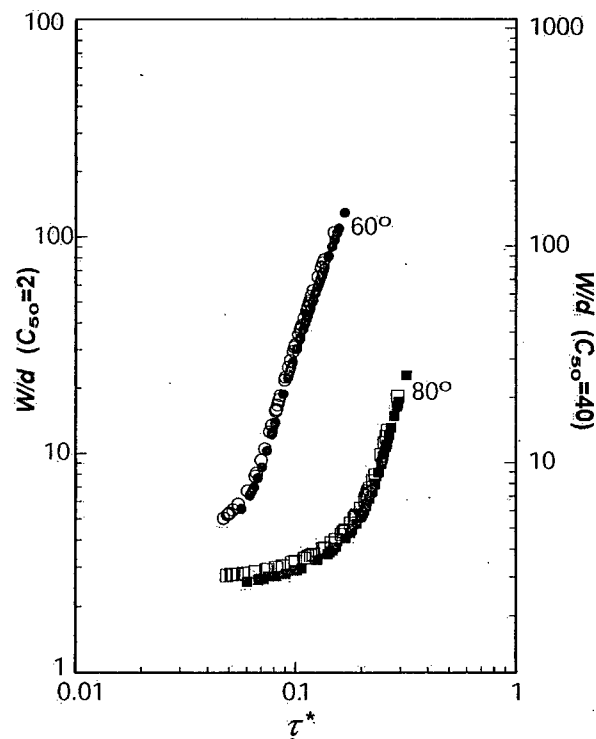


Figure 9: Sensitivity of scaling relations to assumed form roughness. The form roughness, represented by the parameter  $C_{50}$ , is varied from 2 (open symbols) to 40 (closed symbols) for two different bank strength values. The effect of increasing  $C_{50}$  is to translate the individual data points upwards along the scaling function. For clarity, the values for  $C_{50} = 2$  and  $C_{50} = 40$  are slightly offset by shifting the  $y$  axis for  $C_{50} = 40$ .

### 2.5.3 Effect of Form Roughness

The model uses the parameter  $C_{50}$  to scale the characteristic grain diameter ( $D_{50}$ ) to a roughness length,  $k_s$ . The value of  $C_{50}$  has been shown to vary by more than an order of magnitude in gravel bed rivers, and may be interpreted as the relative effect of within-channel form roughness ( $f''$  in

Equation 21) on flow resistance (Millar, 1999). The foregoing analysis assumes a constant value of  $C_{50}$  (6.8), and thus ignores the potential for a channel to respond to changes in the governing conditions by an adjustment of the flow resistance. This section examines the impact of varying  $C_{50}$  from a value of 2 to 40, which encompasses much of the natural range in this parameter reported by Millar (1999) for gravel bed streams.

Changing the value of  $C_{50}$  does not change the form of the dimensionless scaling relations, but it does displace individual data points along the trajectory of the scaling relations. Figure 9 presents curves assuming  $C_{50} = 2.0$  (open symbols) and  $C_{50} = 40$  (closed symbols) for two different bank strengths. A single function describes the data using both values of  $C_{50}$ . The effect of changing  $C_{50}$  is more clearly demonstrated when a single data point is considered. By setting  $Q$ ,  $S$ ,  $D$  and  $\phi'$  constant, and then varying  $C_{50}$ , a wide range of predicted dimensionless and scale parameters results.

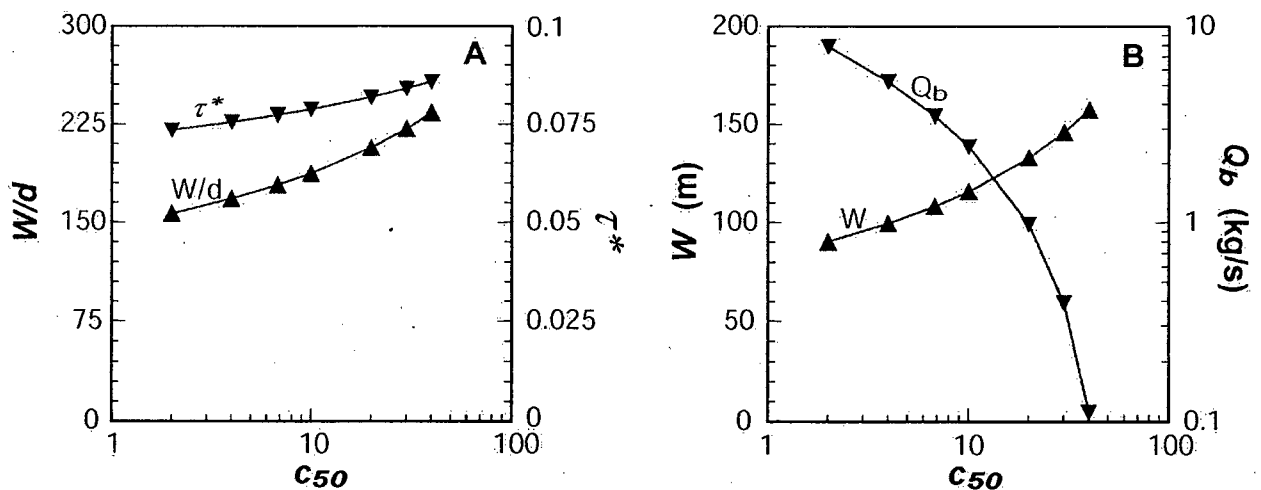


Figure 10: Effect of varying  $C_{50}$  on (a) dimensionless scaling parameters,  $W/d$  and  $\tau^*$ ; and (b) scale measures,  $W$  and  $Q_b$ .  $Q$ ,  $D$ ,  $\phi'$  and  $S$  are held constant at arbitrary values of  $102 \text{ m}^3/\text{s}$ ,  $19 \text{ mm}$ ,  $40^\circ$ , and  $0.004 \text{ m/m}$ , respectively.  $Q_b$  is estimated using the grain shear stress.

Figure 10 presents the variations in both dimensionless parameters ( $W/d$  and  $\tau^*$ ) and scale parameters ( $W$  and  $Q_b$ ) as  $C_{50}$  is increased. As  $C_{50}$  increases, both  $W/d$  and  $\tau^*$  increase modestly (Figure 10a), representing a translation up the scaling relation for the specified value of  $\phi'$ . An obvious consequence is that the width,  $W$ , will also increase (Figure 10b). Thus, as form roughness increases, the predicted channel will become wider and deeper (since  $\tau^*$  increases and  $S$  is held constant), and will be characterized by a larger average shear stress. Since both  $W$  and

$\tau^*$  increase, one might suppose that the total sediment load (predicted using the Parker equation) would increase, as well. However, only the shear stress acting on grains can contribute to sediment transport, and form roughness represents a dissipation of energy within the system that does not result in transport (e.g. Einstein and Barbarossa, 1951; Van Rijn, 1984; Millar, 1999). If only the shear stress acting on the grain is applied to the sediment transport law, a rapid decrease in the total transport is revealed (Figure 10b).

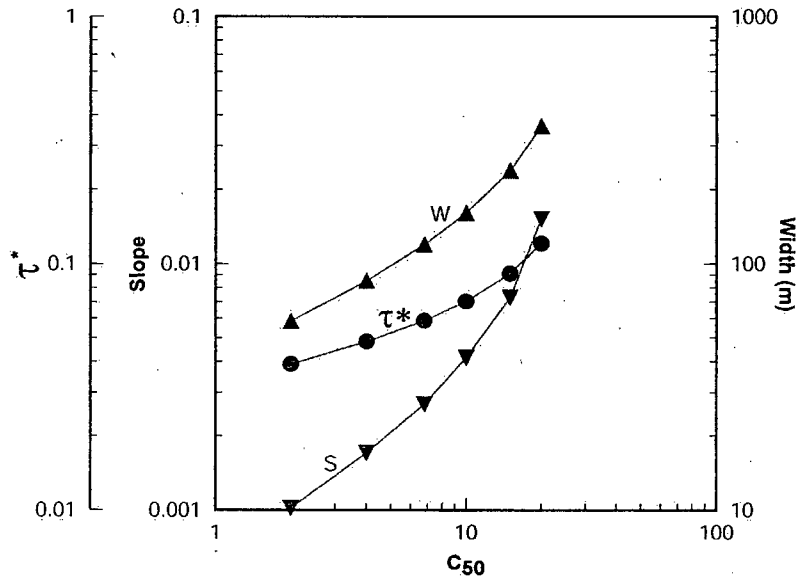


Figure 11: Effect of varying  $C_{50}$  on  $\tau^*$ ,  $S$ , and  $W$ .  $Q$ ,  $D$ ,  $\phi'$  and  $Q_b$  are held constant at arbitrary values of  $383 \text{ m}^3/\text{s}$ ,  $44 \text{ mm}$ ,  $40^\circ$ , and  $0.03 \text{ kg/s}$ , respectively.  $Q_b$  is related to the grain shear stress.

Alternatively, one can choose to hold  $Q$ ,  $D$  and  $Q_b$  constant, and examine the impact of varying  $C_{50}$  on the predicted channel dimensions and gradient. This is the natural set of variables to hold constant when describing an alluvial system, and reflects the conceptual understanding of the physical nature of optimality theory presented in the discussion of Figure 4. As  $C_{50}$  increases,  $W$ ,  $S$ , and  $\tau^*$  all increase rapidly to maintain the same  $Q_b$  (Figure 11). In fact,  $S$  varies by over an order of magnitude as a result of a ten-fold increase in  $C_{50}$ . The inference to be made is that form roughness represents a powerful potential adjustment of the system. If  $C_{50}$  can vary in natural systems in response to a change in the governing conditions, then it may dictate the channel adjustments to the imposed change. Figure 11 indicates that a system can easily adjust to a two-fold increase in gradient (imposed, for example, by tectonic uplift) by a similar adjustment in  $C_{50}$ , which may or may not be expressed at the scale of channel pattern.

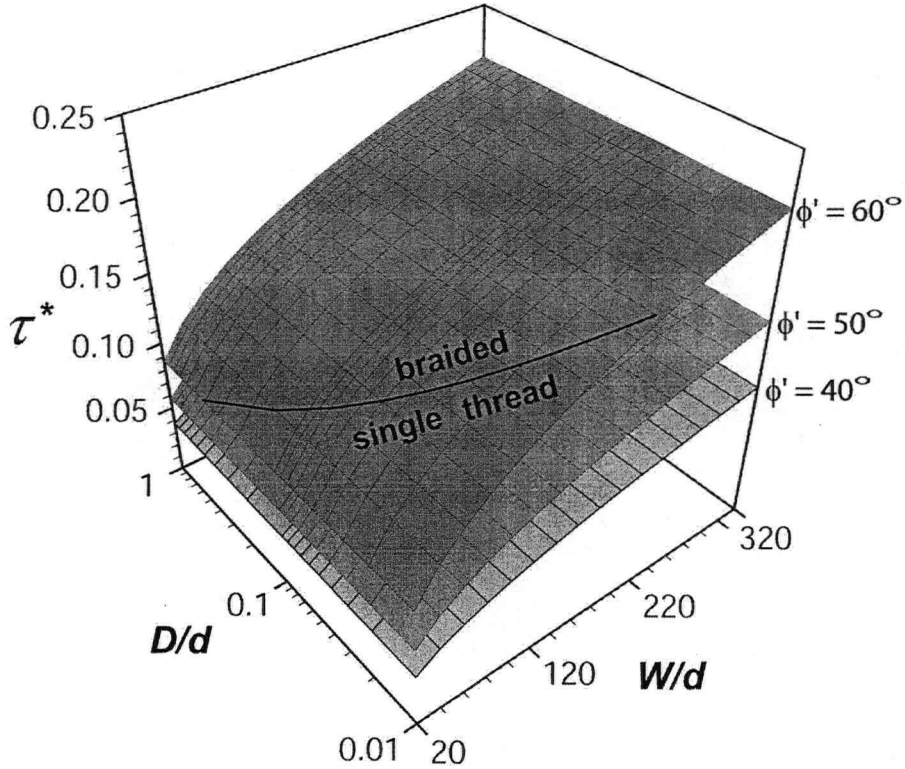


Figure 12: Alluvial state diagram for  $\phi' = 40^\circ, 50^\circ$  and  $60^\circ$ , using the  $W/d, D/d, \tau^*$  coordinate system. Each point on the plane represents an alluvial state characterized by unique  $Fr, S$  and  $Q_b/Q$  values. Parker's (1976) threshold for the inception of braiding is shown on the  $\phi' = 60^\circ$  plane (solid line). The regime model predictions are valid only for the single thread channels below the Parker threshold.

### 2.5.4 Limits of Applicability

This regime model is designed to describe single thread channels only. It does not describe wandering or braided channels, since the geometry upon which the model is based (i.e. a trapezoid) is not appropriate for describing multi-thread channels. Parker's (1976) function for predicting the onset of braiding can be applied to establish limits in the dimensionless alluvial state space ( $W/d, D/d, \tau^*$  or  $S$ ) beyond which the model is no longer valid. Parker originally specified a critical gradient,  $S^*$ , that represents the meandering – braiding transition. The critical gradient can also be expressed as a critical dimensionless shear stress:

Equation 22..... 
$$\tau_b^* = \frac{\gamma_d S^*}{(\gamma_s - \gamma) D} = \left( \frac{\gamma}{\gamma_s - \gamma} \right) \frac{d}{D} \frac{Fr}{W/d}$$

At the threshold between meandering and braiding,  $\tau_b^* = \tau^*$ . This equality defines a single curve in  $W/d, D/d, \tau^*$  space for unique values of  $\phi'$ , and has the property that, for geometrically similar channels, the Parker criterion forces approximate dynamic similarity by specifying a unique  $Fr$  value (see Section 3.2 for more details on dynamic similarity). The alluvial scaling relations and the meandering-braiding threshold can be combined on an alluvial state diagram (Figure 12). Each point on the plane represents a unique alluvial state, characterized by single values of  $Fr, S,$  and  $Q_b/Q$ : that is, each point represents a suite of channels of varying absolute size that exhibit  $Fr$  similarity. The model is valid only for the single thread channels lying below Parker's (1976) threshold.

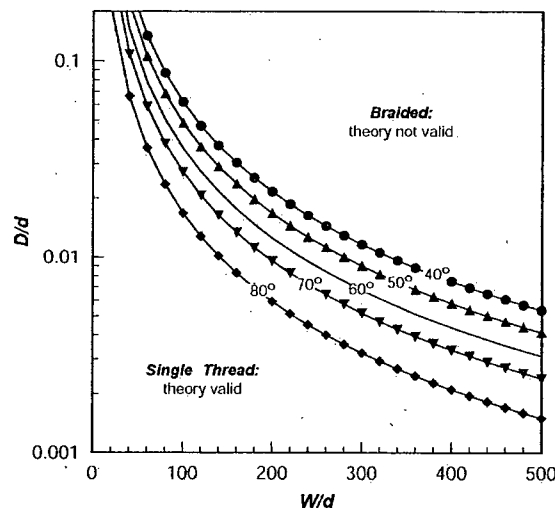


Figure 13: Braiding threshold for various values of  $\phi'$  projected onto the  $(D/d, W/d)$  plane. Each threshold lies within a plane defining the alluvial states for the relevant  $\phi'$  values.

The alluvial state diagram shown in Figure 12 can be transformed by substituting  $S$  for  $\tau^*$ , making it evident that the typical  $Q-S$  diagrams used to distinguish meandering and braided channel patterns (e.g. Lane, 1957; Leopold and Wolman, 1957; Begin, 1981) likely reflect the correlations between  $D/d, W/d$  and  $Q$  that exist in a particular dataset, and do not capture the fundamental controls of channel pattern, thus supporting previous criticisms of the  $Q-S$  approach (e.g. Carson, 1984; Carson and Griffiths, 1987).

As the bank strength increases, the braiding threshold translates along the plane toward lower  $W/d$  ratios. This outcome is clearly demonstrated by projecting the threshold lines for a range of  $\phi'$  values onto the  $D/d, W/d$  plane (Figure 13). Each curve on Figure 13 represents the limit of

validity for the specified value of  $\phi'$ ; power functions describing these relations are summarized in Table 3. All of the relations have similar exponents; (none is statistically different at  $\alpha = 0.01$ , and only the highest ( $50^\circ$ ) and the lowest ( $80^\circ$ ) are different at  $\alpha = 0.05$ ), with the onset of braiding associated with decreasing  $W/d$  ratio as bank strength increases, for a constant value of  $D/d$ . This behaviour reflects the positive correlation between  $Fr$  and  $\phi'$  for a given  $Q$  and  $D$ . For example, a channel characterized by  $Q = 776 \text{ m}^3/\text{s}$  and  $D = 42 \text{ mm}$  first becomes braided at  $W/d = 69$  for  $\phi' = 80^\circ$ , with an associated  $Fr$  of 1.5, whereas the same channel becomes braided at  $W/d = 166$  and  $Fr = 0.61$  for  $\phi' = 40^\circ$ : in both cases, the critical value of  $D/d$  is about 0.03.

Table 3: Power relations fit to braiding-meandering threshold

$\phi'$	$a^1$	$b$	$R^2$
$40^\circ$	67.8	-1.52	0.998
$50^\circ$	55.6	-1.53	0.999
$60^\circ$	39.5	-1.52	0.998
$70^\circ$	28.5	-1.51	0.998
$80^\circ$	16.8	-1.50	0.998

<sup>1</sup>The fitted model is:  $D/d = a(W/d)^b$

### 2.5.5 Comparison with Existing Data

There are two issues to be considered when comparing the behaviour of natural alluvial systems to the predictions from these models. The first is the accuracy with which the parameters used by the model can be determined in the field. In particular, it is not immediately obvious that one can determine appropriate values of  $Q$  and  $D$ , given the variability of both discharge (temporally) and the bed material grain size (spatially) in most alluvial systems. Nor is this a matter of simply choosing the right criteria to determine the formative discharge and characteristic grain size in the field, since the model describes the behaviour of an idealized system in which  $Q$  and  $D$  are by definition sufficient to describe the system, while the behaviour of natural systems can be much more complex.

The second issue is whether or not alluvial systems attain an equilibrium form that can be described by the model. Some channels may not be stable, exhibiting ongoing change in average channel dimensions over time, or they may persist at points on the stability curves (see Figure 2 and Figure 3) that are different than the optimum values. Such behaviour need not imply that the model approach presented above is wrong; it may equally be evidence of insufficient time

between significant perturbations to reach the equilibrium condition, or that certain states have been rendered inaccessible by the prior condition of the system (e.g., a heavily armoured bed).

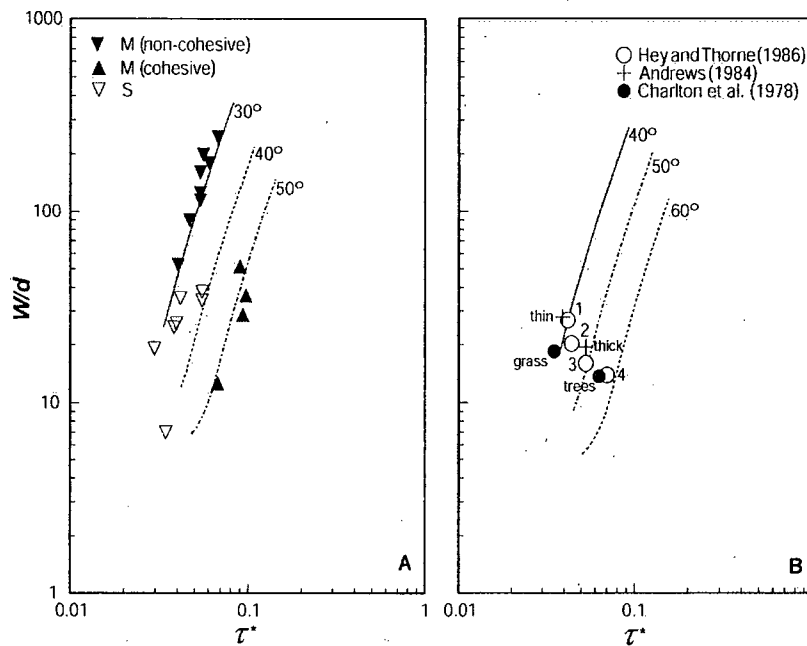


Figure 14: Comparison of channels developed in the laboratory and in the field with predicted scaling relations. (a) The data from laboratory experiments of Schumm and Khan (1972) are plotted on an alluvial scaling diagram based on the model assuming  $\phi = 30^\circ$ ,  $\tau^*_c = 0.035$  (after Yalin, 1971b). Unlike natural gravel bed channels, the minimum bank strength corresponds to  $\phi = 30^\circ$ , which reflects the dependence of the angle of repose on absolute grain size (Henderson, 1966 p. 420). “M” refers to channels exhibiting a meandering thalweg and/or planform, and “S” refers to straight channels. The lines represent scaling functions assuming various bank friction angles. (b) The average behaviour of natural gravel channels classified by bank vegetation class is plotted over the gravel bed scaling diagram (Figure 6). See text for discussion of the various bank vegetation classes and data sources.

Data to test the model remain very limited because the information necessary to apply the theory has almost never been reported. In particular, bank strength is, at best, ever characterised only qualitatively, and one has had to make assumptions in order to have any data at all. The best supporting evidence arises from the laboratory meandering channels described by Schumm and Khan (1972). The bed and banks of their channels were composed of poorly sorted sand with a mean grain size of 0.7 mm, discharge for all experiments was constant (4.25 L/s), and gradient was varied for the different experimental runs. In one set of experiments no cohesive material was added to the system, hence the value for  $\phi'$  is simply the angle of repose for the sediment,

and gradient varied from 0.0026 to 0.013. These experiments are well described by the scaling relation produced by the model for  $\phi' = \phi = 30^\circ$  (Figure 14a). In another set of experiments, kaolinite was added to the water, imparting a cohesive resistance to the bed material, thus causing an increase in  $\phi'$ . These channels are also well described by the model scaling relations, this time for  $\phi' = 50^\circ$ . While there is no way to verify the value of  $\phi'$  for the cohesive bed material experiments, the increase in bank strength is consistent across a range of imposed shear stresses, and is consistent with the range of bank strengths reported by Millar and Quick (1993) for natural gravel bed channels. The comparison of Schumm and Khan's (1972) meandering flume experiments with the model predictions suggests that – under carefully controlled experimental conditions – the model is capable of predicting the behaviour of alluvial systems.

Also shown in Figure 14a are Schumm and Khan's (1972) straight channels developed in non-cohesive bed material. The data generally support the structure of the alluvial scaling relations, but some seem paradoxically to imply a higher bank friction angle than for the meandering channels. The reason for this deviation is not entirely clear. However, the straight channels are all associated with lower channel gradients and lower sediment transport rates, and it may be that these channels failed to reach equilibrium, since the rate-of-change for the straight channels must be lower than for meandering ones. Thus, one might interpret the straight channels as representing non-equilibrium forms, giving rise to the appearance of increased bank strength. Equally, the lower valley slopes may give rise to insufficient stream power, such that at least part of the bed material grain size distribution was no longer mobile, and the coarse tail behaved as some sort of fluvial lag, inhibiting significant deformation of the bed. Unfortunately, Schumm and Khan do not present sufficient data to resolve this question.

Turning to natural channels, a significant problem becomes evident: the bank friction angle is not easily approximated. Given the effects of vegetation (Hickin, 1984; Millar and Quick, 1993) and cohesive sediment (Millar and Quick, 1998), it is not sufficient to assume that a friction angle near the material angle of repose adequately describes the bank strength. One can expect a wide range of bank strengths to occur in nature. Some datasets (Charlton et al., 1978; Andrews, 1984; Hey and Thorne, 1986) exist in which a characteristic bank vegetation density is assigned to each channel. While the individual channels associated with each vegetation class exhibit substantial scatter, the average behaviour of each class supports the scaling implied by the model. The average  $W/d$  and  $\tau^*$  values for each vegetation class for the three datasets are presented in Figure

14b. Hey and Thorne's (1986) data best illustrate the point to be made. They grouped their channels into four classes, ranging from minimal bank vegetation (class 1) to forested banks (class 4). The centroids for the four classes exhibit a progressive and systematic increase in  $\tau^*$  and decrease in  $W/d$  as bank vegetation density and thus bank strength increase. Their class 1 channels are well described by a friction angle of  $40^\circ$ , indicating that they behave as if the banks were unvegetated and non-cohesive. At the other end of the spectrum, the class 4 channels are consistent with a friction angle approaching  $60^\circ$ . The data from Charlton et al. (1978) and Andrews (1984) show a similar trend. Huang and Nanson (1998) also examined these data, and they similarly concluded that bank strength as inferred from vegetation class is an important determinant of channel form.

One can also examine the effect of bank strength by plotting the ratio of the observed channel width for Hey and Thorne's data against the width predicted by a regime model *without* a bank stability constraint. This model is identical to the one presented earlier, except that the bank stability analysis is omitted, and the bank angle is set at  $45^\circ$ , after White et al (1982). This is equivalent to the complete regime formulation in the limit  $\phi' \rightarrow 90^\circ$ , at which Equation 16 becomes undefined. The observed widths are (unsurprisingly) nearly all greater than the widths calculated using the unconstrained regime model (Figure 15). Furthermore, the degree by which the width is under-predicted (the mean bias, after Gomez and Church, 1989) as defined by the ratio  $W_{predicted}/W_{observed}$  varies systematically from an average value of 0.45 for vegetation Type 1 channels to 0.69 for Type 4 channels, implying that, as the bank vegetation becomes more dense, the difference between the observed and the predicted widths becomes smaller, as expected based on the analysis summarized in Figure 14.

In addition to this mean bias related to vegetation class, there also appears to be a local bias related to the scale of the channel, in that the effect of vegetation density appears to be most prominent for smaller channels. The parameter  $Q_{bf}^{1/2}$  is used as an index of channel scale in preference to width because, unlike width,  $Q_{bf}^{1/2}$  is independent of bank vegetation effects. Many empirical regime studies have demonstrated that  $W$  scales in proportion to  $Q_{bf}^{1/2}$  (e.g. Hey and Thorne, 1986). The results shown in Figure 15 demonstrate a consistent scale-dependence of vegetation-induced bank strength, for a given vegetation density. The scatter in these plots is undoubtedly the result of the general nature of the vegetation classes: it is probable that more information on the vegetation – such as the species, age, stem density and rooting depth – could

be used to substantially reduce this scatter. Linear regressions relating the ratio  $W_{predicted}/W_{observed}$  and  $Q_{bf}^{1/2}$  were fitted to the data (shown in Figure 15) in order to isolate the local bias effect: the regression slope coefficients and their statistical significance levels are reported in Table 4.

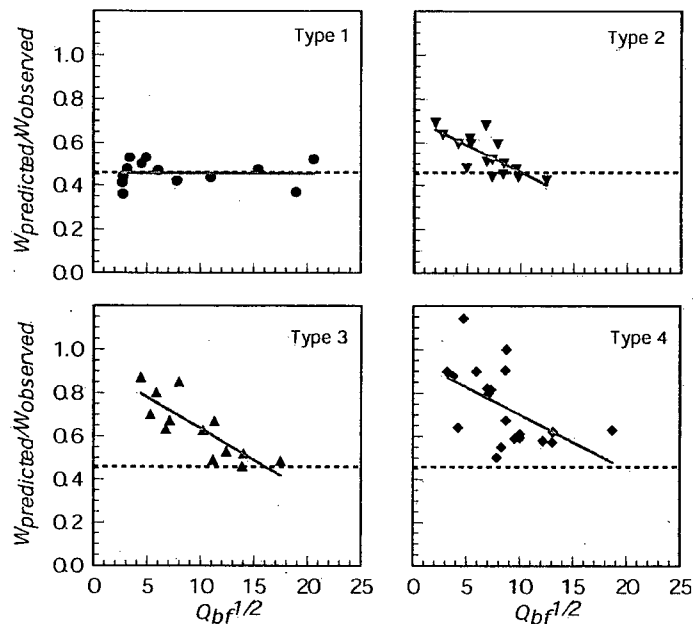


Figure 15: Degree of under-prediction for unconstrained MTC models (given by the ratio  $W_{predicted}/W_{observed}$ ) plotted against  $Q_{bf}^{1/2}$  for gravel bed channels, classified according to bank vegetation density (Hey and Thorne, 1986). Linear regressions of  $W_{predicted}/W_{observed}$  on  $Q_{bf}^{1/2}$  for each vegetation type are shown (solid line), as is the mean degree of under-prediction in the absence of a vegetation effect i.e. class 1 (horizontal dashed line). Slope coefficients and  $P$ -values for the regressions are presented in Table 4.

The largest mean bias between model predictions and observations occurs for the Type 1 channels: however, there appears to be little or no local bias associated with channel scale, and the regression line coincides with a horizontal line representing a mean  $W_{predicted}/W_{observed}$  ratio of 0.45, implying that the observed channels are about twice as wide as those predicted by an unconstrained model, regardless of channel scale. This reference line is also shown on the plots for Types 2, 3 and 4. At the other end of the spectrum, the Type 4 channels have the smallest mean bias, but exhibit a statistically significant local bias. While the smallest Type 4 channels are rather well described by the model, since  $W_{predicted}/W_{observed}$  approaches unity, there is increase in the degree of under-prediction with increasing discharge. At  $Q_{bf}^{1/2} = 20$  ( $400 \text{ m}^3/\text{s}$ ), the regression line intersects the reference curve for the Type 1 channels: the intersection represents

the scale at which vegetation-related bank stability nominally disappears. There are similar, statistically significant trends in the local bias for channel Types 2 and 3, but the intersection point with the reference line varies systematically with vegetation type, such that the vegetation effect vanishes at about  $Q_{bf}^{1/2} = 10$  ( $Q = 100 \text{ m}^3/\text{s}$ ) for Type 2 channels, and at about  $Q_{bf}^{1/2} = 15$  ( $225 \text{ m}^3/\text{s}$ ) for Type 3. Based on the observed hydraulic geometry for the Type 1 channels, these discharge thresholds correspond to critical channel depths – below which vegetation stabilization becomes ineffective – of about 1.5 m, 2 m, and 2.5 m for channel Types 2, 3 and 4 respectively.

Table 4: Slope coefficients for regression of bias against channel scale

Vegetation Type	<i>a</i>	Regression slope <i>P</i>	<i>n</i>
1	-0.0001	0.957	13
2	-0.0249	<0.001	16
3	-0.0290	<0.001	13
4	-0.0254	0.015	20

Note: the fitted regression model is:

$W_{predicted}/W_{observed} = a(Q_{bf})^{1/2} + b$ ; *P* refers to the probability that the slope is not different from zero and that there is no detectable local bias.

It is reasonable to infer that the role of bank strength, as described by the model, in controlling the equilibrium channel dimensions is at least qualitatively consistent with the behaviour exhibited by natural channels when it is assumed that vegetation density represents a reasonable surrogate for bank strength, and furthermore recognize that the scale of the channel relative to the scale of the vegetation is important, as well.

Another way of testing the model is to examine the limits of applicability implied by the Parker (1976) threshold (Equation 22). As demonstrated in Figure 13, the different meandering-braiding thresholds can be projected onto the  $W/d, D/d$  plane. One expects the meandering channels to plot to the left of the threshold for the relevant bank friction angle, and the braided channels to plot to the right. The meandering and braided channels presented by Van den Berg (1995) are plotted on the  $W/d, D/d$  plane, along with the threshold curves based on a range of assumed bank friction angles (Figure 16). With the exception of a single case, all the meandering channels plot to the left of the threshold for  $\phi' = 40^\circ$ . All but three of the braided channels plot to the right of the curve for  $\phi' = 80^\circ$ . Between the two curves, one finds both meandering and braided channels, which is consistent with our expectations. This relatively successful separation of the channel patterns based on a dimensionless representation of the

alluvial state further suggests that the model is adequately describing some of the fundamental aspects of alluvial systems.

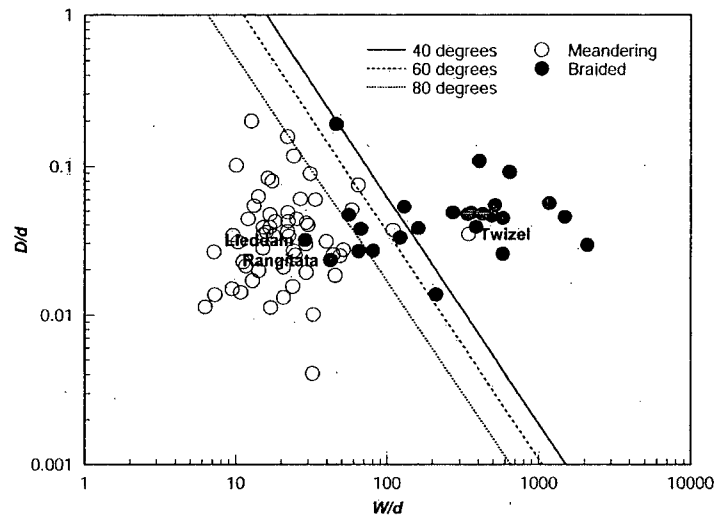


Figure 16: Data from meandering and braiding streams (Van den Berg, 1995) are plotted on the  $W/d, D/d$  plane. Threshold curves based on Parker's (1976) meandering-braiding equation are presented for a range of bank friction angles.

### 2.5.6 Construction of a Response Framework

Figure 12 represents a dimensionless, general framework for alluvial channel response to changes in the governing conditions. Models of channel response to changes in the governing conditions can be constructed in dimensional form, as well. These models are specific to an individual prototype stream, and thus are not generally applicable. However, models constructed for different prototypes will exhibit the same general pattern of interactions, and they have the advantage of explicitly representing all of the governing conditions, rather than subsuming them in dimensionless parameters.

One such model is presented on Figure 17 for a range of  $Q$  and  $Q_b$ . According to regime theory, an equilibrium channel with  $Q = 60 \text{ m}^3/\text{s}$  and  $Q_b = 50 \text{ kg/s}$  (Point "A", Figure 17) should ultimately respond to a doubling in discharge by adjusting its slope while maintaining a nearly constant cross sectional channel geometry (point "B"). While both  $W$  and  $d$  will increase, a slight decrease in the  $W/d$  ratio is predicted. If  $Q_b$  was then doubled, both slope and channel scale would increase (Point "C"), but the slope would be lower and the channel scale larger than that at "A". The net result is that a proportional, simultaneous, increase in both  $Q$  and  $Q_b$  results in a

lower equilibrium channel gradient (primarily as a result of the change in  $Q$ ) and a larger channel scale (change in  $Q_b$ ), even if bed material calibre and relative bank strength are held constant. This is consistent with the observed downstream hydraulic geometry exhibited by alluvial streams, wherein channel width increases more rapidly than channel depth, and slope characteristically declines.

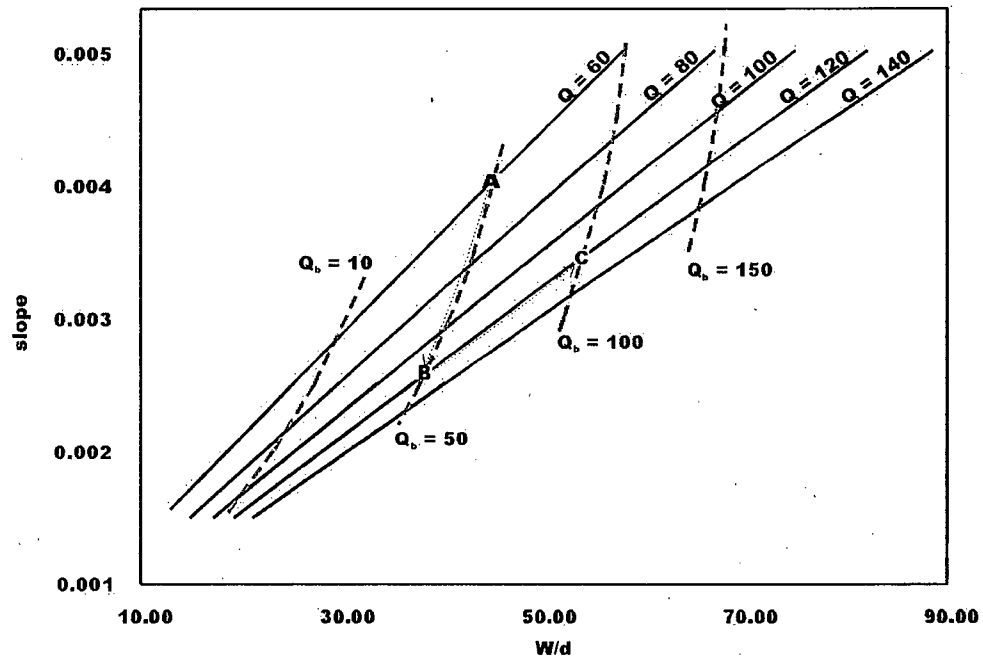


Figure 17: Optimum channel slope and scale ( $W/d$ ) as a function of  $Q$  and  $Q_b$ . For this case,  $\phi' = 40^\circ$ , and  $D_{50} = 32$  mm. The effect of doubling  $Q$  is shown by the trajectory between points “A” and “B”, while the effects of doubling  $Q_b$  is shown by the trajectory between “B” and “C”. Proportional increases in both  $Q$  and  $Q_b$  would follow a trajectory from “A” to “C” (not shown).

Similar diagrams can be constructed by holding either  $Q$  or  $Q_b$  constant and permitting  $\phi'$  and/or  $D_{50}$  to vary. For example, if  $Q = 100$  m<sup>3</sup>/s and  $D_{50} = 32$  mm, then the effect of changes in sediment supply and bank strength (two common potential impacts associated with land use changes in smaller alluvial streams) can be graphically displayed (Figure 18). For constant  $\phi'$ , an increase in  $Q_b$  results in an increase in slope and in channel scale. The relative rates of increase in slope and channel scale depend on the value of  $\phi'$ ; for relatively strong banks (e.g.  $\phi' = 80^\circ$ ), slope changes quickly while scale remains nearly constant whereas, for less resistant banks (e.g.  $\phi' = 40^\circ$ ), both slope and scale change substantially. Channel scale is particularly sensitive to changes in  $\phi'$  for values near  $40^\circ$ , according to the regime model. A decrease in  $\phi'$  from  $50^\circ$  to

40° results in the same change in scale as an increase in  $Q_b$  by a factor of four. Clearly, obtaining an accurate estimate of the bank strength is seen to be critical, since the predicted optimal solution is particularly sensitive to this parameter. Furthermore, validation of the regime theory must examine departures for the modelled slope and scale, taken together. For example, adequate prediction of  $W/d$  ratio for a channel with resistant banks (e.g.  $\phi' = 80^\circ$ ) clearly does not provide much information, since the range is quite small; for these channels, accurate prediction of the channel slope is more indicative of model performance.

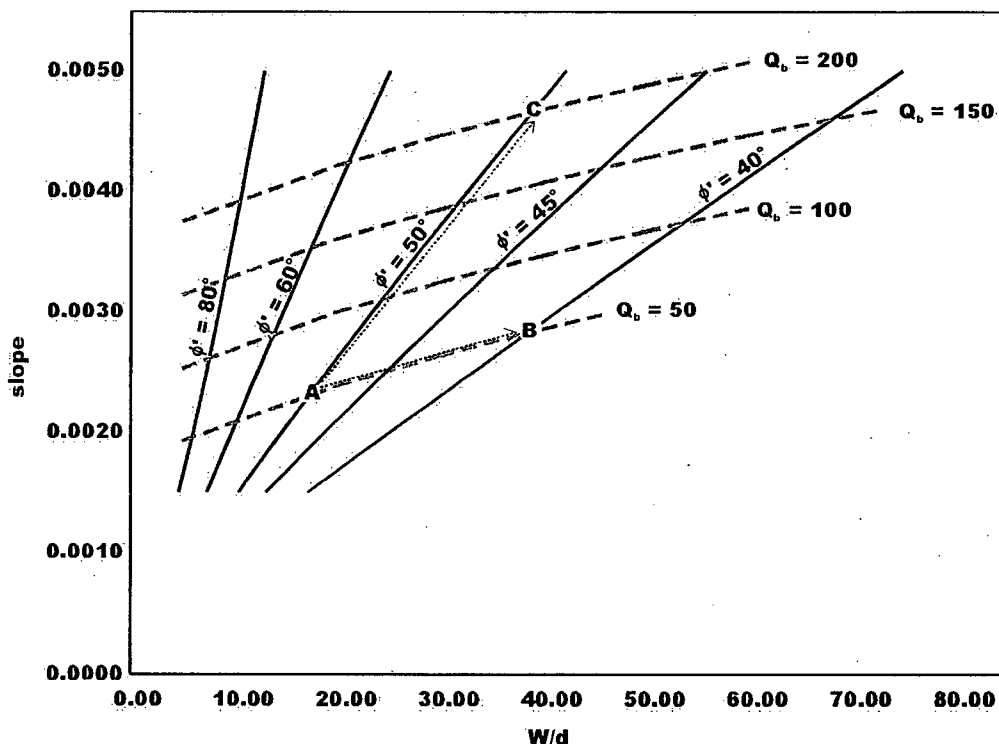


Figure 18: Optimal channel slope and scale ( $W/d$ ) as a function of  $\phi'$  and  $Q_b$ .  $Q$  is held constant at  $100 \text{ m}^3/\text{s}$ , and  $D_{50} = 32 \text{ mm}$ . A decrease in  $\phi'$  from  $50^\circ$  to  $40^\circ$  (Point "A" to "B") produces a change in channel scale similar to that effected by increasing  $Q_b$  by a factor of 4 ("A" to "C")

No published data are suitable for an unambiguous test of the foundations of regime theory, since there is always some significant aspect of the system condition or behaviour that is unaccounted for.

### 3.0 EXPERIMENTAL DESIGN

#### 3.1 HYPOTHESES FOR EXPERIMENTAL TESTS

A more informative test of the foundations of regime theory is needed before the regime approach can be used as a basis for quantifying the likely channel response to changes in the governing conditions. While the regime approach makes many simplifying assumptions about river behaviour, all models similarly reduce the complexity of the system (Dooge, 1986).

The key question is not whether the model reproduces all aspects of river behaviour; it does not, since it is formulated at the reach-scale and thereby averages out any processes occurring at smaller scales. The question is whether the model reproduces the most important characteristics of the system at the reach scale; hence whether it provides a suitable framework for understanding channel behaviour. For example one might ask: how accurate are the model predictions? Or, how much of the observed behaviour can the model predict? Such an assessment of model performance cannot be made if important parameters, such as the sediment transport rate and the relative bank strength, are unknown, nor if the basic assumption of regime condition does not hold.

An appropriate set of research hypotheses should test the degree to which the model describes channel characteristics and channel response to changes in the governing conditions. The hypotheses should be specified such that the critical assumptions made in the model are explicitly tested. The following are the critical hypotheses that we believe test the basis for applying regime theory: all pertain to the fundamental relation between the channel slope and the valley slope.

Hypothesis #1: The flow resistance within the system will be highest at equilibrium channel slope, and an adjustment toward equilibrium should be characterized by a consistent increase in flow resistance for the system.

Hypothesis #2: Channel dimensions and slope are functionally related to the governing conditions,  $Q$  and  $Q_b$ .

In other words, the relative sediment supply to the system determines the minimum possible slope, and hence the degree of sinuosity that may be achieved to maximise flow resistance in the system. B) Changes in  $Q$  and  $Q_b$  are reversible.

Hypothesis #3: The average channel dimensions are predictable, and well described by a regime model.

This requires that a suitable characteristic grain size and the effective channel width and depth be identifiable, and be suitably averaged.

### 3.2 SCALE CONSIDERATIONS AND MODEL LIMITATIONS

Testing the critical assumptions of regime theory in an experimental context requires a physical model that is similar in some fundamental sense to typical river systems in the field. Non-trivial similarity (in the classical sense discussed by Yalin (1971b) between a laboratory model and a natural prototype stream requires that – while the dimensional quantities differ – some characteristic dimensionless variables must remain the same. An obvious approach is to make the model and prototype the same shape (i.e. hold  $W/d$  ratio and  $D/d$  constant). However, this alone is not sufficient, since it does not guarantee that the forces in the model and prototype will obey the same scaling (Henderson, 1966). Since alluvial systems involve two different fluxes (water and sediment) one must consider the dimensionless variables that pertain both to hydraulic conveyance:

Equation 23.....  $\pi_{h1} = \frac{v}{\sqrt{gd}}, \pi_{h2} = \frac{vd}{v}, \pi_{h3} = \frac{W}{d}, \pi_{h4} = \frac{D}{d}, \text{ and } \pi_{h5} = S$

and to sediment transport:

Equation 24.....  $\pi_{s1} = \frac{u^*}{\sqrt{gd}}, \pi_{s2} = \frac{Du^*}{v}, \pi_{s3} = \frac{\rho_s}{\rho}, \text{ and } \pi_{s4} = \frac{D}{d}$

Since the modeller is not able effectively to vary the values of parameters such as the acceleration of gravity, the density of water, or the viscosity of water, true dynamical similarity (involving both geometric similarity and a similarity of all forces) is not possible. As a result, the modeller must evaluate which forces are the most important and which aspects of similarity can be sacrificed without losing the desired similarity of key processes between model and prototype.

The most common approach is to scale using the Froude number ( $h\pi_1$  above, abbreviated as  $Fr$ ), while permitting both the Reynolds number ( $\pi_{h2}$  above,  $Re$ ) and the grain Reynolds number ( $\pi_{s2}$  above,  $Re^*$ ) in the model to be different from the prototype, but only within certain limits, in order to preserve phenomena. While  $Re^*$  need not be scaled in the model, some minimum value is usually invoked below which the modelling approach is not considered to be valid. Yalin (1971b) places the limit in the range  $70 < Re^* < 150$ . Others have suggested minimum values of  $Re^*$  as low as 15 (Parker, 1979) or even 5 (Jaeggi, 1986). Most of the discussion pertains to some average  $Re^*$ , often associated with something like the  $D_{90}$  and there is very little guidance for specifying a design grain size distribution (GSD). Peakall and Warburton (1996) also nominate the Weber number – which describes the importance of surface tension – as an important dimensionless parameter. However, since there has been relatively little work done on identifying the specific effects of surface tension on channel dynamics in scale models, little can be said about the importance of the Weber number. Since even relatively large particles on the bed can be suspended on the water surface as the channel is wetted, surface tension is clearly much different in the model than in a field prototype. The effect of this once the channel is wetted up is less clear, but may influence the fluid force acting upon the stream banks. In comparison with the gravitational forces (scaled by Froude number), this effect is likely to be of secondary importance.

Such Froude-scale models reproduce geometric similarity, while applying the same fluid density and sediment density to both model and prototype. Since geometric similarity is maintained, the length ratios for the model and the prototype (e.g.  $W_r = W_m/W_p$ , subscripts  $r$  referring to relative quantities,  $m$  to the model dimensions, and  $p$  to the prototype dimension) will be the same:

Equation 25 .....  $W_r = D_r = d_r$ .

As a result,  $W_r$ ,  $d_r$  and  $D_r$  can all be represented by a characteristic relative length,  $L_r$ . When Froude scaling is invoked, the following scale ratios exist for velocity ( $v_r$ ), time ( $T_r$ ), discharge ( $Q_r$ ) and force ( $F_r$ ), as described by Henderson (1966):

Equation 26 .....  $v_r = \rho_r L_r^{\frac{1}{2}}$ ,  $T_r = L_r^{\frac{1}{2}}$ ,  $Q_r = L_r^{\frac{5}{2}}$ , and  $F_r = \rho_r L_r^3$

For the purpose of testing the applicability of optimality criteria in the context of alluvial channel pattern prediction, it is not clear what the appropriate prototype system is, nor that strict similarity as described by Yalin (1971b) need be invoked. Hooke (1968) and Schumm et al. (1987) advocate that experimental models be considered as systems in their own right, and that the processes observed in these small systems may be informative for considerations at larger scales.

In designing a model for examining the action of optimality criteria, then, one need not develop a model of a specific prototype, since one's interest is rather more general, pertaining to the behaviour of an entire class of alluvial systems. However, it is still necessary to maintain the values of key dimensionless parameters such as  $Re^*$ ,  $Fr$  and  $D/d$  in the model within a reasonable range of possible values, and to replicate a suitable range of prototype grain sizes in the model. Based on work done by Dade and Friend (1998), an approximate range in relative roughness ( $0.01 < D/d < 0.6$ ) and bankfull dimensionless shear stress ( $0.03 < \tau^* < 0.1$ ) can be identified that corresponds to what they refer to as bedload channels. One can add to these conditions a requirement about the flow conditions in the model based on what is expected in most alluvial prototypes ( $Fr < 1$ ), and a statement about the maximum deviation from the prototypes tolerated in the model ( $Re^* > 5$ ). Based on these considerations, experiments can be designed considering the apparatus available and the amount of data required, as well as more practical considerations.

### 3.3 DEFINING GEOMORPHIC EQUILIBRIUM

Since one is primarily interested in the regime channel conditions, some equilibrium or steady state must be established within the constraints of the experimental setup. Terms like "equilibrium" and "steady state" in geomorphology tend to be imprecise and occasionally confused (Thorn and Welford, 1994), so it is necessary to define them. In this work Howard's (1988) terminology is adopted, wherein equilibrium refers to the behaviour of a single system variable, not to the system as a whole.

Steady state refers to the conditions governing the system response: one cannot begin to think about equilibrium issues until the governing conditions have reached a steady state. Howard also discusses the issue of scale, writing "the selection of an appropriate scale of averaging is generally influenced by the characteristic response time of the output variables (and)...mismatching of spatiotemporal scales for measurement of input and output parameters...will generally complicate or obliterate any possible equilibrium relationships." (p.

51). Thus, if one is interested in equilibrium channel patterns, which are manifested in the field over several years or decades and characterize channels over some substantial length, the process-form interaction must be resolved at similar time and space scales if an equilibrium relation is to be identified.

Steady state – with respect to the governing conditions ( $Q$  and  $Q_b$ ) – must be achieved during the experiments, so that one can be certain the governing conditions are acting over the length of the stream. Steady state is said to occur when the mass fluxes at the downstream end of the stream table are equal to those at the upstream end, when averaged appropriately. Steady state discharge conditions in laboratory experiments may be established very quickly, but steady state sediment transport takes longer to establish because the channel itself may be undergoing net change for some time, with corresponding net gain or loss of sediment along the channel. The point at which steady state sediment transport is achieved can feasibly be determined only after analyzing the recorded sediment output data.

### **3.4 EXPERIMENTAL ARRANGEMENTS**

Various experimental arrangements were used at different stages during the research project. The objectives at each stage were defined as a result of the lessons learnt during the previous stage. The research program can be divided into four phases, each associated with a unique experimental arrangement. Phases 1 and 2 were pilot studies conducted at the University of British Columbia with two different sediment mixtures, wherein natural channels were allowed to develop within an erodible floodplain. During Phase 3, channels were similarly allowed to develop upon an erodible floodplain in the Soil and Water Laboratory, Lincoln University, New Zealand. The last phase (Phase 4) comprises a series of experiments with a mobile bed established between fixed but permeable channel banks. The Phase 4 experiments were conducted at the University of British Columbia.

#### **3.4.1 Rationale for Experimental Arrangement**

In an investigation of the factors controlling channel pattern or potential channel changes, it is appropriate to nominate  $D$ ,  $Q$ ,  $Q_b$ , and  $S_v$  as independent variables (Schumm, 1971) and to consider the channel morphology as the primary adjustable quantity. Over sufficiently long periods of time and on sufficiently mild gradients, alluvial deposits are formed by the river, and the valley slope is a consequence (albeit a complex one) of the bed material sediment supply,

sediment calibre, and discharge during the period. The timescale within which channel pattern in the field may achieve an equilibrium form and within which  $S_v$  and  $D$  can be treated as constants lies between the shortest timescale at which the hydrologic forcing and sediment supply can be viewed as constant (of order 10 a), on average, and the rate for reworking of the floodplain (of order 100 to 10,000 a, according to Everitt, 1968; Gottesfeld and Gottesfeld, 1990; O'Connor et al., 2003). At this graded timescale (c.f. Mackin, 1948), channel pattern can be viewed as the product the mass fluxes ( $Q_b$  and  $Q$ ), constrained by the set of boundary conditions, of which  $S_v$  is an important member. With appropriate arrangements, the functional relations amongst these quantities may be investigated experimentally.

To the author's knowledge, however, previous stream table experiments (e.g. Ackers and Charlton, 1970; Schumm and Khan, 1972; Ashmore, 1982) have not treated  $Q$ ,  $Q_b$ , and  $S_v$  as independent variables; either  $Q_b$  and  $S_v$  have been co-varied, following no particular theoretical basis, or the sediment transported by the stream has been recirculated. These types of experiments do not permit the relation between the channel planform and the governing conditions to be discerned.

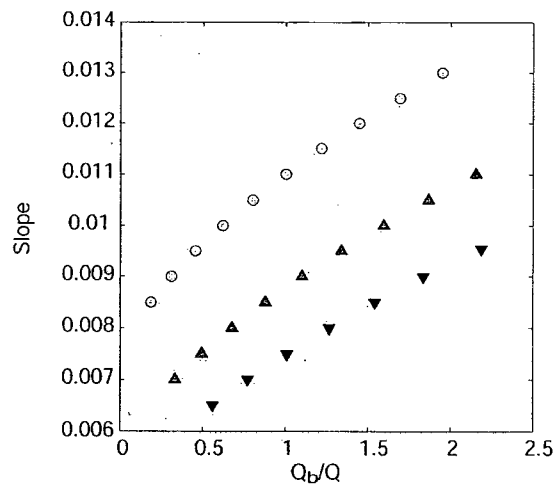


Figure 19: Predicted relation between channel slope and sediment concentration (g/L) for an appropriately configured regime model, using a range of bank strengths. The circles represent the relation assuming  $\phi' = 30^\circ$ , the upward pointing triangles  $\phi' = 35^\circ$  and the downward pointing triangles  $\phi' = 40^\circ$ . The specified discharge in the rational regime model was held constant at 3.4 L/s, and a characteristic grain size of 2 mm was chosen, based on the degree of surface armouring observed during the Phase 3 experiments, discussed in Section 3.4.3

A regime model predicts a relation between sediment concentration and channel slope (Figure 19). The function is slightly nonlinear, but over an appropriately wide range of sediment concentration, a linear trend describes the data adequately. The regime model predicts the channel sinuosity as the ratio<sup>c</sup> between the valley slope and predicted channel slope, after Hey and Thorne (1986). A scaling similar to that shown in Figure 19 is expected to occur during the experimental trials, and would constitute support for the regime approach. Since  $S$ ,  $Q_b$  and  $Q$  are the key variables, this sort of relation is the critical test of the applicability of regime theory.

The Phase 3 experiments (Section 4.2) show that it is reasonable to treat  $Q$ ,  $Q_b$  and  $S_v$  as the independent variables and channel slope/sinuosity as the primary response variable. However, the results obtained are meaningful only when the bed and bank material are equally erodible ( $\phi' = 30^\circ$ ), which is often not the case. In fact, the role of bank strength is emphasised in Chapter 2 as another independent variable in a regime formulation.

Regime model predictions assuming a range of bank strengths are also shown Figure 19. For the same slope, increasing bank strength produces an increase in the amount of sediment that can be transported by the specified flow. For an imposed sediment concentration, the regime slope is reduced as bank strength increases.

However, varying bank strength in the laboratory is complicated by the difficulty of replicating the effects of cohesion (another grain-size scaling phenomenon) and/or the stabilizing effect of vegetation. One would also require a reliable method of estimating the parameter,  $\phi'$ , for any such treatment, which is extremely difficult to do. Furthermore, the Phase 3 experiments suggest that the average wetted channel width does not reflect the regime adjustment, at least over some reasonably constrained range. Rather, the local conditions along the channel thalweg within what may be referred to as the effective width – where most of the fluid and sediment flux occurs – are adjusted in accordance with regime theory. This is in part due to the inability to model all prototype grain sizes and thus all prototype processes – namely bank advance – which obscures the scaling of the effective channel dimensions.

---

<sup>c</sup> Since the valley slope is  $dZ/dL_{valley}$  and the channel slope is  $dZ/dL_{channel}$  then their ratio is equivalent to  $L_{channel}/L_{valley}$ , which is the usual definition of sinuosity, provided both slopes represent the same net drop in elevation.

Thus, the following additional hypothesis is proposed and tested in Phase 4: as bank strength increases, progressively larger sediment loads may be carried at the same channel gradient. Therefore, if the bank positions (and, by inference, the thalweg location) are fixed, a range of sediment concentrations should be able to pass through the system while maintaining the same equilibrium channel gradient, and should represent a range of bank strengths. Effectively, then, if the results of the mobile bank experiments (Section 4.2) represent a transect through the alluvial state space in one direction (i.e. along one of the curves in Figure 19), the results of the fixed bank experiments (Section 4.3) represent a transect horizontally across Figure 19, and normal to the alluvial scaling planes shown in Figure 12.

### **3.4.2 Objectives for the Various Experimental Phases**

The pilot studies (Phases 1 and 2) were designed to establish an appropriate range of model parameters for the main experimental work. Their purpose was to identify any problems in the experimental procedures, clarify the data requirements, and to resolve any scaling issues. There were no specific objectives identified for these initial experiments.

The general objective of the Phase 3 experiments was to test the hypotheses identified in Section 3.1. Two sets of experiments were conducted. In one set,  $S_v$  was held constant while  $Q$  and  $Q_b$  were varied. In the other set, channel sinuosity ( $L^*$ ) was held approximately constant by co-varying  $Q_b$  and  $S_v$  in accordance with the understanding generated from the first set of experiments. The specific objectives for Phase 3 were: (i) to examine the trajectories by which equilibrium channel configurations are reached; (ii) to identify functional relations between the equilibrium channel conditions and the governing conditions; (iii) to compare the equilibrium channel characteristics for the two sets of experiments; (iv) to establish the range of governing conditions for which equilibrium channels can be developed; and (v) to explain the nature of the thresholds bounding this range in terms of flow competence and bed material mobility.

The general objective for Phase 4 was to test the additional hypothesis identified at the end of Section 3.4.1. The specific objectives were: (i) to assess the trajectories toward equilibrium in terms of morphological adjustments and sediment transport characteristics; (ii) to determine if, in fact, different sediment concentrations can be passed with the same channel slope in the fixed bank model; and (iii) to determine if the fluid force on the boundary of the channel supports the inference that increased sediment concentration is associated with a higher boundary shear, and hence bank strength, for the same channel slope.

### 3.4.3 Experimental Apparatus

The initial pilot study conducted at UBC (Phase 1) investigated the behaviour of a narrowly graded sediment having a  $D_{50}$  of about 500  $\mu\text{m}$ , in which an initially straight channel was formed in an erodible floodplain (1.5 m wide by 8 m long), all composed of the same material. The grain size distribution is shown on Figure 20a, and some reference grain sizes are reported in Table 5. A subsequent pilot study was conducted at UBC (Phase 2) using the same apparatus, but a modified grain size distribution. The new distribution had about the same mean size, but represented a range of grain sizes similar to the prototype Sainte Marguerite River described by Eaton and Lapointe (2001). The experiments conducted during Phase 2 represent a severely reduced-scale model, wherein  $Re^*$  was of the order 27, and much of the grain size distribution fell below the apparently critical threshold of 350  $\mu\text{m}$ , beyond which particle behaviour no longer seems to scale appropriately (Ashmore, pers. comm. 2002).

Table 5: Reference grain sizes for all experimental grain size distributions

Size	Phase 1	Phase 2	Phase 3	Phase 4
$D_{90}$	670 $\mu\text{m}$	1.1 mm	3.1 mm	2.3 mm
$D_{75}$	610 $\mu\text{m}$	680 $\mu\text{m}$	2.1 mm	1.4 mm
$D_{50}$	510 $\mu\text{m}$	430 $\mu\text{m}$	1.1 mm	720 $\mu\text{m}$
$D_{25}$	410 $\mu\text{m}$	230 $\mu\text{m}$	580 $\mu\text{m}$	460 $\mu\text{m}$

Based on the results of the pilot studies, the Phase 3 experiments were designed to avoid any scaling problems. These experiments were conducted on a stream table at the Soil and Water Laboratory, Lincoln University, New Zealand. The physical model was a generic, 1:32 scale representation of a moderately steep ( $\sim 1\%$ ), meandering gravel bed river with a  $D_{50}$  of about 22 mm. The grain size distribution was based on bed material samples taken from the Sainte Marguerite River, as it was for Phase 2. The design grain size distribution excluded sediment less than 177  $\mu\text{m}$ , in order to maintain approximate dynamic similarity ( $Re^*$  was about 110). To accommodate this lower limit, the original prototype distribution was truncated at 5.6 mm: the prototype  $D_{50}$  for this truncated distribution is about 32 mm. A commercially available sand mixture matched the design distribution tolerably well, as shown in Figure 20b, and was used to create a floodplain approximately 12 cm deep on the stream table with  $D_{50} \sim 1$  mm. It is perhaps significant to note that this material was collected from a naturally sorted beach deposit, and thus that the grain size distribution was the product of a transport process. The distribution was not modified during excavation on-site, nor was any additional sediment added to it in the laboratory.

Phase 4 was conducted in the UBC stream tray, using a grain size distribution part way between that for phases 2 and 3 (having only a small portion of the distribution below 350  $\mu\text{m}$ ), but with fixed, non-erodible channel banks. The bed material for this phase was derived by removing the sediment finer than 250  $\mu\text{m}$  from the Phase 2 sediment, then adding coarser material to shift the entire distribution upwards in size. The end result is that the proportion of the distribution finer than 350  $\mu\text{m}$  is similar to that for the Phase 3 experiments.

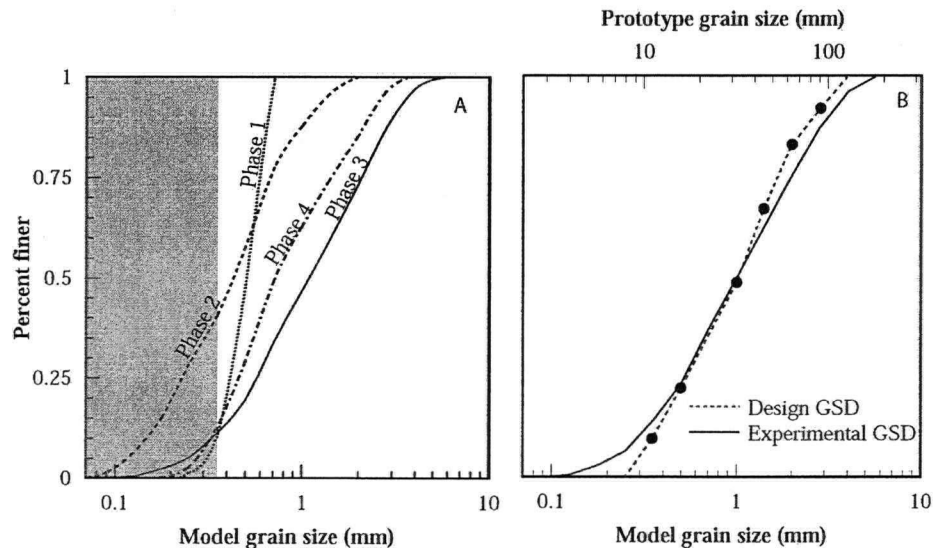


Figure 20: (a) bed material grain size distributions for Phase 1 to Phase 4 experiments. The range of grain sizes less than 354  $\mu\text{m}$  is shaded in grey. (b) design and experimental grain size distributions for Phase 3 experiments. The design grain size distribution represents the bed material from a meandering gravel bed stream in Quebec, Canada. The experimental grain size distribution is that of a commercially available sand mixture.

The tilting stream table used in New Zealand is 30 cm deep, 3 m wide and 20 m long. Water flowed onto the center of the stream table at the upstream end through a 1 m long metal tray with a rectangular section (40 cm by 5 cm), oriented at  $25^\circ$  relative to the stream table centerline, so as to generate an initial bend at the inlet (after Schumm and Khan, 1972). A sediment feed unit introduced the desired sediment supply to the system at the inlet tray, using material with the same grain size distribution as the floodplain sediment. All sediment leaving the stream table at the downstream end was captured in a sediment trap. A load cell and data logger recorded the weight of sediment in the trap every 2 minutes during the experiment. These readings were used to generate average transport rates for 30-minute intervals, which are sufficiently long to average out most of the short-term variation in  $Q_b$ .

The stream table at UBC is half the linear size of the one in New Zealand (15 cm deep, 1.5 m wide, 10 m long). During the Phase 1 and 2 experiments, water flowed onto the center of the stream table at the upstream end through a 60 cm long plastic tray with an adjustable rectangular section, oriented at about 25° relative to the stream table centerline. During the Phase 4 experiments, a weir was constructed out of concrete bricks. It was oriented at an angle of about 45° to the stream table centreline, and was about 50 cm wide (across the channel), and 20 cm long (in the direction of flow). A sediment feed unit introduced the desired sediment supply to the system at the inlet tray/weir crest, using material with the grain size distributions specified in Figure 20. All sediment leaving the stream table at the downstream end was captured in a sediment trap. During the Phase 1 and 2 experiments, a load cell and data logger recorded the weight of sediment in the trap every 2 minutes during the experiment. During Phase 4, the sediment transport collected during 15 minute intervals was recorded, and samples of the grain size distribution were taken.

### **3.5 MEASUREMENT TECHNIQUES**

#### **3.5.1 Water Surface Elevations and Bed Topography**

Measurements of the water surface elevation and of the bed topography were made using a point gauge mounted on a cart which, in turn, was mounted on rails parallel to the floodplain surface. Both stream tables had measurement systems with nearly the same precision. The stated resolution refers to the precision to which the data were recorded, which was the same, in both cases. The  $x$  position (along the stream table) was recorded within a resolution of  $\pm 2$  mm, the  $y$  position (across the stream table) within  $\pm 1$  mm, and  $z$  within  $\pm 0.2$  mm. The water surface elevation at the channel thalweg was measured at the apices of the meander bends, the cross-over points, and at locations approximately half way from one apex/cross-over to the next cross-over/apex. The average channel slope ( $S$ ) was estimated from linear regression lines fitted to the recorded water surface elevation plotted against distance along the thalweg. Channel sinuosity was estimated by forming the ratio of the thalweg length to the valley length (a straight line parallel to the  $x$ -axis) using the water surface elevation data. Surveyed cross sections were located at each apex and cross-over to characterize the channel bed topography. Additional reference cross sections were surveyed for the Phase 4 experiments. Descriptions of the alluvial system presented herein are based on measurements from the middle half of the stream table,

away from any potential inlet and outlet effects (total study length of ~10 m at Lincoln and ~5 m at UBC.).

### 3.5.2 Sediment Transport and Bed Surface Texture

Samples of the bed and bank surface texture were collected following each experiment using a flexible rubber plate covered with a layer of wet clay. A 4 cm by 8 cm plate was used, covered with clay about 1 to 2 mm thick. The plate was pressed firmly against the bed surface, and then dipped into water to release any sediment adhering by soil moisture tension.

For the Phase 3 experiments, samples were taken of the bed armour, approximately located at the thalweg, for each cross section. Samples of the bank surfaces at the eroding cut banks and at the stable cross-overs were also collected. For the Phase 4 experiments, samples were taken of the armour near the bar head, at the cross-overs. The objective was to sample the surface layer, one grain thick, but there was invariably some plastic deformation of the clay paste around the surface grains. To avoid the errors associated with transforming these surface-based samples to bulk equivalents, reference samples of the undisturbed bed material on the floodplain were also taken. These samples represent the subsurface material in the channel, against which the surface samples were compared.

### 3.6 LIMITATIONS

Limitations of the Phase 3 experiments must be acknowledged. In practice, the experiments were run until equilibrium channel sinuosity ( $L^*$ ) was observed. One can also identify an equilibrium water surface slope, but this condition was not necessarily established at the same time as equilibrium  $L^*$ . More importantly, all experiments with significant channel sinuosity ended up producing a multiple thread channel. The initial response of the system was (usually) to maintain a single channel with a coherent thalweg, which evolved rapidly toward an equilibrium sinuosity, then to maintain that state as the channel bars migrated downstream. Once the migrating thalweg eroding the initial floodplain near the bend apex encountered the downstream bar top, the flow stripped the bar surface, and a multiple thread channel formed as the back of the bar eroded (c.f. Ashmore, 1991). The long-term instability of sinuous, single thread channels in laboratory experiments is discussed by Paola (2002), who claimed that either vegetation or cohesive sediment is necessary to maintain a single thread channel, primarily because they introduce a significant difference between the depositional and subsequent

erosional thresholds. This condition would prevent the sort of process described above. Considering that the physical models are based on truncated distributions which do not include even the non-cohesive sand fraction, one can make the more general statement that laboratory models are incomplete physical models of the field prototypes, since they do not construct upper banks.

Furthermore, due to the dramatic change in particle behaviour in fluid transport for sizes much smaller than medium sand, it is not possible to reproduce the entire range of prototype particle sizes and still maintain a similarity of the grain behaviour and interaction. The grain size distribution for this physical model, as for most other models, represents a truncated grain size distribution. In this case, most of the prototype particle sizes that contribute to bar development and bank construction are absent from the model, since only 3% of the bed material is less than 5.6 mm, prototype equivalent (Figure 20b). The bar tops encountered by the migrating thalweg in the model are lower than they would be in the field prototype, the processes and size fractions responsible for floodplain formation being absent.

Provided Froude scaling is maintained, models with the necessarily truncated grain size distributions appear to accurately reproduce the behaviour of the equivalent prototype grain sizes, (Ashmore, 1991), which correspond approximately to the bed load component of the load. This undoubtedly represents an important aspect of channel dynamics in gravel bed streams. As long as the limb of the migrating thalweg along the eroding bank does not encounter the incompletely formed bar tops, the model represents a reasonable approximation of the single thread prototypes. More generally, it implies that a generic representation of a prototype (discussed in Section 3.2) is all that may be achieved in the laboratory, and that models of specific prototype streams are all likely to be seriously flawed if the phenomenon being studied is strongly influenced by suspended sediment dynamics.

While it is acknowledged that equilibrium *single thread* configurations were transient and would eventually have been abandoned as the bars migrated downstream, it is argued that, since thalweg sinuosities did reach constant values after initial periods of rapid adjustment, they are sufficient to study the bedload transport dynamics in their single thread prototypes. The thalweg is taken to represent the path for the bulk of both water and sediment flux, and is assumed to represent the likely prototype channel sinuosity in the presence of floodplain load, cohesive sediment, and/or vegetation.

## 4.0 EXPERIMENTAL RESULTS

### 4.1 PHASES 1 AND 2: PILOT STUDIES

The pilot studies served to identify several important principles for designing physical models. The first pilot study using very narrowly graded sand did not develop a meandering planform, despite a range of sediment feed rates. The primary morphologic change involved the development of local scour holes with sheets of eroded material immediately downstream (Figure 21). Initially, these scour hole-unit bar couplets formed in pairs, one on either side of the channel, at more-or-less regular intervals downstream (Figure 22). After several hours, the bed usually exhibited a series of overlapping scour holes and unit bars (Figure 23). Throughout, the channel remained relatively straight, but widened and became increasingly complex. The system-scale flow resistance parameter,  $f_{sys}$ , increased rapidly at first, and then more gradually (Figure 24), suggesting that the frictional adjustment proposed as a basis for channel adjustment in Chapter 2 holds, even if the form of the channel planform is unexpected.

It was surmised from these experiments that the source of the unexpected behaviour was the limited range of grain sizes. In gravel-bed streams, armouring of the bed and banks is an important process that helps establish and maintain a stable morphology. A systematic horizontal sorting of sediment is also common, associated with the development of bars, which may also be an important stability-related process. Neither of these two processes is effective for a nearly uniform grain size distribution. It was therefore decided to attempt the same experiments with a wider range of grain sizes (the Phase 2 experiments). These experiments did develop the expected meandering channel planform (Figure 25). However, the material transported out of the system had a different grain size distribution than that for the bed material/sediment feed mixture. In fact, the coarsest half of the grain size distribution was over-represented in the transport, and the finer half was under represented. Figure 26 demonstrates this: for each grain size fraction, the transported grain size distribution is normalized by the bed material/feed distribution, such that values in excess of one imply an over-representation of that particular grain size in the transported load, and values less than one imply under-representation. Clearly, the results are inconsistent with any notion of a steady state equilibrium condition with respect to bedload and bed material grain size distribution.

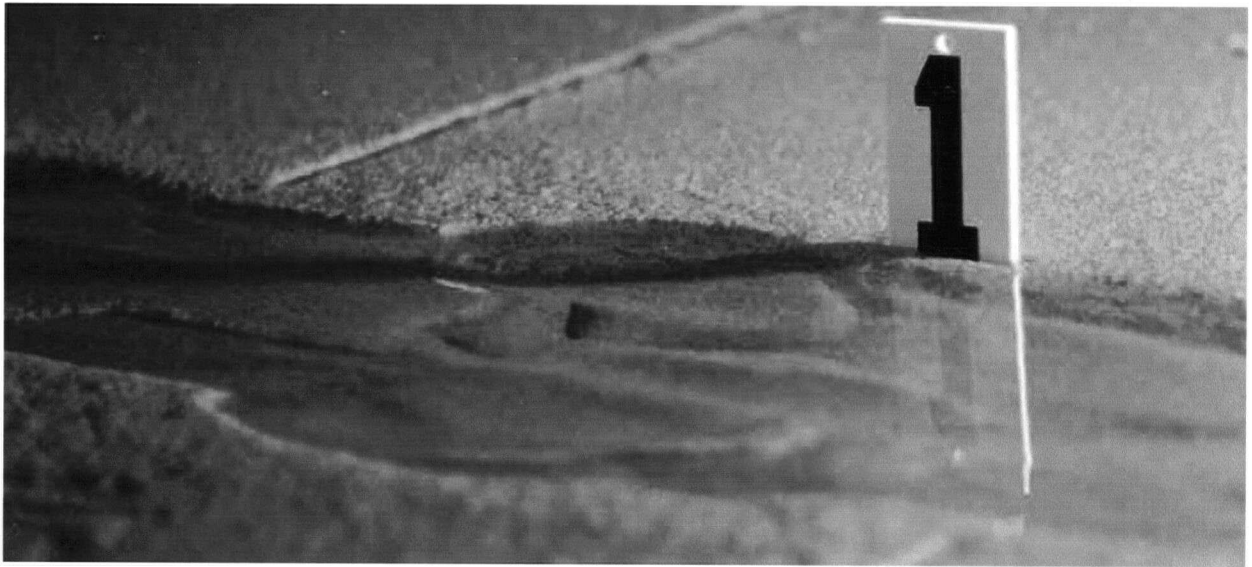


Figure 21: Scour holes and sheets of sand deposited downstream (typical of Phase 1 experiments). Flow is from left to right.

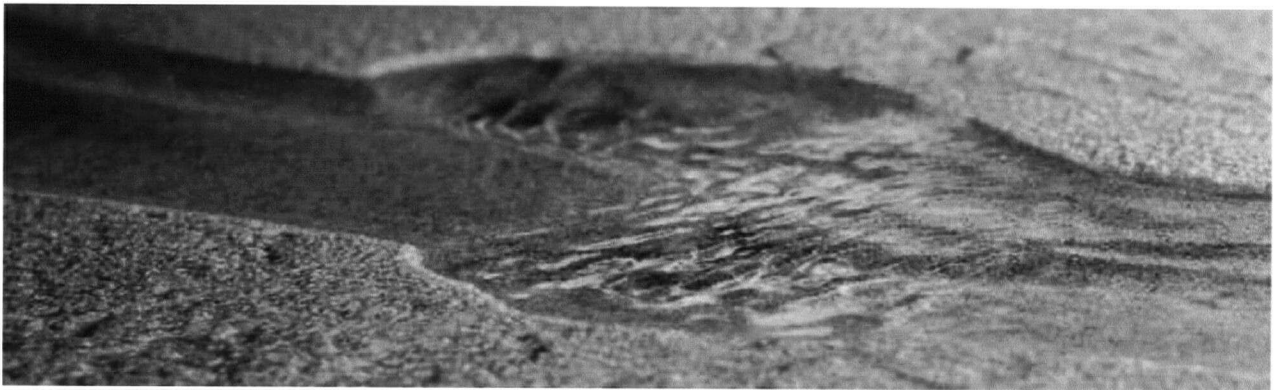


Figure 22: Initial stages of channel development during Phase 1 experiments, involving evenly spaced, paired scour holes. Flow is from left to right.



Figure 23: Typical morphology for Phase 1 experiments, with overlapping unit bars and scour holes. Flow is from left to right.

The general bar stratigraphy is also inconsistent with the expected stratigraphy. The coarsest sediment is generally found on the bar tops, where the fluid force is relatively low, while the finest sediment is found in the channel thalweg (Figure 27). The obvious inference is that the grain size-process scaling is not appropriate. The finer particles are apparently less easily entrained than the coarser ones, indicating that they are not protruding out of the laminar sub-layer, and the flow conditions in the channel thalweg are approaching a hydraulically smooth condition. The net effect is that it becomes more difficult for the flow to entrain and transport the finer fractions, leading to the characteristics of the transport distribution and bar stratigraphy already identified.

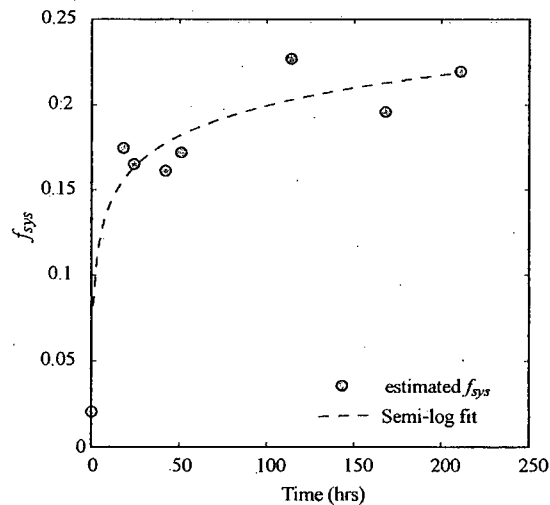


Figure 24: Adjustment of system-scale friction factor during a Phase 1 experiment. The fitted curve is based on a linear regression of  $f$  on  $\text{Log}(\text{Time})$ .

So, while the increased range of grain sizes did lead to a change in style of channel adjustment, producing the more usual meandering – alternate bar morphology, the severe scale reduction ( $Re^* \sim 26$ ) introduced a distortion of process similarity associated with the grain size distribution. The net result is a channel that appears to behave in much the same way as the generic prototype would, but which fails to achieve anything close to an equilibrium configuration. There are few conclusions that can be drawn from this second pilot study, save that the processes resulting in alternate bar development are somehow associated with the existence of a range of particle sizes, and that scale models of gravel bed streams that exhibit  $Re^*$  much below the critical limit of 70 proposed by Yalin (1971b) may fail to reach an equilibrium condition, particularly if a wide range of grain sizes is being modelled.



Figure 25: Meandering pattern with alternate bars typical of Phase 2 experiments

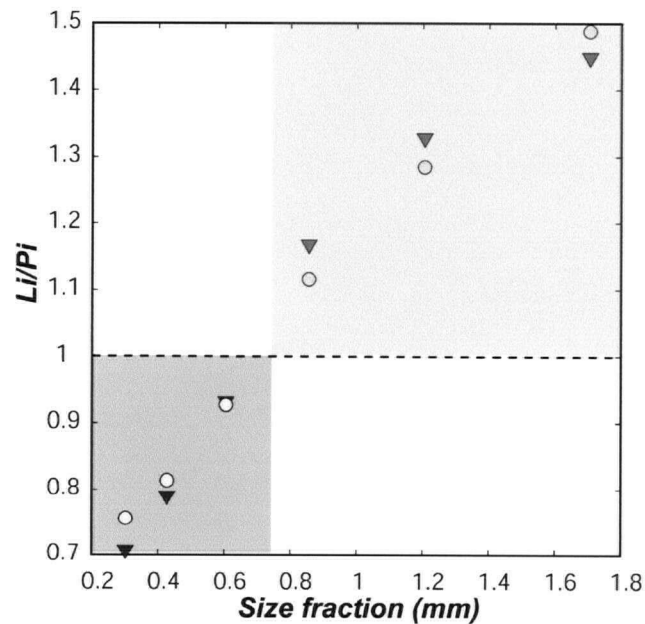


Figure 26: Fractional transport analysis for Phase 2 experiments.  $L_i$  is the proportion of the transported material for the  $i^{\text{th}}$  size fraction, and  $P_i$  is the corresponding proportion for the bed material (subsurface). The two curves represent the average condition for two different experiments based on between 6 and 10 samples of the transported load. Both the transport distributions and the bed material distributions were truncated at  $250 \mu\text{m}$  since this was the size of the mesh in the sediment traps, and trap efficiency below this was uncertain. The lighter grey area delineates that part of the distribution that is over-represented, while the darker grey area delineates the under-represented part.



Figure 27: Typical bar texture for Phase 2 experiments, where the finer (white) sediment is found along the thalweg and the coarser material is found on the bar top.

#### 4.2 PHASE 3: MOBILE BANK EXPERIMENTS

Two sets of experiments were run using the Phase 3 experimental configuration, all of which were characterized by  $Re^*$  numbers about 110, and Froude numbers below unity. In the first set of experiments, the valley slope was held constant, and the sediment supply and discharge were varied over a range similar to that which might be expected for a river in the field as a result of changes in the climate and/or landuse, anticipating evolution toward some equilibrium state. Table 6 summarizes the governing conditions for these experiments, and presents the initial specific discharge ( $q$ ), which is a useful index of the shear force at the beginning of the experiments. From this first set of experiments, a strong relation between the thalweg slope and the sediment concentration emerged – consistent with the theory presented in Chapter 2 as discussed in the results section. Accordingly, a second set of experiments was conducted wherein the valley slope and the sediment supply were co-varied according to this relation so as to produce a selected degree of channel sinuosity. That is, the system constants were manipulated according to the apparent functional relation observed in the first series of experiments to produce a desired single-thread channel pattern. Each experiment in this second phase, then, represents a test of the initial relation. The initial conditions are also shown in Table 6.

Table 6. Governing conditions and equilibrium response for Phase 3 experiments

Experiment	Initial $q$ (L/s/dm)	Governing conditions				Equilibrium Response					
		$Q_b$ (g/min)	$Q$ (L/s)	$S_v$ (%)	Time <sup>+</sup> (hr)	$S$ (%)	$L^*$	$W$ (cm)	$A$ (cm <sup>2</sup> )	$f_{sys}^*$	
Constant $S_v$	1-1	0.85	128	3.4	1.09	8.5	0.97	1.122	99.4	129	0.11
	1-2	0.75	128	3.0	1.09	17.5	1.00	1.012	48.3	80.9	0.07
	1-3	1.08	128	4.3	1.09	24	0.96	1.061	82.5	126	0.14
	1-4	0.66	214	4.3	1.09	1	1.00	1.108	91.8	152	0.15
	1-5a*	0.68	214	3.4	1.09	4	1.04	1.029	61.7	107	0.13
	1-5b	n/a	186	3.4	1.09	4	1.01	1.050	64.8	101	0.10
	1-6	0.66	186	4.3	1.09	1	0.99	1.072	78.4	125	0.13
	1-7†	0.65	128	2.6	1.09	n/a	1.08	1.067	59.4	87.2	0.04
Constant $L^*$	2-1	0.61	434	3.4	1.28	1	1.18	1.051	67.1	95.5	0.09
	2-2	0.65	370	3.4	1.22	1	1.15	1.074	70.2	111	0.15
	2-3	0.65	270	3.4	1.12	1	1.09	1.049	65.8	107	0.13
	2-4	0.65	320	3.4	1.15	1	1.10	1.052	66.8	108	0.13
	2-5‡	0.62	540	3.4	1.30	n/a	1.17	1.115	72.2	112	0.16
	2-6‡	0.62	537	3.4	1.28	n/a	1.12	1.083	79.6	120	n/a
	2-7‡	0.62	520	3.4	1.28	n/a	1.09	1.136	82.0	131	0.15
	2-8‡	0.65	560	3.4	1.20	n/a	1.15	1.082	72.4	109	0.13
	2-9‡	0.65	560	3.4	1.20	n/a	1.11	1.083	73.8	110	0.15

For these experiments,  $Re^*$  was about 110, and  $Fr$  ranged from 0.66 to 0.95 with a mean of about 0.8. <sup>+</sup> Time to reach graded channel configuration. <sup>\*</sup> This experiment is the template for the constant  $L^*$  experiments, and is plotted with them on the relevant figures and included in the relevant analysis. <sup>†</sup> The flow strength for this experiment was below the competence limit. <sup>‡</sup> These experiments did not reach equilibrium between the sediment feed rate and the sediment output.

#### 4.2.1 Trajectories Toward Equilibrium

The equilibrium channel planform for these experiments was approached by a number of paths. Experiment 1-1 provides a particularly good example of the typical response of the system. The sediment supply concentration for this experiment was 0.63 g/L, which is near the lower end of the range for these experiments. Figure 28 presents the thalweg location at various times during the experiment. During the first 4 hours, channel sinuosity increased rapidly. Figure 29 shows the channel morphology at low flow after 4 hours, looking upstream. Between 4 hours and 8 hours, the average sinuosity changed only slightly, as the system stabilized but, by 12 hours into the experiment, the bar tops were exposed and eroded, leading to a multiple thread pattern. For the sake of simplicity, only the dominant thread at 12 hours is shown on Figure 28; its location clearly indicates that the bar tops have been exploited during the change in channel pattern.

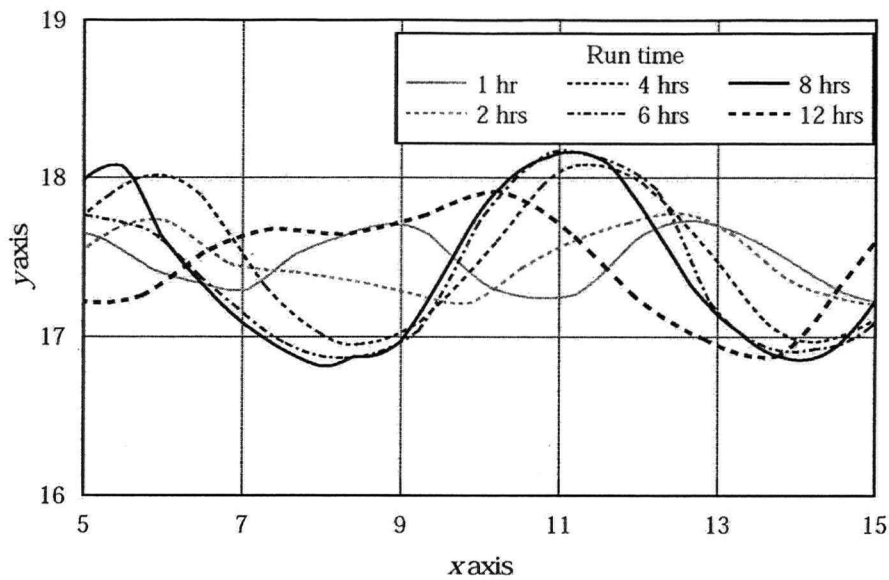


Figure 28: Thalweg locations during experiment 1-1. Flow is from right to left. The equilibrium single thread channel occurred at 8 hours. The thalweg at 12 hours reflected the occurrence of chute cut-offs across the top of the point bars as the channel developed a multiple thread pattern.

For this experiment, the system configuration after 8 hours is considered to represent the equilibrium state, an interpretation that is supported by the sediment transport data. The average sediment export from the system between 7.5 and 8 hours was approximately 134 g/min, quite close to the sediment feed of 128 g/min, and consistent with a steady state mass flux. The 30-min average transport rate for the earlier stages of the experiment were much higher, though they declined steadily after 2.5 hours (Figure 30a). Since the recorded transport represents only the net export from the system, it may not describe the transport rate upstream of the outlet, and the stable thalweg configuration after about 4 hours may reflect a local transport rate in the middle part of the stream tray that was similar to the sediment supply. Since steady state mass flux is generally first established near the inlet, and then progresses downstream from there, the relatively high transport rates between 4 and 7.5 hours likely indicate that the steady state condition had not yet propagated all the way to the outlet.

The material transported out of the stream table between 4 and 8 hours had a grain size distribution that was very similar to the material used to construct the bed and provide the sediment supply (Figure 30b). Since the sediment trap used a 160  $\mu\text{m}$  mesh screen, both distributions shown in Figure 30b were truncated at 180  $\mu\text{m}$ . The main difference between them is a slight under representation of the particles at either end (less than about 500  $\mu\text{m}$  and greater than about 4 mm) in the transported material. The finer particles may be missing due to some

inefficiency in the trap, since water occasionally overflowed the trap when the mesh became clogged with fine sediment. The largest particles in the bed material were absent from the transported material, and remained on the bed surface as an armour layer. However, the  $D_{25}$ ,  $D_{50}$  and  $D_{90}$  of both distributions remained nearly identical.

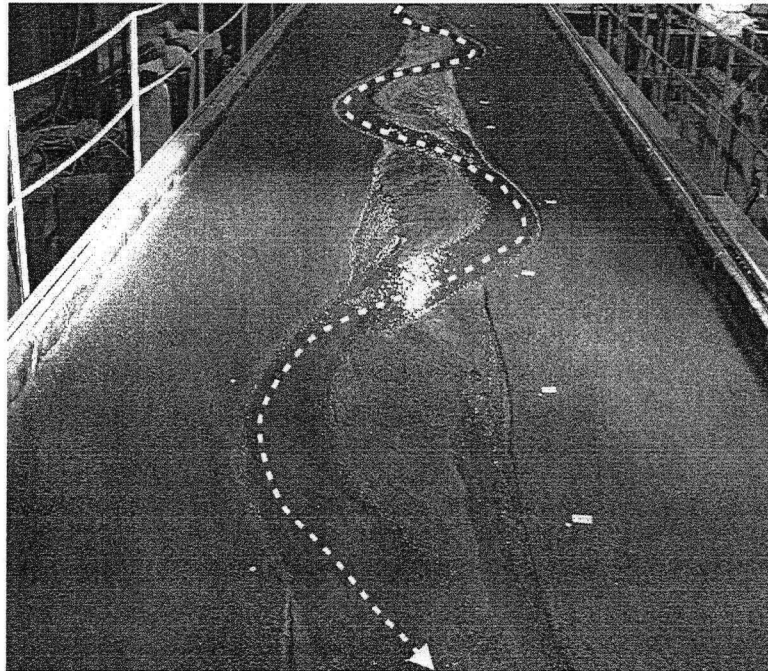


Figure 29: Photograph of channel planform after 4 hours during experiment 1-1. This photograph shows the channel at low flow: at the design discharge, the bars were entirely covered by water. The approximate thalweg location and flow direction are shown.

The rate at which a given experiment approached equilibrium was observed to depend strongly on the initial conditions. For initial channels in which the shear force was low (as indexed by  $q$  in Table 6), channel sinuosity increased very rapidly, and stabilized after 1 to 4 hours (experiments 1-4, 1-5a, 1-6, and 2-1 to 2-9). Unfortunately, these experiments moved on just as quickly to multiple thread configurations, making data collection problematic. When the initial shear force was higher, the system sometimes initially degraded while remaining relatively straight, without widening its channel appreciably. Only after many hours, when the channel slope was substantially reduced, did the channel become sinuous.

Experiment 1-3 demonstrates this two-phase system response, wherein an initial degradational response gave way to a lateral channel pattern response. Figure 31 presents the thalweg locations and water surface elevations for the experiment. For the first 7 hours, the primary response was

vertical degradation, especially near the inlet, while thalweg sinuosity changed only slightly. Between 7 and 16 hours, the trend was reversed, with most of the adjustment occurring after 11 hours (the thalweg profile at 11 hours is not shown since it is nearly identical to the profile at 7 hours). After 11 hours, the channel shifted laterally, increasing the sinuosity. Only after about 24 hours did the channel sinuosity reach equilibrium.

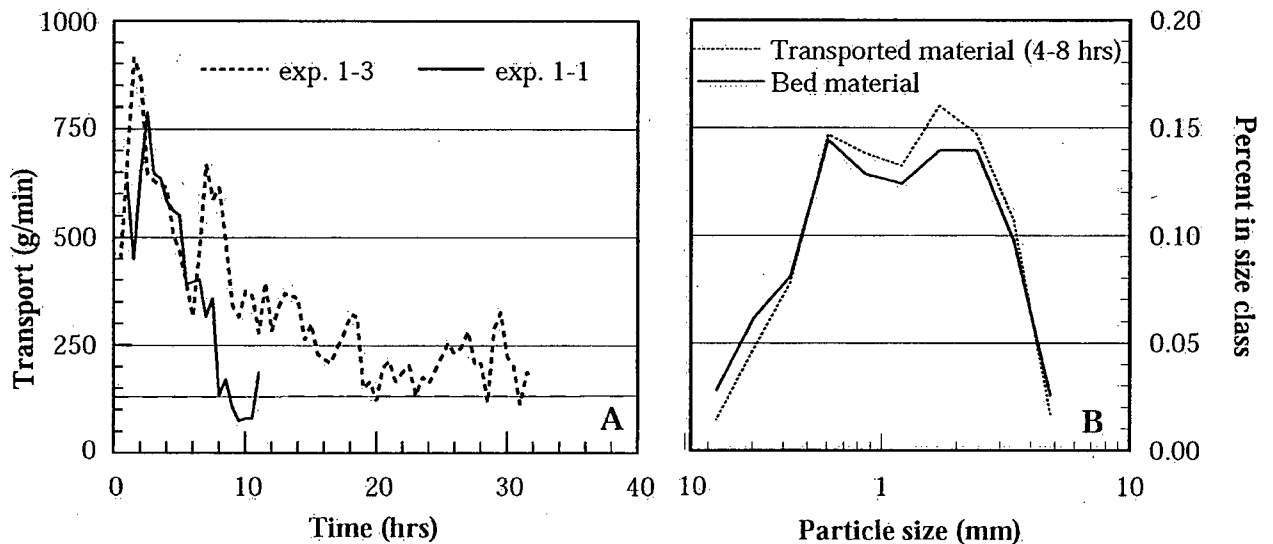


Figure 30: (a) Sediment transport (30 minute averages) recorded at the stream table outlet for experiments 1-1 and 1-3. For both experiments the sediment feed rate is 128 g/min, shown with a horizontal dashed line. (b) Comparison of the bed material and the transported material for experiment 1-1. The sample of the transport between 4 and 8 hours is presented. Other samples of the transported material for different time periods and for the other experiments presented here have similar distributions.

The grain size distribution of the transported material is similar to that for experiment 1-1, wherein the primary differences between the bed material and transport grain size distributions occur in the tails. The sediment transport rate for experiment 1-3 (see Figure 30a) exhibits a range of values similar to that for experiment 1-1. The pattern of change is also similar, exhibiting a continuous decrease in the sediment transport rate over time, but transport during experiment 1-3 reached steady state after about 20 hours, before the equilibrium channel pattern was attained. Similarly, an equilibrium thalweg slope was reached by about 20 hours, well before the channel planform became stable. The configuration surveyed after 24 hours was used to represent the equilibrium configuration.

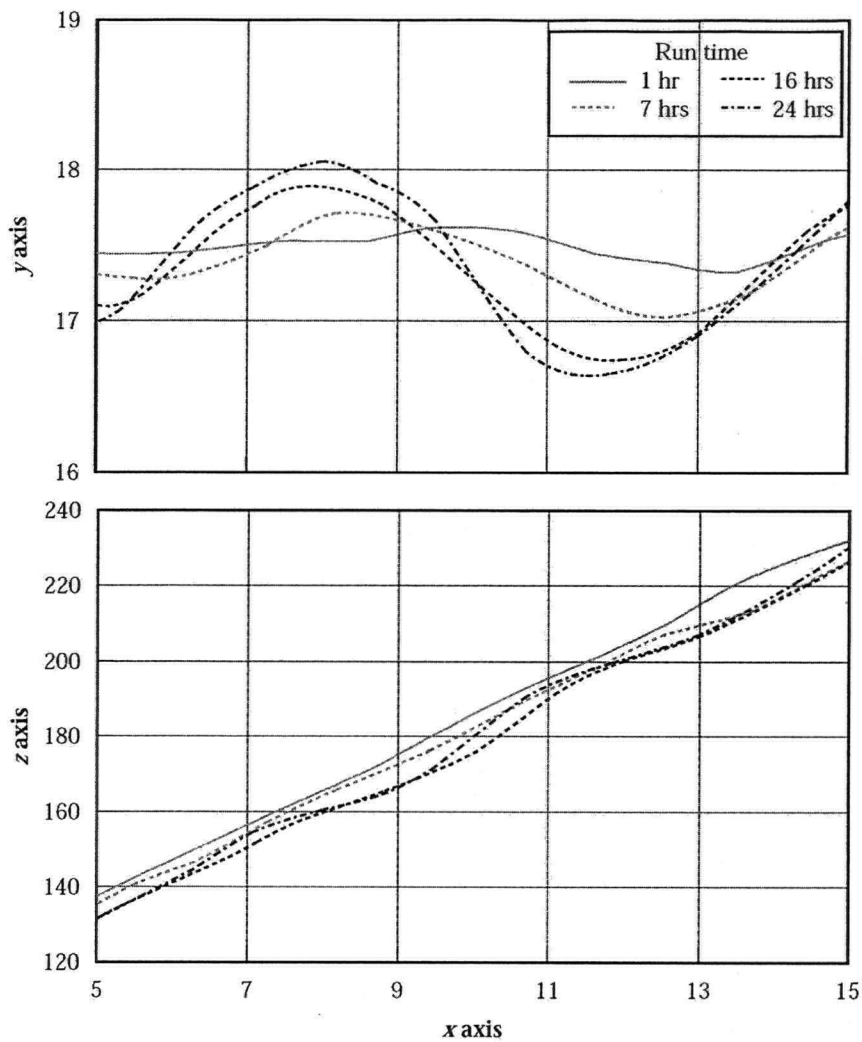


Figure 31: Thalweg locations and elevations during experiment 1-3. The  $x$  and  $y$  coordinates are measured in meters, relative to the datum parallel to the floodplain surface, and the  $z$  coordinate is measured in mm.

The more rapid transitions toward equilibrium configurations were more difficult to document since adjustment occurred more rapidly than the data could be collected. The channel response for these experiments involved only lateral channel adjustment, wherein a sinuous thalweg developed very rapidly so the system quickly reached steady state mass flux. Experiment 1-5 provides the best example of the rapid transition. Since there was very little difference in any of the thalweg profiles, the changes over time are best observed by examining the thalweg slope. Figure 32 presents the thalweg slope at one-hour intervals. For the first 4 hours of the experiment (1-5a),  $Q$  was held constant at 3.4 L/s and  $Q_b$  at 214 g/min. The slope converged to a constant value after about 3 hours: equilibrium was assumed to occur at 4 hours. Almost all the sinuosity adjustment occurred during the first hour, reaching a value of about 1.025; during the

next 3 hours, the sinuosity increased by less than 0.5% to 1.029. The changes in channel slope between the surveys at 1 hour and 4 hours were just slightly larger, at 1.5%.

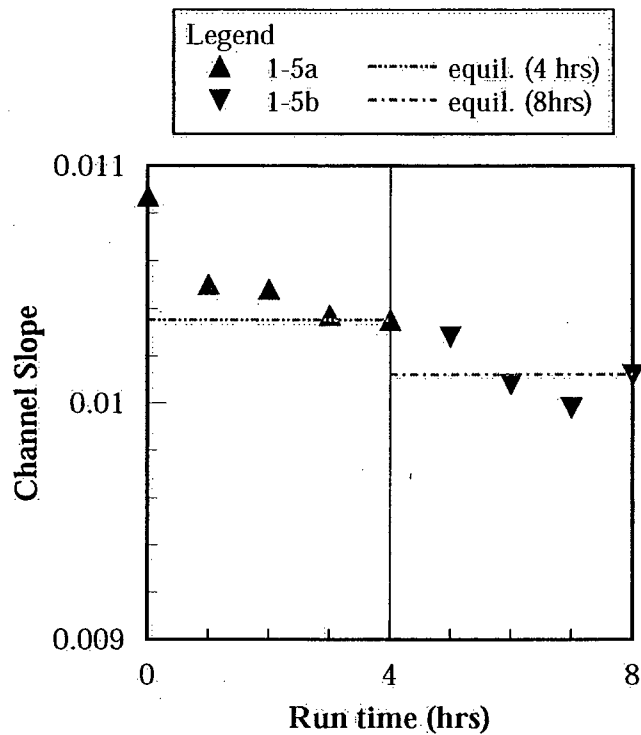


Figure 32: Water surface slope along the thalweg during experiments 1-5a and 1-5b. For the governing conditions for 1-5a and 1-5b, refer to Table 6.

In the second half of the experiment (1-5b),  $Q_b$  was reduced to 186 g/min. The response in channel sinuosity and slope was immediate. By 6 hours (2 hours after the change in  $Q_b$ ) the channel sinuosity stabilized at 1.05, and the channel slope reached what is believed to be the equilibrium value. The channel slope fell below that slope between 6 and 7 hours, but returned to it by 8 hours; channel sinuosity was constant throughout, so the small variation in slope can be attributed only to vertical changes in the local bed height and/or to changes in local flow resistance. The second equilibrium configuration is characterized by the channel condition at 8 hours.

#### 4.2.2 Constant Valley Slope Experiments

**Adjustment of resistance:** In the first set of experiments, in which discharge and sediment supply were varied at constant valley gradient, seven of eight runs reached a steady-state configuration,

wherein the transport rate and grain size distribution at the outlet were consistent with the sediment feed rate at the inlet. For experiment 1-7 the measured transport rate at the outlet was consistent with the sediment feed rate, but the grain size distribution of the transported material was different than that of the bed material, and from the transported material for the other seven experiments. We will defer an extended discussion of this experiment to a later section (Section 4.2.4).

The leading hypothesis underlying the theory presented in Chapter 2 (Hypothesis #1, Section 3.1) is that flow resistance should be highest for the equilibrium channel configuration, and that transitions toward equilibrium should be characterized by a consistently increasing  $f_{sys}$ . It is known that an equivalent conjecture is that channel gradient is minimized subject to the capacity to pass the imposed sediment load, provided that  $f'$  and  $f''$  remain essentially constant. While it is not possible to demonstrate directly that the flow resistance for the equilibrium condition is at a maximum or that the equilibrium slopes are at a minimum, we can investigate the trajectories toward equilibrium using the results of experiments 1-3 and 1-5a, for which the appropriate data exist.

Since net degradation occurred during some of the experiments, the valley slope,  $S_v$  for the experiments was not always consistent with the interpretation of  $S_v$  upon which the derivation of Equation 20 is based (Chapter 2), which really refers to the water surface slope for a channel running straight down the valley. This slope can be estimated for the experiments using a regression of the water surface elevation data against distance down the stream table. If we define this quantity to be the system slope ( $S_{sys}$ ), then:

Equation 27 .....  $S_{sys} = S_v - \Delta S_{deg}$

where  $\Delta S_{deg}$  represents the effect of degradation on the water surface, relative to the valley surface (i.e. the distribution of vertical incision). This is effectively a partitioning of  $S_v$  into a component related to the reach scale flow resistance,  $S_{sys}$ , and a component associated with degradation. The changes in the system associated with  $\Delta S_{deg}$  may be incorporated in the adjustments of  $f'$  and/or  $f''$ , while the adjustment of the channel slope relative to  $S_{sys}$  is incorporated in  $f'''$ . This partitioning of  $S_v$  is theoretically important, but practically the difference is small, with an average difference of 2.8% between the equilibrium values of  $S_v$  and

$S_{sys}$ , and a maximum difference of 7.5% during the degradational phases of experiments 1-2 and 1-3. Since  $f_{sys}$  is linearly dependent on the value of slope used, the differences associated with this correction are of the same magnitude. So, when calculating  $f_{sys}$ , the slope  $S_{sys}$  is used in Equation 20.

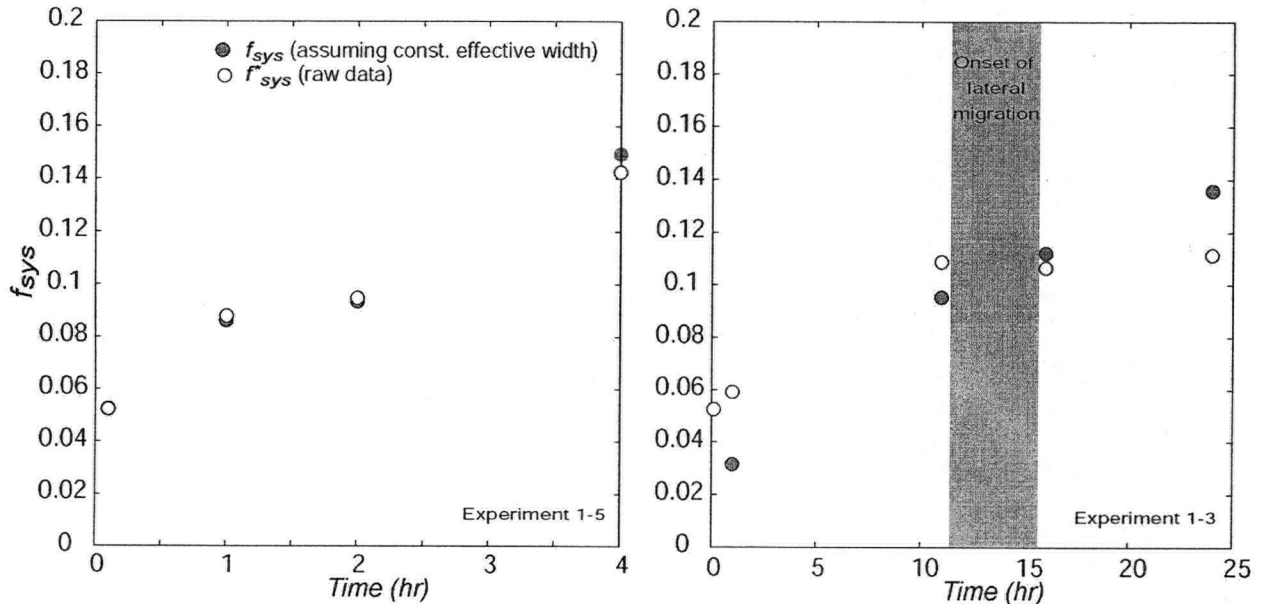


Figure 33: System-scale flow resistance, indexed by  $f_{sys}$ , is plotted against time. Equilibrium was reached after 4 hours for experiment 1-5 and after 24 hours for experiment 1-3. Two definitions were used;  $f_{sys}$  is based on the raw data, and  $f_{sys}^*$  on the assumption that – for sinuous channels – 90% of the flow is carried within a cross section with an effective width of 60 cm. The values of  $f_{sys}$  closest to the  $y$  axis represent the flow resistance in the initial rectangular channel cut straight down the stream table.

The most easily interpreted data come from experiment 1-5a. A plot of  $f_{sys}$  against time shows a consistent increase over time toward a local maximum at equilibrium (Figure 33). Data from experiment 1-3 also exhibit the same general behaviour, but the pattern is complicated by the positive correlation between  $W/d$  and sinuosity, discussed later in this section. It is argued that this positive correlation is the result of the absence of bank advance in the model, and should not be expected of the prototype.

To mitigate this channel width distortion for the sinuous channels, a modified  $f_{sys}$  was also calculated. It is assumed that, while the channel width is unrealistically large, the mean velocity – calculated by  $Q/A$  – is more-or-less representative. Furthermore, it was estimated from observations during the course of the experiments that at least 90% of the discharge is

transmitted through an area with an effective width ( $W_{eff}$ ) of about 60 cm. By substituting the approximation:

Equation 28.....  $R = d = \frac{0.9Q}{W_{eff}v}$

into Equation 20, and including the appropriate slope term, we get:

Equation 29.....  $f_{sys}^* = \frac{8g(0.9Q)S_{sys}}{W_{eff}v^3}$

Thus, one can recalculate  $f_{sys}$  by imposing a constant effective width. When the sinuosity of the channel is relatively low, nearly all of the flow will be transmitted through the effective width, since the effective width and the wetted width will be nearly identical, but when the channel becomes significantly sinuous,  $f_{sys}^*$  will be greater (and more representative), than  $f_{sys}$ . A key assumption in the above argument is that the mean velocity based on the average dimensions is more-or-less correct, particularly given the dependence of  $f_{sys}^*$  on  $v^3$  in Equation 29. To verify the validity of this approach, the cross sectional area associated with the specified effective width was calculated for the experiment 1-3 surveys at 16 hrs and 24 hrs, for which the  $W_{eff}$  was most different from the total  $W$ . Based on the assumption that 90% of the discharge was passed through this part of the channel, the average velocity was calculated. In both cases, the difference in the calculated velocities was less than 3%.

This alternative definition ( $f_{sys}^*$ ) is also shown on Figure 33. For experiment 1-5a, the actual wetted width is close to 60 cm and there is little apparent change in the data and, in fact,  $f_{sys}^*$  is slightly lower than  $f_{sys}$ , since more than 90% of the discharge is actually being transmitted through the assumed effective width of 60 cm. But for experiment 1-3, a divergence occurs between the two. The onset of this divergence is coincident with the onset of significant lateral activity, and  $f_{sys}^*$  based on the effective width definition increases consistently to a local maximum at equilibrium. The evident divergence is thought to be the result of a progressive bias in the estimate of the mean depth produced by the inclusion of extensive shallow areas on the bar tops that don't contribute much to the overall cross sectional area, but which greatly inflate the

wetted width. The consistency of the trends in Figure 33 provide support for the theory presented in Chapter 2.

There are insufficient bed survey data to analyze the trajectories for the other experiments, particularly those that reached equilibrium after about 1 hour, for which there is only a single bed survey. However, the calculated values of  $f^*_{sys}$  using Equation 29 are similar to the equilibrium values in Figure 33 for all the other experiments, ranging between 0.10 and 0.15, except for experiment 1-2, for which  $f^*_{sys}$  is anomalously low (0.07). This is probably due to the fact that this experiment was terminated before significant lateral deformation occurred: the anomalous  $f^*_{sys}$  value may thus indicate that there was further potential for the system to deform and thereby increase the system scale flow resistance. Further consideration of the system-scale flow resistance is presented in Section 4.2.3 below.

**Slope adjustment:** The channel slope,  $S$ , represents the reach-scale component of the adjustment of  $f_{sys}$  in Equation 21. In our experiments, channel slope is positively correlated with the sediment supply, and negatively correlated with the discharge, and is well described by a multiple regression of the form:

$$\text{Equation 30} \dots\dots\dots \hat{S} = 0.0368(Q_b) - 0.0244(Q) + 0.983 \quad SE = \pm 0.0084 \quad R^2 = 0.93$$

where  $\hat{S}$  is expressed as a percent,  $Q_b$  is reported in g/s and  $Q$  is reported in L/s. SE is the standard error for the estimate,  $\hat{S}$ . Both coefficients and the intercept are statistically significant at  $\alpha = 0.02$ . We can improve on this simple, underlying correlation by relating the dimensionless channel response ( $S$ ) to some dimensionless measure of the governing conditions ( $Q_b/Q$ ), consistent with the analysis in Chapter 2. In fact, a slightly better statistical relation exists between slope and sediment concentration (g/g). The equilibrium slope for the first set of experiments is plotted against the sediment concentration in Figure 34a: the equilibrium slope is well predicted by a linear function of the form:

$$\text{Equation 31} \dots\dots\dots \hat{S} = 136 \left( \frac{Q_b}{Q} \right) + 0.892 \quad SE = 0.0068 \quad R^2 = 0.94$$

This expression has the advantage of being more easily interpreted since as  $Q_b/Q$  drops to zero, the value of  $\hat{S}$  approaches the threshold for transport. The constant in the regression therefore represents a critical slope for entrainment for our physical model (i.e. the slope of a self-formed threshold channel). Standard errors for the coefficient and the intercept of this regression are provided in Table 7.

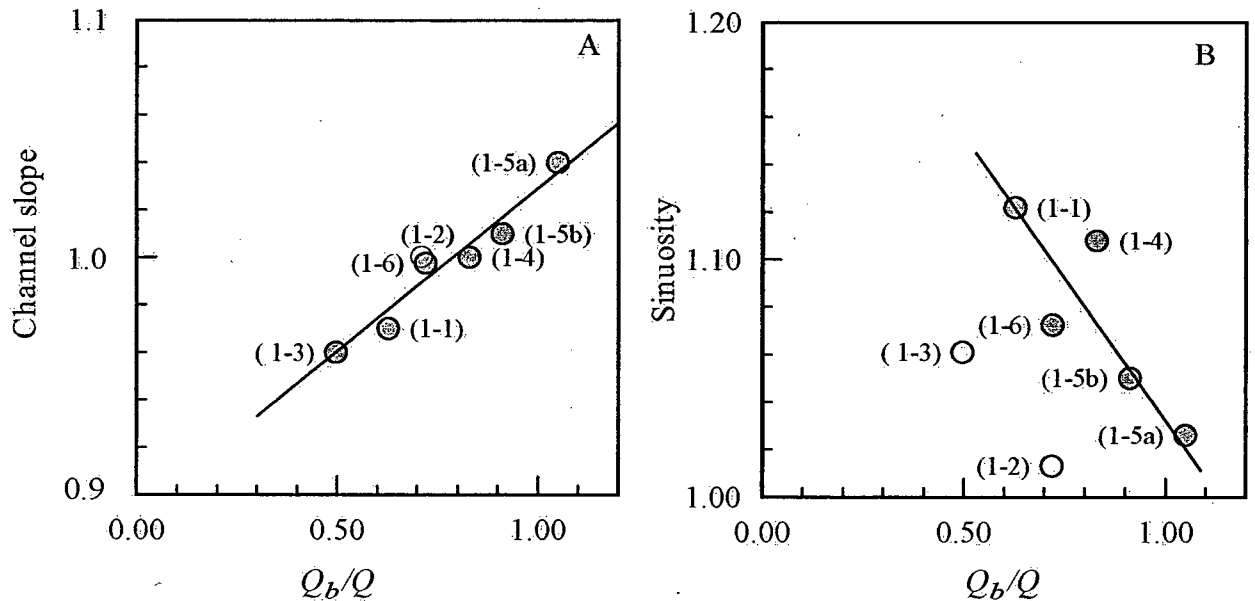


Figure 34: Constant valley slope equilibrium channel configuration: (a) thalweg water surface slope (%) and (b) sinuosity (m/m) vs. sediment concentration in the typical units (g/L): the line in panel b has been fitted by eye to the data having nearly the same  $S_{sys}$ .

Table 7. Regressions of  $S$  against  $Q_b/Q$

Dataset	Coefficient <sup>†</sup>	Intercept <sup>†</sup>	n	$R^2$
Constant $S_v$	$136 \pm 30$	$0.892 \pm 0.024$	7	0.94
Constant $L^*$	$133 \pm 31$	$0.901 \pm 0.024$	5	0.96
All data	$139 \pm 11$	$0.891 \pm 0.014$	11	0.98

<sup>†</sup>The ranges correspond to a 95% confidence interval

The equilibrium channel sinuosity, which is another way of expressing the reach-scale flow resistance, is also plotted against the sediment supply concentration ( $Q_b/Q$ ), as shown in Figure 34b. The observed channel sinuosity is correlated with  $Q_b/Q$ , but the trajectories by which equilibrium was reached – involving changes in  $S_{sys}$  relative to  $S_v$  due to vertical incision ( $\Delta S_{deg}$ ) – introduce scatter that is not evident in the plot of channel slope. The clearest examples of this are experiments 1-2 and 1-3 which result from a prolonged period of vertical degradation at the

beginning of the experiments; producing  $S_{sys}$  values of 1.01% and 1.04%, respectively. Experiment 1-6, which had nearly the same imposed sediment concentration as experiment 1-2 but reached equilibrium quickly by primarily lateral adjustments (due to the lower  $q$  at the beginning of the experiment), reached a statistically identical channel slope, but a much higher channel sinuosity. Experiment 1-4, which exhibits a higher sinuosity than seems consistent with the remaining data, reached a value of  $S_{sys}$  of about 1.11% by aggrading the upper part of the stream table. The remaining experiments – for which a line has been fitted by eye on Figure 34b – have  $S_{sys}$  values between 1.05% and 1.07%.

Table 8. Armour ratios for Phase 3 experiments

Experiment		Time <sup>+</sup> (hrs)	$\frac{D_{50} \text{ surf.}^*}{D_{50} \text{ b.m.}}$	$\frac{D_{90} \text{ surf.}^*}{D_{90} \text{ b.m.}}$
Constant $S_y$	1-1	8.5	1.57	1.29
	1-2	17.5	1.76	1.44
	1-3	24	1.73	1.41
	1-4	1	1.56	1.36
	1-5a	4	1.68	1.34
	1-5b	8	1.73	1.36
	1-6	1	1.53	1.36
Constant $L^*$	2-1	1	1.49	1.30
	2-2	1	1.49	1.31
	2-3	1	1.54	1.34
	2-4	1	1.55	1.40
	2-5	1	1.35	1.29
	2-6	1	1.61	1.34
	2-7	1	1.56	1.34
	2-8	1	1.46	1.34
	2-9	1	1.46	1.31

<sup>+</sup> For armour development. <sup>\*</sup> Ratios are based on  $D_{50}$  and  $D_{90}$  for the surface and the bed material

**Surface adjustment:** Another often-cited possible adjustment that could stabilize the stream channel is a change in the surface armouring (e.g. Talbot and Lapointe, 2002b, 2002a). Surface samples were used to estimate the average armour ratio, based on both the  $D_{50}$  and the  $D_{90}$  of the bed material and of the armour that developed in the channel as the system adjusted. Neither definition of the armour ratio (Table 8) shows a discernable correlation with the sediment concentration for these experiments (Figure 35a), probably because of the narrow range in sediment concentration employed. However, both measures of the armour ratio show a consistent – but statistically insignificant ( $\alpha < 0.125$  for the  $D_{50}$ -based ratio and  $\alpha < 0.154$  for the  $D_{90}$  ratio) – correlation with the time required to reach equilibrium (Figure 35b).

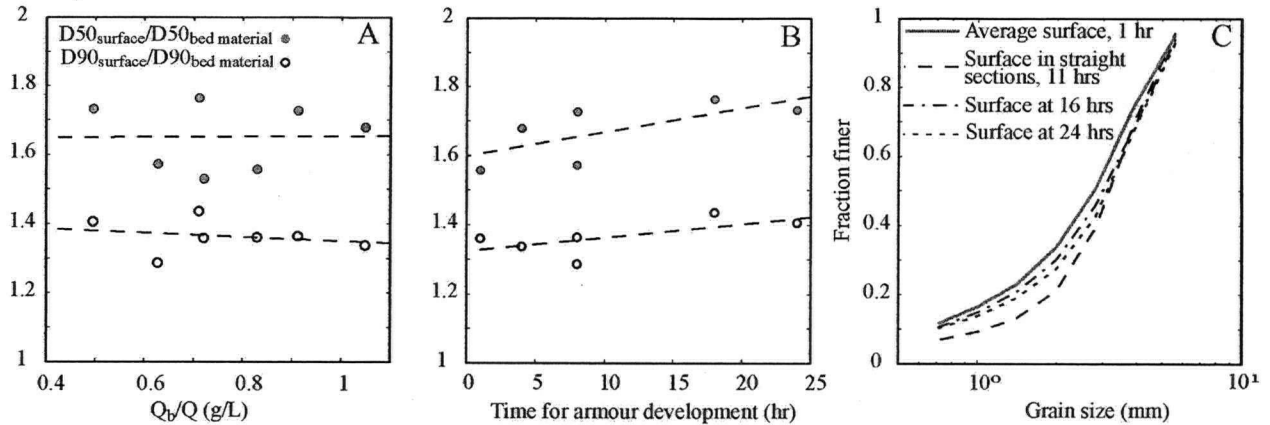


Figure 35: (a) Armour ratios for the constant  $S_v$  experiments, based on two separate definitions, are plotted against sediment concentration. (b) Armour ratios plotted against the time available for armour development. Regression lines relating the armour ratios and the independent variable are shown. None is significant at  $\alpha = 0.05$ . (c) Grain size distributions for experiment 1-3 prior to the development of alternate bar morphology (lower part of the stream table at 11 hrs) and during the development of appreciable sinuosity (surface at 16 and 24 hrs). The average surface grain size distribution for the graded channel experiments with a duration of 1 hr are shown for comparison.

Nevertheless, armouring clearly plays an important role in the trajectory toward equilibrium. The surface grain size distributions for experiment 1-3 at various times during the experiment are shown in Figure 35c, along with the average grain size distribution for the experiments with time-to-equilibrium of 1 hour. The surface in the straight reach immediately before the onset of lateral activity was clearly coarser than the surfaces typical for shorter experiments. It was this degree of armouring that stopped the initial degradation and permitted the lateral activity to commence. The armour surfaces that developed subsequently during this experiment became progressively finer, but remain coarser than for the shorter experiments. Despite this, the development of differential degrees of surface armour does not seem to have introduced a detectable bias into the relation between the slope and the sediment concentration, though it may contribute to the variance about the relation. That there is very little scatter about that relation suggests that the range of armouring that developed during these experiments was not sufficiently large to introduce a detectable effect.

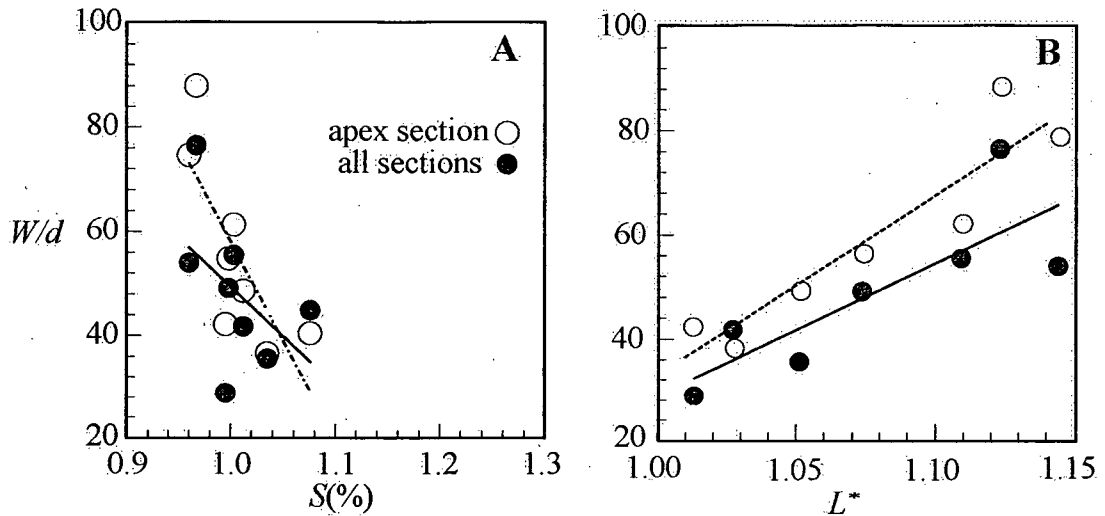


Figure 36: Average  $W/d$  ratio is plotted against channel slope (a) and then against sinuosity (b) for the constant  $S_v$  experiments. Data calculated from all cross sections and from only the apex cross sections are plotted separately, and linear trends are fit to each data series.

**Section adjustment:** There is also the possibility that systematic changes in the average channel dimensions contributed to the achievement of equilibrium, as discussed in Chapter 2. In that case, the parameters describing the channel cross section, representing secondary adjustments, should be correlated with the channel slope, which appears to be the primary adjustment. The width-to-depth ratio ( $W/d$ ) is the common measure of channel shape. Figure 36a summarizes the  $W/d$  ratio of all the surveyed cross sections and for just the bend apex sections. Both the average  $W/d$  and the apex average  $W/d$  are negatively correlated with  $S$ , with low  $R^2$  values (0.13 and 0.38, respectively). Since  $S$  is a surrogate for  $Q_b/Q$ , according to Figure 34 (Equation 31 is essentially a rating relation between total stream power and sediment load), this type of relation runs counter to the observed behaviour of alluvial systems in the field, where experience suggests that, as sediment concentration increases, so too does the  $W/d$  ratio (Schumm, 1969). However, there is a better correlation between the observed  $W/d$  ratios and channel sinuosity (Figure 36b), which is the result of the limitation of the physical model, since it cannot recreate bank advance so that, the more sinuous the channel becomes, the wider it becomes. Thus, the total wetted width for these experiments was progressively distorted (relative to the field prototypes that *do* produce bank advance) as channel sinuosity increased, since the cut banks retreated, but the inner banks did not advance. The effective width (based on visual observations), through which most of the sediment and fluid flux pass, did not seem to be similarly distorted, and was estimated to be about 60 cm for all of these experiments. To reveal any scaling of the effective width with the

governing conditions, it was therefore necessary to attempt to control channel sinuosity and the attendant change in the average channel shape. This is an objective of the constant sinuosity experiments discussed in Section 4.2.3.

#### 4.2.3 Constant Sinuosity Experiments

As a test of the generality of the behaviour implied by Equation 31, additional experiments were conducted wherein the sediment supply and the valley slope were co-varied according to the relation in Equation 31, whilst  $Q$  was held constant, so as to produce the same degree of channel sinuosity (1.05). The channel pattern was allowed to develop as in the experiments previously described. The design sinuosity was kept deliberately low so as to minimize the effect of not reproducing bank advance in the physical model, and to reveal any functional relation between the effective width and the governing conditions. These experiments also represent a deliberate test of the notion presented by Schumm and Khan (1972) that there is some inherent relation between valley slope and channel sinuosity, independent of sediment concentration. In comparison with the first set of experiments, they constitute a test of the sensitivity of the slope adjustment to the degree of sinuosity achieved and provide an opportunity to investigate further the relation between sediment concentration and channel cross-section adjustment.

**Slope adjustment:** In four of the experiments, steady state sediment transport was reached and, in each case, the achieved equilibrium channel sinuosity was *not statistically different from the design value*, based on Equation 31 (the 95% confidence interval for sinuosity is estimated to be  $1.05 \pm 0.03$  m/m). The results are shown on Figure 37. A regression similar to that in Equation 31 was fitted to the data: the relations for the two different sets of experiments are not statistically different from each other, nor are they different from a regression line fit to a dataset combining both sets of experiments, as shown by the regression statistics in Table 7.

**Surface adjustment:** The degree of surface armouring that occurred during these experiments is similar to that achieved during the constant  $S_v$  experiments of the same duration (Table 8). There is no statistically significant correlation between the two measures of the degree of armouring and the sediment concentration in these experiments (Figure 38a), and differential degrees of armouring is not an avenue by which these experiments reached a stable channel morphology. There does, however, appear to be a general trend for the surface to become finer, as the imposed sediment concentration increases.

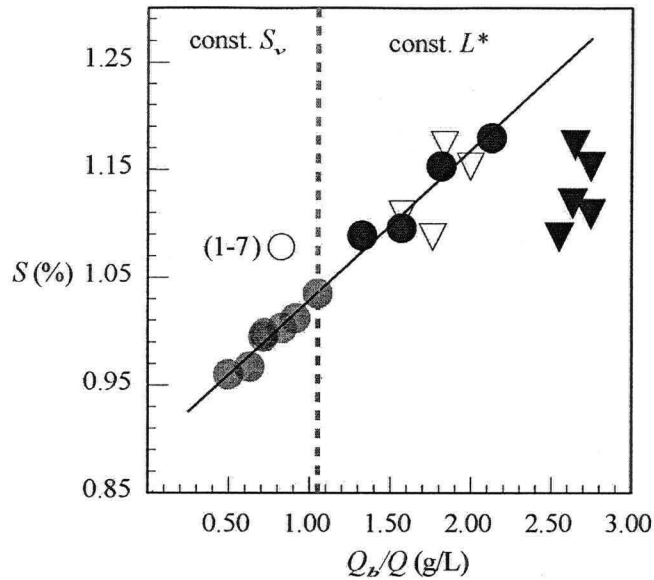


Figure 37:  $S$  is plotted against sediment concentration for both sets of Phase 3 experiments. Symbols for equilibrium experiments (solid circles) are scaled to represent a measurement uncertainty of  $\pm 1$  standard error for estimates of  $S$ . The solid triangles represent  $Q_b/Q$  for non-equilibrium experiments based on the imposed governing conditions while the open ones represent  $Q_b/Q$  based on the measured sediment output in the same experiments. Note that transport records exist for only 4 of the 5 non-equilibrium experiments. The anomalous experiment 1-7 is indicated by an open circle.

**Section adjustment:** By producing channels with similar sinuosity, we have presumably removed much of the effect related to the inability of our physical model to produce bank advance, which should more clearly reveal the predicted correlation between the governing conditions and the average channel dimensions. Indeed, the relation between  $W/d$  and  $Q_b/Q$  now exhibits the expected positive correlation (Figure 38b). It is likely that the wetted channel widths for these experiments more closely represent meaningful (effective) channel widths, and the scaling shown in Figure 38b is probably typical of streams in the field. A linear relation between  $W/d$  and  $Q_b/Q$  has the form:

Equation 32..... 
$$\frac{W}{d} = 10.2 \frac{Q_b}{Q} + 25.7 \quad R^2 = 0.97$$

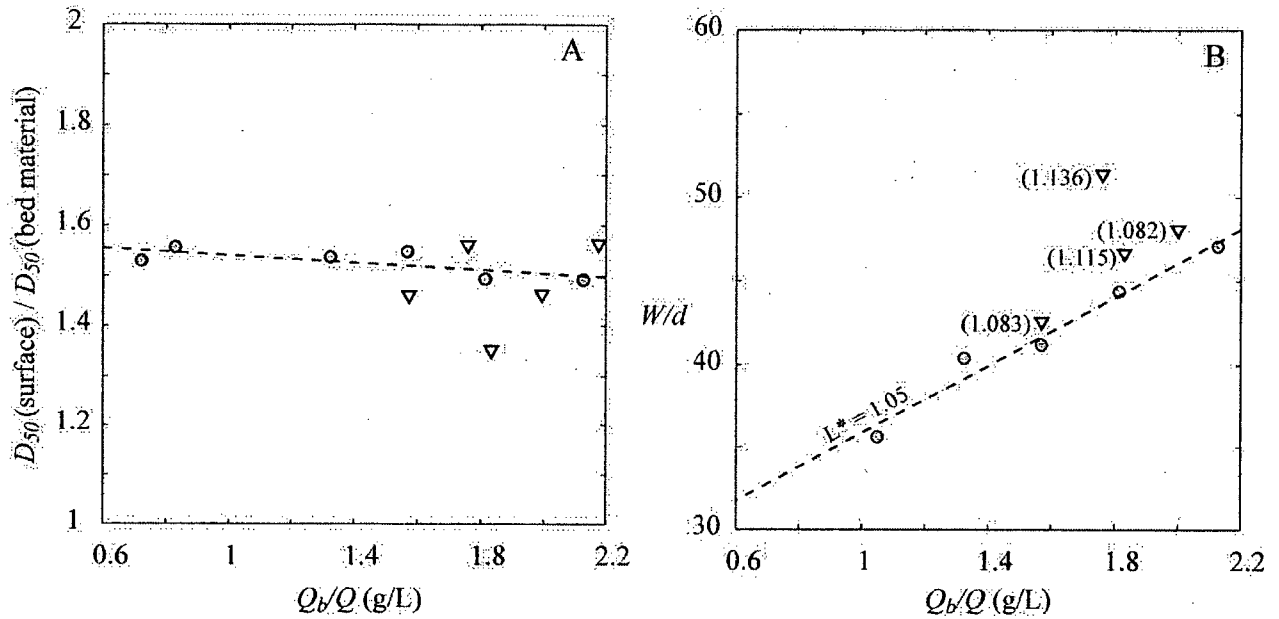


Figure 38: (a) armour ratios for the experiments above the maximum sediment influx threshold (open triangles) are plotted against sediment concentration using the measured transport at the outlet. The same data for the graded channels that reached equilibrium after 1 hr are shown for comparison (circles). (b) the average  $W/d$  ratios for the above-threshold experiments are plotted against the same independent variable, while the data from the graded constant  $L^*$  experiments are shown for comparison. Sinuosity for the above-threshold channels is presented in brackets

**Adjustment of resistance:** The results above allow us to make more accurate estimates of the flow resistance for the system ( $f_{sys}^*$ ), based on a *variable* effective width. Assuming the relation between  $W/d$  and  $Q_b/Q$  revealed for the constant sinuosity experiments represents the scaling of the effective width, we can back-calculate the effective widths for the constant valley slope experiments. We also need to estimate the effective depth, since any estimate of depth is dependent on the width and cross sectional area of the cross section. Based on the constant sinuosity experiments, the effective depth ( $d_{eff}$ ) is related to  $Q_b/Q$  by a linear regression of the form:

Equation 33 .....  $d_{eff} = 2.00 - 0.254 \frac{Q_b}{Q} \quad R^2 = 0.91$

The average effective width, then, for the constant valley slope experiments turns out to be 60 cm, and ranges from 57.5 cm to 61.8 cm. The revised estimates of the equilibrium  $f_{sys}^*$  values are plotted in Figure 39 and reported in Table 6.

The equilibrium  $f_{sys}^*$  values are assumed to represent the approach toward some maximum flow resistance, if not the maximum itself. An appropriate initial assumption is that the maximum flow resistance which can be attained is a function of the strength properties of the material in which the stream channel develops. Therefore, one expects  $f_{sys}^*$  at equilibrium to be similar for all of the experiments. To some extent, the data from the equilibrium experiments confirm this expectation (Figure 39a).

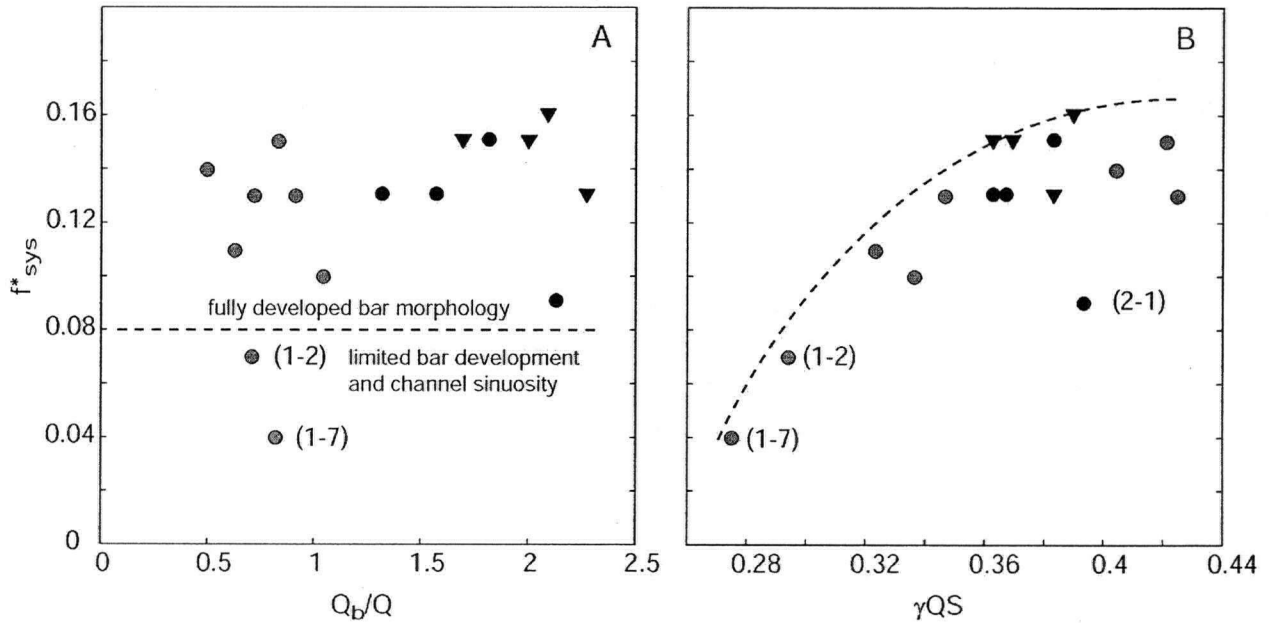


Figure 39: (a) equilibrium  $f_{sys}^*$ , based on the effective width and depth scaling implicit in the constant sinuosity experiments, is plotted against  $Q_b/Q$  for the constant  $S_v$  experiments (grey circles), the graded constant  $L^*$  experiments (black circles), and the non-equilibrium constant  $L^*$  experiments (triangles). (b)  $f_{sys}^*$  is plotted against total stream power ( $\gamma QS$ ). In (a) the data are stratified (horizontal dashed line) by the degree to which the experimental channels produced the expected alluvial behaviour. In (b) the inferred maximum possible flow resistance is indicated by an envelope curve, drawn by eye (dashed line).

Experiments 1-2 and 1-7 are notable outliers. In experiment 1-2, the equilibrium  $f_{sys}^*$  value is lower than this typical range, at about 0.04. As discussed above, this experiment was likely not run long enough for the onset of significant lateral activity, which may be a partial explanation for the low  $f_{sys}^*$  value. Similarly, experiment 1-7, (discussed in detail in Section 4.2.4), has an anomalously low  $f_{sys}^*$  value and did not undergo significant lateral adjustment. The reasons for this are similar; lateral erosion was limited, and the channel form was unable to adjust.

Generally, it seems that the data can be stratified based on the observed morphologic behaviour. For those experiments that did not fully develop sinuous thalwegs and alternate bars,  $f_{sys}^*$  remained relatively low, while for those that did develop the typical alluvial morphology,  $f_{sys}^*$  varied between 0.08 and 0.16. This range seems to be characteristic for both the constant  $S_v$  and the constant  $L^*$  experiments, and therefore presumably does not depend significantly on the imposed initial valley slope or sediment supply.

However, it is also possible that the maximum possible flow resistance for the system varies systematically. At high enough stream power, the bed itself may achieve some significant velocity, relative to the water. The effect of this would be to essentially reduce the drag on the water column due to the boundary, since the boundary itself is in motion. This frees up the system to perform additional boundary deformation and thalweg adjustment, which would result in an apparent increase in  $f_{sys}^*$ , since the bed velocity is not accounted for. This speculation leads to a more general statement that the maximum possible  $f_{sys}^*$  value is related to stream competence by a continuous function. This idea is tested by plotting  $f_{sys}^*$  against total stream power, as shown in Figure 39b. There does indeed appear to be a consistent increase in  $f_{sys}^*$  as a function of total stream power ( $\gamma QS$ ). The dashed line on the figure indicates the apparent envelop curve, representing the maximum possible flow resistance. Most of the experiments exhibit equilibrium  $f_{sys}^*$  values close to the envelope curve: the only significant outlier is experiment 2-1, which lies well below the envelope curve. The reason for this discrepancy is probably related to the channel slope, which was the highest of any of the experiments. Based on the individual cross sections and recorded water surface elevations, several sections in this experiment had supercritical flow: when the velocity is re-calculated based on just those sections with sub-critical flow,  $f_{sys}^*$  increases to 0.14, which is consistent with the envelop curve.

Interestingly, experiments 1-2 and 1-7, which are anomalies in Figure 39a, conform to this envelope-curve interpretation. However, the physical basis for a constant variation of  $f_{sys}^*$  with stream power is not clear. The topic requires additional theoretical and experimental investigation, since there remains much that is not understood about those factors determining the flow resistance (system-scale or otherwise) that an alluvial system will achieve. Additionally, there is certainly relevant information that cannot be incorporated in a simple plot of  $f_{sys}^*$  against stream power; most importantly, information on sediment supply and bed mobility.

**Comparison with regime model:** As discussed in Chapter 2, one cannot make direct comparisons between a regime model and natural channels based on measures involving  $Q_b$ , since the value of sediment transport predicted by any transport equation is a scale representation of the real transport at best. However, the relation between  $W$ ,  $d$  and  $S$  (for the same  $Q$ ) is not affected by this problem, and – since  $S$  and  $Q_b/Q$  are nearly linearly related for our experiments – one can make a meaningful comparison between the regime model and the experimental data on this basis, as shown in Figure 40.

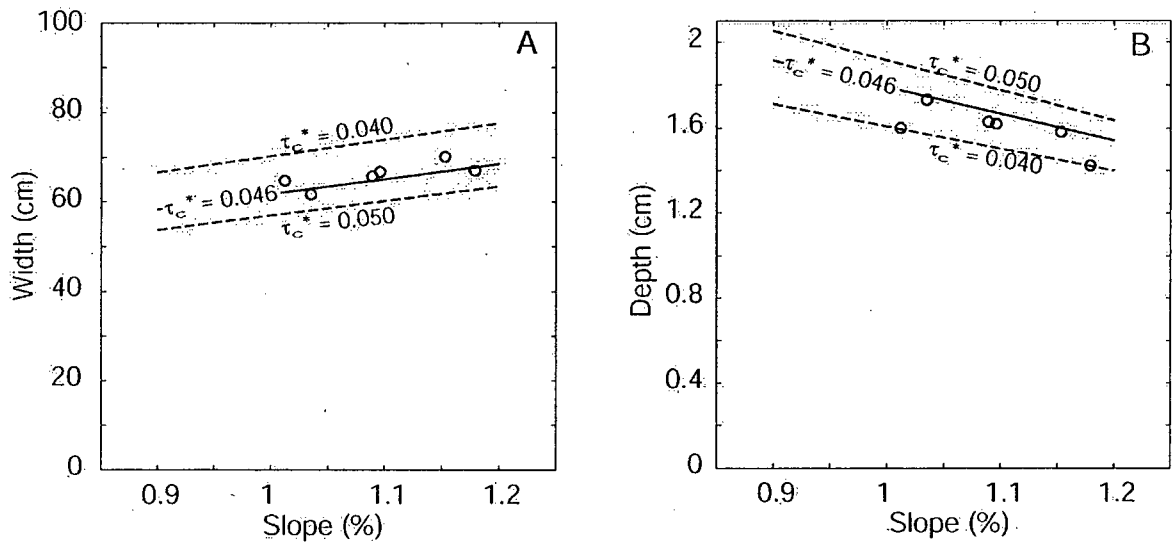


Figure 40: Comparison of  $W_{eff}$  and  $d_{eff}$  for channels with similar sinuosity (and with  $Q = 3.4$  L/s), plotted against channel slope, with  $W$  and  $d$  predicted by a regime model assuming,  $\phi' = 30^\circ$ ,  $D = 2.0$  mm and specifying a range of entrainment thresholds for the bank material ( $\tau_c^*$  for the bank ranges from 0.04 to 0.05).

The relation between  $W_{eff}$  and channel slope is very similar to that predicted by a regime model assuming  $\tau_c^* = 0.046$ , which is very close to the threshold reported by Meyer Peter and Muller (1948). The relations predicted assuming a range in  $\tau_c^*$  between 0.04 and 0.05 are shown to give the reader an idea of the sensitivity of the regime model predictions to the choice of  $\tau_c^*$  used. The observed  $d_{eff}$  is similarly consistent with the relation predicted by a regime model assuming  $\tau_c^* = 0.046$ , though there is more scatter in the data. As for  $W_{eff}$ , all of the data fall within the range of values predicted by a regime model assuming  $0.04 \leq \tau_c^* \leq 0.05$ . That some scatter exists is not surprising given the simplified nature of the regime formulation, and the difficulty of isolating the effective width and depth in physical models that do not produce full bank development and advance. Indeed, the usefulness of regime modeling – for understanding

channel response, at least – derives from the ability to predict the direction, and approximate magnitude of a channel response, rather than predicting a given alluvial state. The results shown in Figure 40 represent a successful test of regime theory, and a validation of Hypothesis 3 in Section 3.1, albeit a qualified one.

#### 4.2.4 Non-graded Responses

For a subset of the experiments in Table 6, the water surface slope along the thalweg for both the constant  $S_v$  and the constant  $L^*$  experiments is well predicted by a linear function (Figure 37). These stream channels are at-grade in the sense that their slopes are functionally adjusted to the sediment supply and fluid flow, which is approximately the definition of a graded river proposed by Mackin (1948). The form of the relation (Equation 31) is identical to the governing relation proposed by Lane (1955) for constant grain size. For another subset, there appears to be no evidence of a graded channel adjustment. When the sediment feed rate exceeded about 450 g/min, the graded relation over-predicted the slopes at which the morphology became stable and the systems never reached steady state sediment transport conditions. At the other end of the spectrum, when the specified discharge was below 3.0 L/s, the graded relation predicted a much lower slope than was reached by the stream channel. We refer to the constraints implied by these results as the “sediment influx threshold” and the “stream power threshold”, respectively. The upper value of the feed rate and the lower value of the discharge quoted above represent the range of conditions within which graded channel behaviour occurred for our physical model. The existence of the thresholds is inferred on the basis of the observed deviation from the graded relation.

For the experiments above the maximum sediment influx threshold (experiments 2-5 through 2-9),  $S_v$  ranged from 1.20 to 1.30%. In all cases, the initial channel slope was greater than the equilibrium slope predicted by Equation 31. Rather than remaining relatively straight, the channels over-adjusted, developing a larger degree of sinuosity and reaching a lower channel slope than expected. The slopes reached were lower than that for experiment 2-1 ( $Q_b = 430$  g/min), which had an initial channel slope of 1.28%, implying that the breakdown of the graded relation is not related to the shear force acting on the boundary but somehow to the sediment supply rate. For these experiments, the channel slopes measured in the study reach are not representative of configurations at equilibrium with the sediment supply at the inlet, since steady state transport was not achieved. Channel sinuosity in the study section did stabilize (probably

temporarily) at a constant value, as did channel slope, albeit at lower-than-expected values (Figure 37). Since sediment supply exceeded sediment output, net aggradation must have occurred by definition, but this was not evident in the study section, which was 5 m downstream of the inlet. However, when the slopes for these channels are plotted against  $Q_{bo}/Q$ , where  $Q_{bo}$  is based on the sediment output rather than the sediment supply, the points collapse onto the graded relation. Although the scatter in the data using the measured sediment output is greater, due to the temporal variations in sediment transport, the measured sediment output likely represents a more accurate value for the sediment supply to the study reach. Fan-style aggradation was limited to the upper 5 m of the stream table during these relatively short duration experiments.

The armour ratio for these non-equilibrium experiments is also shown in Figure 38a, from which it is clear that the surface texture of the experiments above the sediment influx threshold is similar to the surface texture for the graded channels with comparable run time, although the data do not confirm the apparent trend with sediment concentration evident for the equilibrium experiments. Similarly, the average  $W/d$  ratios are plotted against sediment concentration (Figure 38b). While the  $W/d$  ratios are all higher than the trend established for the constant  $L^*$  graded channels, this appears to be the likely effect of an increased degree of channel sinuosity, as implied by Figure 36b, since the departures from the trend line are generally proportional to the measured channel sinuosity. The recorded  $W/d$  ratios thus represent the combined effect of varying both sinuosity and sediment concentration. Similarly, the calculated values of  $f_{sys}^*$  (Figure 39a and b) are consistent with the data for the graded experiments. The channel adjustments for these experiments are similar to those for graded channel experiments.

Below the stream power threshold (experiment 1-7), the equilibrium channel slope was substantially higher than that predicted by Equation 31 and the lower part of the channel did not become appreciably sinuous, nor did the typical sequence of lateral bars develop.

While the nature of the changes in alluvial behaviour at both thresholds is incompletely understood – since the experiments were not designed to study them – the thresholds seem to be related to the mobility of the bed material. In Figure 41, the ratio of the transported material and the bed material is plotted for each  $\frac{1}{2}$  phi size class greater than the  $D_{50}$ . Most of the size fractions near  $D_{50}$  were transported in proportion to their occurrence in the bed, while the coarsest size fractions tended to be under-represented, implying some degree of size-selective transport. However, there was a small but consistent difference in the degree of under-

representation between the at-grade experiments (those channels consistent with the graded relation shown in Figure 37), and the experiments above the maximum sediment influx threshold ( $Q_b > 450$  g/min). The largest 3 size classes (2.8 – 4 mm, 4 – 5.6 mm, 5.6 – 8 mm) for the at-grade experiments were under-represented in the samples of the transported material (Figure 41). The degree of under-representation ranges from about 20% for the 2.8 – 4 mm size class to essentially 100% for the 5.6 – 8 mm class, reflecting the fact that this sediment size was almost never present in the transported load. For the experiments above the sediment influx threshold, only the largest size class was under-represented in the load, and then by only about 50%, on average.

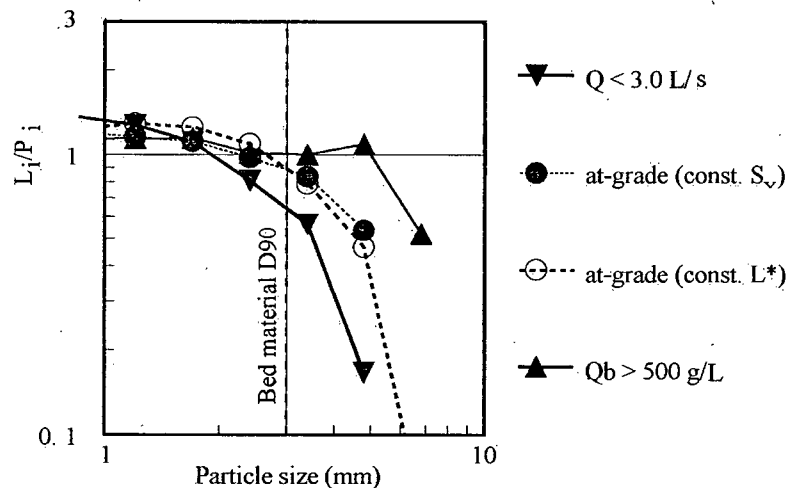


Figure 41: Bed mobility for at-grade channels, for channels below the lower threshold ( $Q < 3.0$  L/s) and for channels above the upper threshold ( $Q_b > 450$  g/L). The proportion of the transported grain size in each size fraction ( $L_i$ ) is normalized by the proportion of the bed material grain size in the same size fraction ( $P_i$ ), after Wilcock and Southard (1989). A ratio near 1 indicates that the size fraction is transported in proportion to its occurrence in the bed material. Material  $> D_{50}$  shown.

The inferred stream power threshold is also distinctive on the plot of bed material mobility (Figure 41), in that all the bed material fractions coarser than 2 mm are under-represented in the transport sample.

#### 4.2.5 Discussion of Phase 3 Experimental Results

The form of the graded relation between  $S$  and  $Q_b/Q$  does not detectably depend on the average  $W/d$  ratio or the degree of surface armouring, and is not influenced by the time-to-equilibrium or

the sequence of vertical and lateral adjustments by which equilibrium is achieved. Accordingly,  $S$  is interpreted to be functionally related to  $Q_b/Q$ , as illustrated in Figure 37. That is, there is a cause-and-effect link between the channel slope and the imposed sediment concentration. We propose that the link works through the maximization the reach-scale flow resistance component of the system scale flow resistance. We consider that  $S$  reflects the reach scale flow resistance ( $f'''$ ), which appears to be the most significant component of the system scale flow resistance,  $f_{sys}$ .

The other possible adjustments ( $f'$  and  $f''$ ) seem to be less important. Despite the reversal in the sense of the correlation between  $W/d$  (an approximate index of  $f''$ ) and  $S$  between the constant  $S_v$  and constant  $L^*$  experiments, there is no statistical difference between the graded relations for the two different sets of experiments (Table 7): channels that were wider and shallower, on average, did not stabilize at higher slopes than did narrower, deeper channels with the same imposed sediment concentration. Perhaps the best example of this comes from a comparison of experiments 1-2 and 1-6. Both experiments have similar sediment concentrations ( $\sim 0.71$  g/L) and reach statistically identical channel slopes (0.01 m/m). However, the stable  $W/d$  ratio for experiment 1-6 was just over 70% larger than the  $W/d$  ratio for experiment 1-2. If nearly doubling the average  $W/d$  ratio does not produce any detectable effect on the equilibrium slope reached, then obviously  $W/d$  has a very small second order effect. This outcome suggests that the limitations of the physical model, which does not reproduce bank advance, are not nearly so severe as they may at first appear. Indeed, visual observations (and the supporting analysis in the discussion of  $f_{sys}^*$ ) suggest that the effective widths for these two experiments were likely of comparable magnitude.

Similarly, the magnitude of the surface armouring (an index of  $f'$ ) does not seem to be an important adjustable variable in these experiments. No statistically significant systematic trends occurred in armour ratios. Thus  $f'$  does not adjust sufficiently during our experiments to have an appreciable effect on the equilibrium channel configuration.

While neither  $f'$  nor  $f''$  seems to be an important component of the adjustments documented in these experiments, this is almost certainly not the case in the field. There, resistant channel banks may limit the degree to which channel sinuosity (and hence  $f'''$ ) can adjust, while the geomorphic history can create highly armoured and structured surfaces that make the sort of

adjustments documented in these experiments impossible because the armour cannot be breached. Our experiments do demonstrate, however, that the order of system adjustments is significant in determining the final channel geometry. For the two cases in which early degradation and bed armouring occurred, the equilibrium configuration remained less sinuous than in other experiments because part of the slope adjustment was taken up by the early degradation.

The regime model predicts that, for a specified bank strength,  $Q$  and  $Q_b$ , there is a range of possible slopes and stable channel configurations that can accommodate the specified fluxes, ranging from channels with steep slopes where sporadic transport occurs over a relatively large width to channels with lower slopes having intense sediment transport over a much more restricted part of the channel bed (see Figure 3). If alluvial states are in reality randomly distributed in the space of stable solutions, there is no reason why the behaviour shown in Figure 37 should necessarily arise: the channels should be able to stabilize over a range of slopes by adjusting their width and surface texture, rather than just their slope. Certainly, given the experimental design, the channels did have access to these higher slope solutions. This implies that there should have been substantial scatter about the  $S$  versus  $Q_b/Q$  relation, and that the residuals should be correlated with differences in  $W/d$  and/or the armour ratio. There was no significant residual variance about the regression (see Figure 37), despite large variations, particularly in the  $W/d$  ratio. This implies that not all parts of the theoretical stability curve based on regime theory are equally attractive, absent other constraints. It also implies that there is no obvious correlation between the average  $W/d$  ratio and the width of the channel active in transporting sediment.

Our data demonstrate that graded channels with erodible banks consistently by-pass higher slopes that – according to regime theory presented in Chapter 2 – are capable of transmitting the sediment supply given the available discharge. We refer to this tendency for the systems to move toward minimum slope as *slope minimizing behaviour* (SMB), in order to distinguish this behaviour from the claim that the system achieves a minimum slope. Since there is very little scatter in the  $S$  vs.  $Q_b/Q$  relation and since these slopes can be reached by various combinations of vertical and lateral adjustments, we suppose that the channels inhabit the *same* part of their respective stability curves. This behaviour is relevant to the stability of solutions predicted by a regime formulation, and is at the root of a physical explanation for extremal hypotheses.

Extremal hypotheses simply choose points having the same relative position on their stability curves (i.e. homologous points); thus the action of extremal hypotheses such as the minimum slope hypothesis (Chang, 1979), or any of the equivalent extremal hypotheses (Davies and Sutherland, 1983), are implicit in the observed *SMB*. Whether a true minimum slope – or more pertinently, a true maximum flow resistance for the system – is actually reached cannot be determined. Indeed, it is difficult to imagine an experimental test that would permit such a claim to be accepted. But the monotonic approach of our model systems toward equilibrium is suggestive of such behaviour.

However, some of the experiments did not behave in accordance with the graded relation described by the regressions in Table 7, and these deserve some attention. There appear to be thresholds related to a minimum stream power and a maximum sediment influx rate beyond which the system response changes fundamentally.

Below the stream power threshold, the channel failed to erode its banks in the lower reaches, did not develop any appreciable bar-forms there, and could not transport material much coarser than the  $D_{90}$  of the bed material and feed (experiment 1-7). This threshold is independent of the sediment influx rate, since other experiments with the same supply did adjust their sinuosity and develop typical alluvial bed features throughout their length. The only difference between experiment 1-7 and the at-grade experiments was its lower initial stream power ( $QS_i$ ) and lower equilibrium stream power ( $QS$ ).

While the transport rates at the outlet during experiment 1-7 were similar to the supply rates at the inlet, the system was not at equilibrium with the sediment feed. It is likely that the coarsest part of the feed grain size distribution was deposited in the channel upstream of the study reach. The difference between the imposed feed rate and the measured transport at the outlet is, by definition, small – we are considering the upper 10% of the sediment size distribution – and could not be detected given the fluctuations in the measurements at the outlet. The system was most likely aggrading in response to a competence limit that became evident once the imposed total stream power fell below a critical level. This aggradation seems to have been limited to that part of the stream table above the study reach. Even though this experiment was run for 16 hours, an assumed 10% disparity between feed rate and the measured sediment output results in a net deposition of only 12 kg which, when distributed evenly throughout the upper 5 m of the stream tray, results in an average change in bed elevation of only 3 mm. Such a small change in

bed elevation could not be detected without high resolution topographic survey data. However, if the experiment had continued for a sufficient length of time, we presumably would have observed an aggradational adjustment to an equilibrium state.

The study reach had a bed that was significantly coarser than the sediment that could be transported by the available flow and, if the competence-induced deposition was limited to the upper 5 m of the stream table as we suspect, the study reach was likely supplied with sediment having a grain size distribution that was fundamentally different from the material forming the channel boundary. Since there was a significant difference between the grain size distribution of the bed material in the study reach and the grain size distribution that the flow was competent to transport, experiment 1-7 does not represent a fully alluvial system. It represents an experimental limit beyond which the combination of bed material, slope and discharge is no longer reasonable.

The behaviour above the sediment influx threshold is less easily explained. Upstream of the study reach, it seems that – again – aggradation was occurring, but this time in response to an excess sediment supply – a “transport capacity” limitation. As a result of this aggradation, the sediment supply rate at the upstream boundary of the study reach was likely similar to the sediment transport rate recorded at the outlet, though we have no proof of this (beyond the satisfactory collapse that its assumption produces). Given the short duration of the experiments, even the largest difference between the sediment feed rate and the sediment transport rate amounts to an average elevation increase of only about 2.5 mm over the upper 5 m of the stream table. Let us assume that the stream tray upstream of the study reach was behaving like a fan, storing between 30 and 40% of the sediment supplied to it. The study reach, then, can be compared to an alluvial channel downstream of a fan, which was supplied with sediment at a rate similar to that recorded at the outlet. This scenario would explain why the channel configuration stabilized in the study reach at a slope that was consistent with the graded relation in Figure 37.

The other system adjustments (bed armour;  $W/d$  ratio), when analyzed on the assumption that the measured sediment output actually represents the supply to the study reach, are entirely consistent with the other graded channels. If we accept that the sediment supply at the upstream end of the study reach was probably closer to the sediment transport measured at the outlet, the response of these channels ceases to be a mystery, since they simply represent additional examples of the graded-style adjustment.

However, two issues remain unclear: (i) why did the sediment output from the upper part of the stream table drop below the maximum transport rate for the upper limit of the graded experiments (2-4); and (ii) what is the significance of the differences in bed mobility between the experiments above the sediment influx threshold and the experiments below the threshold (Figure 41). These are likely related issues, and may imply that full mobility of the entire grain size distribution destabilizes the channel morphology. However, these problems require further study and, since we have insufficient data from the section of the stream table upstream of the study reach, we can do no more than point out these perplexing aspects of channel adjustment as a topic for further study.

#### 4.3 PHASE 4: FIXED BANK EXPERIMENTS

The Phase 4 experiments were designed to challenge the apparent implications of the Phase 3 experiments that: (i) slope is the only significant adjustable quantity; and (ii) the average wetted width is not a fundamental descriptor of the system. Regarding this second implication, these experiments effectively test *how much* of a disparity between the effective width and the wetted width can be permitted before the system behaviour changes.

These tests were achieved by deliberately constraining both the lateral adjustment of the thalweg and the wetted width of the experimental channels by fixing the location of the channel banks. The design criteria for the Phase 4 model are based on typical morphologic dimensions for the Phase 3 experiments, assuming that the Phase 4 experiments represent a  $\frac{3}{4}$  scale model of the Phase 3 experiments.

While the general measurement procedures and bulk sediment properties are discussed in Chapter 3, additional specific information on the experimental design is presented here. Practically, the banks were constructed of strips of foam rubber with a triangular cross section having 1:1 side slopes, the surface of which was covered with a layer of particles, about 1 to 2 mm in diameter, in order to generate a surface roughness similar to alluvial banks. The area between the fixed banks was filled to a depth of 6 cm with sediment having the grain size distribution as shown in Figure 20. The resultant alluvial bed between the foam banks had a width of approximately 44 cm: this was based on the estimated effective width for the constant valley slope experiments ( $W_{eff} = 60$  cm). The fixed banks were constructed about a sinusoidal centerline curve (wavelength 275 cm, amplitude 40 cm), producing a channel centerline sinuosity of about 1.19 (Figure 42). This design wavelength was based on a typical wavelength of 365 cm

for the Phase 3 experiments, and the amplitude was made as large as possible – so as to maximise the degree of sinuosity – given the width of the stream tray at UBC. The imposed discharge and sediment supply were varied, as they were in Phase 3 experiments (see Table 9), based on a nominal design discharge of about 3.4 L/s which, under the  $\frac{3}{4}$  scale geometric contraction, becomes about 1.7 L/s (see Equation 26). The valley slope was held constant at 1.1%, as it was for the constant valley slope experiments conducted during Phase 3. The experiments were run for a total of four or five hours, typically involving a bed survey after 1 hour and then again at the end of the experiment.

Table 9: Governing conditions and equilibrium response for Phase 4 experiments

Experiment	Governing conditions ( $S_v = 1.1\%$ )			Equilibrium Response	
	$Q$ (L/s)	$Q_b$ (g/min)	$Q_b/Q$ (g/L)	$S$ (%)	$L^*$ (m/m)
4-1	1.85	75	0.68	0.72	1.244
4-2	1.76	103	0.98	0.76	1.210
4-3 <sup>+</sup>	1.20	113	1.57	n/a	1.215
4-4	1.30	101	1.29	0.75	1.172
4-5 <sup>+</sup>	1.83	177	1.61 <sup>*</sup>	0.83 <sup>*</sup>	1.167
4-6	1.83	93	0.83	0.73	1.176
4-7	1.83	125	1.14	0.76	1.172

<sup>+</sup> These two experiments did not reach equilibrium with respect to sediment transport rate

<sup>\*</sup> While never reaching equilibrium with the sediment supply, the system attained this stable slope and sediment output of about 1.32 g/L during the last 2 hours of the experiment, which is used to determine the plotting position in subsequent figures.  $L^*$  is the sinuosity of the self-formed thalwegs, which are shown in Figure 44.

#### 4.3.1 Trajectories Toward Equilibrium

The bank alignment for the Phase 4 experiments is shown in Figure 42: as a result of fixing the bank alignment, the general morphologic structure developed during every experiment was essentially the same. A sequence of bars and pools developed quickly throughout the length of the stream table, typically within the first 5 to 10 minutes of the experiment. Bars were deposited downstream of the bank apices, with pools developing across the channel from them. Riffles extended across the channel near the bank apices. The thalweg alignment was offset relative to the banks, with the thalweg apices occurring downstream. Figure 43 shows the typical arrangement of riffle, bar and pool that developed at each meander bend. The study reach, for which cross sectional data and water surface slope estimates are reported, extends from  $x \sim 225$  cm at the upstream end to  $x \sim 675$  cm at the downstream end (Figure 42).

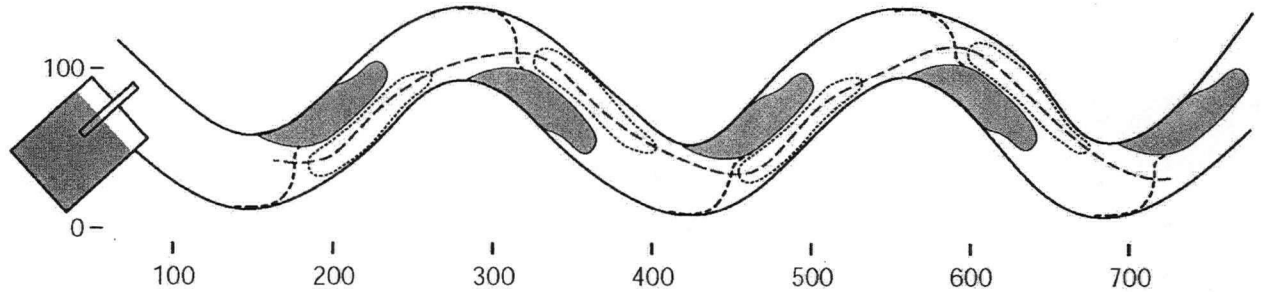


Figure 42: Experimental apparatus for the fixed bank experiments. Flow is from left to right. The average thalweg alignment is indicated with a dashed line, as are the typical pool and riffle configurations. The bars are shown (schematically) in grey, as is the sediment feeder at the upstream end of the channel. The channel bank crests and the thalweg location are drawn to scale; the dimensions are in cm.

The thalweg alignments for the various experiments are shown in Figure 44, and the thalweg sinuosity for each experiment is reported in Table 9. The thalweg locations shown in Figure 44 were generally established after about 10 minutes, and then remained effectively static during the remainder of the experiment. Clearly, by imposing a fixed bank condition, the thalweg alignment is essentially fixed, and – unlike the Phase 3 experiments – the development of sinuosity during the experiments cannot be used to assess the trajectories toward equilibrium.

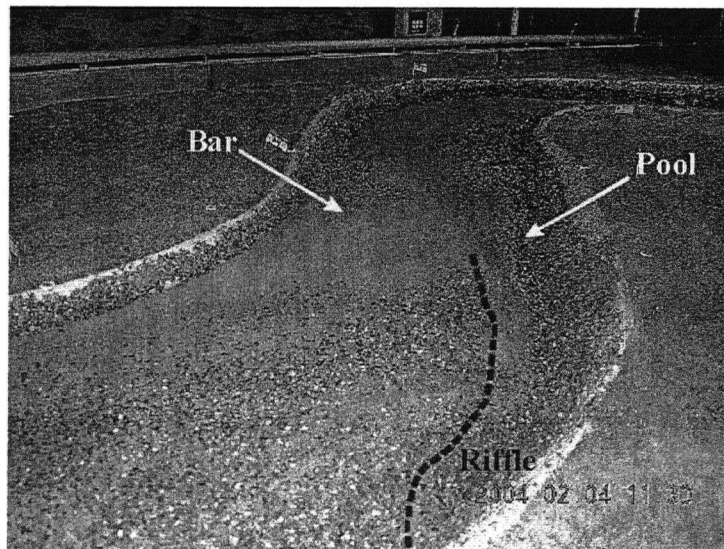


Figure 43: Photograph after 4 hours (experiment 4-4), looking downstream from cross section 7, near the middle of the study reach. Note the riffle in the foreground, the bar deposited along the left bank and the pool along the right bank.

The primary method by which equilibrium conditions were identified was through examination of the sediment transport rates during the run. The average transport rate was calculated for 15 minute intervals: these data are plotted against time for each experiment in Figure 45, along with the imposed sediment supply for reference. Clearly, some experiments reached equilibrium almost immediately (4-2, 4-6, and 4-7 in Table 9). Experiment 4-1 exhibited a gradual decline in the transport rate as the system approached equilibrium. It attained a transport rate equal to the sediment supply after about 3 hours, after which equilibrium was maintained.

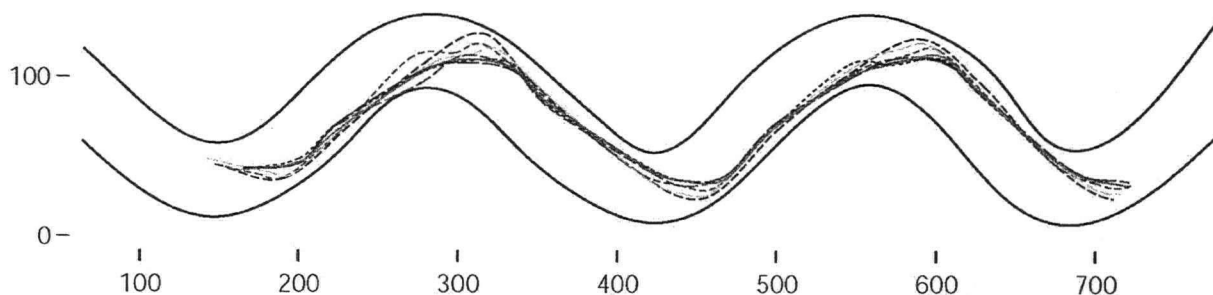


Figure 44: The surveyed thalweg locations for all Phase 4 experiments are shown. The fixed bank alignments are shown for reference. The scale is in cm. Since the thalweg alignment and sinuosity ratio are nearly constant, the various experiments have not been individually identified on the figure.

The trajectory by which equilibrium was attained during experiment 4-4 requires more careful consideration, and can best be understood with reference to the dynamics at the outlet of the channel (see Figure 46). Initially, the sediment transport leaving the channel was noticeably lower than transport throughout the rest of the channel (based on qualitative, visual appraisal) and, importantly, it was lower than in the study reach. The recorded sediment output increased progressively as a fan developed near the outlet. After about 2 hours, the fan had steepened sufficiently to bring the sediment output in line with the transport rates characteristic of the study reach, and to establish equilibrium, based on the recorded transport rates.

This equilibrium condition persisted for about 30 minutes, after which time the sediment output declined precipitously. During this interval of equilibrium behaviour, the surface of the fan seemed to have stopped aggrading, but was modified texturally, as a layer of coarse sediment accumulated over much of the surface, as shown in Figure 46. The surface coarsening is thought to have produced the observed drop in the sediment transport rate after 2½ hours by inducing aggradation just upstream. However, after about 3 ½ hours, the armour near the left bank was

breached, and a scour pool developed through which sediment was efficiently routed to the outlet (visible on Figure 46); this again brought the system back into equilibrium at the outlet. However, during the entire experiment, the sediment transport rate in the study reach appeared to be unaffected by the dynamics around the outlet (see comparison of cross sectional surveys at 2 hrs and 4 hrs, below).

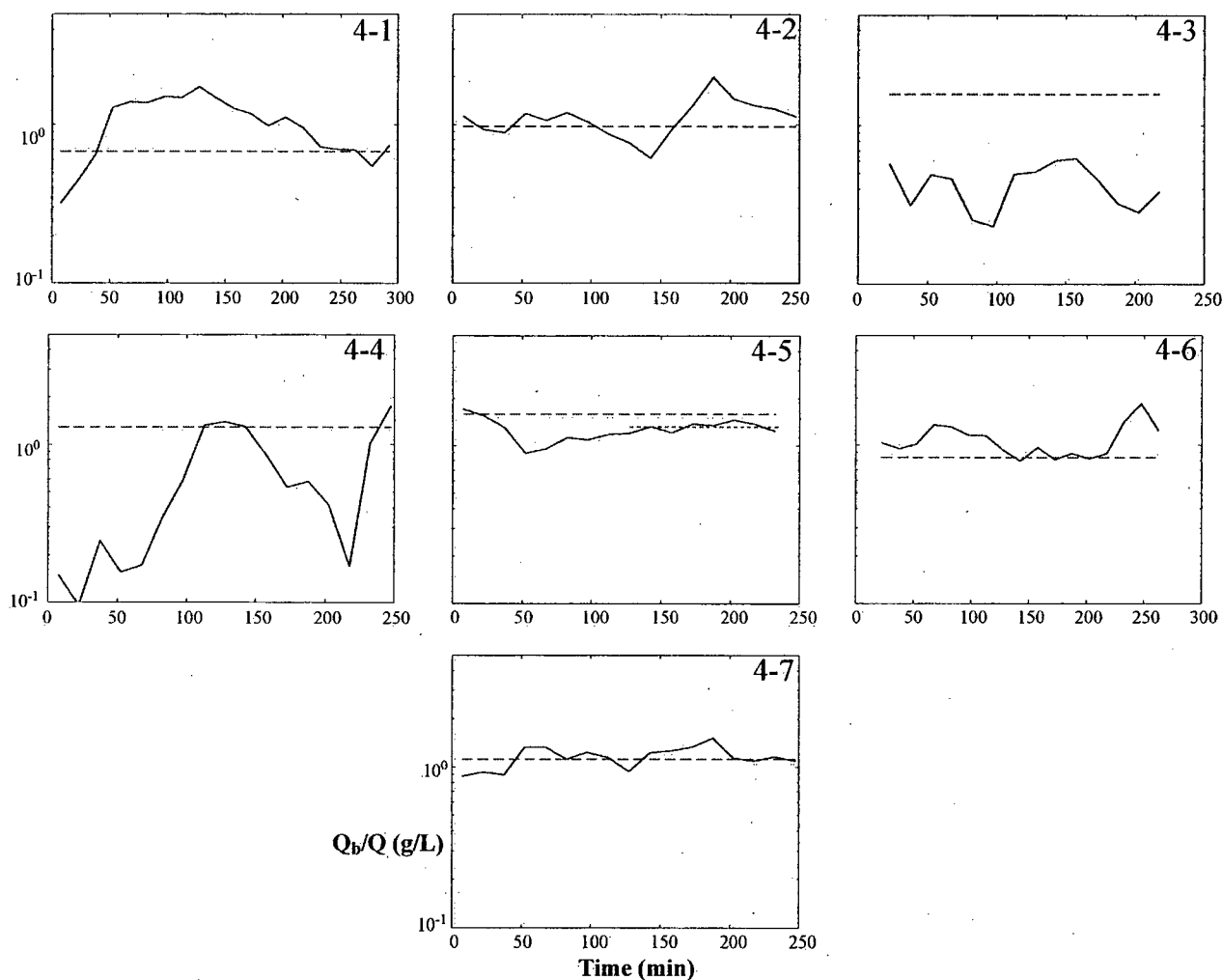


Figure 45: Recorded sediment output for all Phase 4 experiments is plotted against time. The data represent 15 minute average transport rates, and are reported as a sediment concentration (g/L) to permit direct comparison. The experiment number is shown in the upper right hand corner of the relevant panel. The sediment feed rate is shown for comparison (horizontal dashed line), as is the quasi-equilibrium sediment output during the last two hours of experiment 4-5 (dotted horizontal line).

The deposition of a coarse alternate bar near the outlet and the development of a deep scour pool adjacent to it were typical of all of the experiments that reached equilibrium. However, in the

other experiments, it developed much more quickly, and had a less dramatic effect on the transport record. This dynamic appears to be related to the ability of the system to transport the coarsest part of the sediment load which, based on the results of the Phase 3 experiments, is directly related to the total stream power, and hence to discharge. Since the discharge was relatively low for experiment 4-4 (1.30 L/s), it had the lowest total stream power and was closest to the competence limit discussed in Section 4.2. The experiments with higher imposed discharge were less dramatically affected. However, in experiment 4-2 – which had the next lowest discharge (1.76 L/s) – the characteristic drop around 2 hours followed by a subsequent rise is clearly evident.



Figure 46: Photograph of the channel near the outlet (below the study reach) after 4 hours (experiment 4-4). Note the coarse textured alternate bar along the right bank, and the scoured pool along the left bank.

In the remaining experiments, transport rates remained consistently below sediment supply, and did not reach equilibrium (4-3 and 4-5). However, for experiment 4-5, the slope and transport rate stabilized during the last 2 hours of the experiment, reaching a quasi-equilibrium configuration with nearly the same slope and sediment transport rate as experiment 4-4.

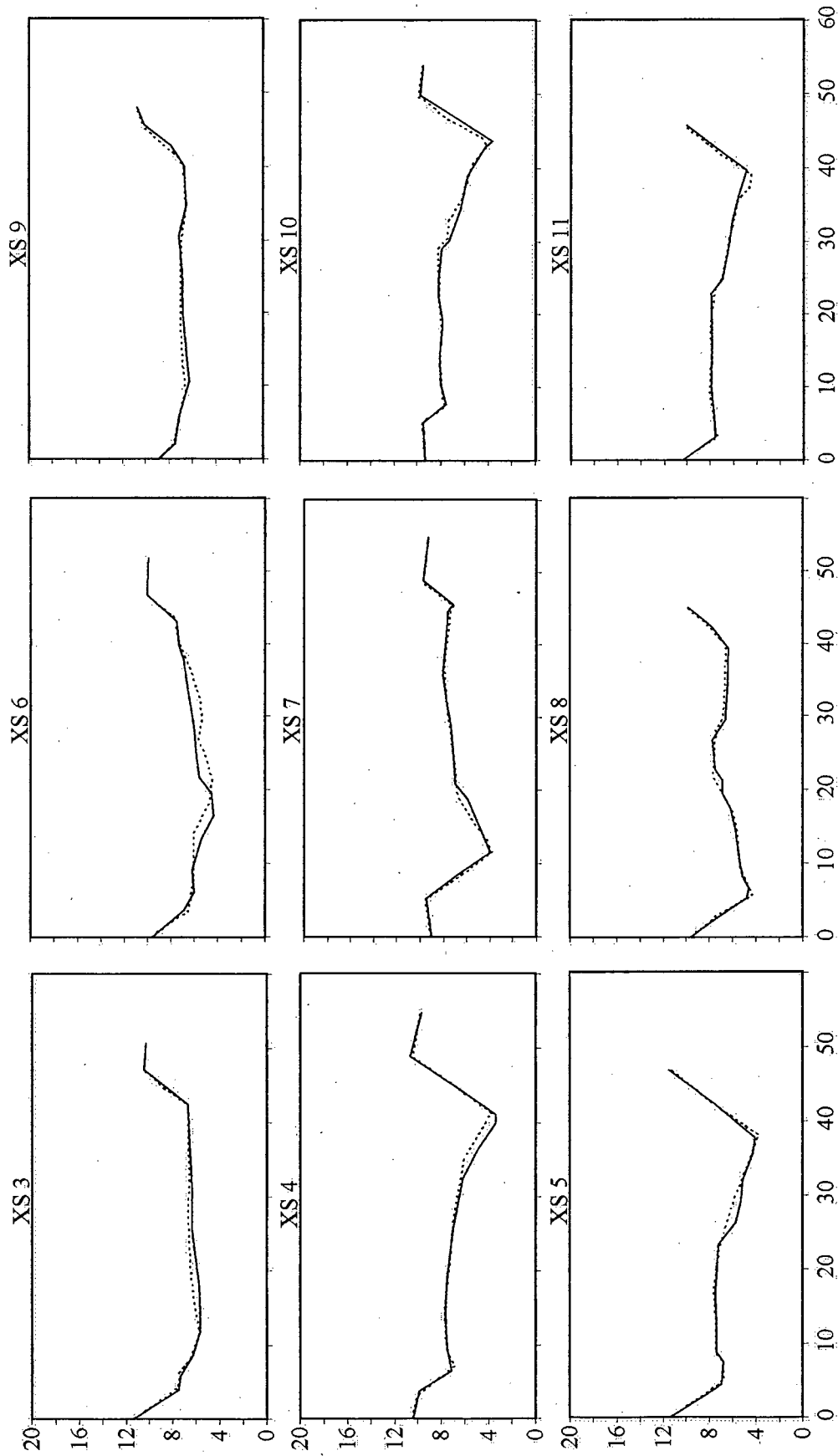


Figure 47: Cross sections for experiment 4-2 at 1 hour (dashed line) and at 4 hours (solid line). The dimensions are reported in cm, and the vertical scale is exaggerated by a factor of 2. The cross section numbers increase in the downstream direction. Sections 3, 6 and 9 (top row) represent the cross-overs, just upstream of the bar-pool unit. Sections 4, 7 and 10 (middle row) represent the thalweg apex, and cut through the bar and adjacent pool. Sections 5, 8 and 10 (bottom row) represent reference sections half way between subsequent bars.

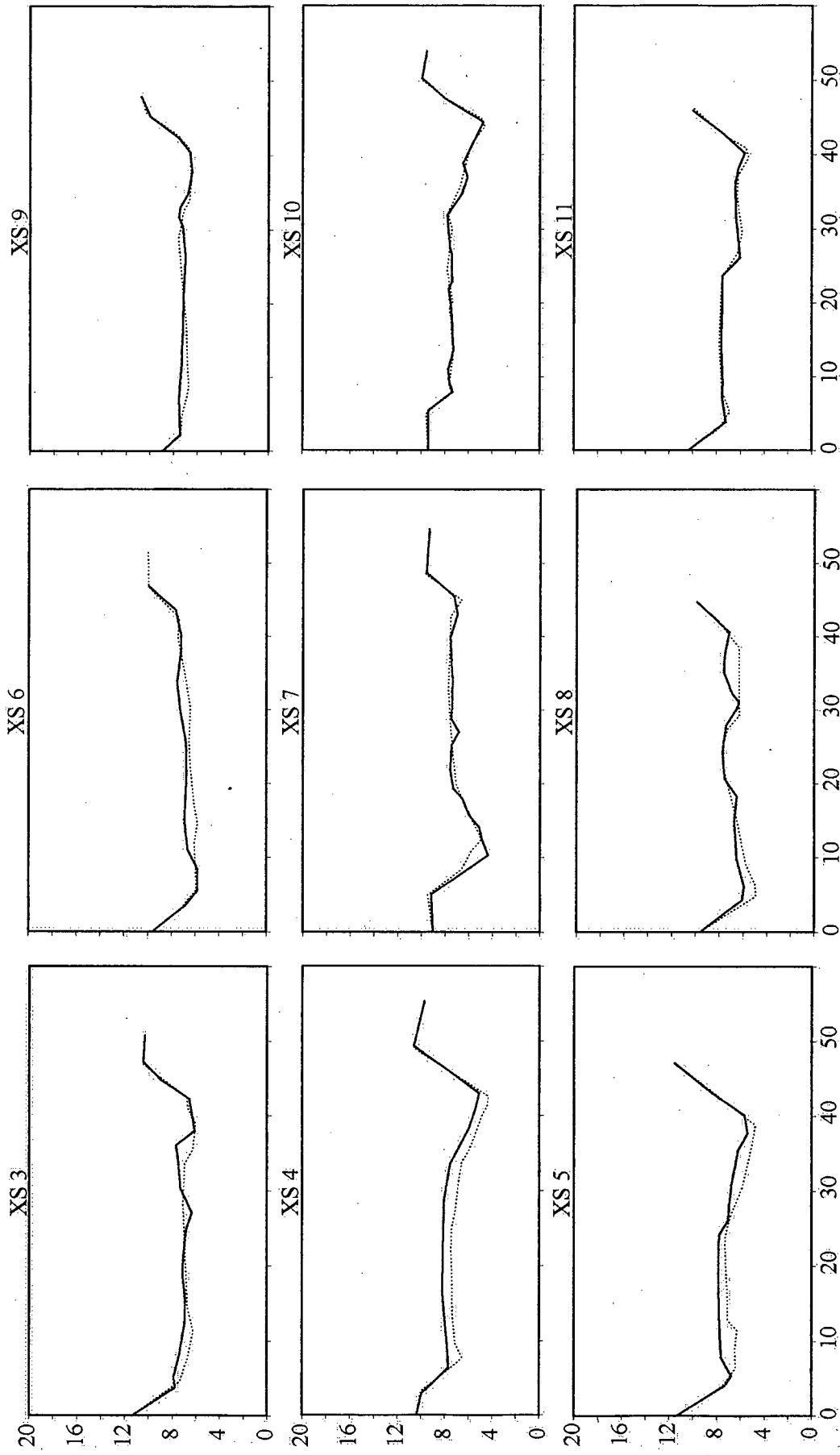


Figure 48: Cross sections for experiment 4-3 at 1 hour (dashed line) and at 4 hours (solid line). See Figure 47 for additional information.

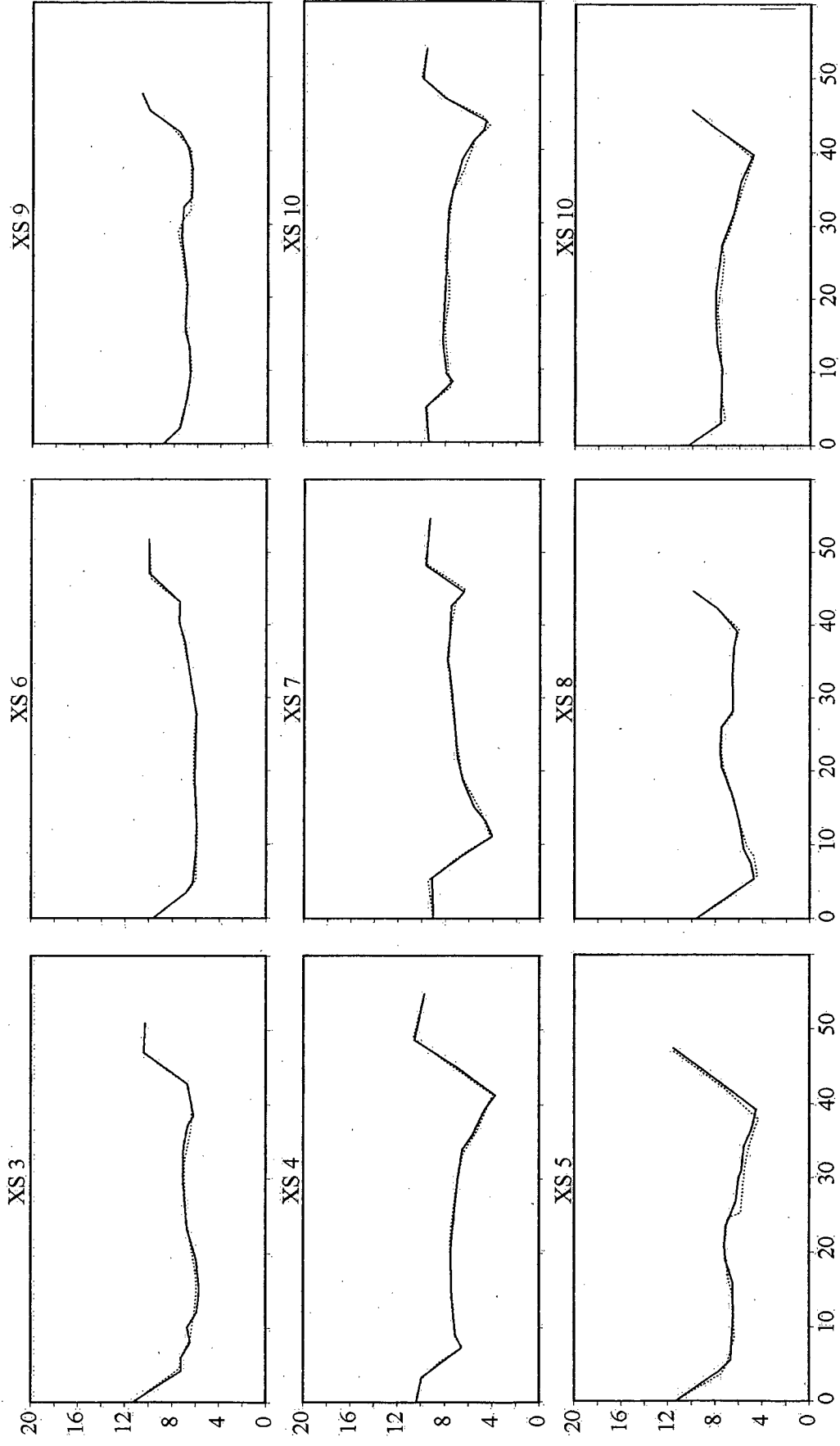


Figure 49: Cross sections for experiment 4-4 at 2 hours (dashed line) and at 4 hours (solid line). See Figure 47 for additional information.

Repeated cross sectional surveys at a number of fixed locations along the channel were also used to assess whether or not equilibrium had been achieved. After 1 or 2 hours, when it appeared that equilibrium had approximately been reached, the flow was stopped and the bed was surveyed. The same cross sections were surveyed again after 4 hours of runtime. Typically, almost no difference between the surveys was detectable. The surveys for experiment 4-2 – which are typical – are shown in Figure 47. There appears to have been very slight degradation at the first apex (XS 4), and some shifting of the thalweg location at the second cross-over (XS 6), but otherwise there is little detectable change.

In contrast, comparison of the surveys for experiment 4-3, which did not reach equilibrium, show substantial net aggradation in the upper part of the study reach between 1 hour and 4 hours (Figure 48). All of the sections in the upstream half of the study reach aggraded, while the sections in the lower half remained relatively stable.

Returning again to experiment 4-4, a comparison of the bed survey at 2 hours, when equilibrium appeared to be first established at the outlet, with a survey at 4 hours, when the transport rates again reached equilibrium values, reveals almost identical cross sectional configurations. This supports the contention that the variation in transport rate at the outlet between 2 and 4 hours was not indicative of conditions in the study reach, and that the channel there had likely reached an equilibrium configuration by 2 hours.

#### **4.3.2 Equilibrium Results**

In Section 4.2, the dominant response in the mobile bank experiments to changes in the governing conditions (indexed by  $Q_b/Q$ ) was an incremental, linear change in thalweg slope, achieved primarily by changing the thalweg sinuosity. The average thalweg slope during the period of equilibrium for the fixed bank experiments is plotted against  $Q_b/Q$  in Figure 50. The quasi-equilibrium values for experiment 4-5 are plotted, and the slope measured after 4 hours for experiment 4-3 is also plotted against the imposed sediment supply concentration.

It is clear from Figure 44 and Table 9 that differential lateral thalweg adjustments did not occur once the bank alignment was fixed, and the channel slopes shown in Figure 50 imply that there was similarly little differential vertical adjustment (the linear trend fit to the data is statistically significant only for  $\alpha > 0.14$ ). In contrast, the slope for the Phase 3 experiments is much steeper, and the trend in the data is more consistent, even though the data from the compound responses

above the sediment influx threshold are included for comparison. One might expect that, since the Phase 4 experiments are a scale model of the Phase 3 experiments, they should have nearly the same equilibrium slopes, but clearly the Phase 4 slopes are much lower. This may be partly attributable to the approximate nature of the scale reduction, particularly for the bulk material grain size distribution (see Figure 20 and Table 5). It is also likely related to the nature of the banks for Phase 4, which permit a much greater degree of channel asymmetry to develop (i.e. deeper, narrower pools), hence increasing the local transport capacity, as discussed in detail in Chapter 5 and permitting the imposed load to be carried at a lower channel gradient.

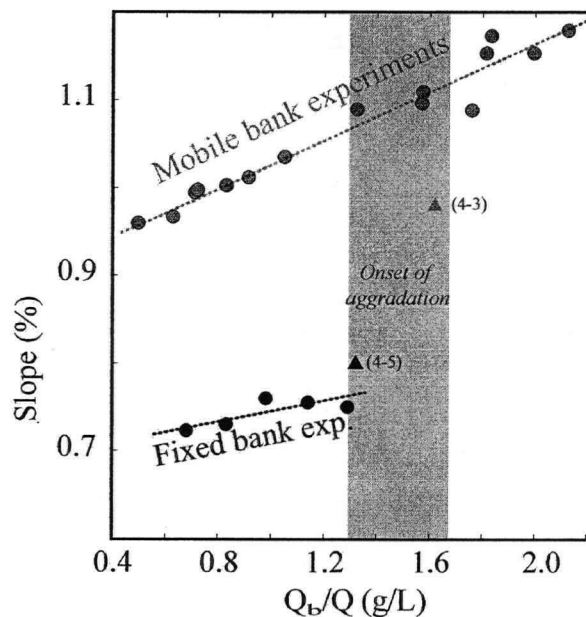


Figure 50: Equilibrium thalweg slope plotted against sediment concentration. The data for the Phase 4 experiments that reached equilibrium are represented by black circles: a linear trend was fitted to these data. The trend for the Phase 3 experiments with mobile banks is shown in grey, for comparison. Experiment 4-5 is indicated with a black triangle: the plotting position is based on the quasi equilibrium conditions during last two hours. Experiment 4-3 is indicated by the grey triangle, and the slope recorded at 4 hours is plotted based on the imposed sediment supply.

Effectively, the equilibrium data for the fixed bank experiments imply that, once bank erosion is constrained, a range of sediment concentrations can be accommodated by channels having nearly the same slope and wetted width. The adjustment of  $f'''$  has been severely constrained by fixing the bank location. The behaviour evident for the Phase 3 experiments, in which  $S$  is adjusted to the imposed governing conditions, cannot be interpreted simply as a relation between channel

gradient and sediment supply, but must be also associated with some adjustment of the system scale flow resistance, as was suggested in Section 4.2.

At some point ( $Q_b/Q \geq 1.3$  g/L), the system can no longer maintain a constant slope and begins to aggrade its bed. This is evident in the behaviour documented in experiments 4-3 and 4-5. Neither of these channels achieved equilibrium with respect to the imposed sediment supply, and both exhibited net aggradation in the upper part of the study reach between 1 hour and 4 hours. Equilibrium could only be achieved at a slope similar to that for the other experiments by narrowing the channel and increasing the average shear stress (assuming discharge is constant). It is trivial to show that equilibrium could be established at lower slopes with a narrower channel. This is the basis for canal design and the original regime formulations. The result is implicit in Figure 3.

Since slope and sinuosity remain nearly constant for the fixed bank experiments, the question remains: what else is adjusted within the system to bring about equilibrium? The potential adjustments of  $f''$  can be assessed by examining the cross sections after 4 hours for different experiments. In Figure 51, the cross sections at the thalweg apices for a range of imposed discharges and a range of imposed sediment concentrations are shown. In general, there is a relation between pool dimensions and discharge wherein larger discharges produce deeper and wider pools. This is shown by the comparison of cross sections at the same location for different discharges in the left-hand column of Figure 51. However, when discharge is held approximately constant and sediment concentration is varied, there appears to be no systematic adjustment of cross section shape (see the right-hand column of Figure 51). These results imply that the cross sectional shape is not functionally related to the sediment concentration: it is determined primarily by the flow structure that presumably results from the effect of the imposed discharge within the fixed banks.

Surface texture is the remaining system component that can be adjusted, representing the grain scale flow resistance,  $f'$ . Samples of the surface texture near the bar heads were taken following the procedure described in Section 3.5.2. These samples were taken in the thalweg where it crossed the riffle: they represent the locations over which sediment transport occurred, and were observed (visually) to undergo significant textural adjustment during a run as equilibrium was achieved.

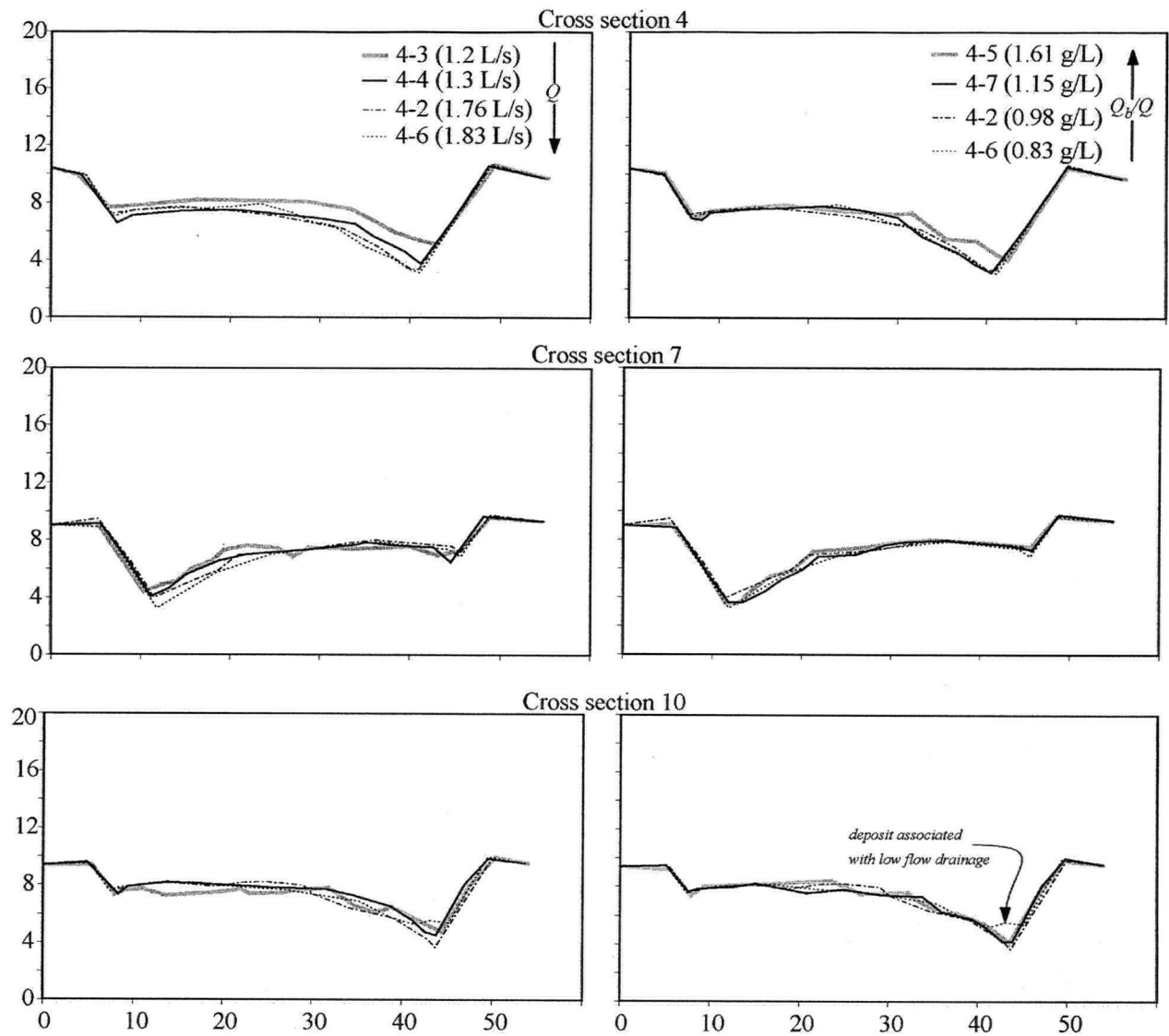


Figure 51: Cross sections through the meander apices at 4 hours for various experiments. The column on the left represents the sections for a range of discharge values, and the column on the right represents a range of imposed sediment supply concentrations for similar discharge. The sections for experiments that did not reach equilibrium (4-3 and 4-5) are shown in grey. Where identifiable, features associated with the drop in flow at the end of the experiment are identified.

Examination of the grain size distributions for the various experiments reveals a consistent general difference between the distributions for the experiments at equilibrium and those that were characterized by aggradation (Figure 52). Those experiments that reached equilibrium exhibit a coarsening of the upper half of the distribution, relative to the bed subsurface. The equilibrium experiment for which this coarsening is most weakly developed is 4-4, which is near the threshold for the onset of aggradation. In contrast, for experiment 4-3 and 4-5, which clearly aggraded their beds, this characteristic surface coarsening was suppressed.

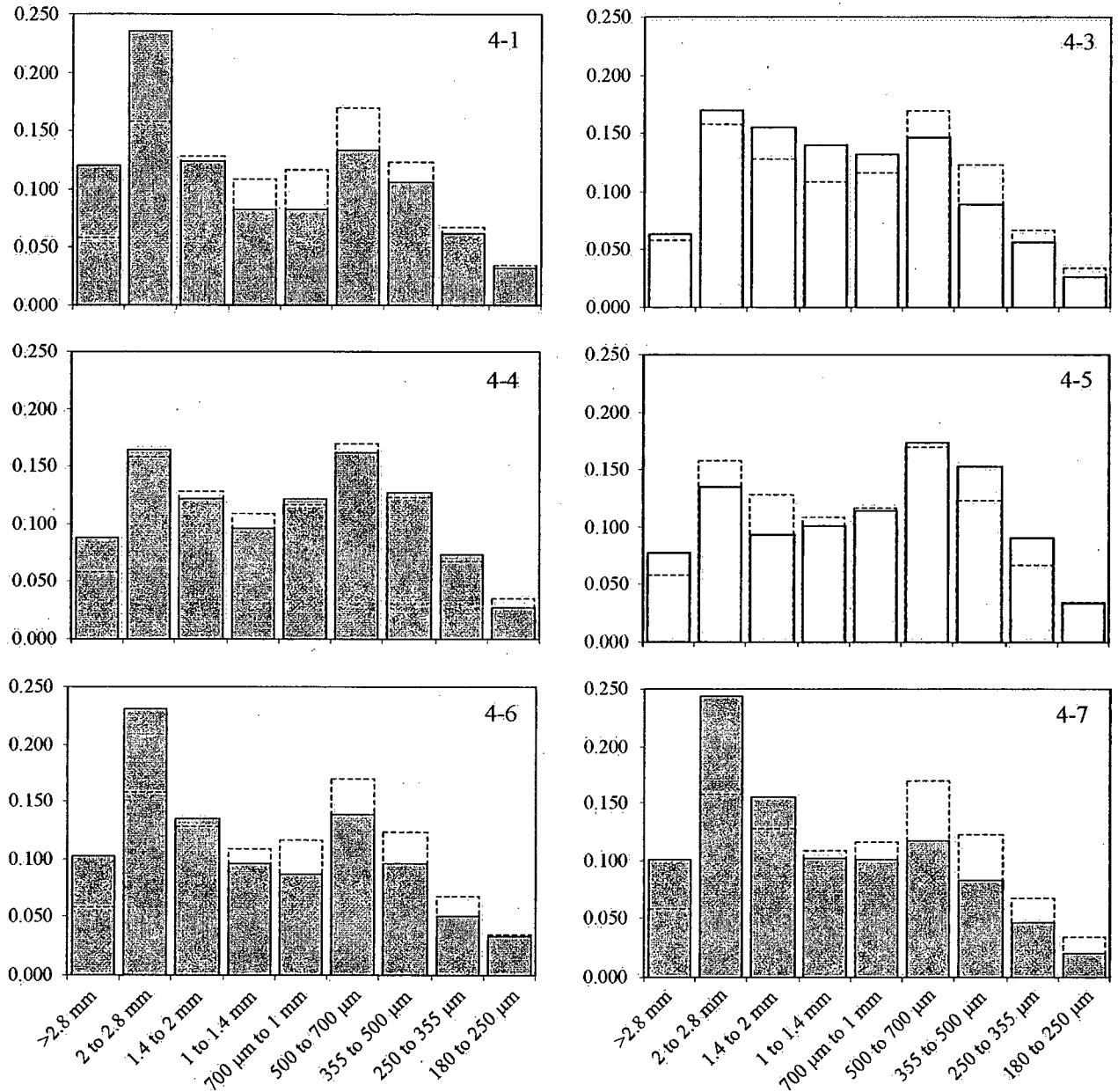


Figure 52: Surface grain size distribution for fixed bank experiments. The proportion of the surface in each size class is shown for all Phase 4 experiments, except 4-2 (data missing). The experiments that reached equilibrium have grey-shaded bars. For reference, the distribution for the bed subsurface is shown with dashed lines.

Three indices were extracted from the cumulative grain size curves for these experiments:  $D_{90}$ ,  $D_{75}$ , and  $D_{50}$ . The data are plotted against sediment concentration in Figure 53a. They show a consistent decrease in surface coarsening with increasing sediment concentration up to the onset of aggradation. Fractional representations of the grain size distributions in Figure 52 – shown in Figure 53b – similarly show that, below a sediment concentration of 1.3 g/L (experiments 4-1, 4-

6 and 4-7), there is a characteristic adjustment of the surface texture relative to the bed material, and that above this concentration (experiment 4-3 and 4-5), the pattern breaks down. These results imply that, in order to facilitate higher sediment transport rates, the surface texture fines (c.f. Parker et al., 1982; Parker and Klingeman, 1982), thereby increasing the exposure of the grains passing over it and reducing the potential for grain hiding. After aggradation begins, there does not appear to be any further adjustment of the surface texture, which is presumably related to the onset of aggradation.

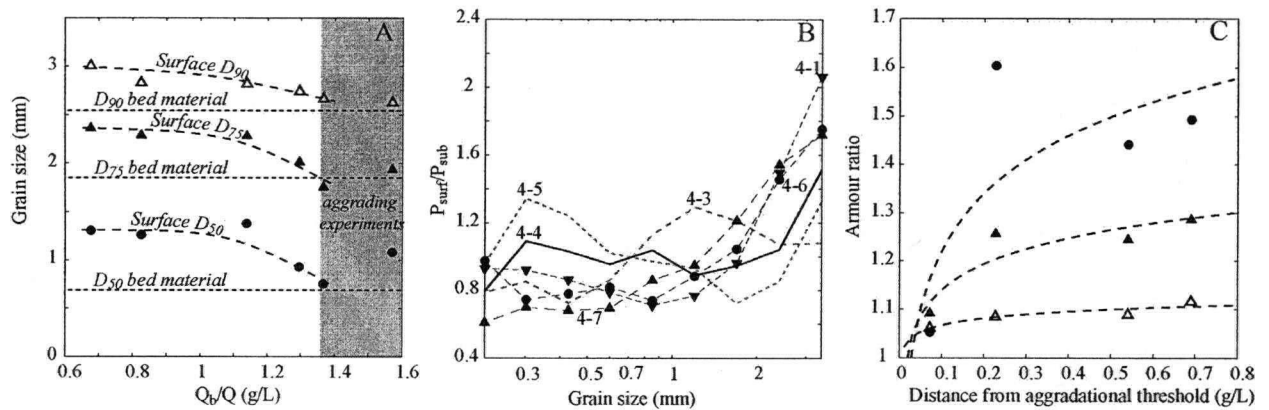


Figure 53: Analysis of surface grain size distributions for Phase 4 experiment. (a) relation between three indices of the cumulative grain size distribution and the governing condition,  $Q_b/Q$  for the Phase 4 experiments.  $D_{90}$ ,  $D_{75}$  and  $D_{50}$  values based on the cumulative curves have been plotted. Dashed lines representing the general trend of the data were fitted by eye to the data from equilibrium experiments. The reference indices for the bed material are indicated using dotted horizontal lines. (b) fractional representation of the surface distribution, relative to the subsurface distribution.  $P_{surf}$  refers to the proportion of the surface grain size distribution in each size class (represented on the x axis by the mean size for the class).  $P_{sub}$  refers to the same quantity for the subsurface. (c) logarithmic fits to relation between armour ratios and distance from threshold, per data and symbols in (a).

From these data, armour ratios were calculated, based on the  $D_{90}$ ,  $D_{75}$  and  $D_{50}$ ; these ratios were then regressed against  $Q_b/Q$  (Table 10). The relation between the armour ratio based on  $D_{90}$  and sediment concentration is quite strong, with a relatively high  $R^2$ , low standard error and a slope coefficient that is statistically significant at all commonly accepted significance levels. The relation is less clear for the ratio based on  $D_{75}$ , which has a slope coefficient that is only significant if one chooses the relatively generous significance criterion,  $\alpha = 0.10$ . The relation based on the median grain size is not statistically significant: the statistical significance of these relations is severely constrained by the small number of data. However, upon inspection of the

data in Figure 53a, it seems likely that functional relations between armour ratios and the governing conditions are nonlinear (becoming progressively more so as one approaches the median grain size), which may in large part account for the change in the degree of statistical significance. Indeed, logarithmic fits to relations between the armour ratio and the distance (in units of g/L) from the threshold for aggradation (taken to be 1.37 g/L, based on experiment 4-5) are visually quite reasonable (Figure 53c) although the statistical power is not improved, since one data point (4-5) had to be dropped in defining the threshold.

A similar trend may be evident for the Phase 3 experiments (see Figure 38), wherein the armour ratio falls with an increase in sediment concentration. However the trends for the Phase 3 experiments are not statistically significant for any definition of the armour ratio, even if we set  $\alpha = 0.1$ . Nevertheless, it is possible that: (i) surface texture adjustments were systematically occurring during the Phase 3 experiments; and (ii) the sediment influx threshold encountered there is analogous to the threshold encountered here, beyond which channel aggradation must occur to produce equilibrium.

Table 10: Linear regression statistics for relation between armour ratios and sediment concentration

	$\frac{D_{90}(\text{surface})}{D_{90}(\text{bed material})}$	$\frac{D_{75}(\text{surface})}{D_{75}(\text{bed material})}$	$\frac{D_{50}(\text{surface})}{D_{50}(\text{bed material})}$
N	5	5	5
R <sup>2</sup>	0.86	0.68	0.53
SE (estimate)	0.022	0.090	0.249
F score	17.8	6.5	3.4
P value (coefficient)	0.024	0.084	0.163

### 4.3.3 Discussion of Phase 4 Experimental Results

The Phase 4 experiments demonstrate that slope adjustments are not the primary system response when decoupled from the lateral channel adjustment represented by  $f'''$ . The channel remained entirely free in the fixed bank experiments to undergo net aggradation or degradation such that channel slope would be demonstrated to be the dominant response: indeed, beyond some threshold sediment concentration (i.e. for experiments 4-3 and 4-5), slope does seem to become a necessary component of the system response. Additionally, the wetted width seems to be of limited importance, since equilibrium can be established for sediment concentrations ranging

from about 0.6 to 1.3 g/L. Within this range of sediment concentrations, equilibrium seems to be produced as the bed surface evolves to accommodate the sediment supply.

However, there is insight to be gained from the fact that the system does break down at some point, and must aggrade to achieve equilibrium at the given width (or, alternatively, the width must be narrowed, thereby increasing the average shear stress to produce equilibrium at the given slope). It is clear from the 1D analysis presented in Chapter 2 that, had the wetted width been reduced (thereby increasing the mean shear stress) as the sediment supply was increased, an equilibrium configuration with the same slope as the other equilibrium experiments could have been produced for the higher sediment supply conditions. These results show: (i) that for some range of sediment concentrations, established by the possible bed adjustment, such adjustments in width and mean shear stress need not occur to produce an equilibrium condition at a given slope; and (ii) that for sufficiently large increases in sediment supply, the channel must somehow narrow and deepen its cross section, even when the banks are non-erodible.

In a regime context, an increase in mean shear stress is associated with an increase in bank strength but clearly, changing the strength of the outer banks under erosive attack is not sufficient since the fixed banks in our experiments were non-erodible, but the system was unable to exploit this essentially infinite bank strength to produce the necessary increase in the mean shear stress. This implies that *bank construction* is a key component of systems in the field, and that bank deposition drives channel evolution toward higher system scale flow resistance by narrowing the (stable) cross section and thereby permitting an increase in channel sinuosity. This sort of process requires that deposition occur along the inner bank of the channel such that the channel becomes narrower and deeper, and thus capable of transporting the sediment supply at a lower slope. Channel slopes in the field are likely the product of a mutual adjustment between processes producing channel narrowing (i.e. by deposition of the finer fractions of the bed material load and by vegetation colonization) and processes increasing the system scale flow resistance (primarily by changing the channel sinuosity), all subject to the ability to transport the imposed sediment supply.

The range of sediment concentrations for which equilibrium can be established in our experiments gives some indication of the maximum adjustment that the system can make without adjusting the average width and average shear stress. Larger adjustments require that the average width and shear stress change, as implied by the typical regime model formulation, which will

involve the sort of longer-term evolution described above. Thus, the mean wetted width and average shear stress are important constraints on the equilibrium configurations available to the system, and there is some finite, maximum distortion between the wetted width and the effective width that can occur.

Interestingly, differential adjustment of  $f''$  does not seem to be an independent part of the system adjustment. Indeed, it seems that cross sectional shape is not independent of the reach scale flow resistance (which we have effectively held constant by fixing the bank alignment), and is probably a trailing phenomenon, wherein the cross channel geometry is determined by the planform channel alignment, along with the imposed discharge. This is essentially the position taken in so-called “bend theory” models of channel morphology (e.g. Bridge, 1977; Blondeaux and Seminara, 1985; Sun et al., 2001), wherein the channel centerline alignment and the channel width are specified, and the cross sectional geometry is determined. That such models have been relatively successful in predicting alluvial channel shape suggests that cross section shape and the associated bedforms are indeed trailing phenomena, determined by the reach scale form resistance. There would therefore appear to be only two truly independent components of  $f_{sys}$ : the grain-scale flow resistance and the reach-scale form resistance, both of which will be influenced by the processes setting the channel width.

These findings suggest that the graded relation observed in Phase 3 is really only meaningful insofar as it represents the adjustment of the system scale flow resistance, since slope itself does not appear to be a fundamental adjustment of the system: it gains meaning only in the context of the boundary material properties. When the boundary materials are uniformly erodible, then slope adjusts via the reach scale form resistance according to a graded relation, but when the boundary is non-erodible, then slope does not adjust appreciably, within some range of sediment concentration within which textural adjustments can produce equilibrium conditions, instead. Between these two end-members, alluvial behaviour is likely transitional between the two dominant responses. Furthermore, previous optimality criteria, such as the minimum slope hypothesis, are inconsistent with the type of response evident in the Phase 4 experiments: the implication is that they are clearly too limited in the range of adjustments that they embrace. In contrast, the maximum flow resistance hypothesis proposed in Chapter 2 can accommodate this complex response, since it acknowledges more completely the degrees of freedom that alluvial systems have.

## 5.0 PHYSICAL MODEL FOR SLOPE MINIMIZATION

The regime model formulation and treatment of the experimental data have considered the alluvial state from the 1D, reach scale perspective. Nothing specific has been said about the process-form interactions occurring at the sub-reach scale, at the level of individual bars, riffles and pools. The argument that  $f_{sys}$  becomes maximized as the channel tends toward the most stable equilibrium is really only an arbitrary assumption, based on a probabilistic view of system behaviour. The striking regularity of the meanders produced in the laboratory, and the organized way in which equilibrium was achieved does not seem to support the position that channel change is a random process, guided in only a general way by a drift toward stability.

Linear stability models (LSMs) of alternate bar development (Engelund and Skovgaard, 1973; Parker, 1976; Fredsoe, 1978) represent an initial attempt to model the apparent regularity. However, the form of the bed adjustment (the perturbation, in the language of stability analysis) is specified at the outset: usually a double harmonic perturbation of diminishingly small amplitude is imposed, in which the development of alternate bars (as represented by the sinusoidal surface) is a forgone conclusion if the initial condition is susceptible to perturbation. Remarkably, there is no substantive discussion of why a double harmonic disturbance is appropriate, nor how such a configuration might be reached. Its only apparent qualification is that alternate bars – once developed – look somewhat similar to a double harmonic surface. As a result, LSMs produce a morphology that is consistent with what is observed in the field and in the laboratory, but they are unable to explain why or exactly how such morphology is achieved.

Even the more recent LSMs that couple the alternate bar-scale analysis with an analysis of the channel alignment using some form of bank erosion relation (Blondeaux and Seminara, 1985; Johannesson and Parker, 1989; Sun et al., 2001) must severely constrain the system and specify the form of the perturbation. Speaking about the alternate bar LSMs, Callander (1978) comments “what causes meanders is still a question wanting a complete answer, although the case for dynamic instability (a.k.a. bar theory) is strong. There is a danger in the study of instability that mathematical techniques will be used which are too precise, given the crudity of the empirical relationships available to close the problem. Perhaps it will be better to study in a rather rough way the effects of bank erosion and perturbations that are not infinitesimal than to apply increasingly sharp mathematical tools to linear analysis.” This criticism still seems appropriate, since no fundamental explanation of meandering has yet emerged, despite more and

more mathematically sophisticated LSMs. It is particularly clear that some sort of physical justification of the ubiquitous, sinusoidal perturbation is required.

If a reasonable physical process can be identified that produces the sinusoidal perturbations assumed by the linear stability models, then we arrive at a rather convincing argument explaining meandering as the result of the interaction between the fluid flux carried by a channel and the sediment flux generated by erosion of the boundary. Such a physical process will provide a justification for the assumptions of the LSMs, while in turn the previously published LSMs provide a detailed understanding of the range of conditions over which such a process can act.

A feedback process is described in this chapter, between the asymmetry of the cross sectional shear stress distribution and the local transport capacity. This feedback explains why uniform shear stress distributions are nearly always susceptible to instability, once perturbed (e.g. Parker, 1976), and is conceptually linked to generation of periodic, alternating bars, similar to the perturbations assumed in LSMs. In addition to presenting the feedback mechanism, this chapter explores the proposition that optimality criteria (Chapter 2) are simply formalisms that describe a cross-scale linkage, thereby permitting the description of a three-dimensional phenomenon (SMB) by a one-dimensional regime model. The SMB process embodied in this cross-scale linkage is implicit in the existing LSMs, and demonstrates that they fundamentally describe the action of some sort of optimality criterion in a regime theory context.

We do not claim that the feedback described here represents all necessary and sufficient conditions to describe alluvial channel behaviour. It is presented rather as a demonstration of one important principle among several that inform alluvial system dynamics. We will: (i) present a theoretical basis founded on a simplified representation of the shear stress distribution to estimate the sediment transport capacity; and (ii) present evidence from the experiments discussed in Chapter 4 that demonstrates the action of the hypothesized feedback mechanism that produces equilibrium channels.

This discussion is limited to fluvial systems with single-thread channels, since these are quite common in the field and since they are conceptually transparent within the context of the analysis to be presented. Multiple-thread channels are likely to behave according to the same principles, but the added degree of freedom introduced by channel bifurcations and confluences requires a more sophisticated modeling approach than is consistent with the use of regime theory in this thesis. Furthermore, the simple substitution of depth distribution for shear stress distribution that

is employed is appropriate only for the condition at which the instability described by LSMs is triggered by the feedback process.

### 5.1 TRANSPORT CAPACITY FOR ASYMMETRIC SHEAR STRESS DISTRIBUTIONS

The physical basis for the feedback process generating SMB operates locally, at the level of the channel cross section. Once initiated, it propagates through a system, since meanders are essentially self-replicating (Keller, 1972), generating a channel morphology similar to the perturbation assumed in LSMs. The feedback is described by employing a simplified shear stress distribution, described by a width ( $W$ ), mean shear stress ( $\bar{\tau}$ ) and a parameter ( $\beta$ ), as shown in Figure 54.  $\beta$  is a measure of the variance for the shear stress distribution.

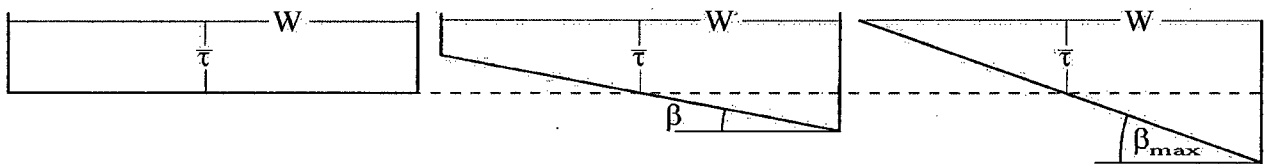


Figure 54: Assumed shear stress distributions employed by the theoretical model to evaluate the transport capacity. For all three configurations,  $W$  and  $\bar{\tau}$  are constant. Only the variance of the distribution changes.

In the limit case when  $\beta$  equals 0, the distribution becomes uniform, and corresponds with a reference transport capacity ( $\overline{TC}$ ). An additional parameter is required to describe the reference transport capacity, the characteristic grain size,  $D$ : once  $D$  is known, the transport capacity is estimated to be:

Equation 34.....  $\overline{TC} = W\xi[\bar{\tau} - \tau_c]^{1.5}$

wherein  $W$  is the channel width,  $\xi$  is a constant,  $\tau_c$  is the critical shear stress for entrainment (given by  $\tau_c = 0.045(\gamma_s - \gamma)D$ ) and  $\gamma_s$  is the unit weight of the sediment.

For non-uniform distributions ( $\beta > 0$ ) the sediment transport capacity increases, since the transport law is nonlinear and bounded by zero. The transport capacity ( $TC$ ) in this case is given by:

Equation 35.....  $TC = \xi \int_{x_c}^{x_o} [\tau(x) - \tau_c]^{1.5} dx$

where  $x_o$  corresponds to the maximum shear stress ( $\tau_o$ ) and  $x_c$  is the point at which  $\tau(x) = \tau_c$ . There is a maximum value of  $\beta$  that can be imposed while still maintaining the same  $W$  and  $\tau$  as the equivalent uniform distribution. This limit, expressed as an angle based on the approximation  $\bar{d} = \bar{\tau}/\gamma S$ , is given by:

Equation 36.....  $\beta_{max} = \tan^{-1}\left(\frac{2\bar{\tau}}{\gamma SW}\right)$

Ferguson (2003) presents a more complete treatment of the difference between the quantities defined by Equation 34 and Equation 35, in which he employs a shear stress distribution represented by two planar surfaces: a shape parameter,  $b$ , is varied between the limits 0 and 1, representing distribution shapes ranging from uniform to a convex dogleg, respectively. A distribution with a triangular geometry, similar to those in Figure 54, is described by  $b = 0.5$  in Ferguson's framework. Ferguson observes that the distribution of shear stress in one particular test case (Fraser River, British Columbia) is consistent with a simple distribution ( $b \sim 0.4$  to  $0.7$ ). It may be inferred, then, that the simple shear stress distributions assumed in this analysis are adequately realistic.

Ferguson (2003) observes that the distributions of shear stress and water depth,  $d$ , are similar, though they may differ locally. However, since we are concerned primarily with the relative (in)stability of a flat bottomed, straight channel and are, in part, discussing the physical basis for the assumed infinitesimal double harmonic perturbation employed by LSMs, we can usefully apply the uniform flow approximations, wherein the distribution  $\tau(x)$  has a direct correspondence to  $d(x)$  (after Lane, 1955). The distributions in Figure 54 can be interpreted as representations of the stream cross section.

The nature of the feedback – described in detail in Section 5.3 – depends on how the ratio  $TC/\overline{TC}$  behaves. When there is a disparity between the two quantities, a local excess transport capacity results around any locally asymmetric section, which will necessarily deform the system until the disparity is reduced. For all  $\beta$  in the range  $\beta_{max} > \beta > 0$ , this ratio becomes infinite in

the limit ( $\bar{\tau} \rightarrow \tau_c$ ), since  $\overline{TC}$  approaches 0 but  $TC$  remains finite, if small. At the other extreme ( $\bar{\tau} \rightarrow \infty$ ), the ratio approaches 1. The behaviour between these limits depends on the channel width ( $W$ ) and the distribution variance ( $\beta$ ).

If feedback strength is expressed as  $\left(\frac{TC - \overline{TC}}{\overline{TC}}\right)$ , excess shear stress is expressed as  $\left(\frac{\bar{\tau} - \tau_c}{\tau_c}\right)$ , and shear stress distribution variance is expressed as a proportion of the theoretical maximum ( $\beta/\beta_{max}$ ), then the dependency on  $W$  drops out. The strength of the feedback tendency is functionally related to excess shear stress for given values of  $\beta/\beta_{max}$ , as shown in Figure 55a. These functions are approximately described by equations of the form:

$$\text{Equation 37} \dots \log\left(\frac{TC - \overline{TC}}{\overline{TC}}\right) = a_1 \log\left(\frac{\bar{\tau} - \tau_c}{\tau_c}\right)^3 + a_2 \log\left(\frac{\bar{\tau} - \tau_c}{\tau_c}\right)^2 + a_3 \log\left(\frac{\bar{\tau} - \tau_c}{\tau_c}\right) + a_4$$

The parameter values ( $a_1$  to  $a_4$ ) for the range of relative variance are given in Table 11. These functions were derived by numerically evaluating Equation 35 at selected values of  $\left(\frac{\bar{\tau} - \tau_c}{\tau_c}\right)$ , and then fitting curves to the resultant data fields (Figure 55b). Equation 37 and the relations in Figure 55 form the basis of our description of the feedback mechanism.

Table 11: Coefficient for polynomial fits, per Equation 37

Relative variance	$a_1$	$a_2$	$a_3$	$a_4$
$\beta_{max}$	0.0340	0.228	-0.966	-0.254
$\beta_{max}/2$	-0.00370	0.0149	-1.34	-0.895
$\beta_{max}/4$	0.0689	0.235	-1.32	-1.53
$\beta_{max}/8$	0.172	0.646	-0.984	-2.07
$\beta_{max}/16$	0.234	0.964	-0.587	-2.53

## 5.2 SLOPE MINIMIZING FEEDBACK MECHANISM

The feedback is based on the general principle that: (i) a disparity between  $TC$  and  $\overline{TC}$  will produce net erosion centered around the peak of the shear stress distribution; and (ii) this local erosion will increase the variance of the shear stress distribution, thus increasing the disparity between  $TC$  and  $\overline{TC}$ , and producing a positive feedback. This ultimately necessitates a change

in the mean shear stress via the channel slope in order to establish a stable, meandering channel pattern.

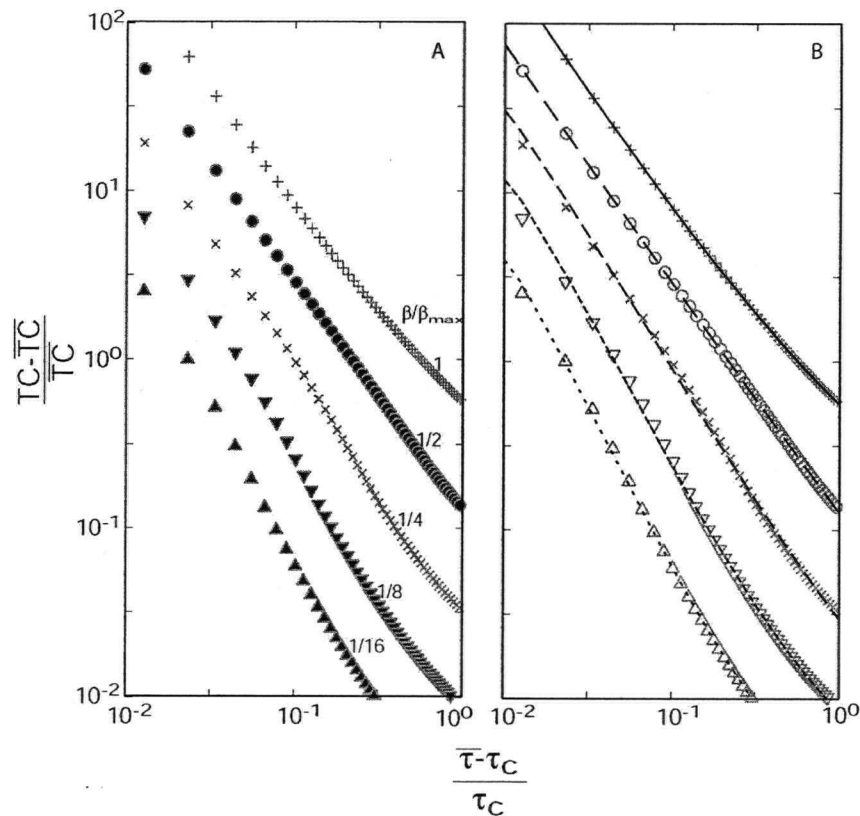


Figure 55: (a) proportional increase in  $TC$  relative to  $\overline{TC}$  is plotted against excess shear stress for a range of relative variances ( $\beta/\beta_{max}$ ). (b) polynomial curves fit to the data from (a) are shown.

### 5.2.1 Characteristics of Positive Feedback Mechanism

There are two key points to make before describing in detail the feedback mechanism: for this purpose, the functions on Figure 55a are used to generate a 3D surface of feedback intensity (Figure 56). The first point has to do with proximity to threshold conditions. It is evident on Figure 56 that as the mean shear stress approaches  $\tau_c$ , the effect on the local transport capacity of the distribution variance ( $\beta/\beta_{max}$ ) is proportionally greater. For example, a mean shear stress 50% greater than  $\tau_c$ , has a transport capacity only 30% greater than  $\overline{TC}$ , assuming a relatively high variance ( $\beta/\beta_{max} = 0.5$ ). For the same distribution variance, a shear stress only 10% larger than  $\tau_c$  has a transport capacity that is fully 300% greater than  $\overline{TC}$ . Clearly, the effect of

distribution variance is greatly increased near threshold conditions, and therefore so too is the potential strength of the feedback mechanism.

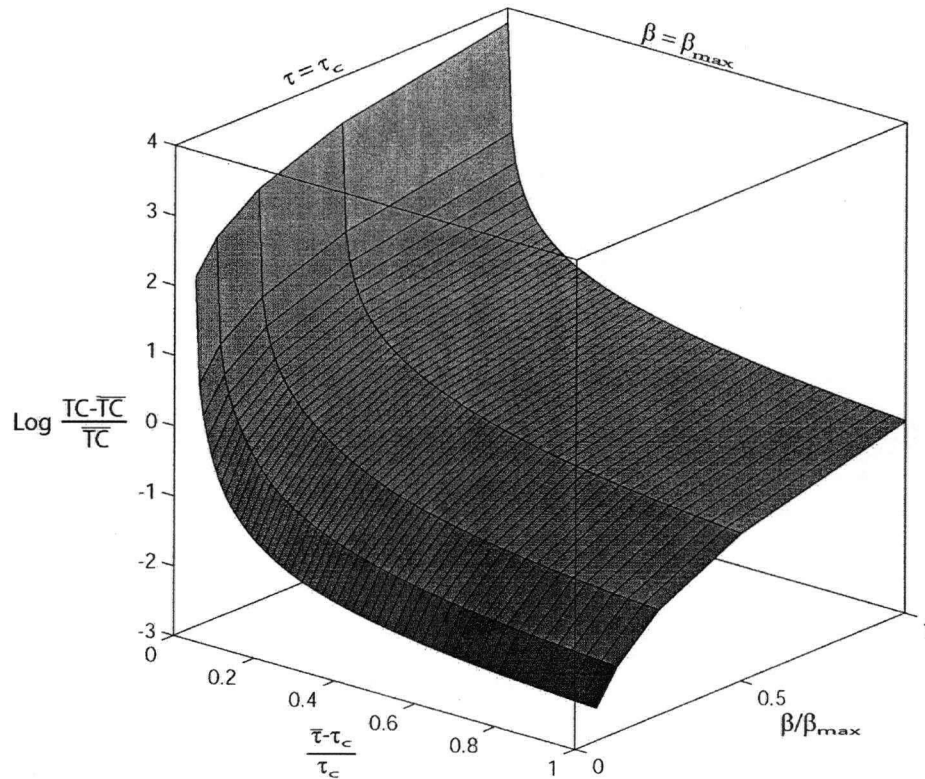


Figure 56: A surface of excess  $TC$  is generated from the curves shown in Figure 55a. Both the excess shear stress and the relative shear stress variance ( $\beta/\beta_{max}$ ) are plotted on arithmetic axes.

This brings us to the second point, which addresses the rate-of-change of potential feedback strength. Provided the mean shear stress ( $\bar{\tau}$ ) does not change (which amounts to holding the channel slope constant), the feedback intensifies as  $\beta/\beta_{max}$  increases. Once the feedback starts, it quickly increases the local disparity between the sediment supply (which can be no larger than  $\bar{TC}$  for an initially uniform distribution) and the local transport capacity,  $TC$ . For a constant excess shear stress,  $TC$  – initially close to zero – increases quickly with increasing  $\beta/\beta_{max}$  (Figure 56). If, for example, the excess shear stress is 25%, then  $TC$  is 5% greater than  $\bar{TC}$  when  $\beta/\beta_{max}$  is about 1/8, and 80% greater when  $\beta/\beta_{max}$  is about 1/2.

### 5.2.2 Linking the Positive Feedback to Planform Adjustment and Stability

Figure 56 implies that an initial perturbation (due to an as-yet unspecified cause, explored further in Section 5.2.3) produces a disparity between  $TC$  and  $\bar{TC}$  by increasing the variance  $\beta$ , and will

quickly amplify itself through localized net erosion at an increasingly rapid rate, just as predicted by the standard LSMs<sup>d</sup> (see Rhoads and Welford, 1991, for a general discussion). For flow conditions that are nearly uniform, an increase in  $\beta$  results primarily by changing the local depth. Since the excess transport capacity will always coincide with the peak deviation of  $\tau(x)$  from the mean value (i.e. at deepest part of the channel,  $Y_o$ , if we employ the uniform flow approximation), the resultant net erosion will increase the asymmetry of the shear stress distribution.

The feedback mechanism describes such an amplification of an initial perturbation, resulting first in modification of the channel cross section, and then in modification of the channel planform – the cross-scale linkage referred to in Section 5-1. The feedback described necessarily abandons the assumption that  $\bar{\tau}$  remains constant, and includes a countervailing mechanism that produces a stable meander form. Figure 57 is a schematic description of the sequence of channel adjustments from an initially uniform shear stress distribution toward an asymmetric one associated with an equilibrium meandering channel, while Figure 58 is a diagrammatic representation of the processes, feedbacks and adjustments implicit in Figure 57. Both are based on an assumed direct correspondence between the shear stress distribution and the local depth (after Lane, 1955, in his derivation of threshold channel geometry), which is approximately true only for wide shallow channels with low sinuosity. Clearly, the geometry implicit in Figure 57 is consistent with the double harmonic perturbations that are the basis for LSMs.

Assuming an initial uniform shear stress distribution, a small *local* perturbation is imposed. The sediment throughput ( $Q_b$ ) for the system is equal to  $\overline{TC}$ , which is the maximum that can be supported by the initial configuration. The thalweg remains straight, and the water surface slope remains unchanged. However,  $TC$  is slightly increased at the perturbation, due to the slight increase in  $\tau_o$ , and the system is no longer stable. The increase in  $TC$  is localized around the initial perturbation, and since  $Q_b$  is not increased, more net scour occurs, increasing  $\tau_o$  (and thus the maximum depth,  $Y_o$ ) as well as the variance of the shear stress distribution ( $\beta$ ). This process is primarily vertical, and the banks are assumed to remain stable.

---

<sup>d</sup> LSMs generally show that, for  $W/d$  ratios common in bedload dominated streams, any such infinitesimal perturbation will tend to amplify, rather than decay.

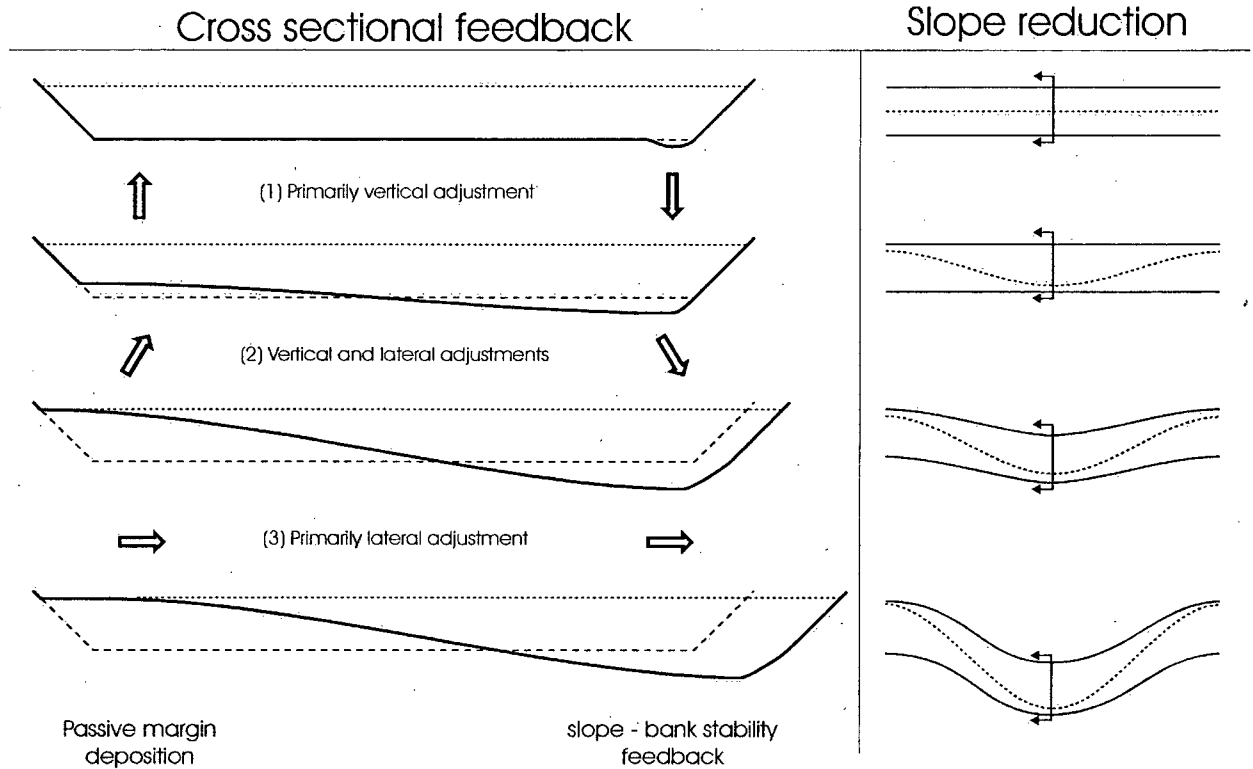


Figure 57: Schematic diagram of cross sectional and planimetric adjustments resulting from the action of the positive and negative feedback described in Figure 55.

The development of a local perturbation necessarily results in a concomitant deposition of sediment downstream, where the shear stress distribution remains uniform. The deposition will affect the flow structure and shear stress distribution at that cross section and thereby spawn another perturbation in the form of local scour on the opposite side of the channel from the original one. This raises a general point: the alluvial channel forms develop at a rate that is not so much related to the sediment throughput as it is to the local variations in the sediment transport rate, which in turn affect the shear stress distribution: i.e. the divergence of the sediment flux field replicates the initial perturbation. The longitudinal scale of the flux divergence sets the wavelength for the emergent channel bars, which is presumably related to the step length for sediment transport at formative discharge (Pryce and Ashmore, 2003). The characteristic wavelength issue is discussed in more detail below.

The feedback between local scour and local excess transport capacity accelerates rapidly, as implied by Figure 56, producing the second channel configuration in Figure 57. Note that it is also assumed that local deposition is occurring near the opposite bank, in accordance with our

observations about the downstream replication of the initial perturbation in response to divergence of the sediment flux field. The increase in excess  $TC$  will cause further net erosion, around the deepest part of the channel, thereby further increasing  $\beta$  and further increasing the contrast between  $TC$  and  $Q_b$ . This interaction is described by the positive feedback loop shown at the top of Figure 58.

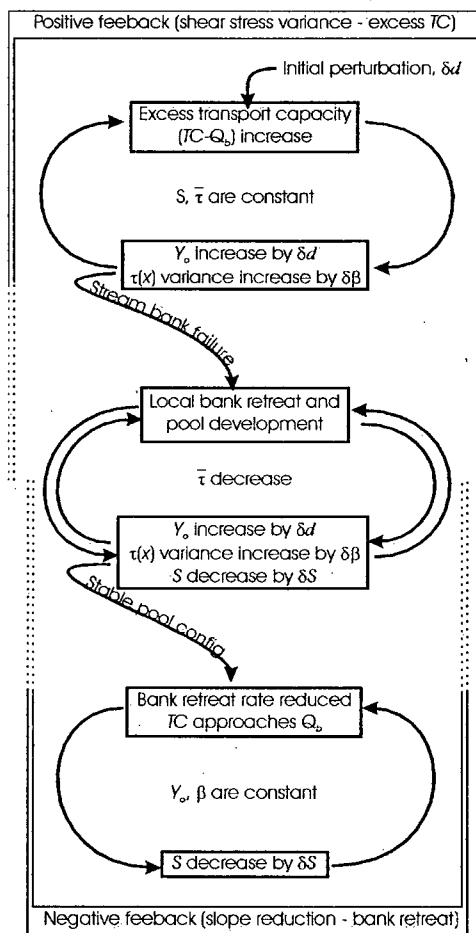


Figure 58: Flow chart representing the feedback responsible for the initiation of meander development and the feedback halting meander development at the equilibrium slope and sinuosity.

At some point, the vertical degradation will cause the adjacent stream bank to fail by oversteepening it, introducing a lateral component to the adjustment and producing the third configuration in Figure 57. The onset of bank erosion is a critical to the development of meanders (Friedkin, 1945), at which time the flux divergence increases rapidly (see Dietrich and Smith, 1983) and channel slope begins to adjust dramatically. A negative feedback is initiated, and lateral adjustment comes to dominate the system. As a result channel morphology develops

rapidly, while channel sinuosity increases and slope decreases (negative feedback, Figure 58). The stable channel morphology is produced as a result of the reduction in channel slope (fourth configuration, Figure 57).

Local variations in the slope will develop within the system, as well. Since the positive feedback mechanism is relatively strong near threshold and accelerates as asymmetry develops, the local slopes obviously cannot remain constant for long. In fact, the slopes over the apex of the bend (i.e. the zone of most intense positive feedback) are quickly reduced, and the slope over the cross-over (where there is little asymmetry-related amplification of the transport capacity) will increase due to the drawdown effect of pool deepening (downstream of the cross-over) and the deposition of sediment eroded from the pool (on the upstream side of the cross-over). At equilibrium, the cross-over sections cannot have the same local slope as the apex sections if they are to transport, on average, the same throughput sediment load. This dynamic is further addressed using a reformulation and reinterpretation of regime theory in Chapter 6.

There remains the issue of the wavelength for the adjustment. In the field, meander wavelength is remarkably consistent, ranging from about  $5W$  to  $15W$  (Leopold et al., 1964; Yalin, 1971a; Rhoads and Welford, 1991). In laboratory experiments (e.g. Garcia and Nino, 1993), the wavelength of alternate bars developed between fixed, straight banks is nearly constant, despite a range of flow depths and channel gradient. On all evidence, the critical length scale appears to be the width of the channel. Yalin (1971a) argues that this is the result of some spatial sinusoidal autocorrelation with a characteristic length scale equal to the channel width. He attributes the autocorrelation to channel width-scale turbulent eddies, but this seems an unlikely control given the circulation cell flow structure typical of meandering rivers (Bathurst et al., 1979; Dietrich and Smith, 1983).

Since meandering does occur in ocean currents and in the atmospheric jet stream, it has been posited that there must be some universal cause (Davy and Davies, 1979). To an extent, this must be true: meandering is the spatial pattern produced by harmonic oscillatory behaviour, combined with constant lateral displacement in a direction normal to the oscillation. However, the source of both the lateral displacement and the characteristic oscillations must be very different for meandering in different media. For example, the oscillatory component of meandering ocean currents (and the jet stream) is probably similar to the Kelvin-Helmholtz instability, which is based on pressure gradients (Tritton, 1988 p. 268), while the bulk transfer is

related to the general circulation due to differential heating of the earth by the sun and the coriolis force of fluid. Meandering has also been observed in ice sculpted by meltwater, where the lateral displacement is due to the force of gravity, just as it is in alluvial open channels: the oscillatory component is obviously related to thermal processes, and the production of meanders must be related to the transfer of heat by the system and/or abrasion by sediment or ice particles carried by the stream.

We relate the characteristic meandering wavelength to the diffusion of an initial perturbation across the channel as a sediment wave. This is consistent with Parker's (1976) analysis, which concludes that sediment transport is the primary cause of alternate bar-type instability, and with Smith's (1998) observation that channel width-scale bedload deposition is the key mechanism giving rise to meandering in his stream tray experiments. Since, at formative discharge, the bed is generally in motion, the perturbation need not propagate by lateral momentum diffusion, which is a relatively slow process, since cross stream velocity components are typically on the order of a few percent of the downstream flow velocity (Tracy, 1965). The maximum rate at which information can propagate in a fluid medium is that of a gravity wave ( $v_g$ ). Therefore, we can assume that the sediment wave emanating from the perturbation can propagate laterally by influencing the flow structure at a speed ( $v_p$ ) which is proportional to  $v_g$  (c.f. Werner, 1951; Anderson, 1967), thus:

Equation 38.....  $v_g = \sqrt{gd}$  and  $v_p = \alpha v_g$

where,  $\alpha$  is a parameter between zero and unity. The maximum angle at which the disturbance can propagate across the channel is given by the ratio  $v_p/v$ , where  $v$  is the average stream velocity. Figure 59a shows a schematic representation of the diffusion process. As the perturbation grows and generates excess sediment supply to the downstream sections, a sediment wave diffuses across the channel. Once the edge of the wave approaches the opposite bank, the flow and sediment can no longer diverge laterally, since divergent flow encounters the bank and strengthens the turbulent circulation cells that are present along the banks even in straight channels (Tominaga et al., 1989). This stalls the advance of the wave front. Although sediment can be transported across the front of the sediment wave, it is no longer accreted to the front of the wave. Upstream of this point, the divergence associated with the growth of the sediment

wave is effectively unconstrained. However, downstream, the development of strong secondary circulation adjacent to the bank forces the flow to converge and limits the lateral bar growth, thereby distorting the wave. The distortion of the sediment wave (and the associated patterns of sediment deposition), combined with the development of convergent flow between the wave front and the channel bank produce conditions that trigger another local scour and a new sediment wave that diverges across the channel in the opposite direction. This view of the process is consistent with empirical evidence presented by Pryce and Ashmore (2003), who observed that, at formative discharge levels, the typical transport distance for sediment eroded from a pool to the next bar downstream, and thus the system can be viewed as a sequence of nearly-closed erosion and deposition cells with length scales of  $0.5\lambda$ .

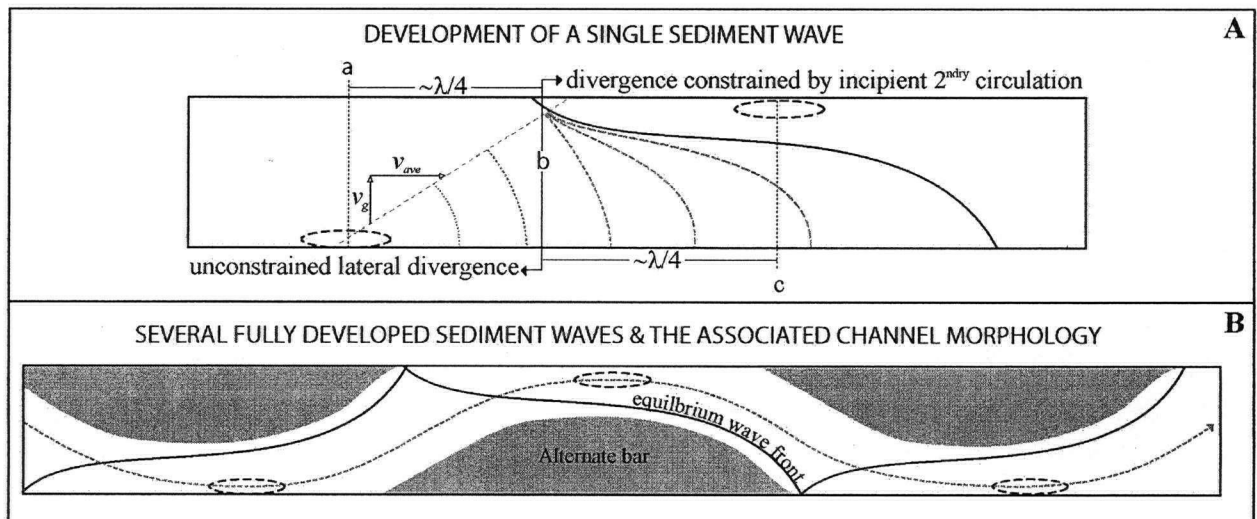


Figure 59: (a) diffusion of a sediment wave originating at an initial perturbation. (b) the resultant morphology associated with a number of such equilibrium, morphologically expressed wave fronts.

The point at which the proximity of the bank first produces an effect sufficient to stall the advance of the wave front corresponds to the location of the root of the riffle (point "b" in Figure 59). The interplay between the tendency for the sediment wave to diffuse laterally and increasingly strong secondary circulation between the wave front and the channel bank results in the equilibrium wave front configuration and the associated alternate bar deposit (Figure 59b). If we assume that the centroid of a riffle is approximately midway between the upstream and downstream pools ( $\overline{ab} \approx \overline{bc}$ ), then we can relate the distance  $\overline{ab}$  on Figure 59 to the wavelength

for the alternate bars, since  $\overline{ac} = \lambda/2$ . Thus, we can combine the divergence angle ( $v_p/v$ ) with the channel geometry parameters ( $W, \lambda$ ), such that, from geometrical similarity:

Equation 39.....  $\frac{\lambda}{4W} = \frac{v}{v_p}$

Substituting Equation 38 into the expression and realizing that  $Fr = \frac{v}{v_g}$  gives:

Equation 40.....  $\lambda = \left(\frac{4Fr}{\alpha}\right)W$

The theoretical equation for predicting wavelength presented by Parker and Anderson (1975), modified by Ikeda (1984) can be expressed in a similar form:

Equation 41.....  $\lambda = \left(\frac{5Fr}{\kappa}\right)W$ , where  $\kappa = \sqrt{S\left(\frac{W}{d}\right)}$

Equation 41, then, can be interpreted as an expression of the dynamics shown in Figure 59. By analogy, then, the scaling predicted by sediment wave diffusion (Equation 40) is consistent with the scaling predicted by linear stability analysis. The advantage of Equation 40 over Equation 41 is that it is resolved in physically meaningful terms and is based on a (simplified) physical argument:  $W$  has the obvious interpretation of the natural scale that constrains wave diffusion and  $Fr$  reflects the rate at which information can be transmitted through a moving fluid. The least well understood component is the coefficient,  $\alpha$ . The components of the coefficient  $\kappa$ , which, since they are originate from a linear stability model, have no particular physical basis, do seem

to suggest that the channel shape and possibly the relative roughness<sup>c</sup> may inform the behaviour of the coefficient,  $\alpha$ .

We can estimate  $\alpha$  based on data from the field and from laboratory experiments. Given the nature of the argument, it is most appropriate to consider the scaling associated with development from an initially straight, flat-bottomed channel. Lewin (1976) provides a good example of this sort of adjustment in the field: he describes the reestablishment of a series of alternate bars in a gravel bed river following straightening, wherein  $Fr \sim 0.85$ . He reports that the initial characteristic wavelength for the alternate bars was about 6.1 times the initial width (220 m), and that the ultimate stable wavelength, once cut-banks and point bars developed, was slightly greater (270 m). Lewin attributes the change to the expansion of the channel margins via bank erosion. When the equilibrium channel width (estimated to be about 40 m) is used to normalize the equilibrium wavelength, we obtain  $\lambda = 6.75W$ . This result suggests that the constant  $\alpha$  in Equation 40 is about 0.5.

Data from laboratory experiments generally support this estimate. The wavelengths for the constant sinuosity experiments in Chapter 4 – for which we know the effective width tolerably well – are on average about  $7.3W$ . The Froude number is about 0.83, and  $\alpha$  is about 0.46. For comparison, the value of  $\kappa$  (Equation 41) for the same experiments averages out to about 0.68, which predicts wavelength scaling  $\lambda = 6.1W$ .

However,  $\alpha$  appears to co-vary with  $Fr$ , as shown in Figure 60. Data from experiments on alternate bar development in straight channels reported by Garcia and Nino (1993) are also shown: they are consistent with the same general trend, despite the fact that the wavelengths they report are all higher than those for the constant sinuosity experiments, with  $\lambda = 9W$ , on average.

That  $\alpha$  is not constant suggests that there is some additional dynamic that needs to be considered, possibly related to channel shape and/or relative roughness. The covariance between  $\alpha$  and  $Fr$  yields relative wavelengths that are generally consistent with the  $\lambda = 2\pi W$  scaling suggested by Yalin (1971a), and conform to the lower range of the reported wavelengths for fully developed

---

<sup>c</sup> We know that, for a given  $W/d$  and  $\tau^*$ ,  $S$  is functionally related to  $D/d$  in the alluvial state space in Chapter 2. That gives rise to the speculation that, since  $\tau^*$  will be near critical for the sorts of channel under consideration here,  $S$  may be acting as a surrogate for  $D/d$  in the LSM analysis.

meanders in natural channels. Since the argument above is based on the maximum possible rate of cross-channel diffusion, it is expected that the analysis should represent the lower bound, and that other factors, such as the role of secondary circulation and bank erosion, could easily distort the alternate bar wavelengths predicted by Equation 40. Nevertheless, the correspondence between observation and theory support the idea that propagation of sediment waves across an initially uniform bed sets the characteristic length scale, and this is likely the dynamic that Yalin (1971a) was actually describing with his autocorrelation function.

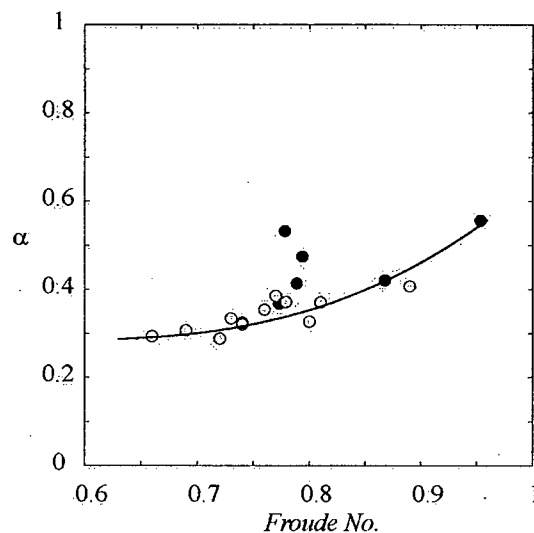


Figure 60: Relation between  $\alpha$  from Equation 40 and Froude number for the constant sinuosity experiments reported in Chapter 4 (black circles) and the development of alternate bars in a straight channel (grey circles) reported by Garcia and Nino (1993). An approximate curve describing the general trend of the data was fitted by eye.

Meandering is fundamentally produced (in bedload dominated channels) by the routing of sediment through the system, which is consistent with Parker's (1976) finding that sediment transport is a key component of meander development. And, according to Parker, the development of significant secondary circulation is a trailing phenomenon that enhances the development of meandering, and informs the ultimate stable channel morphology. That secondary circulation is not incorporated in our model is not a serious limitation, since we are concerned with understanding the initiation of the meander structure, not predicting the ultimate meander geometry.

### 5.2.3 On the Persistence of the Instability

The LSMs presented by Engelund and Skovgaard (1973) and Parker (1976) show that, provided the bed is actively transporting sediment, some sort of instability always occurs. Fredsoe (1978) predicts general instability for  $W/d$  greater than 8. However, these analyses fail to address a fundamental point: they assume that the perturbation, though infinitesimal, is ubiquitous, and that bars will emerge spontaneously everywhere. We have suggested a mechanism that produces a perturbation of similar geometry with an appropriate length scale, but which diffuses downstream from an initially localized perturbation via sediment flux divergence.

Two important questions remain: (i) what is the initial cause of the local perturbation; and (ii) why does a perturbation not decay. One possible cause of a local perturbation is the effect of a channel wall on the flow structure and turbulence intensity. It has long been known that in a straight channel, the turbulence intensity is greatest adjacent to the side-wall (Gessner and Jones, 1965), but Tominaga et al. (1989) demonstrate that the production of vorticity there leads to the development of secondary circulation cells adjacent to the bank, based on time-averaged data. According to Tominaga et al. (1989), the scale of the resultant secondary flow cell is on the order of the water depth: they are not large enough to affect the entire channel cross section, but they are sufficiently large to act on the bed near the base of the wall and generate an initial perturbation. The streamwise scale of the cells also increases as banks become progressively more rough, which is consistent with results reported by Einstein and Shen (1964), who observed alternate bar formation only in the presence of rough channel banks. Note that, since  $Fr$  will generally increase with  $D/d$  for the same  $\tau^*$  and  $W/d$  ratio (Figure 7), and since bank roughness in alluvial channels is related to  $D/d$ , the scaling of these cells may underlie the relation between  $\alpha$  and  $Fr$  in Figure 60.

That high intensity turbulence and turbulence-induced secondary circulation are characteristic along the channel banks in straight channels suggests both a mechanism for an initial perturbation and its continued action. More than that, it seems to suggest that such perturbations should be ubiquitous along the channel walls, leading to the question, why don't channels form central shoals with linear depressions adjacent to the banks? The secondary circulation is a time averaged representation of the flow structure, and thus obscures any possible coherent spatiotemporal structure parallel to the banks. Allen (1994) and Smith (1996) summarize the turbulent structure along the banks as a series of corkscrew vortices that are periodically

disrupted by a horseshoe vortex, and which may coalesce and grow in scale. These two scales of periodic behaviour are implicit in the time-averaged secondary flow cell, and may be responsible for the initiation and maintenance of a perturbation for long enough that the feedback between cross sectional shear stress variance, flow structure and transport capacity can begin. So, for perturbations that seem to grow exponentially and which are subject to at least some temporal variability, it is hard to imagine how all perturbations everywhere could develop at an identical rate, which is the necessary condition if one exponentially growing perturbation is not to come to dominate all others. Note that the feedback will amplify exponentially only when most of the bed material can be entrained: it is not effective under conditions substantially different from full mobility, which are, by definition much different from the formative flows that are responsible for reach-scale alluvial channel morphology.

However, the cause and persistence of a local perturbation must fundamentally lie in the interaction between the probability that a perturbation will produce local erosion, and the probability that an altered sediment supply from upstream due to some other perturbation will interact with it, thereby suppressing or enhancing the net erosion. The time-averaged probability of an initial perturbation is probably uniform, along the banks. The interaction with upstream perturbation events is clearly linked to the step length between erosion and subsequent deposition since, if sediment is transported essentially infinite distances once eroded, there can be no interaction, and indeed, no divergence in the flux field. While step length may be set, essentially, by the spatiotemporal structure of the flow over a nearly uniform bed or, later, by the larger scale structure of pools and bars (Pryce and Ashmore, 2003), it is appropriate to view it as a probabilistic statement about mean distances of movement, and is thus related primarily to the mean boundary shear stress.

### 5.3

### COMPARISONS WITH EXPERIMENTAL DATA

The argument presented above suggests that the feedback mechanism should produce some characteristic features in alluvial systems. The phase 3 experiments on a stream table where  $Q$ ,  $Q_b$  and  $S_v$  are treated as independent variables demonstrate many of these expected features.

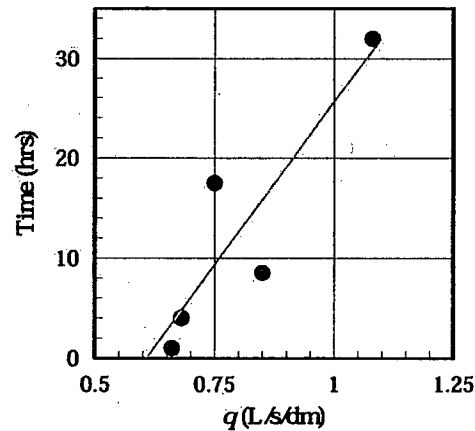


Figure 61: Time to equilibrium versus initial specific discharge for stream table experiments.

Most obviously, the experiments demonstrate that initially straight channels with mobile beds increase their sinuosity until they reach equilibrium configurations at slopes less than the initial slope. The equilibrium slope depends on the sediment supply to the system, holding  $Q$  constant (Figure 37b). The phase 3 experiments show sinuosity increasing monotonically over time as the channels approach a sinuous equilibrium configuration – the so-called slope minimizing behaviour. They also demonstrate that the response of systems at equilibrium to subsequent changes in the governing conditions is consistent with the hypothesized feedback mechanism (experiments 1-5a, 1-5b). When the sediment supply is lowered, the channel – initially at equilibrium with the higher feed rate – responds by instigating another phase of bank erosion at the apices producing an increase in sinuosity until equilibrium is re-established at a lower slope. However, when the sediment supply to an equilibrium channel is increased, the reverse occurs. While no equilibrium channels were established after an increase in sediment supply, (since the single thread channel tended to give way to a multiple thread one), the results do seem to imply that the slope associated with the equilibrium thalweg sinuosity was the minimum that was capable of transporting the load.

The rate of sinuosity change for the Phase 3 experiments was also consistent with the behaviour implied in Figure 55 and Figure 56. When the shear stress acting on the bed is much larger than  $\tau_c$ , the theoretical amplification of the transport capacity due to non-uniformity of the transverse shear stress distribution is small, and thus the feedback is relatively weak. However, as the average shear stress approaches the critical value for entrainment, the strength of the feedback increases rapidly (Figure 56). Figure 61 plots the initial specific discharge ( $q$ ) against the time it took for the constant  $S_v$  experiments to reach equilibrium, which must be related in some general way to the strength of the feedback mechanism. Since the initial channel slope (i.e.  $S_v$ ) and the bed material grain size distribution were kept constant,  $q$  is a surrogate for shear stress, with the threshold for bed entrainment estimated to be about 0.6 L/s/dm. There is a strong positive correlation between the time required to establish equilibrium and the initial  $q$ . For the longest running experiment (1-3), increases in channel sinuosity did not occur until around 10 hours, when the sediment transport rate (and, by inference, average shear stress) was substantially reduced, and the strength of the feedback increased. It took a further 14 hours to reach equilibrium. In contrast, when the initial  $q$  was near threshold, equilibrium configurations were reached after one or two hours.

There is another way to look at this issue. It could be suggested, for example, that the higher rates of sediment transport associated with higher mean shear stress should result in a more rapid approach to equilibrium. But, it is clear that the lateral change in channel morphology implicit in our feedback mechanism requires that the sediment flux field diverge. Equivalently, deposition must be possible within the channel. When the mean shear stress is high and the mean step length is long, relative to channel width, then there can be very little divergence of the sediment flux. As a result, construction of an alluvial morphology by deposition is very limited, even though substantial morphologic modification may occur due to net degradation. It is only when the mean shear stress approaches the value for entrainment that divergence (and deposition) can occur. Thus, while higher mean shear stress results in a higher sediment throughput, it produces a lower rate of the constructional morphologic change, as pictured in Figure 57, and – since lateral, constructional, adjustments involve far less geomorphic work than vertical, degradational adjustments – a much slower approach to equilibrium overall.

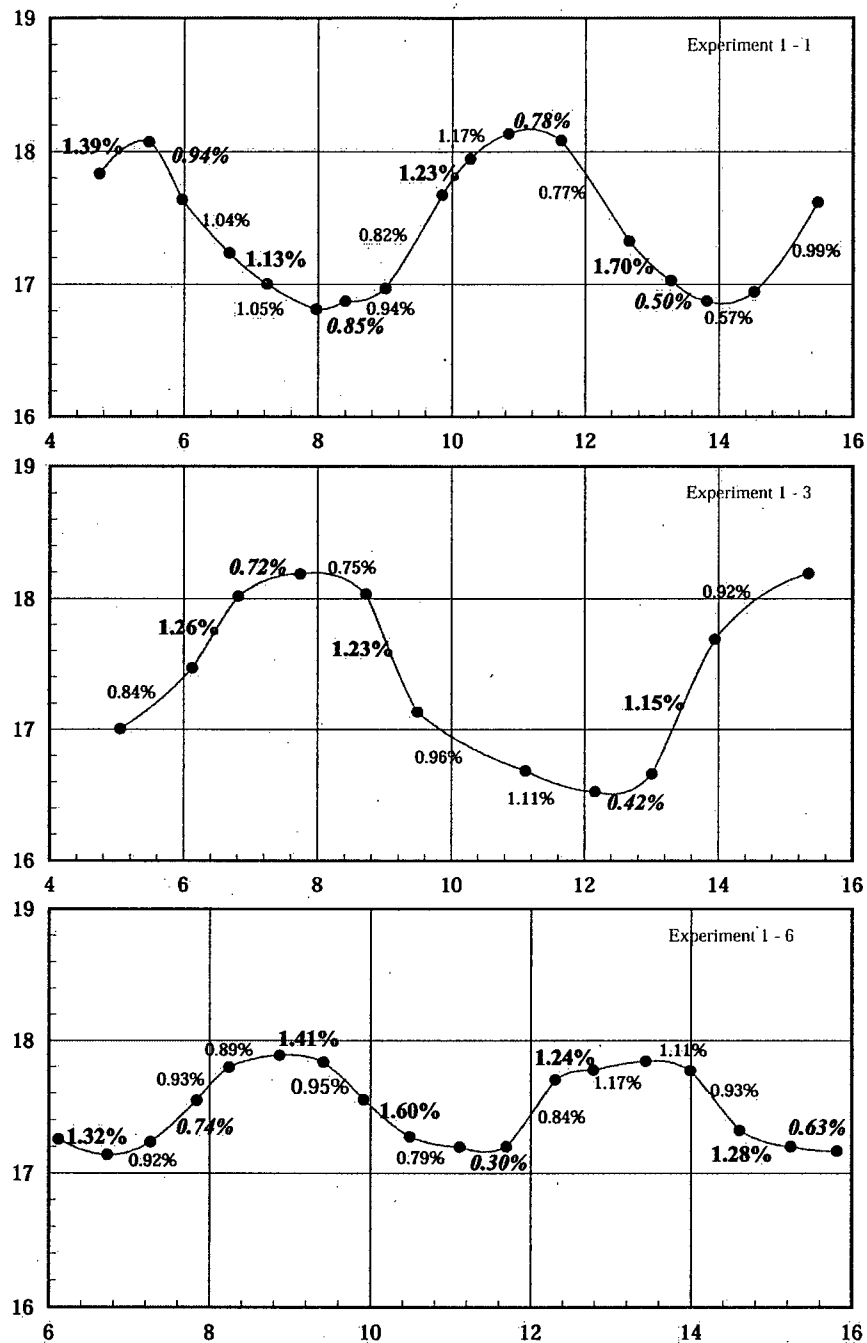


Figure 62: Water surface slopes along the thalweg for three equilibrium channel configurations. The minimum slope in each bend is shown in bold italics, and the maximum is shown in bold.  $S_v$  is 1.09 for these experiments. The direction of flow is from right to left.

The inferred difference in  $\beta$  between bend apices and cross-overs implies that a higher water surface slope must exist at the cross-overs – according to the feedback model – if they are to transport the same sediment load. The water surface slopes for three experiments are presented in Figure 62. The experiments represent a range of thalweg sinuosities and initial transport intensities. For the higher thalweg sinuosities channels (panels A and B), the pattern is relatively

clear: the lowest slopes are associated with the bend apices and the highest slopes are associated with the entrances to and exits from the bends. This pattern is also evident for a lower sinuosity equilibrium channel (Panel C), but there are notable exceptions to this general rule. This most likely implies failure of the simple reasoning that relates  $\beta$  to position along the thalweg trace: the details associated with the individual bedforms that undoubtedly affect the transverse distribution of shear stress seem to become relatively more important as the sinuosity decreases.

Interestingly, the typical pattern exhibited in these experiments is also evident in fixed bank, mobile bed experiments as well. Hooke (1975) discusses experiments conducted in a meandering channel based on a sine-generated curve described by an angle  $\Phi$  as a function of downstream distance,  $m$  in meters  $\left( \Phi = 55^\circ \sin \frac{2\pi m}{13.2} \right)$  with a mobile sand bed. Upstream of the bend apex, the energy slope is higher than downstream of it, where bar-pool units typically form, and where helicoidal flow strength (and presumably asymmetry of the shear stress distribution) is greatest. The difference in surface slopes is similar to the differences between the maximum and minimum slopes shown on Figure 62 for our experiments.

## 6.0

## IMPLICATIONS FOR REGIME THEORY

### 6.1

### EXPERIMENTAL EVIDENCE

The experiments discussed in Chapter 4 offer some evidence in support of the application of a regime model to the study of alluvial systems. The primary theoretical obstacle is selection of a single point from a solution curve to describe an alluvial state (for example, see Figure 3). A regime model predicts that, for a specified  $Q$  and  $Q_b$ , a range of possible slopes and stable channel configurations can accommodate the specified fluxes, ranging from relatively wide channels with steep slopes to narrow ones with lower slopes. To overcome this, modellers employ some sort of optimality criterion that essentially chooses a homologous point on the relevant stability curve.

If alluvial states are in reality randomly distributed along the stability curves, there is no reason why the behaviour shown in Figure 37 should necessarily arise. In all of the experiments, the equilibrium slope is less than the initial one and, as the sediment concentration declines, the equilibrium slope is reduced concomitantly, in a very predictable way. This implies that not all parts of the theoretical stability curve based on regime theory are equally accessible and equally stable. There is a tendency for the equilibrium slope to inhabit that part of the curve with lower slopes, so long as there is no constraint on bank erodibility and no significant development of surface armouring. Since there is very little scatter in the  $S$  vs.  $Q_b/Q$  relation for the Phase 3 experiments and since these slopes can be reached by various combinations of vertical and lateral adjustments, it is likely that the mobile bank channels inhabit the *same* part of their respective stability curves. That is, they tend to occupy homologous points on their respective curves. The most obvious homologous point on the stability curves invoked above is the minimum slope that is capable of transporting the sediment supply for a given flow. The application of a minimum slope hypothesis (Chang, 1979) or any of the other equivalent optimality criteria (Davies and Sutherland, 1983) seems to have some basis in fact. They do not seem to represent any missing physical process – a second coming of entropy, as it were – as some of their advocates imply. Rather, optimality criteria are formalisms that permit a one dimensional model to describe a three dimensional reality (i.e. they represent the effect of missing dimensionality of the problem, rather than missing physics), choosing the form that seems to be most stable.

In Chapter 2, we show that by minimizing the channel slope, the flow resistance for the fluvial system is maximized within the context of a regime model. The behaviour evident in Figure 37 is consistent with this hypothesised optimization principle. Stability in the context of a 1D model or a 1D description of an alluvial system results from reducing the energy available to deform the system to a minimum, subject to the ability to pass the sediment supplied with the available discharge.

However, one can go further by incorporating the notion of the feedback mechanism discussed in Chapter 5 with the regime model formulation described in Chapter 2. The resulting model is formulated at the scale of an individual cross section, representing part of the channel within a single meander, rather than some average representation of the average channel dimensions. While the channel sinuosity is not explicitly addressed in this formulation, the local variations in channel geometry, cross sectional shear stress variance, and local energy gradient (see Figure 62) are addressed, insofar as upper and lower threshold values are identified.

## 6.2 A REVISED FORMULATION OF THE REGIME MODEL

The feedback mechanism discussed in Chapter 5 implies that the traditional regime model solution based on a trapezoidal channel (the *minimum variance solution*) represents an inherently unstable state, since it has a uniform shear stress distribution (shape factor  $b = 0$ , after Ferguson, 2003). The positive feedback mechanism between local erosion, variance of the shear stress distribution and the associated sediment transport capacity will quickly cause such trapezoidal channels to develop a non-uniform cross section, provided the boundary material is erodible. The ultimate form predicted by the feedback mechanism will exhibit the maximum cross sectional variance that can be supported by the boundary material, which can be approximated by a triangular cross section ( $b = 0.5$ ), as shown on Figure 63.

The reader is reminded that the shapes in Figure 50 are interpreted as representations of the shear stress distribution, which is assumed to be similar to the depth distribution (Ferguson, 2003). The *maximum variance solution*, associated with the triangular cross section, will be characterized by a cut-bank that is critically stable, since the meander amplitude is constant at equilibrium. This implies that natural rivers will tend to exhibit, on average, a larger variance in the shear stress distribution than predicted by the minimum variance solution and, as a result, will tend to inhabit lower channel slopes than those predicted by the usual formulation of the

regime model. Unfortunately, precise comparisons between theory and reality are impossible given the current uncertainty associated with the available sediment transport laws.

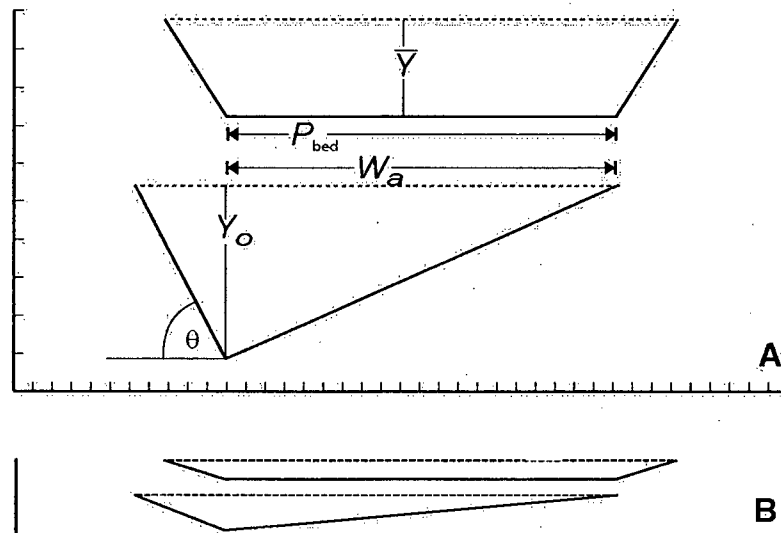


Figure 63: Geometry of the maximum variance regime solution. The minimum variance regime solution geometry is shown for comparison. (a) shows the two channel shapes with 4 times vertical exaggeration, and (b) at true scale.

### 6.2.1 The Maximum Variance Solution

It remains to be demonstrated that the maximum variance solution, in fact, exists. This solution is associated with an asymmetric cross sectional geometry, corresponding roughly to a bar face, pool and cut-bank morphology. The cut-bank must be stable, since this solution represents the meander apex, and it is assumed that the meander amplitude is constant at equilibrium. Both sediment and fluid continuity must be achieved. Additionally, the width of the section must be similar to the width of the trapezoidal solution, since large changes in channel width are not likely over short distances, and are seldom observed in the field, except when associated with large changes in the governing conditions.

The shear stress distribution in a bend is complicated (Bathurst et al., 1979) and no general theory for predicting it yet exists. Additionally, the existing sediment transport formulae are based on measurements taken under uniform flow conditions, and do not incorporate the effect of spatially variable shear force, bed topography or sediment texture. Therefore, one cannot specify

a realistic fluid or sediment transport flux without resorting to coupled numerical models of fluid flow and sediment transport, which are still in the developmental stage. As a consequence, one cannot reproduce anything like the actual cross section shape. Instead, uniform flow approximations are applied to a linear channel geometry to describe the shear stress distribution and the associated sediment transport field, just as in Chapter 5. In this case, the maximum variance solution is associated with a triangular channel geometry, comprising an active width,  $W_a$ , thalweg depth,  $Y_o$ , and cut-bank angle ( $\theta$ ) (Figure 63). As mentioned above, this is not critical, since the channel shape can properly be interpreted as a representation of the shear stress distribution, which should be similar to the depth distribution, but need not exhibit a one-to-one correspondence.

There are two key differences between regime solutions of this kind and those based on the standard trapezoidal geometry. The first difference is in the calculation of the sediment transport rate. Since the shear stress distribution in the maximum variance case is non-uniform, it is no longer sufficient to estimate transport based on the mean bed shear stress and scale it by the width of the bed (e.g. Equation 19 in Chapter 2) – the transport must be integrated cross the channel, as indicated by Equation 35 in Chapter 5. The second difference appears in the estimation of the shear stress acting on the channel bank. The original method for distributing shear stress between the bed and banks is based on a trapezoidal channel geometry, and cannot be applied to a triangular section. Furthermore, in estimating the sediment transport along the inner bank or bar face, one is making assumptions about the shear force acting there, and the bank stability analysis must be consistent with these assumptions to be valid.

**Sediment Transport:** The Meyer-Peter and Muller equation is used in this analysis, and the total transport is estimated by:

Equation 42..... 
$$Q_b = \left( \frac{\rho_s}{\rho_s - \rho} \right) \int_0^{x_c} \frac{\left( \frac{\tau(x)}{\gamma} - 0.047D \left( \frac{\gamma_s - \gamma}{\gamma} \right) \right)^{3/2}}{\left( 0.25/\rho \right) \left( \rho/g \right)^{1/3}} dx$$

where  $D$  is a characteristic grain size and  $\tau(x)$  represents the cross sectional shear stress distribution. Transport is assumed to occur only on the bar face;  $x = 0$  corresponds to the thalweg

location, and integration proceeds toward the bar top, until the limit  $\tau = \tau_c$  is encountered at  $x = x_c$ . The value of  $x_c$  depends on the slope, active width and thalweg depth of the cross section, and can be solved by combining the geometric definition of local depth  $\left( d(x) = Y_o - x \frac{Y_o}{W_a} \right)$  with the critical condition  $\left( \frac{\tau_c(x)}{\gamma} = 0.047D \left( \frac{\gamma_s - \gamma}{\gamma} \right) \right)$ . It is given by:

Equation 43 ..... 
$$x_c = \frac{W_a}{Y_o} \left( Y_o - 0.047D \left( \frac{\gamma_s - \gamma}{\gamma} \right) \frac{D}{S} \right)$$

The solution of a regime model that is further complicated by the presence of an integral is no easy task. Additionally, since one is interested in determining the maximum variance solution for a previously calculated, minimum variance solution, one is, in fact, operating the regime model in reverse. The standard approach, described in Chapter 2 holds the channel slope constant and maximizes the transport for that imposed slope. However, in this case total transport rate and discharge are held constant, and the minimum slope (assuming an asymmetric triangular channel) is identified. For this to be practical,  $S$  has to be expressed as a function of  $Q$ ,  $Q_b$  and the channel geometry.

The solution presented here is to first constrain part of the system, then obtain equations describing the change in  $Q_b$  as a function of the remaining, geometric, variables. Since channel width does not vary much between the riffles and pools in natural streams, the initial constraint imposed upon the system is the condition that the active width of the triangular section ( $W_a$ ) is equal to the active width of the trapezoidal section ( $P_{bed}$ ), as shown on Figure 63. Once  $W_a$  is specified (in addition to  $D$ ), estimating  $Q_b$  as a function of  $S$  and  $Y_o$  is relatively straightforward.

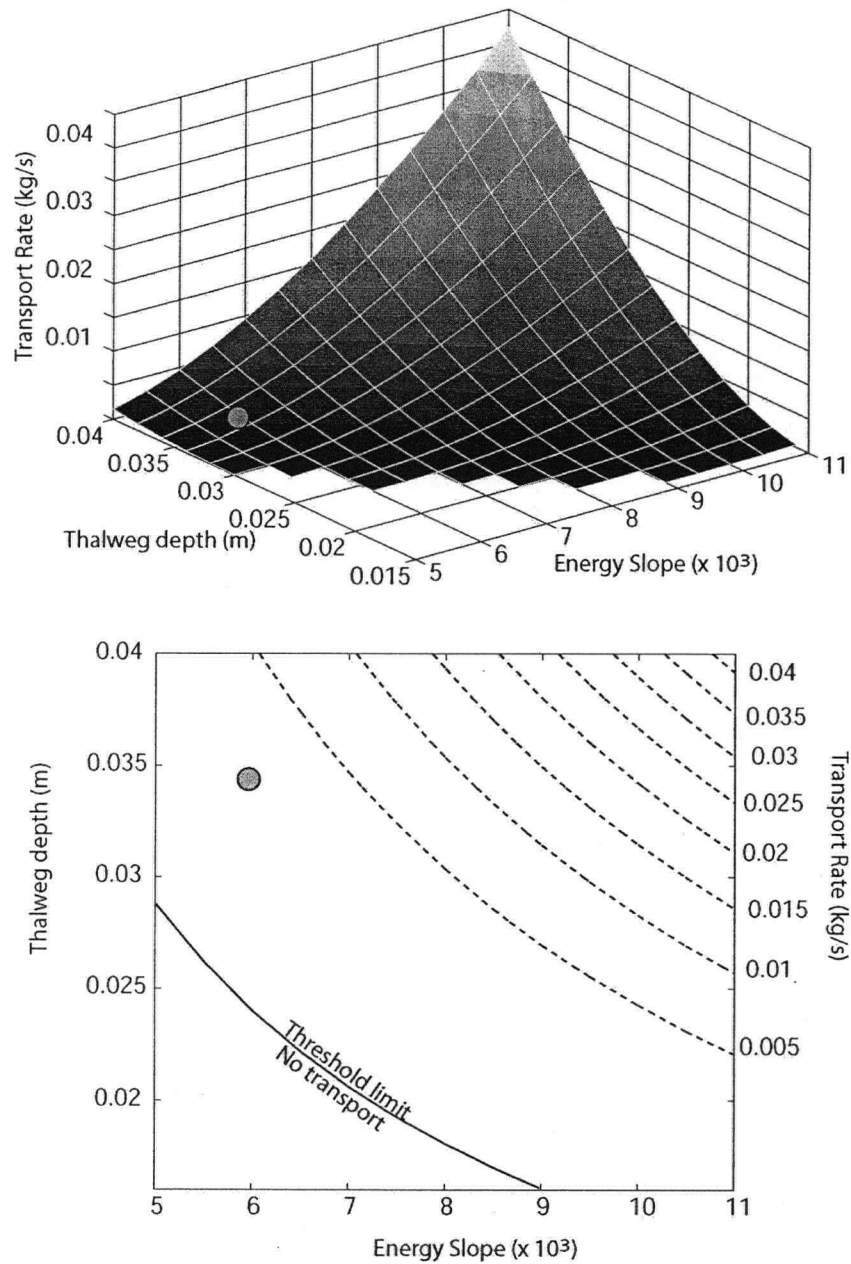


Figure 64: Sediment transport rate as a function of the thalweg depth ( $Y_o$ ) and the energy slope ( $S$ ), assuming an active width of 0.77 m. On the contour map in the lower panel, the threshold for zero transport is shown. The maximum variance solution for a sediment concentration of 0.63 g/L (see Table 12) is indicated on both panels with a grey circle.

The procedure is as follows. First, a range of possible values of  $Y_o$  is chosen, corresponding to a given minimum variance solution. For example, a minimum variance regime model fit approximately to the Phase 3 experiments described in Chapter 4 with an imposed channel slope of 0.011 m/m predicts a width of 0.77 m and a trapezoidal depth ( $\bar{Y}$ ) of 1.5 cm. An appropriate range for  $Y_o$  would then be about 1.5 cm to 4 cm, based on the observed difference between the thalweg depth in the pools and upon the riffles for the Phase 3 experiments. Similarly, an

appropriate range of channel slopes is chosen. Continuing with the example above, an appropriate range of slopes is 0.004 to 0.011 m/m. Then, the integration given above in Equation 36 is performed<sup>f</sup> for all possible combinations of  $S$  and  $Y_o$  within the specified ranges, producing a 3D surface of sediment transport rate, as shown in Figure 64. Along the contours of this surface, a given value of  $Q_b$  is satisfied by various combinations of  $S$  and  $Y_o$ . Somewhere along the contour for the desired transport rate, it is supposed that a cross sectional configuration can be found that satisfies both bank stability and flow continuity – the maximum variance solution. The problem now is reduced to describing the transport surface by equations that can be used in a regime formulation.

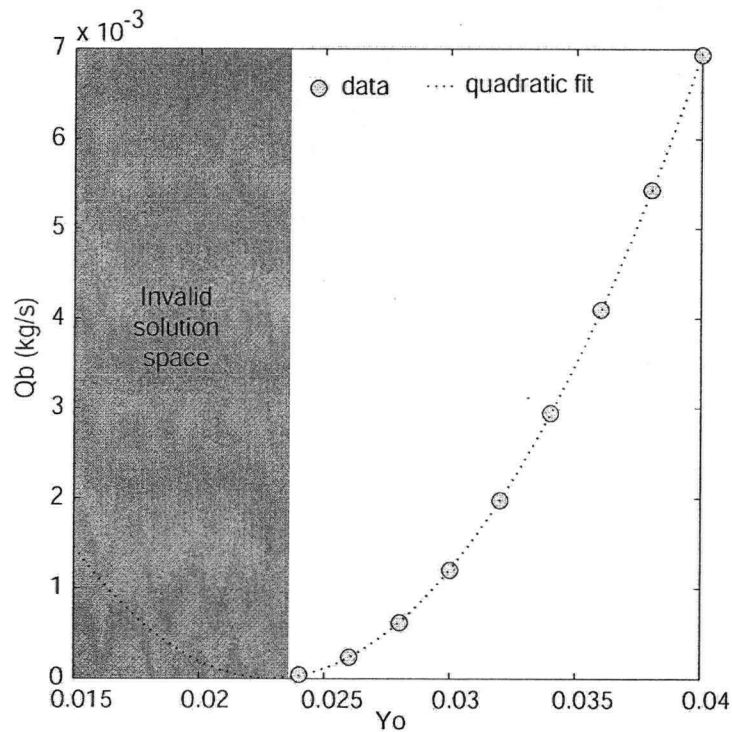


Figure 65: Calculated transport and the quadratic function fit to the data.  $W_a = 0.77$  m,  $S = 0.0065$  m/m,  $D = 2$  mm. The data represent points along a vertical section at  $S = 0.0065$  on Figure 64.

To achieve this,  $Q_b$  is plotted against  $Y_o$ , and functions of the form  $Q_b(Y_o)$  are fit to the data for each value of  $S$  in the range. In this analysis, quadratic equations described the data adequately well. A typical example is shown in Figure 65 for a width of 0.77 m and a slope of 0.0065 m/m.

<sup>f</sup> The integration was achieved using a numerical approach in the MATLAB programming environment.

This figure also demonstrates an important limitation to this approach: the solutions must fall within the specified range of the input arguments, or invalid solutions associated with the subsequent increase of  $Q_b$  beyond the range of the data may result. Put another way, when one realizes that Figure 65 represents the polynomial fit to the data along a vertical slice at  $S = 0.0065$  on Figure 64, it is clear that the upturn in  $Q_b$  below a slope of about 0.024 must be invalid since that region in Figure 64 is clearly below the threshold for entrainment.

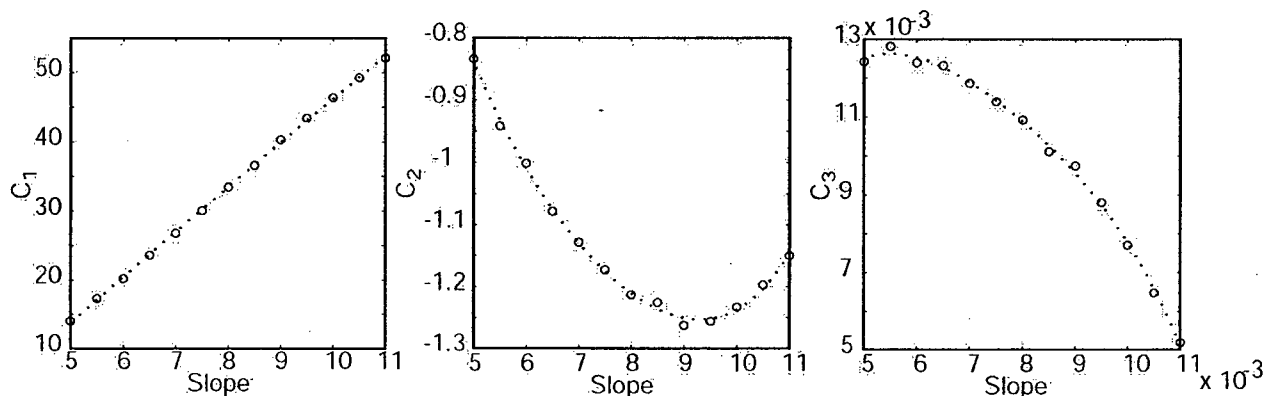


Figure 66: Coefficients for quadratic fits, assuming  $W_a = 0.77$  m and  $D = 2$  mm.

Once similar functions have been fitted to the data for each slope value in the range, the coefficients ( $C_1$ ,  $C_2$  and  $C_3$ ) for all of the fitted quadratic equations were plotted against  $S$ , and functions of the form  $C_i(S)$  were fitted to those data. Figure 66 presents the coefficients and the polynomial fits describing those coefficients as functions of  $S$ . Quadratic functions were fitted to the coefficient  $C_1$ , and fourth degree polynomials were fitted to coefficients  $C_2$  and  $C_3$ . The result is an expression for estimating sediment transport as a function of the channel geometry with the form:

Equation 44.....  $Q_b(Y_o, S) = C_1(S)Y_o^2 + C_2(S)Y_o + C_3(S)$

Individual equations are valid only for the imposed active width used to solve for  $Q_b$  over the ranges of  $Y_o$  and  $S$ .

**Evaluation of Bank Shear Stress:** The total shear force acting on the channel is given by the expression:

Equation 45.....  $F_{st} = \gamma PRS$

where  $P$  is the total wetted perimeter. One has already assumed that the shear force acting on the active width (or bar face) is adequately described by the uniform flow approximation, and thus accounts for a shear force equal to:

Equation 46.....  $F_{s1} = \gamma(W_o^2 + Y_o^2)^{1/2} \frac{Y_o}{2} S$

The residual shear force, then, is assigned to the cut-bank, and the mean shear stress is estimated by distributing this residual shear stress along the bank perimeter. So:

Equation 47.....  $\tau_{bank} = (F_{st} - F_{s1}) \frac{\cos\theta}{Y_o}$

More sophisticated estimation procedures are undoubtedly possible, but this one has the advantage of being self-consistent, since one begins by assuming that a certain proportion of the shear force is acting on the bar face. Any other approach for estimating the shear stress distribution that predicts either higher or lower shear stress on the cut-bank is tantamount to claiming that there is either more or less energy being dissipated within the channel than is consistent with Equation 45.

**6.2.2 Comparison of Minimum and Maximum Variance Solutions**

Once sediment transport functions of the form given in Equation 44 have been developed, the maximum variance regime solution can be determined. The maximum variance solution for the example presented above (trapezoidal slope = 0.011 m/m,  $P_{bed} = 0.77$  m,  $\bar{Y} = 1.5$  cm) is plotted on Figure 64 (yellow circle). Similar functions of the form  $Q_b(Y_o, S)$  were developed for active widths of 66, 71, 82, 86 and 90 cm, corresponding to standard regime solutions with slopes of 0.009, 0.01, 0.012, 0.013 and 0.014 m/m. These values represent the approximate range of

slopes and transport rates for the Phase 3 experiments discussed in Chapter 4. The results are summarized in Table 12, along with the data for the equivalent minimum variance states.

Table 12: Regime solution comparison

$Q_b/Q$ [g/L]	Minimum variance solution				$P_{beds} W_a$ [m]	Maximum variance solution				
	$S$ [m/m]	$Y_o$ [m]	$\theta$ [°]	$S$ [m/m]		$Y_o$ [m]	$\theta$ [°]	$x_c$ [m]	$x_c/W_a$ [%]	
1.93	0.0140	0.013	14.6	0.91	0.0096	0.026	8.1	0.40	44	
1.44	0.0130	0.013	14.2	0.86	0.0082	0.029	12.7	0.35	41	
1.00	0.0120	0.014	14.1	0.82	0.0070	0.031	17.0	0.30	37	
0.63	0.0110	0.015	14.0	0.77	0.0061	0.034	18.8	0.25	33	
0.33	0.0100	0.016	14.0	0.71	0.0055	0.036	19.9	0.22	31	
0.10	0.0090	0.017	13.9	0.66	0.0047	0.040	21.8	0.17	26	
<i>1.44</i>	<i>0.0130</i>	<i>0.013</i>	<i>14.2</i>	<i>0.66</i>	<i>0.0080</i>	<i>0.0310</i>	<i>7.9</i>	<i>0.29</i>	<i>44</i>	
<i>1.44</i>	<i>0.0130</i>	<i>0.013</i>	<i>14.2</i>	<i>0.71</i>	<i>0.0079</i>	<i>0.0308</i>	<i>9.7</i>	<i>0.31</i>	<i>44</i>	
<i>1.44</i>	<i>0.0130</i>	<i>0.013</i>	<i>14.2</i>	<i>0.77</i>	<i>0.0080</i>	<i>0.0301</i>	<i>10.9</i>	<i>0.32</i>	<i>42</i>	
<i>1.44</i>	<i>0.0130</i>	<i>0.013</i>	<i>14.2</i>	<i>0.82</i>	<i>0.0081</i>	<i>0.0294</i>	<i>11.9</i>	<i>0.34</i>	<i>41</i>	

Note: the sensitivity analysis results are shown in italics

In Figure 67, both solution slopes are plotted against sediment concentration. Clearly the local slope for a graded channel configuration can exhibit substantial variation, since the maximum variance slope tends to be about half the minimum variance slope. Channel slopes averaged over the scale of a meander wavelength – which represent the data typically available from field investigations and that collected during most stream table experiments – fall somewhere between these two limits. Clearly, then, when comparing standard (minimum variance) solutions against average channel slopes from natural rivers, a bias can be expected, since the minimum variance solution curve is an *upper limit* to the range of slopes that a channel will occupy.

Since the sediment transport rate for the maximum variance regime solutions was estimated from equations with the form given in Equation 44, rather than directly with Equation 42, there is the possibility that there exists some bias due to imperfections in the polynomial fits (see Figure 65 and Figure 66). Therefore, the slope and  $Y_o$  values for each maximum variance solution were used to evaluate the integral in Equation 42, to estimate the “true” predicted transport rate. The transport rates predicted directly from the integration are plotted against the transport rates predicted from the polynomial fits (Equation 44) in Figure 68. The transport rates are expressed as sediment concentrations in order to permit a direct comparison with Figure 67 and Table 12. A one-to-one line is also plotted on Figure 68. While there are detectable differences between the two values, the differences are small.

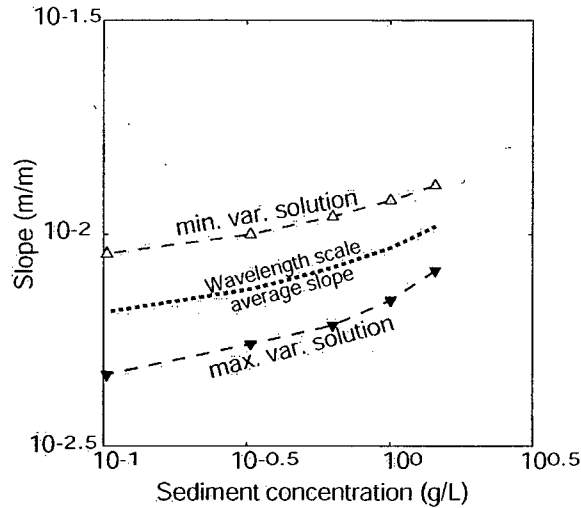


Figure 67: Slopes for the minimum variance and maximum variance solutions given in Table 12 are plotted against sediment concentration.

There is also the issue of the initial constraint on the active channel width. It is possible that the active width in a maximum variance section may tend to be narrower than for a minimum variance section, though it is unlikely to be wider. To evaluate the sensitivity of the maximum variance solutions to the specified active width, a range of narrower active widths was imposed for the solution corresponding to  $Q_b/Q = 1.44$  g/L, and the change in the solution parameters documented (Table 12). The effect of reducing the active width by up to 25% is shown in Figure 69. As  $W_a$  is reduced, the slope required to transport the imposed sediment load declines, but only marginally (<3.5% of the original value, in all cases). The thalweg depth increases somewhat more appreciably, but still the largest increase is less than 10% of the original value. This adjustment most likely reflects the constraints of flow continuity. Bearing in mind that the solution slopes for the minimum and maximum variance solutions differ by a factor of 2, it appears that the maximum variance solutions derived in the manner described above are not overly sensitive to the assumptions upon which the procedure is based, and one may have some confidence that the minimum variance slope, at least, is faithfully represented by the values reported in Table 12.

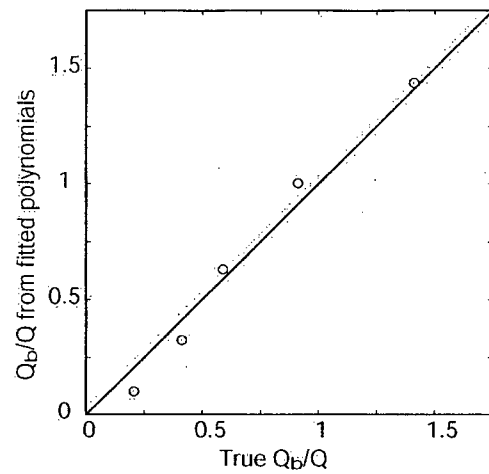


Figure 68: The sediment concentration based on the polynomial fits that describe  $Q_b$  as a function of  $S$  and  $Y_o$ , is plotted against the sediment concentration based on evaluation of Equation 42 using the values of  $Y_o$  and  $S$  in Table 12. A one-to-one line is also shown.

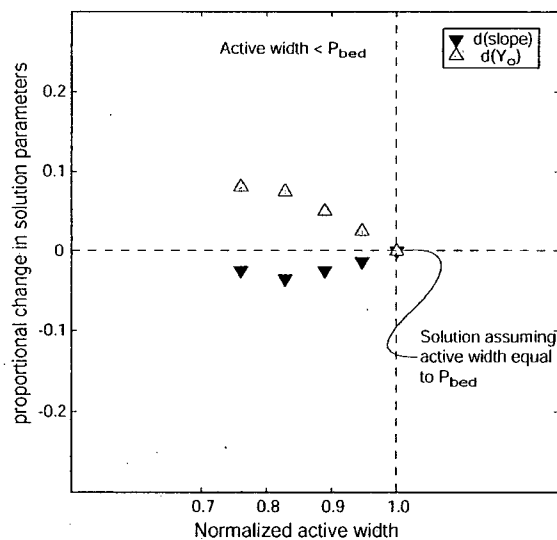


Figure 69: A sensitivity analysis of the maximum variance solution to the imposed value of  $W_a$ . The proportional change in slope and  $Y_o$  is plotted against the normalized  $W_a$ . The initial assumption of  $W_a = P_{bed}$  corresponds to a normalized width of 1.

There is an additional point to be made about the issue of the active width. The width of the bar face is specified, and is called the active width. In fact, it is the potentially active width, and transport may be limited to only part of it. In Table 12, the actual width over which transport is occurring is given. It is equivalent to the critical distance,  $x_c$ , defined by Equation 43. The proportion of the bar face over which transport is occurring varies from about 45% of  $W_a$  for the highest sediment concentration to about 25% for the lowest. The results of the sensitivity

analysis described above indicate that the change in the actual width of the transport zone is relatively conservative, varying from 41% to 44% of  $W_a$  (see Table 12).

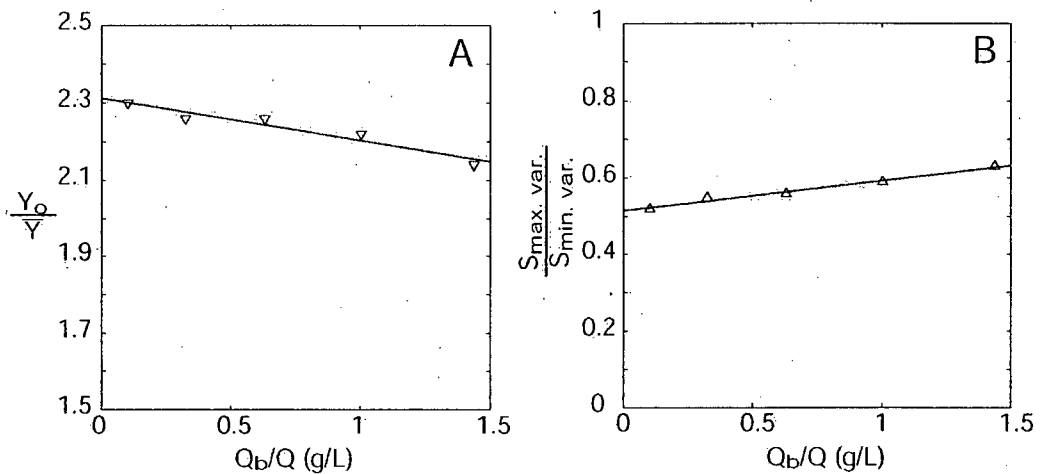


Figure 70: a) the ratio of thalweg depth ( $Y_o$ ) to trapezoid depth ( $\bar{Y}$ ) is plotted against sediment concentration. b) the ratio of the maximum variance slope to the minimum variance slope is plotted against sediment concentration.

Some interesting patterns emerge from a comparison of the two solution states for the same governing conditions presented in Table 12. When the ratio of the thalweg depth for the maximum variance solution ( $Y_o$ ) to the trapezoid depth ( $\bar{Y}$ ) is plotted against sediment concentration, a progressive decline becomes evident (Figure 70a). Similarly the ratio of the slopes indicates a progressive decrease in the difference between the maximum and minimum variance solutions (Figure 70b).

The behaviour evident in Figure 70 may represent the effect of the different shear stress partitioning procedures for the two solution types. To assess this, the ratio of the predicted bank shear stress to the average cross sectional shear stress was plotted against sediment concentration for all the solution pairs in Table 12. Since the two partitioning methods produce divergent trends, there is reason to believe that this may be part of the underlying cause. The divergent trends are also likely related to the diminishing importance of the variance of the shear stress distribution on the sediment transport capacity with increased average shear stress. This effect is clear in Figure 56, where the feedback intensity (related to the difference in transport capacity for different channel shapes with the same channel slope) declines with increasing shear stress. Since the trends shown in Figure 70 may be a product of the specification of the model, one

cannot be certain that they actually represent a physical process. So, the most conservative interpretation of the modelled results is that the trends actually represent a range of possible solutions.

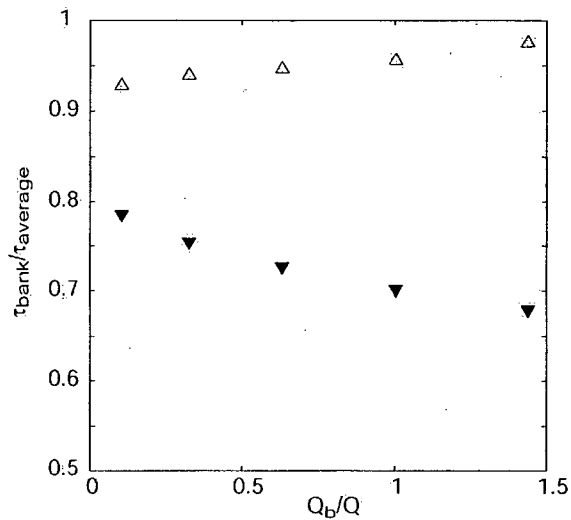


Figure 71: Ratio of predicted shear stress acting on the channel bank(s) to the average cross sectional shear stress. The maximum variance solutions are shown with the upward pointing triangles, the minimum variance solutions with the downward triangles.

### 6.2.3 Comparison with Experimental Results

The results above can be compared with the results from the Phase 3 experiments. The average maximum local slope and the average minimum local slope (per half meander wavelength) were calculated for each experiment (Figure 72). While there is considerable scatter in the minimum and maximum local slope estimates, there are consistent linear trends evident in the data. Similarly, the average thalweg depth at each apex section and the average channel depth were calculated for each experiment, though these data show no clear pattern of variation with sediment concentration (not shown).

The average ratio of the thalweg depth to the mean cross section depth at each apex cross section was then calculated. This is conceptually similar to the ratio  $Y_o/\bar{Y}$  in Figure 70. Similarly, the ratio of highest and the lowest local slopes (Figure 72) was used to estimate the mean slope ratio for each experiment (similar to  $S_{max}/S_{min}$ , Figure 70).

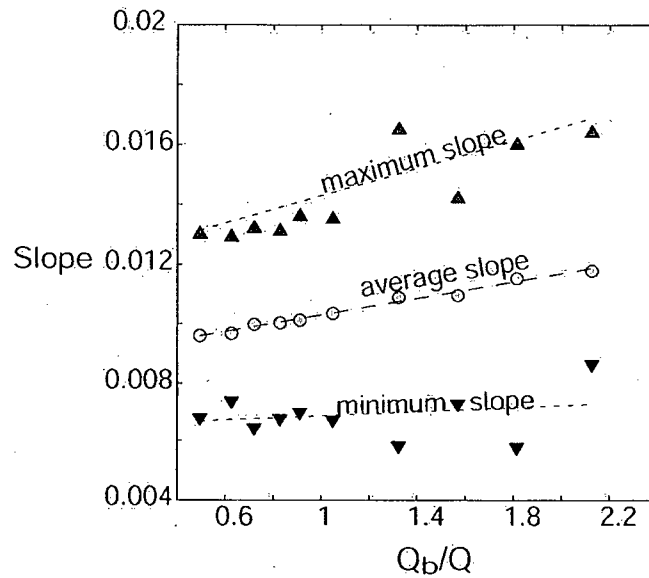


Figure 72: Measured average maximum and minimum slopes per half wavelength for the phase 3 experiments. The average slopes are shown for reference. The dashed lines represent linear fits to the data.

The ratios for the experiments are compared against the theoretical predictions (presented in Table 12) in Figure 73. In panel A, the independent variable is sediment concentration. However, since we have already made the point that sediment transport formulae are at best scale representations of the actual phenomenon, this is a potentially flawed comparison. A more appropriate comparison is shown in panel B, where the ratios are plotted against the mean channel slope, which produces nearly the same result. The mean slope for the regime model is estimated to be the arithmetic average of maximum variance slope and the minimum variance slope. Both plots show the same general relation, however. The observed ratios are generally similar to the range of ratios predicted by the regime model. There seems to be a systematic over prediction of the ratio of the local slopes by the regime model, but the difference is relatively slight (~12%), and is hardly surprising, given: (i) the rather simplified nature of the regime model; and (ii) the relatively wide spacing of topographic data used to estimate the local slope<sup>g</sup>. There is no evident support for the predicted change in the ratios with increasing sediment concentration or channel slope. In fact, the experimental data, though scattered, tend to imply

<sup>g</sup> There were 9 measurements of water surface elevation per meander wavelength, which is satisfactory for estimating the reach-average slope, but less than ideal for estimating the local minimum and maximum slopes.

trends in opposite directions, where the slope ratio declines with increasing sediment concentration, while the depth ratio increases.

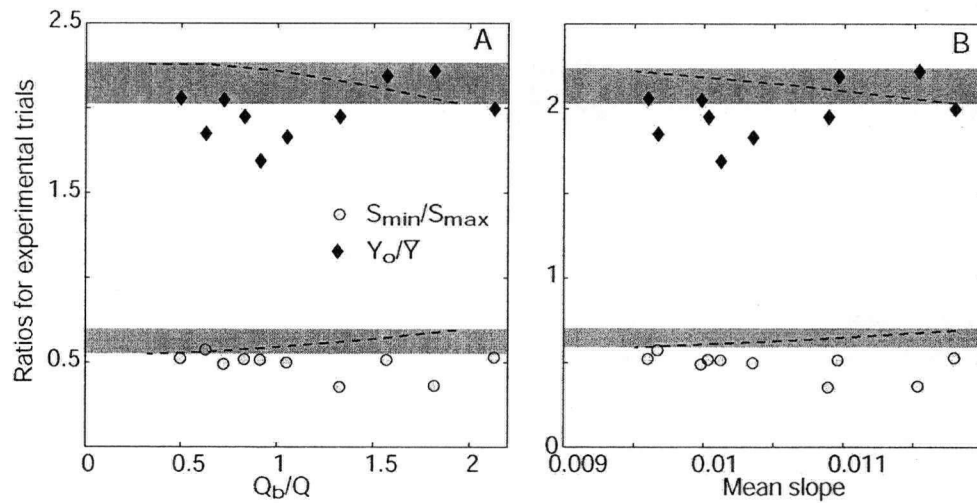


Figure 73: Ratios of the local slopes and depths from the Phase 3 experiments. The ratio of the local minimum slope to the local maximum slope and the ratio of the thalweg depth to the average depth are plotted against sediment concentration (a), and mean channel slope (b). The analogous ratios predicted by the regime model (shown in Figure 70) are reproduced as dashed lines.

Nevertheless, the close correspondence between the experimental results and the range of the theoretical predictions implies that the maximum/minimum variance approach to understanding local channel geometry captures an important component of the system behaviour, albeit in a simplified form. If, in fact, the trends in the theoretical ratios do represent a physical process, then some other aspect of the system behaviour (possibly related to the 3D pattern of fluid force and sediment transport) overwhelms it. It seems more likely that they represent the effect of different shear stress partitioning and bank stability assessment approaches.

Rational regime models are reasonable and flexible choices for describing the potential adjustments of alluvial streams to changes in the governing conditions at the scale of a channel reach. The key is the identification of a physically sound optimality criterion that embraces a sufficiently wide range of possible channel responses. The best candidate that we have identified is the maximization of flow resistance for the fluvial system, which embraces a broader range of possible system adjustments than the previously proposed criteria. System-scale flow resistance embraces three scales of alluvial response: (i) grain-scale resistance,  $f'$ ; (ii) bedform-scale form resistance,  $f''$ ; and (iii) reach-scale form resistance,  $f'''$ . Since the existence of more than one degree of freedom for channel response permits the existence of multiple equilibria, such models may have little predictive power for understanding channel response to changes in the governing conditions. In particular, the development of a predictive relation for determining  $f''$  seems to be the main obstacle. But regime models do have postdictive power, in that they can be used to understand the channel response, once it has occurred and  $f''$  is known. They also provide a means to decide whether or not an observed response represents a patently non-equilibrium behaviour (which is the common interpretation of complex fluvial behaviour), or an equilibrium behaviour moderated by variable governing conditions.

The numerical analysis presented in Chapter 2 demonstrates that there exists a range over which different optimality criteria produce similar scaling relations. Thus, when considering the geometry of wide channels in non-cohesive material, the choice of optimization is not crucial. However, as bank strength increases and  $W/d$  ratio decreases, there are significant differences between the optimizations based on fluid force (MUSP and MSS) and the optimizations based on sediment transport capacity (MTC), as shown in Figure 8. Furthermore, differences among the MTC optimizations may arise for very strong banks as the result of the choice of sediment transport formula, implying that transport formulae are incomplete correlations. Fortunately, most gravel-bed rivers do not exhibit such strong banks, and this issue may often be irrelevant in channels dominated by bedload transport.

The most general form of the response model is represented by a dimensionless alluvial state-space based on the equilibrium channel dimensions predicted by the regime model (Figure 12). At one level, all predictions, regardless of specific values of  $Q$ ,  $D$  or  $S$ , can be collapsed onto unique functions relating the aspect ratio,  $W/d$ , to dimensionless shear stress ( $\tau^*$ ) for specified

values of bank strength ( $\phi$ ). Furthermore, each point ( $W/d, \tau^*$ ) represents a set of channels with a wide range of relative roughness values which, in turn, are associated with unique functions predicting  $S$ ,  $Fr$  and  $Q_b/Q$ . The alluvial state, then, is represented by a plane in the 3-dimensional space ( $W/d, D/d, \tau^*$  or  $S$ ), for which each point represents all channels that exhibit Froude similarity. Within the alluvial state space defined by the model, the meandering-braiding threshold proposed by Parker (1976) is used to define the limit of applicability of the model, which purports to describe only single thread channels.

Previously published data are consistent with the structure of the alluvial state-space implied by the model, though they do not represent critical tests because it is not possible to determine the value of key parameters such as  $\phi'$ . Nonetheless, the data behave as one would expect based on the model, since the range of channel positions in the ( $W/d, \tau^*$ ) plane is consistent with the range that would occur if one assumes that natural rivers exhibit a range of bank strengths. Furthermore, the scaling exhibited in laboratory experiments, where the bank friction angle is approximately known, is well described by the model.

Additional tests of the theory were conducted using physical models of a generic, meandering gravel bed stream. Physical models are powerful tools for the study of complex natural phenomena. Their power derives from the fact that they are natural systems, not numerically generated approximations of them. There are some scaling issues that do affect the applicability of the models. These issues have no bearing on the *truth* of such physical models, since they are natural systems in their own right, but they do impact the relation between a model and its field prototype.

Essentially, the physical models discussed in Chapter 4 represent the bedload component of a prototype, having all suspended load deposits stripped away. Herein lies an important scale mediated distortion, since those particles that typically form the upper parts of the fluvial stratigraphy are absent from the model. The absence of this "floodplain load", as well as the absence of vegetation and cohesive sediment, has the consequence that the physical model cannot reproduce the processes of bank advance that act in the field prototype. As a result, the physical model can persist as a single thread channel only until meander progression encounters the incompletely formed bar tops where a fully formed floodplain deposit would exist in the field analogue. At this point, the sedimentological differences between the model and the intended prototype overwhelm the process similarities and the single thread pattern gives way to a

multiple thread form where its prototype would not. Interpretation of the results from physical models must be tempered with this understanding of the relation between model and prototype, since it guides our expectations of where similarities and differences between the two may exist.

The analysis of the Phase 3 experiments is based on the assumption that the thalweg path in the model represents something close to the prototype channel path, and that the thalweg slope represents a quantity that is adjusted to produce an equilibrium channel configuration. The equilibrium water surface slope (along the thalweg) is functionally determined by the governing conditions  $Q$  and  $Q_b$ , as proposed by Mackin (1948) and Lane (1957), the experimental base remaining rather narrow, and is considered to represent a regime (or graded) slope ( $S_{reg}$ ). It also represents an index of the reach-scale flow resistance proposed in Chapter 2, and appears to be the dominant component of the system-scale adjustment of flow resistance, which we argue is maximized as alluvial systems approach equilibrium. There appears to be a similar scaling of the effective width and depth with the governing conditions, consistent with the predictions of a regime model, but the matter is complicated by the absence of bank advance in the physical model.

Our experiments demonstrate that  $S_{reg}$  may be approached either by vertical degradation or by lateral erosion leading to increased sinuosity. The system may initially respond by degrading vertically with little change in the channel sinuosity or channel pattern. However, once  $S$  approaches  $S_{reg}$  by this degradational mechanism, sediment begins to deposit locally in the channel, and lateral deformation is initiated. Under the appropriate initial conditions, the adjustment may be entirely lateral. Regardless of the response trajectory, channel slope is the primary adjustable variable producing a maximization of the system scale flow resistance when the banks are relatively erodible, which is consistent with the concept of the graded stream advanced by Mackin (1948).

Once the capacity of the reach scale flow resistance to adjust is constrained by fixing the bank locations, slope changes cease to be the dominant response producing equilibrium. Instead, the Phase 4 experiments – which investigated the response of a fixed bank, mobile bed physical model to changes in the governing conditions – reveal that surface texture (and thereby grain-scale flow resistance) adjustments appear to dominate the system response, while channel slope remains nearly constant. As sediment concentration increases, the surface progressively fines: this relation is clearly demonstrated in Table 10 using regressions of armour ratio (based on three

characteristic grain size indices) against the governing conditions ( $Q_b/Q$ ). Interestingly, the cross sectional shape for these experiments seems to be independent of the sediment concentration. Indeed, the adjustment of the cross sectional form seems to be a trailing phenomenon, determined primarily by the bank alignment (if this turns out to be true, it may a relatively simple matter to combine rules governing when  $f'$  and  $f'''$  tend to dominate the system response, and thereby increase the predictive power of regime models). Thus,  $f''$  would appear to be determined by the reach-scale flow resistance ( $f'''$ ), with the grain-scale resistance ( $f'$ ) seemingly the only other independent system parameter.

The graded response evident in the Phase 3 data is bound by thresholds beyond which the graded relation breaks down. Between these thresholds,  $S$  can be predicted by the sediment concentration,  $Q_b/Q$ . The implication is that the Phase 3 results are restricted to alluvial channels with similar characteristics, and with erodible channel banks. The lower threshold is associated with a competence limitation, and the upper threshold appears to be related to a maximum permissible sediment influx rate.

In fact, both the Phase 3 and the Phase 4 experiments indicate that some sort of sediment influx threshold exists. For the Phase 3 experiments, it was not possible to achieve steady state transport for sediment concentrations greater than about 2.4 g/L, and the system seemed to react via a compound response comprising fan-style deposition upstream of the study reach and more-or-less graded style channel behaviour in the study reach in response to a reduced local sediment supply. Above a sediment concentration of about 1.3 g/L, Phase 4 channels were unable to achieve equilibrium without aggrading, and thereby increasing the channel slope. Beyond this threshold, the surface texture for the Phase 4 channels ceased to change appreciably. Given that a similar (but statistically insignificant) negative correlation between armour ratio and sediment concentration is evident for the Phase 3 experiments up to the Phase 3 sediment influx threshold (see Section 4.2.5), beyond which little discernable textural adjustment occurs, it is quite possible that both thresholds represent aspects of the same dynamic.

For channels that are similar to the Phase 3 prototype, slope is adjusted, relative to  $S_v$ , mainly by changing the channel sinuosity, and a range of graded channels can exist for a given  $S_v$  in accordance with a four-fold range of sediment concentration. That is, there is no unique pairing of sediment concentration and valley slope, contra the suggestion of Schumm and Khan (1972), and the degree of channel sinuosity depends on the sediment concentration for a given  $S_v$ . Within

this four-fold range of sediment concentration, our experimental results suggest that changes in  $Q_b/Q$  will produce channel adjustments consistent with the regime relation summarized in Equation 31, primarily by changing the channel sinuosity, unless the geomorphic history of the system and/or particularly inerodible boundaries render this response inaccessible. However, sand bed rivers, where the bed material is fully mobile for much of the year and where bank stability controls the system dynamics, may exhibit quite different behaviour, involving aspects of the response documented during Phase 4. Gravel bed rivers confined between relatively resistant valley walls will also tend to respond preferentially via surface texture changes. Similarly, in (steep) channels where locked arrangements of individual particles dominate, the dynamics are very different, though the principle of system-scale flow resistance maximization, proposed in Chapter 2 may still hold.

By changing the scale of inquiry from the reach-scale to the scale of individual morphologic units, one can gain an understanding of the optimality criterion necessary to complete the regime formulation presented in Chapter 2, and evident in the graded channel response documented in Chapter 4. In Chapter 2, the optimality criterion was interpreted as a maximization of the system scale flow resistance, which is conceptually equivalent to a potential energy well. The principle of resistance maximization can be explained by a simplified theoretical model relating transport capacity to the variance of the transverse shear stress distribution, which implies the existence of a feedback mechanism that acts to reduce the channel slope in bedload-dominated channels: slight initial variations in the shear stress distribution result in local net scour, which increases the local transport capacity by increasing the variance of the shear stress distribution, which leads to further local net scour, and so on. The local net scour may be primarily vertical until the channel banks begin to fail, at which point the scour will produce a lateral shift of the channel and initiate the negative feedback between bank erosion and local transport capacity by changing the channel sinuosity and slope. If one assumes that the sediment supply to the fluvial system is equivalent to  $\overline{TC}$  for an initial rectangular channel configuration, then the channel slope,  $S$ , cannot remain constant for long since more material is leaving the system than entering, at least at the locally asymmetric sections. The system adjusts by eroding the channel bed and ultimately the channel banks, thereby changing  $S$ .

Once one initial bend develops, others necessarily follow, because of the non-uniform cross sectional distribution of sediment transport. That is, the local increase in sediment transport

resulting from the net scour at an asymmetric cross section will induce significant divergence in the sediment flux field, expressed as periodic deposition downstream on alternate sides of the channel. Order is generated in the system by alternating cycles of erosion and deposition on either side of the channel. The longitudinal scale for this cycle can be modelled as the product of the diffusion of a sediment wave across the channel, moving laterally at a speed similar to that for a gravity wave. The initiation of meandering, then, is proposed to be related to the characteristics of the sediment transport field: the secondary circulation flow structure that is closely related to the meandering pattern is thought to be a trailing phenomenon that develops as a consequence of the sediment transport field dynamics, but which ultimately influences the equilibrium channel form.

Based on the feedback process, we can identify two features of an equilibrium produced this way, beyond the definitive equality of local transport capacity and sediment supply. First, if a constant meander amplitude is reached, then the cut-bank at the bend apex must be critically stable. In the sequence of events described by Figure 57 and Figure 58, the shear stress exerted on the bank at equilibrium must be equal to the critical value of bank erosion, and hence at the threshold of further retreat. This may not be generally true in the field, where the channel configuration may be approached by a more complicated sequence of process-form interactions resulting from time-varying fluid and mass fluxes, but it is reasonable to expect cut-banks to be near the threshold of motion, at least more so than banks elsewhere. In any case, this condition appears to characterize equilibrium laboratory channels, where a reduction in the sediment supply results in the onset of additional bank erosion, as predicted by the feedback argument. Clearly, bank stability is a key feature of equilibrium.

The second point relates to the shear stress distribution. A channel formed in erodible material has some maximum limit to the variance in the shear stress that can be sustained without the bed failing, just as banks can withstand only a certain shear stress before bank retreat occurs. That is, there is some configuration at which the variance is maximized and beyond which the boundary will fail, thereby reducing the variance. In our framework, this is equivalent to maximizing  $\beta$  by maximizing  $Y_o$ , subject to the strength of the channel boundary. However, since – for a specified slope – an increase in variance will produce an increase in  $TC$ , the system will tend to exhibit a maximum variance consistent with cross sectional stability. If the variance is not maximized, then there is still scope for the positive feedback shown in Figure 58 to act on the system, causing

further deformation and increasing  $\beta$ . Therefore the equilibrium channel configuration will be characterized by cut banks at the apices which are at the threshold of movement and by a cross sectional shape that exhibits the maximum variance that can be supported by the bed material. Incidentally, this is the most natural way of understanding the apparent dependence of  $f''$  on  $f'''$ .

However, since cross-overs between two apices will have a lower  $\beta$ , the feedback mechanism described above implies that water surface slope must vary systematically downstream in order to maintain a steady state mass flux throughout the system. Experimental observations from stream table experiments and from fixed bank physical models support this implication. The theory also predicts that the strength of the feedback mechanism falls off rapidly as excess shear stress increases. This is consistent with the observed time-to-equilibrium for laboratory experiments for a range of initial shear stresses. The theory is also consistent with the response of experimental equilibrium channels when the sediment supply was reduced, which re-initiated meander amplitude increases and resulted in slope reduction.

In all of the Phase 3 experiments presented in Chapter 4, the equilibrium channel form was produced by reducing the channel slope. The equilibrium slope achieved is functionally determined by the sediment concentration, while other possible adjustments, such as changes in the resistance coefficients (e.g. Manning's  $n$ ), could not be identified. This slope minimizing behaviour is the product of the initiation and development of pools on alternating sides of the channel. In this way, a three-dimensional interaction amongst channel morphology, local hydraulics and sediment transport responsible for pool growth informs the one-dimensional properties of the fluvial system, and produces the observed SMB. SMB is consistent with the cross-scale linkage described by the feedback mechanism that occurs between the width-scale variables  $Y_o$  and  $\beta$  and the length scale variables  $P$  and  $S$ .

Since SMB is similar to the behaviour predicted by the minimum slope hypothesis (and by extension, all analogous optimality criteria), the process-form interactions embodied in the feedback mechanisms suggest a physically based, rational interpretation of what such hypotheses actually represent. Regime models are one dimensional, and since they cannot explicitly consider the transverse distribution of shear stress, they cannot distinguish which solution among the many possible solutions admitted by the model is actually stable in a three dimensional fluvial system. That is, they cannot explicitly describe the self-forming action of the fluvial

system. The selection of a single, stable solution is accomplished by application of an optimality criterion, which – far from being some mystical new law of physics – simply facilitates the description of a three-dimensional reality by a one dimensional model.

The feedback explicitly invokes bank stability in the generation of an equilibrium channel form, and makes clear the necessity of such constraints in regime models, such as those described by Millar and Quick (1993; 1998). A properly constrained regime model approximates the action of SMB and incorporates the important role of bank stability in determining the resultant channel configurations, and therefore represents many of the important processes determining channel pattern, despite being one-dimensional.

However, the regime approach can be reformulated and applied to individual morphologic units, as well. An additional solution for a set of governing conditions ( $Q$ ,  $Q_b$  and  $D$ ) can be produced, assuming a triangular channel geometry, similar to that employed in the analysis of the feedback mechanism described in Chapter 5. These solutions, referred to as the maximum variance solutions since they represent the maximum cross sectional shear stress variance, have slopes that are roughly half those predicted by a regime model assuming a trapezoidal cross section (the minimum variance solution). The thalweg depths predicted by the maximum variance solutions are typically about twice the mean depth predicted by the minimum variance solutions. For a given set of governing conditions, these two solutions represent the bounds on the local slopes and channel geometries. The minimum variance solutions are interpreted in the context not as representations of the average reach-scale channel dimensions, but as the typical riffle dimensions. The maximum variance solutions are interpreted as the channel cross sections at the apices of the meander bends, which are generally assumed to correspond to a bar-pool type section.

Comparisons of the ratios of these two limits with analogous ratios for the experimental channels described in Chapter 4 reveal a fair correspondence. The observed ratio of the maximum and minimum local slopes is about the same as that predicted by the two regime solutions, as is the ratio of the thalweg depth and the mean channel depth. Given this support for the regime approach applied at the local scale, one can use the two solution types as bounding conditions, and proceed to develop an understanding of meandering as a metastable condition.

At the reach-scale, stability is argued to result from the maximization of the system scale flow resistance, and the minimization of the available energy to deform the system. However, at the

scale of morphologic units, stability is conditional, at best, and there appears to be a continual oscillation between various states along the stream channel and over time. It was previously argued in Chapter 5 that the minimum variance solution is inherently unstable as a result of the implicit uniform shear stress distribution. However, a maximum variance solution with the associated asymmetric cross sectional form is also unstable. Transitions from minimum variance states to maximum variance states are achieved by changing the channel path length, and thereby lowering the channel gradient. They become intimately linked with the centripetal acceleration of flow around a bend, and the development of secondary circulation currents as a result. When the centripetal acceleration ceases and the secondary currents weaken, sediment that was tracking along the bar face descends and deposits around the thalweg reducing the cross channel shear stress variance and necessitating an increased slope to transport the incoming sediment. That is, the maximum variance solutions are stable, conditional on the existence of sufficient centripetal acceleration to maintain their asymmetric cross sectional form.

This dynamic can be understood using the analogy of electromagnetic dipoles. Consider the maximum variance state as being an attractor that has a spatial direction, or polarity. The spatiotemporal pattern of channel adjustment involves the attainment of a maximum variance state with one polarity (a triangular cross section with the thalweg along the right bank, for example), followed by the abandonment of that state for one with a nearly uniform shear stress distribution, and ultimately followed by the development of a maximum variance state with the opposite polarity (thalweg along the left bank) (Figure 74).

There is no single, stable state: alluvial streams maintain stability by oscillating between the trapezoidal, minimum variance solution and the triangular, maximum variance solution or, more properly, by oscillating between two maximum variance attractor states with opposite polarity, with the minimum variance state being occupied during the transition between the two. Thus, meandering can be viewed as a metastable dynamic, produced by the attraction toward the maximum variance conditions which are conditionally stable, provided that a sufficient centripetal acceleration produces the required flow structure necessary to maintain an asymmetric cross section. This oscillation is responsible for the characteristic pattern of alternating pools with asymmetric cross sectional shear stress distributions having a large variance, separated by riffles, where the shear stress distribution is generally more uniform. This can be interpreted as a

spatial oscillation along the path of sediment and fluid flux, or alternatively as a temporal oscillation at a fixed point, produced by the downstream migration of the meander form.

Where the banks are sufficiently resistant, and/or the entire width of the channel is actively degrading, the feedback may take on a symmetrical, non-uniform shape, resulting in vertical incision, rather than a lateral planform adjustment. In this case, the metastable, oscillating pattern may tend to be suppressed, and the channel may remain relatively straight as it incises. Indeed, there may be a limit beyond which the lateral planform adjustment is not capable of producing an equilibrium channel form, as implied by the nature of the feedback surface shown in Figure 56. Additionally, the maximum degree of sinuosity is limited by both the width of the alluvial valley and the maximum channel curvature that the bank materials can sustain. If, for example, the sediment supply falls below that associated with this maximum degree of sinuosity, then the system must adjust by vertically incising, unless it is moderated by the progressive coarsening of the surface sediment, as observed in the Phase 4 experiments. A compound response, involving both vertical degradation and surface texture adjustment has been well documented in the field (Talbot and Lapointe, 2002a).

What began as an inquiry into the potential to model channel response has led to an understanding of channel stability and the cause of the establishment meandering and of the associated riffle-pool morphology in bedload streams. Since channel response is, in fact, a manifestation of the processes producing stability, this is hardly surprising. What is somewhat surprising is the critical role of scale. Understanding of the process-form interactions is highly dependent on the scale of the form being investigated. At the scale of a channel reach, where the fluvial morphology is reduced to 1D descriptors, stability can be viewed as the product of maximization of the flow resistance. This is the realm in which optimality criteria apply: the traditional distaste (e.g. Griffiths, 1984) for such criteria seems to originate from the failure to adequately resolve the scale-process-form issues which Howard (1988) warns can obscure any functional relation. At the scale of individual morphologic units, the process by which the maximization of flow resistance is achieved can be understood by the interaction between local scour, local transport capacity and channel morphology.

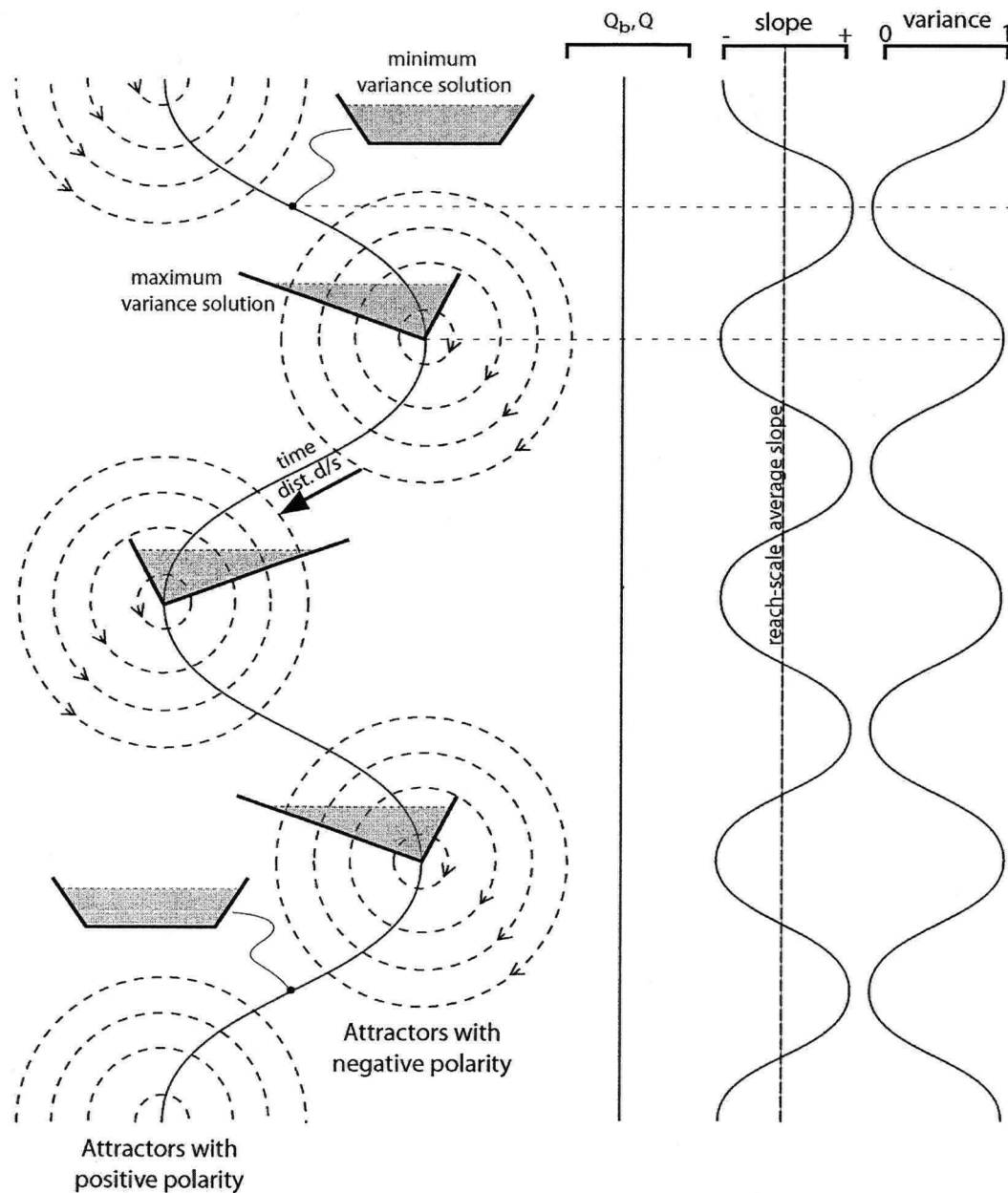


Figure 74: Meandering as a product of oscillation between maximum variance attractor states with opposite polarity. The associated patterns of change for the local slope and cross sectional shear stress variance are shown on the right (variance = 0 implies a uniform shear stress distribution, while variance = 1 implies the maximum variance of the shear stress distribution).

- Ackers P, Charlton FG. 1970. The slope and resistance of small meandering channels. *Proceedings of the Institute of Civil Engineers Supplemental XV*: 349-370.
- Allen JRL. 1994. Fundamental properties of fluids and their relation to sediment transport processes. In *Sediment Transport and Depositional Processes*, Pye K (ed). Blackwell: Oxford: 25-60.
- Anderson AG. 1967. On the development of stream meanders. *Proceedings of the 12th Congress, International Association of Hydraulic Research*. Fort Collins: 370-378.
- Andrews ED. 1984. Bed material entrainment and the hydraulic geometry of gravel-bed rivers in Colorado. *Geological Society of America Bulletin* **95**(3): 371-378.
- Ashmore P. 1982. Laboratory modelling of gravel braided stream morphology. *Earth Surface Processes and Landforms* **7**: 201-225.
- Ashmore P. 1991. Channel morphology and bed load pulses in braided, gravel-bed streams. *Geografiska Annaler* **73**: 37-52.
- Bathurst JC, Thorne CR, Hey RD. 1979. Secondary flow and shear stress at river bends. *Journal of the Hydraulics Division-Asce* **105**(HY10): 1277-1295.
- Begin ZB. 1981. The relationship between flow-shear stress and stream pattern. *Journal of Hydrology* **52**: 307-319.
- Blench T. 1969. *Mobile-Bed Fluviology*. The University of Alberta Press, Edmonton.
- Blondeaux P, Seminara G. 1985. A unified bar-bed theory of river meanders. *Journal of Fluid Mechanics* **157**: 449-470.
- Bray DI. 1975. Representative discharges for gravel-bed rivers in Alberta, Canada. *Journal of Hydrology* **27**: 143-153.
- Bridge JS. 1977. Flow, bed topography, grain size and sedimentary structure in open channel bends: a three - dimensional model. *Earth Surface Processes* **2**: 401-416.
- Buffington JM, Montgomery DR. 1997. A systematic analysis of eight decades of incipient motion studies, with special reference to gravel-bedded rivers. *Water Resources Research* **33**(8): 1993-2029.
- Callander RA. 1978. River meandering. *Annual Review of Fluid Mechanics* **10**: 129-158.
- Cao S. 1996. *Fluvial Hydraulic Geometry*. Chengdu University of Science and Technology Press, Chengdu.
- Carson MA. 1984. The meandering - braided river threshold: a reappraisal. *Journal of Hydrology* **73**: 315-334.
- Carson MA, Griffiths GA. 1987. Bedload transport in gravel channels. *Journal of Hydrology (NZ)* **26**(1): 1-151.
- Chang HH. 1979. Minimum stream power and river channel patterns. *Journal of Hydrology* **41**: 303-327.
- Charlton FG, Brown PM, Benson RW. 1978. The hydraulic geometry of some gravel rivers in Britain. *Report No. IT 180*, Hydraulics Research Station: Wallingford.
- Church M. 1985. Bed load in gravel-bed rivers: observed phenomena and implications for computation. *Canadian society for civil engineering annual conference, CSCE*. Saskatoon: 17-37.
- Church M, Hassan MA, Wolcott JF. 1998. Stabilizing self-organized structures in gravel-bed stream channels: field and experimental observations. *Water Resources Research* **34**(11): 3169-3179.

- Dade WB. 2000. Grain size, sediment transport and alluvial channel pattern. *Geomorphology* **35**: 119-126.
- Dade WB, Friend PF. 1998. Grain-size, sediment-transport regime, and channel slope in alluvial rivers. *Journal of Geology* **106**: 661-675.
- Davies TRH. 1987. Channel boundary shape – evolution and equilibrium. In *Rivers – Environment, Process and Form*, Richards K (ed). IBG Spec. Pub.: 228-248.
- Davies TRH, Sutherland AJ. 1983. Extremal hypotheses for river behavior. *Water Resources Research* **19**(1): 141-148.
- Davy BW, Davies TRH. 1979. Entropy concepts in fluvial geomorphology; a re-evaluation. *Water Resources Research* **15**: 505-512.
- Dietrich WE, Kirchner JW, Ikeda H, Iseya F. 1989. Sediment supply and the development of the coarse surface layer in gravel-bedded rivers. *Nature* **340**: 215-217.
- Dietrich WE, Smith JD. 1983. Processes controlling the equilibrium bed morphology in river meanders. In *River Meandering*. ASCE: 759-769.
- Dooge JCI. 1986. Looking for hydrologic laws. *Water Resources Research* **22**(9): 46S-58S.
- Eaton BC, Lapointe MF. 2001. Effects of large floods on sediment transport and reach morphology in the cobble-bed Sainte Marguerite River. *Geomorphology* **40**: 291-309.
- Einstein HA, Barbarossa NL. 1951. River channel roughness. *Proceedings of the American Society of Civil Engineers* **78**: 1121-1132.
- Einstein HA, Shen HW. 1964. A study on meandering in straight alluvial channels. *Journal of Geophysical Research* **69**(24): 5239-5247.
- Engelund F, Skovgaard O. 1973. On the origin of meandering and braiding in alluvial streams. *Journal of Fluid Mechanics* **57**(2): 289-302.
- Everitt BL. 1968. Use of the cottonwood in an investigation of the recent history of a flood plain. *American Journal of Science* **266**: 417-439.
- Ferguson RI. 1986. Hydraulics and Hydraulic Geometry. *Progress in Physical Geography* **10**(1): 1-31.
- Ferguson RI. 1987. Hydraulic and sedimentary controls of channel pattern. In *Rivers – Environment, Process and Form*, Richards K (ed). IBG Spec. Pub.: 129-158.
- Ferguson RI. 2003. The missing dimension: effects of lateral variation on 1-D calculations of fluvial bedload transport. *Geomorphology* **56**(1-2): 1-14.
- Flintham TP, Carling PA. 1988. The prediction of mean bed and wall boundary shear in uniform and compositely roughened channels. *International Conference On River Regime*, John Wiley & Sons, White WR (ed). Chichester: 267-287.
- Fredsoe J. 1978. Meandering and braiding of rivers. *Journal of Fluid Mechanics* **84**(4): 609-624.
- Friedkin JF. 1945. A laboratory study of the meandering of alluvial rivers, US Waterways Engineering Experimental Station: Vicksberg.
- Garcia M, Nino Y. 1993. Dynamics of sediment bars in straight and meandering channels: experiments on the resonance phenomenon. *Journal of Hydraulic Research* **31**(6): 739-761.
- Gessner FB, Jones JB. 1965. On some aspects of fully-developed turbulent flow in rectangular channels. *Journal of Fluid Mechanics* **23**(4): 689-713.
- Gilbert GK. 1914. The transport of debris by running water. *Professional Paper 86*, United States Geological Survey: Washington.
- Gomez B, Church M. 1989. An assessment of bed load sediment transport formulae for gravel bed rivers. *Water Resources Research* **25**(6): 1161-1186.

- Gottesfeld AS, Gottesfeld LMJ. 1990. Floodplain dynamics of a wandering river, dendrochronology of the Morice River, British Columbia, Canada. *Geomorphology* **3**: 159-179.
- Griffiths GA. 1984. Extremal hypotheses for river regime: an illusion of progress. *Water Resources Research* **20**(1): 113-118.
- Henderson FM. 1966. *Open Channel Flow*. MacMillan, New York.
- Hey RD, Thorne CR. 1986. Stable channels with mobile gravel beds. *Journal of the Hydraulics Division-Asce* **112**(8): 671-689.
- Hickin EJ. 1984. Vegetation and river channel dynamics. *Canadian Geographer* **28**(2): 111-123.
- Hooke R. 1968. Model geology; prototype and laboratory streams; Discussion. *Geological Society of America Bulletin* **79**(3): 391-393.
- Hooke R. 1975. Distribution of sediment transport and shear stress in a meander bend. *Journal of Geology* **83**(5): 543-565.
- Howard AD. 1988. Equilibrium models in geomorphology. In *Modelling Geomorphological Systems*, Anderson MG (ed). John Wiley & Sons: Chichester: 49-72.
- Huang HQ, Nanson GC. 1998. The influence of bank strength on channel geometry: an integrated analysis of some observations. *Earth Surface Processes and Landforms* **23**: 865-876.
- Huang HQ, Nanson GC. 2000. Hydraulic geometry and maximum flow efficiency as products of the principle of least action. *Earth Surface Processes and Landforms* **25**: 1-16.
- Ikeda S. 1984. Prediction of alternate bar wavelength and height. *Journal of Hydraulic Engineering* **110**(14): 371-386.
- Inglis CC. 1949. The behaviour and control of rivers and canals, Central Waterpower Irrigation and Navigation Research Station: Poona, India.
- Jaeggi MNR. 1986. Non distorted models for research on river morphology. *Proceedings of the Symposium on scale effects in modelling sediment transport phenomena*, IAHS: 70-84.
- Johannesson H, Parker G. 1989. Linear theory of river meanders. In *River Meandering*, Ikeda S, Parker G (eds). Water Resources Monograph. American Geophysical Union: 181-213.
- Keller EA. 1972. Development of alluvial stream channels: a five-stage model. *Bulletin of the Geological Society of America* **83**: 1531-1536.
- Kellerhals R, Church M. 1989. The morphology of large rivers: characterization and management. *Proceedings of the International Large River Symposium*, Dodge DP (ed). Ottawa: 31-48.
- Kennedy RG. 1895. The prevention of silting in irrigation canals. *Proceedings, Institution of Civil Engineers* **119**: 281-290.
- Kirkby MJ. 1977. Maximum sediment efficiency as a criterion for alluvial channels. In *River Channel Changes*, Gregory KJ (ed). John Wiley & Sons: Chichester: 429-442.
- Knight DW. 1981. Boundary shear in smooth and rough channels. *Journal of the Hydraulics Division-Asce* **107**(7): 839-851.
- Knight DW, Demetrious JD, Hamed ME. 1984. Boundary shear in smooth rectangular channels. *Journal of the Hydraulics Division-Asce* **10**(4): 405-422.
- Knighton D. 1998. *Fluvial Forms and Processes*. John Wiley & Sons, New York.
- Komar PD. 1987. Selective grain entrainment by a current from a bed of mixed sizes: a reanalysis. *Journal of Sedimentary Petrology* **57**(2): 203-211.
- Lacey G. 1930. Stable channels in alluvium. *Proceedings of the Institution of Civil Engineers* **229**: 259-384.
- Lane EW. 1955. Design of stable channels. *American Society of Civil Engineers, Transactions* **120**: 1234-1260.

- Lane EW. 1957. A study of the shape of channels formed by natural streams flowing in erodible material, US Army Eng. Div., Missouri River: Omaha, Nebraska.
- Langbein WB, Leopold LB. 1966. River meanders – theory of minimum variance. *Professional Paper 422H*, United States Geological Survey: Washington.
- Leopold LB, Maddock T. 1953. The hydraulic geometry of stream channels and some physiographic implications. *Professional Paper 252*, United States Geological Survey: Washington.
- Leopold LB, Wolman MG. 1957. River channel patterns; braided meandering and straight. *Professional Paper 282B*, United States Geological Survey: Washington.
- Leopold LP, Wolman MG, Miller JP. 1964. *Fluvial Processes in Geomorphology*. WH Freeman, San Francisco.
- Lewin J. 1976. Initiation of bed forms and meanders in coarse-grained sediment. *Geological Society of America Bulletin* **87**: 281-285.
- Lewin J, Brewer PA. 2001. Predicting channel patterns. *Geomorphology* **40**: 329-339.
- Li RM, Simons DB, Stevens MA. 1976. Morphology of cobble streams in small watersheds. *Journal of the Hydraulics Division-Asce* **102**(HY8): 1101-1117.
- Lindley ES. 1919. Regime canals. *Proceedings, Punjab Engineering Congress*: 63-74.
- Mackin JH. 1948. Concept of the graded river. *Geological Society of America Bulletin* **59**: 463-512.
- Meyer-Peter E, Muller R. 1948. Formulas for bed-load transport. *Int. Ass. Hyd. Struct. Res: 2nd Meeting, Proceedings*. Stockholm.
- Millar RG. 1999. Grain and form resistance in gravel-bed rivers. *Journal of Hydraulic Research* **37**(3): 303-312.
- Millar RG. 2000. Influence of bank vegetation on alluvial channel patterns. *Water Resources Research* **36**(4): 1109-1118.
- Millar RG, Quick MC. 1993. Effect of bank stability on geometry of gravel rivers. *Journal of Hydraulic Engineering-Asce* **119**(12): 1343-1363.
- Millar RG, Quick MC. 1998. Stable width and depth of gravel-bed rivers with cohesive banks. *Journal of Hydraulic Engineering-Asce* **124**(10): 1005-1013.
- Montgomery DR, Buffington JM. 1998. Channel processes, classification, and response. In *River Ecology and Management*, Naiman RJ, Bilby RE (eds). Springer-Verlag: New York: 13-42.
- Muhlhofer L. 1933. Untersuchung uber die schwebestoff- und geschiebefuhrung des Inn nachst Kirchbichl. *Die Wasserwirtschaft* No. 1-6.
- O'Connor JE, Jones MA, Haluska TL. 2003. Flood plain and channel dynamics of the Quinault and Queets Rivers, Washington, USA. *Geomorphology* **51**: 31-59.
- Odgaard AJ. 1989a. River-meander model. I: Development. *Journal of Hydraulic Engineering* **115**(11): 1433-1450.
- Odgaard AJ. 1989b. River-meander model. II: Applications. *Journal of Hydraulic Engineering* **115**(11): 1451-1464.
- Paola C. 2002. Modelling stream braiding over a range of scales. In *Gravel-Bed Rivers V*, Mosley MP (ed). Caxton Press: Christchurch: 9-46.
- Parker G. 1976. On the cause and characteristic scales of meandering and braiding in rivers. *Journal of Fluid Mechanics* **76**(3): 457-480.
- Parker G. 1979. Hydraulic geometry of active gravel rivers. *Journal of the Hydraulics Division-Asce* **105**: 1185-1201.
- Parker G. 1990. Surface-based bedload transport relation for gravel rivers. *Journal of Hydraulic Research* **28**(4): 417-436.

- Parker G, Anderson AG. 1975. Modelling of meandering and braiding in rivers. *Proceedings of the ASCE Modelling Symposium*, American Society of Civil Engineers. San Francisco: 575-591.
- Parker G, Dhamotharan S, Stefan H. 1982. Model experiments on mobile, paved gravel bed streams. *Water Resources Research* **18**(5): 1395-1408.
- Parker G, Klingeman PC. 1982. On why gravel bed rivers are paved. *Water Resources Research* **18**(5): 1409-1423.
- Parker G, Peterson AW. 1980. Bar resistance of gravel-bed streams. *Journal of the Hydraulics Division, ASCE* **106**(HY10): 1559-1575.
- Peakall J, Warburton J. 1996. Surface tension in small hydraulic river models – the significance of the Weber number. *Journal of Hydrology (NZ)* **35**(2): 199-212.
- Pickup G, Rieger WA. 1979. A conceptual model of the relationship between channel characteristics and discharge. *Earth Surface Processes* **4**(1): 37-42.
- Pickup G, Warner RF. 1984. Geomorphology of tropical rivers II: Channel adjustments to sediment load and discharge in the Fly and Lower Purari, Papua New Guinea. In *Channel Processes – Water, Sediment Catchment Controls*, Schick AP (ed). Catena Supplement: 19-41.
- Pryce RS, Ashmore PE. 2003. Particle path length distributions in meandering gravel-bed streams: results from physical models. *Earth Surface Processes and Landforms* **28**: 951-966.
- Rhoads BL, Welford MR. 1991. Initiation of river meandering. *Progress in Physical Geography* **15**(2): 127-156.
- Richards K. 1982. *Rivers: Form and Process in Alluvial Channels*. Methuen and Co., London.
- Schumm SA. 1963. A tentative classification of alluvial river channels. *Circular 477*, United States Geological Survey: Washington.
- Schumm SA. 1969. River metamorphosis. *Journal of the Hydraulics Division-Asce* **95**(HY1): 255-273.
- Schumm SA. 1971. Fluvial geomorphology; channel adjustment and river metamorphosis. In *River Mechanics*, Shen HW (ed): Fort Collins: 22.
- Schumm SA, Khan HR. 1972. Experimental study of channel patterns. *Geological Society of America Bulletin* **83**: 1755-1770.
- Schumm SA, Mosley MP, Weaver WE. 1987. *Experimental Fluvial Geomorphology*. John Wiley & Sons, New York.
- Simons DB, Albertson ML. 1963. Uniform water conveyance channels in alluvial material. *American Society of Civil Engineers, Transactions* **128**: 65-107.
- Smith CE. 1998. Modeling high sinuosity meanders in a small flume. *Geomorphology* **25**: 19-30.
- Stevens MA. 1989. Width of straight alluvial channels. *Journal of Hydraulic Engineering* **115**(3): 309-326.
- Sun T, Meakin P, Jossang T. 2001. A computer model for meandering rivers with multiple bed load sediment sizes 1.Theory. *Water Resources Research* **37**(8): 2227-2241.
- Talbot T, Lapointe M. 2002a. Modes of response of a gravel bed river to meander straightening: The case of the Sainte-Marguerite River, Saguenay Region, Quebec, Canada. *Water Resources Research* **38**(6): 1073, 1010.1029/2001wr000324.
- Talbot T, Lapointe M. 2002b. Numerical modeling of gravel bed river response to meander straightening: The coupling between the evolution of bed pavement and long profile. *Water Resources Research* **38**(6): 1074, 1010.1029/2001WR000330.
- Thorn CE, Welford MR. 1994. The equilibrium concept in geomorphology. *Annals of the Association of American Geographers* **84**(4): 666-696.

- Todd SP. 1996. Process deduction from fluvial sedimentary structures. In *Advances in Fluvial Dynamics and Stratigraphy*, Carling PA, Dawson MR (eds). John Wiley & Sons: Chichester: 299-350.
- Tominaga A, Ezaki K, Nakagawa H. 1989. Three-dimensional turbulent structure in straight open channel flows. *Journal of Hydraulic Research* **27**(1): 149-173.
- Tracy HJ. 1965. Turbulent flow in a three-dimensional channel. *Journal of the Hydraulics Division-Asce* **9**(HY6): 9-35.
- Tritton DJ. 1988. *Physical Fluid Dynamics*. Oxford University Press, New York.
- Van den Berg JH. 1995. Prediction of alluvial channel pattern of perennial rivers. *Geomorphology* **12**: 259-279.
- Van Rijn LC. 1984. Sediment transport, Part I: Bed load transport. *Journal of Hydraulic Engineering* **110**(10): 1431-1456.
- Werner PW. 1951. On the origin of river meanders. *Transactions, American Geophysical Union* **32**(6): 898-902.
- White WR, Bettess R, Paris E. 1982. Analytical approach to river regime. *Journal of the Hydraulics Division-Asce* **108**(HY10): 1179-1193.
- Wilcock PR. 1993. Critical shear stress of natural sediments. *Journal of Hydraulic Engineering* **119**(4): 491-505.
- Wilcock PR, Southard JB. 1989. Bed load transport of mixed size sediment: fractional transport rates, bed forms, and the development of a coarse bed surface layer. *Water Resources Research* **25**(7): 1629-1641.
- Yalin MS. 1971a. On the formation of dunes and meanders. *Proceedings of the 14th Congress of the International Association of Hydraulic Research*: 1-8.
- Yalin MS. 1971b. *Theory of Hydraulic Models*. MacMillan, Toronto.
- Yang CT. 1976. Minimum unit stream power and fluvial hydraulics. *Journal of the Hydraulics Division-Asce* **102**(HY7): 769-784.